KU LEUVEN

FACULTEIT INDUSTRIËLE INGENIEURSWETENSCHAPPEN

CAMPUS BRUGGE

Building on Mars: geopolymers from in situ resources

Jasper VITSE

Promotor: Prof. dr. Veerle Vandeginste

Co-promotors: Prof. Dr.-Ing. Jiabin Li

MSc Jiawei Tan

Masterproef ingediend tot het behalen van de graad van master of Science in de industriële wetenschappen: Bouwkunde

Academiejaar 2021-2022

Preface

This Master's thesis 'Building on Mars: geopolymers from in situ resources' is the final piece of the curriculum for obtaining the degree of Master of Science in Engineering Technology: Construction. With this thesis I finish my four year trajectory as student Industrial Engineering Sciences at the KU Leuven Campus Bruges. My interest in both chemistry and construction was the motivation behind the choice of this Master's thesis subject.

In the beginning of the Master year, during the month of September, I did my internship at prefab concrete company Lithobeton, in Snaaskerke. My supervisor during that internship told me about the interests and upcoming demanding interest of several companies for geopolymer concrete. With my specific interest in concrete technology and the chemical processes behind the manufacturing procedures made this Master's thesis subject suitable for me.

The subject of this thesis is unique, innovative and challenging for me. During my research work, I could combine the acquired knowledge from my education to apply it in this Master's thesis. During the period from July 2021 to June 2022 in the Master year, I worked on the research by doing literature review in the first semester, preparing and performing laboratory tests in the first part of the second semester and finally writing this Master's thesis typescript.

In the first place, I would like to thank my promotor Prof. dr. Veerle Vandeginste and co-promotors Prof. Dr.-Ing. Jiabin Li and MSc Jiawei Tan for assisting me in carrying out the research and their expertise. Every week, I could contact them to give an insight into my progress in the research work for this Master's thesis. Without their feedback and advice I would not have achieved these interesting results and further developed my knowledge.

A special acknowledgment to PhD researcher Jiawei Tan for explaining several convenient calculation methods for geopolymers. Therefore, I got some new insights to set up a good design method and time schedule. This preparatory work has helped me in better understanding the influence of different factors on geopolymers. For the statistical analysis and interpretation of the data I was assisted by Mr. Rudy Briers. Especially for setting up prediction intervals for outliers, his knowledge within the domain of statistics was quite useful. Therefore a special word of thanks to Mr. Rudy Briers for his assistance during my research work.

During the laboratory research in the second semester, problems arose with the dimensioning of the cylindrical mould of the pellet press. Due to the good work of my promotor Prof. dr. Veerle Vandeginste and Mrs. Joke Margodt, it was possible to contact the manufacturing company Laarmann. Eventually, this problem could be solved internally on the campus in Bruges. Dr. ing. Steven Fevery also deserves a word of thanks for helping me by making the cylinders with the correct dimensions.

My parents Pieter and Nathalie Vitse-Boydens, girlfriend Marie Marchand, Hélène Vandewalle and other colleague-students also deserve a sincere word of thanks for encouraging me to achieve this end result in the research on this quite challenging subject.

Finally, I would like to thank everyone who has supported me in making this Master's thesis. By working on this challenging research project, I was able to gain new insights and, above all, I further developed myself as a person and a fully-fledged engineer.

Jasper Vitse

Bruges, June 2022

Samenvatting

Het onderwerp van deze masterproef richt zich naar het onderzoek van geopolymeren om te kunnen bouwen op de planeet Mars. Het haalbaar maken van leven elders dan op Aarde, op een andere planeet zoals Mars, is namelijk één van de doelstellingen van de Amerikaanse ruimtevaartinstelling National Aeronautics and Space Administration (NASA).

Onze planeet Aarde heeft reeds te maken met een handvol problemen. De exponentiële bevolkingsgroei, klimaatveranderingen, toenemende vervuiling en risico's voor pandemieën vormen een bedreiging voor de mensheid. De uitbraak van COVID-19 is een actueel voorbeeld hiervan. Daarnaast heeft de mensheid meer en meer interesse in ruimtereizen en manieren om de ruimte te ontdekken. Zo werd afgelopen zomer, meer bepaald op 20 juli 2021, de eerste toeristische ruimtevlucht met succes uitgevoerd door het ruimtevaartbedrijf Blue Origin.

Door het samenspel van allerhande factoren heeft de mensheid nood aan een andere plaats om te kunnen overleven. De planeet Mars wordt door reeds voorgaand onderzoek uitgesproken als de meest haalbare kaart voor potentieel leven van de mensheid op een andere planeet.

Vooraleer het mogelijk is om een verre reis naar Mars te maken, is het voorbereidende werk cruciaal om deze doelstellingen succesvol te kunnen volbrengen. De ruimtereis is namelijk niet zonder risico en zal met de toenemende evolutie van de technologie steeds haalbaarder vooropgesteld worden. Eens toegekomen op de planeet Mars, moet er een mogelijkheid zijn om daar te kunnen overleven. Vandaar dat dit onderzoek eerst bestudeert wat de atmosferische condities zijn op deze planeet.

Verder wordt een tweede piste ingeslagen, namelijk het ontwerp van bouwmaterialen. Deze materialen moeten duurzaam zijn en kunnen voldoen aan de extreem lage temperaturen en drukken. Zo zal het bouwen met energie-efficiëntie toepassingen en het gebruik van duurzame materialen niet over het hoofd mogen gezien worden.

Om een geschikt bouwmateriaal te kunnen ontwerpen, moet de context namelijk groter gezien worden dan enkel en alleen maar het bouwen op de planeet Mars. In eerste instantie moet de mogelijkheid voor transport van de Aarde naar Mars in overweging genomen worden. Wat blijkt uit wetenschappelijk vastgelegde feiten, is dat de afstand tussen de planeet Aarde en Mars veel te groot is om een economisch transport van grondstoffen op Aarde naar Mars over te brengen. Door de hoge brandstofkost en de ruimtereis van ongeveer 9 maanden naar Mars, maakt het noodzakelijk om lokaal beschikbare materialen te gebruiken. Deze zogenaamde in situ grondstoffen zullen de basis vormen voor het ontwerp van een duurzaam geopolymeer.

Deze masterproef bevat een belangrijk aandeel literatuurstudie naar de atmosferische en geologische condities op Mars, en naar de eigenschappen van geopolymeren. Daarnaast is het ook de bedoeling om een reeks geopolymeren te ontwerpen en produceren die voldoen aan de vooropgestelde eisen van mechanische en chemische eigenschappen. Naast de literatuurstudie zullen via testen in laboratoriumonderzoek de vooropgestelde verwachtingen kunnen geëvalueerd worden via geregistreerde meetdata.

In de literatuurstudie zal eerst bestudeerd worden wat de extreme condities op Mars inhouden. Hierbij zal ook gezocht worden naar mogelijke beschikbare grondstoffen die kunnen gebruikt worden om te bouwen op de planeet Mars. De bodemsamenstelling en de beschikbaarheid van water zullen hierbij cruciale parameters zijn.

Naast de focus op Mars, zal de term ‘geopolymeer’ verder uitgespit worden. De zoektocht naar duurzame en in situ materialen leidt tot het gebruik van geopolymeren. Deze geopolymeren zullen in eerste instantie dienen om een waardig alternatief voor cement te bieden. Door de lage uitstoot en milieu impact worden deze materialen alsmaar populairder in verschillende bouwkundige toepassingen. De bedoeling is ook dat deze geopolymeren voldoen aan de extreme condities op Mars.

De geopolymeren zullen ontworpen worden gebruik makend van de gesimuleerde Mars ruwe grondstof MGS-1 (Mars Global Simulant). De eigenschappen van deze gesimuleerde grondstof maken het mogelijk om een inschatting te kunnen maken naar de werkelijke stof op Mars. Door de grote hoeveelheid aan keramische mineralen die in de bodem van Mars aanwezig zijn, zal het maken van een geopolymeer via een alkali activatie mogelijk worden. Dit is dé reden waarom gebruik gemaakt wordt van materialen als geopolymeren.

Naast de literatuurstudie, wordt in het onderzoek ook labowerk uitgevoerd. Hierbij zal een ontwerp gemaakt worden van een reeks duurzame geopolymeren die verschillen in chemische samenstelling en uithardingstijd. Om dit ontwerp van de geopolymeren te kunnen maken, zal eerst teruggekoppeld worden naar de literatuurstudie.

De bedoeling van deze reeks geproduceerde geopolymeren is dat de chemische en mechanische eigenschappen van deze materialen voldoen aan de vooropgestelde vereisten. Door het uitvoeren van labotesten zal de chemische en mechanische karakterisering kunnen gebeuren van deze geopolymeren. De chemische karakterisering zal gebeuren door de analyse van de verschillende microstructuren en de samenstelling van de functionele groepen in de moleculen, gebruik makende van FTIR analyses. Voor de mechanische karakterisering zal vooral gefocust worden op de belangrijkste eigenschap voor structurele toepassingen van materialen, namelijk de druksterkte.

Om de vooropgestelde eisen te halen om een alternatief te kunnen vormen voor cement, zal gebruik gemaakt worden van additieven. Deze extra toegevoegde materialen zullen ervoor moeten zorgen dat voldoende sterkte en chemische integriteit gegarandeerd kan worden. In dit onderzoek, waarbij gebruik wordt gemaakt van MGS-1 als gesimuleerde Mars ruwe grondstof, zal metakaoliniet gebruikt worden als additief. De keuze voor het gebruik van metakaoliniet als toeslagmateriaal heeft als doel om de hoeveelheid Al_2O_3 te verhogen. Hierdoor zal het proces van geopolymerisatie positief bevorderd worden.

Het mengselontwerp van de geopolymeren wordt bepaald door de variërende concentraties aan alkali activatoren. Er worden twee soorten geopolymeren gemaakt, een eerste soort op basis van $NaOH$ (8M, 10M en 12M) en een tweede soort op basis van $LiOH.H_2O$ (6M, 8M, 10M en 12M). De bedoeling van dit onderzoek is om op zoek te gaan naar de meest geschikte geopolymeer, gebruik makend van kubusvormige (20x20x20 mm) en cilindervormige (ø20x40 mm) geopolymeren. Vandaar dat een grote hoeveelheid aan variaties in het mengselontwerp zal doorgevoerd worden.

Voor de kubusvormige geopolymeren worden in totaal 11 verschillende mengselontwerpen uitgevoerd, goed voor 120 kubusvormige geopolymeren. Hierbij worden ook 18 cementmengsels (Holcim CEM I 52.5R HES) gemaakt volgens dezelfde vochtverhouding als van geopolymeren, om zo de vergelijking te kunnen maken tussen de sterkte van de geopolymeren en traditioneel cement. De cilindervormige geopolymeren bestaan in totaal uit 7 verschillende samenstellingen, goed voor 83 cilindervormige geopolymeren. In totaliteit worden 203 geopolymeren aangemaakt in groepen van drie of zes per samenstelling.

Daarnaast worden ook nog 18 cementmengsels aangemaakt en getest om dit onderzoek te vervolledigen en een vergelijking te kunnen maken tussen de verschillende mengsels.

De uitharding van de geopolymeren gebeurt in de oven op 70 °C. Zo worden de druksterktes opgemeten na 1 dag, 3 dagen, 7 dagen en na 28 dagen voor de geopolymeren waarbij reeds een goede sterkte werd vastgesteld in het vroege stadium.

De beste resultaten voor de druksterkte van de geopolymeren werd gevonden voor de geopolymeren op basis van $\mathrm{LiOH.H_2O}$. Zowel voor de kubusvormige als cilindervormige geopolymeren wordt de grootste druksterkte bekomen, na 7 dagen uitharden in de oven op 70°C, voor de geopolymeersamenstelling van 8M $\mathrm{LiOH.H_2O} + 7.5\ \mathrm{g\ NaOH}$.

De kubusvormige geopolymeren behalen een druksterkte van 23 ± 3 MPa, terwijl de cilindervormige geopolymeren een druksterkte van 30 ± 2 MPa. De hogere sterkte voor de cilindervormige geopolymeren lijkt in eerste instantie niet onze verwachtingen te volgen. De reden hiervoor is de optimale en uniforme verdichting van de cilindervormige geopolymeren met een pellet press, terwijl dit bij de kubusvormige geopolymeren handmatig gebeurde. Hierdoor kon de verdichting van de kubusvormige geopolymeren niet gelijkmatig gebeuren, waardoor een grotere spreiding en onzekerheid op de resultaten wordt verwacht.

Deze resultaten liggen boven de lijn van de verwachtingen, aangezien initieel gestreefd werd om een minimale druksterkte van 10 MPa te behalen. Bij een recente studie van Chakraborty (2019) op een andere gesimuleerde Mars ruwe grondstof, MMS-1 (Mojave Mars Simulant), werd een maximale druksterkte van slechts 5 MPa behaald. In deze studie werden geopolymeermengsels op basis van NaOH gemaakt. In vergelijking met Holcim CEM I 52.5R HES mengsels, worden gemiddelde druksterktes van 78 MPa behaald, na 7 dagen uitharden in de oven op 70 °C. Volgens de literatuur wordt de druksterkte van cement bepaald na uitharding op kamertemperatuur, waarbij typische sterktes van 35-40 MPa kunnen behaald worden na 28 dagen uitharden op kamertemperatuur (Civil Lead, 2022).

De FTIR analyses voor de geopolymeren met de grootste druksterkte vertonen drie duidelijke pieken volgens het golflengtespectrum. De eerste twee pieken bij golflengtes van 3350 $\mathrm{cm^{-1}}$ en 1630 $\mathrm{cm^{-1}}$ houden respectievelijk verband met de rektrillingen van $-\mathrm{OH}$ groepen en watermoleculen. De piek die waargenomen wordt bij een golflengte van 967 $\mathrm{cm^{-1}}$ vertegenwoordigt de $\mathrm{Si-O-Si}$ asymmetrische rektrillingen in het geopolymeermengsel.

Finaal zal deze meest geschikte geopolymeer verder kritisch bestudeerd worden en kan op deze manier een stapje dichter gezet worden naar een mogelijkheid om te kunnen bouwen op Mars. De menselijke missie én uitdaging voor het mogelijk maken van leven op Mars zullen via de hedendaagse technologieën en ontwikkelingen mogelijk gemaakt kunnen worden. Dit onderzoek naar geopolymeren van in situ grondstoffen vormt alvast een belangrijk aandeel in een potentieel menselijk leven op Mars.

Abstract

The subject of this Master's thesis focuses on the research of geopolymers for building on the planet Mars. Making life feasible elsewhere than on Earth, on another planet such as Mars, is one of the goals of the American space agency ‘National Aeronautics and Space Administration’ (NASA).

Our planet Earth is already dealing with several global challenges. Exponential population growth, climate changes, increasing pollution and risks for pandemics are a threat to humanity. The outbreak of the COVID-19 pandemic is a recent example of this. In addition, humanity is increasingly interested in space travel and ways to explore space. For example, last summer, on 20 July 2021, the first tourist space flight was successfully carried out by the space company Blue Origin.

Due to the interplay of all kinds of factors, humanity needs another place to survive. The planet Mars has been proposed by previous research as the most feasible place for human potential life on another planet.

Before it is possible to make a long journey to Mars, the preparatory work is crucial to successfully accomplish these objectives. Space travel is not without any risk and will become increasingly feasible with the increasing evolution of technology. Once arrived on the planet Mars, there must be a possibility to survive there. That is why this research will first study the atmospheric conditions on this planet.

A second track is also being taken, namely the design of building materials. These materials must be durable and able to withstand extremely low temperatures and pressures. For example, building with energy efficiency applications and the use of sustainable materials should not be overlooked.

In order to be able to design a suitable building material, the context has to be seen as bigger than just building on the planet Mars. Initially, the possibility of transport from Earth to Mars must be considered. What appears from scientifically established facts is that the distance between the planet Earth and Mars is far too great to transfer an economic transport of raw materials on Earth to Mars. Due to the high fuel costs and the space journey of about 9 months to Mars, it is necessary to use locally available materials. These so-called in situ raw materials will form the basis for the design of a sustainable geopolymer.

This Master's thesis contains an important part of literature review on the atmospheric and geological conditions on Mars, and the properties of geopolymers. In addition, it is also the intention to design and make a series of geopolymers that meet the predefined requirements for mechanical and chemical properties. In addition to the literature review, laboratory research will make it possible to evaluate the proposed expectations by measured data.

In the literature review, the extreme conditions on Mars will first be studied. This will also involve looking for possible available resources that can be used to build on the planet Mars. The soil composition and the availability of water will be crucial parameters here.

In addition to the focus on Mars, the term 'geopolymer' will be further explored. The need for sustainable and in situ materials leads to the use of geopolymers. These geopolymers will initially serve to fulfill a worthy alternative to cement. Due to the low emissions and environmental impact, these materials are becoming increasingly popular in various

architectural applications. The goal is that these geopolymers also meet the extreme conditions on Mars.

The geopolymers will be designed using the simulated Mars raw material MGS-1 (Mars Global Simulant). The properties of this simulated raw material make it possible to estimate the actual dust on Mars. Due to the large amount of ceramic minerals in the Martian soil, it will be possible to make a geopolymer through alkali activation. This is the reason why materials such as geopolymers are used.

In addition to the literature study, laboratory work is also a part of this research. A design will be made of a series of durable geopolymers that differ in chemical composition and curing time. In order to be able to make this design of the geopolymers, an extensive literature review will first be conducted into important properties and compositions of geopolymers.

The purpose of this range of geopolymers produced is that the chemical and mechanical properties of these materials meet the specified requirements. By performing laboratory tests, the chemical and mechanical characterisation of these geopolymers will be possible. The chemical characterisation will be done by the analysis of the different microstructures and the composition of the functional groups in the molecules, using FTIR analyses. For the mechanical characterisation, the main focus will be on the most important property for structural applications of materials, namely the compressive strength.

Additives will be used to meet the predefined requirements to be an alternative to cement. These extra added materials will have to ensure that sufficient strength and chemical integrity can be guaranteed. In this research, using MGS-1 as a simulated Mars raw regolith material, metakaolin will be used as an additive. The choice to use metakaolin as an additive is mainly based on increasing the amount of Al_2O_3. This will positively enhance the global process of geopolymerisation.

The mix design of the geopolymers is determined by varying the concentrations of alkali activators. Two types of geopolymers are made, a first type based on $NaOH$ (8M, 10M and 12M) and a second type based on $LiOH.H_2O$ (6M, 8M, 10M and 12M). The aim of this research is to find the most suitable geopolymer, using cube (20x20x20 mm) and cylindrical geopolymers (ø20x40 mm). Hence, a great amount of variations in mix design will be carried out.

A total of 11 different mix designs are performed for the cube geopolymers, accounting for 120 cube geopolymers. In addition, 18 cement mixtures (Holcim CEM I 52.5R HES) are made according to the same moisture ratio as for geopolymers, in order to be able to compare the strength of the geopolymers and traditional cement. The cylindrical geopolymers consist of a total of 7 different compositions, accounting for 83 cylindrical geopolymers. In total, 203 geopolymers are made in groups of three or six per composition. In addition, 18 cement mixtures are also being prepared and tested, in order to complete this research and to be able to make a comparison between the different mixtures.

The curing of the geopolymers takes place in the oven at 70 °C. According to the different curing times, compressive strengths are measured after 1 day, 3 days, 7 days and after 28 days for the geopolymers, for which a good strength was already gained in the early stage.

The best results for the compressive strength of the geopolymers were achieved for the geopolymers based on $LiOH.H_2O$. Both for the cube and cylindrical geopolymers, the highest

compressive strength is obtained for the geopolymer composition of 8M $\mathrm{LiOH.H_2O}$ + 7.5 g NaOH, after curing in the oven at 70°C for 7 days.

The cube geopolymers achieve a compressive strength of 23 $\pm$ 3 MPa, while the cylindrical geopolymers obtain a compressive strength of 30 $\pm$ 2 MPa. The higher strength for the cylindrical geopolymers does not initially seem to follow our expectations. The reason for this is the optimal and uniform compaction of the cylindrical geopolymers with a pellet press, while this was done manually for the cube geopolymers. As a result, the densification of the cube geopolymers could not be done uniformly, which is why a greater variability and uncertainty in the results is expected.

These results are above expectations, as the initial aim was to achieve a minimum compressive strength of 10 MPa. A recent study by Chakraborty (2019) on another simulated Mars raw regolith material, MMS-1 (Mojave Mars Simulant), achieved a maximum compressive strength of only 5 MPa. In this study, geopolymer mixtures based on NaOH were made. Compared to Holcim CEM I 52.5R HES mixtures, average compressive strengths of 78 MPa are achieved after curing in the oven at 70 °C for 7 days. According to literature, the compressive strength of cement is determined after curing at room temperature, with typical strengths of 35-40 MPa, after 28 days of ambient curing (Civil Lead, 2022).

The FTIR analysis for the highest compressive strength geopolymers show three distinct peaks according to the wavelength spectrum. The first two peaks at wavelengths of 3350 $\mathrm{cm^{-1}}$ and 1630 $\mathrm{cm^{-1}}$ are respectively related to the stretching vibrations of $-\mathrm{OH}$ groups and water molecules. The peak observed at wavelength of 967 $\mathrm{cm^{-1}}$ represents the $\mathrm{Si-O-Si}$ asymmetric stretching vibrations in the geopolymer mixture.

Finally, the most suitable geopolymer will be further critically studied to provide a possibility to build on Mars. The human mission and challenge for enabling life on Mars can be made possible through today's improving technologies and developments. This research into geopolymers of in situ raw materials from Mars is already an important step closer for potential human life on Mars.

Keywords: geopolymers; Mars; sustainable materials; cement; FTIR; compressive strength.

Building on Mars: geopolymers from in situ resources

Jasper Vitse[1], Veerle Vandeginste[2], Jiabin Li[3], Jiawei Tan[3], Rudy Briers[4]

[1]Department of Engineering Technology, Master Construction, KU Leuven
[2]Department of Materials Science, Functional Materials (SIEM), KU Leuven
[3]Department of Engineering Technology, Building Materials and Constructions, KU Leuven
[4]Department of Engineering Technology, Core Research and Engineering, KU Leuven

Faculty of Engineering Technology
KU Leuven, Campus Bruges
8200 Bruges, Belgium

***Abstract* — Making life feasible elsewhere than on Earth is one of the goals of the American space agency NASA. Future manned missions to Mars will require the ability to build structures using in situ natural resources. This study focuses on the geopolymerisation of the Martian regolith simulant MGS-1 with the aim to build structures on Mars. Sodium hydroxide, lithium hydroxide and sodium silicate are used as alkali activators during the geopolymerisation process. Next to MGS-1, metakaolin is used as additive to increase the amount of Al_2O_3 of the geopolymer precursor. Metakaolin is available on Mars to use as additive. By varying the alkali concentrations in a range of 6M to 12M, and analysing the mechanical and chemical properties, the most optimal geopolymer mixture will be determined. Both cube and cylindrical geopolymer samples are tested during this study. After oven curing at 70 °C for 7 days, the geopolymer composition of 8M $LiOH.H_2O$ + 7.5 g NaOH obtained the best results in terms of compressive strength. The manual compacted cube geopolymers achieve a compressive strength of 23 ± 3 MPa, while the cylindrical geopolymers, compacted by use of a pellet press, obtain a compressive strength of 30 ± 2 MPa.**

The FTIR analysis for the highest compressive strength geopolymers show three distinct peaks according to the wavelength spectrum. The first two peaks at wavelengths of 3350 cm^{-1} and 1630 cm^{-1} are respectively related to the stretching vibrations of -OH groups and water molecules. The peak observed at wavelength of 967 cm^{-1} represents the Si-O-Si asymmetric stretching vibrations in the geopolymer mixture. This high strength geopolymers indicate the possibility to use this geopolymers for structural purposes. The research shows that lithium hydroxide performs better than sodium hydroxide. This offers further possibilities for the optimisation of the mixture design with lithium hydroxide to obtain even better mechanical properties.

***Keywords* — geopolymer; Mars; MGS-1; lithium hydroxide; compressive strength; FTIR.**

I. INTRODUCTION

The planet Mars (also called the Red Planet) seems to have potential to accommodate humans to live, since researchers have found water sources on this planet. In 2013, indications were obtained for the presence of flowing water. By using the MOXIE (Mars Oxygen In Situ Resource Utilisation Experiment) technology, on April 20th, 2021, Marsrover Perseverance produced oxygen from carbon dioxide in the Martian atmosphere by using solid oxide electrolysis. MOXIE heats Martian carbon dioxide to around 800 °C, this heating process separates oxygen and generates carbon monoxide as a by-product [1].

These technical innovations and recent findings are an indication of the possibility to generate oxygen on Mars. These developments could ensure the realisation of human life on Mars. To shield the oxygen from the carbon-rich atmosphere on Mars, oxygen needs to be produced in a restricted area, which is not in direct contact with the harmful atmosphere of the Red Planet. To build such a restricted area on the planet Mars, building materials are needed appropriate for Mars' extreme environment. The distance between Earth and Mars varies from 54.6 million kilometers to 401 million kilometers, because of the different orbits from Mars and the Earth. The average distance between Earth and Mars is recorded as 225 million km [2]. Due to the high cost of travel and the long trip to Mars, it is not economic to transport water, aggregates, binders, etc. from Earth to Mars because of the long distance between the two planets. To tackle this fundamental problem of high travelling cost, it is almost obligated to use the local materials or also called 'in situ materials'.

Next to the high travelling cost, extreme environmental conditions prevail on Mars. This makes the design of new building materials challenging. The average surface temperature is -63 °C with a maximum daily temperature difference of 60 °C [3]. These lower temperatures are a result of the fact that the planet Mars is further away from the sun than Earth. Also the pressure is only 0.7 % compared to the pressure on Earth, which means that there are almost vacuum conditions on Mars. Several researchers are working on new ideas and ways of innovation to enable human life on the Red Planet. The

goal of this research is to find a suitable geopolymer that is made from the local materials available on Mars. This research is based on the application of MGS-1 (Mars Global Simulant), which is obtained from Gale Crater on Mars.

Alexiadis *et al*. (2017) and Chakraborty (2019) already performed studies on the geopolymerisation of JSC MARS-1A and MMS-1 Martian simulants [4] [5]. Only compressive strengths of respectively 2.5 ± 0.3 MPa after 28 days oven curing at 80 °C and 5.0 ± 0.3 MPa after 7 days oven curing at 90 °C were obtained. Since these studies do not yet show a suitable result for the geopolymerisation of Martian simulants, further research is needed. This research can therefore be seen as an extension of previous studies. A further optimisation based of the good results from previous studies will be made.

In addition, the use of lithium hydroxide as an alkali activator makes this research interesting and innovative. Chen *et al*. (2012) set up an experiment for the geopolymerisation of geopolymer bricks with lithium hydroxide as alkali activator [6]. However, no further research has yet been conducted on the use of lithium hydroxide as an alkali activator for geopolymerisation. Specifically for this study of geopolymers to make building on Mars possible, the use of lithium hydroxide is recommended because this material can offer good resistance to the high galactic cosmic rays on Mars [7].

In this study the results will be presented of the geopolymers made on the basis of sodium hydroxide, lithium hydroxide and sodium silicate as alkali activators. An answer will be provided to the following research question: *"How can we develop a series of geopolymers from in situ Martian materials to build on Mars?"*.

II. Methodology

A. Experimental methodology

The choice of composition and concentrations for the alkali activators was based on a study on the geopolymerisation of another simulated Martian raw material, namely MMS-1 [5]. To achieve an optimal geopolymer composition, two different alkali activators were used. Initially, a series of geopolymers were made, based on sodium hydroxide. Since already many geopolymers have already been made with this commonly used alkali activator, the use of sodium hydroxide is a reliable choice. In addition to the geopolymers made with NaOH as an alkali activator, geopolymers were also made based on lithium hydroxide monohydrate. These two alkali activators will be dissolved in a sodium silicate solution until the desired concentrations are reached. The sodium silicate solution has a chemical composition of 7.9 % Na_2O and 25.9 % SiO_2. From the formation reaction of sodium silicate in Equation 1, the mass and volume concentration can be determined.

$$Na_2O + SiO_2 \rightarrow Na_2SiO_3 \quad (1)$$

The mass percentage w% of the sodium silicate solution is calculated as 11.6 w% Na_2SiO_3, the volume percentage V% is equal to 8.66 V% Na_2SiO_3. The alkali solution is added to the geopolymer precursor MGS-1 and mixed for 3 minutes per 200 ml of geopolymer mixture.

Based on Table 1, it appears that the Martian regolith MGS-1 is very rich in SiO_2 (50.8 w%), but consists to a lesser extent of Al_2O_3 (8.9 w%) and CaO (3.7 w%) [8]. The presence of these three main components are crucial to achieve an efficient geopolymerisation. To increase the amount of Al_2O_3, the decision was made to add the clay mineral kaolinite $Al_2O_3.2SiO_2.2H_2O$ to geopolymer precursor MGS-1. Because kaolinite itself does not show the highest reactivity, it was decided to convert this kaolinite into metakaolin [9]. This is done by putting the kaolinite in a furnace for 180 minutes at 650 °C. The process that takes place during the conversion of kaolinite to metakaolin is called calcination. Due to the heating process of kaolinite, the water between the atoms evaporates. The evaporation of water molecules during the calcination process results in a mass reduction. To enable the conversion of kaolinite into metakaolin, a mass of 50 g of kaolinite was weighed each time the calcination reaction was activated. After the conversion of kaolinite into metakaolin, a mass reduction of 6 g was observed with respect to this 50 g weighed kaolinite. The calcination process changes the internal atomic structure of kaolinite and forms an amorphous aluminosilicate $Al_2O_3.2SiO_2$ [10]. The reaction occurring during this dihydroxylation of kaolinite is presented by Equation 2.

$$Al_2O_3.2SiO_2.2H_2O \xrightarrow{\text{heating at 650 °C}} Al_2O_3.2SiO_2 + 2.H_2O\uparrow \quad (2)$$

Table 1: Chemical composition of Rocknest and MGS-1 [8].

Oxide	RN bulk[a]	Calc. MGS-1[b]	RN amorph.[c]	Calc. MGS-1 amorph.[b]	MGS-1 prototype
SiO_2	43.0	48.3	34.2	47.0	50.8
TiO_2	1.2	0.2	2.1	0.6	0.3
Al_2O_3	9.4	9.5	5.4	7.0	8.9
Cr_2O_3	0.5	0.1	1.4	0.2	0.1
FeO_T	19.2	16.9	23.0	21.0	13.3
MnO	0.4	0.1	1.2	0.2	0.1
MgO	8.7	12.1	4.0	9.9	16.7
CaO	7.3	6.7	4.4	4.5	3.7
Na_2O	2.7	2.6	3.3	1.0	3.4
K_2O	0.5	0.1	1.4	0.3	0.3
P_2O_5	1.0	0.2	2.7	0.6	0.4
SO_3	5.5	3.2	13.9	7.7	2.1
Cl	0.7	0.0	2.0	0.0	–
SUM	100.1	100.0	99.9	100.0	100.0

For this research, 11 different geopolymer compostions are made from NaOH-based geopolymers and 7 different geopolymer compostions from LiOH-based geopolymers. The different geopolymer compositions are obtained by varying the alkali activator concentations in a range of 6M to 12M. The geopolymer samples are produced in cube moulds of 20x20x20 mm and cylindrical moulds of Ø20x40 mm, as shown in Figure 1. After the cube moulds were completely filled and compacted, a plastic film was applied before being placed in the oven at a constant temperature of 70 °C. The reason for applying the film is to prevent water evaporation during the curing process of the geopolymers. From Figure 1 it is also shown that the cylindrical samples can be demoulded fast, while the cube samples require a longer curing time due to the poorer compaction technique.

Figure 1: Cylindrical and cube geopolymer samples.

The compaction of the geopolymer samples is a determining factor for the compressive strength of the geopolymers. For the cube samples, manual compaction was performed by pressing the cubes with a pestle in 10 successive layers, as shown in Figure 2.

Figure 2: Manual compaction of cube geopolymer samples.

The cylindrical samples are produced and compacted by use of a pellet press, as shown in Figure 3. This device performs compaction in 4 equal layers, each time with an imposed compression force of 250 kg. The applied compression force can be converted into compressive pressure by Equation 3.

$$\sigma = \frac{F}{A_{cylinder}} \quad (3)$$

From the known compression force of 250 kg and the dimensions of the cylindrical samples of Ø20x40 mm, the compressive pressure per layer can be calculated using Equation 3. This results in a compressive pressure of 7.81 MPa per layer.

$$\sigma = \frac{250\ \text{kg} \times 9.81\ \text{m/s}^2}{\frac{\pi \times (0.020\ \text{m})^2}{4}} = 7.81 \times 10^6\ \text{N/m}^2 = 7.81\ \text{MPa}$$

Figure 3: Pellet press for compaction of cylindrical geopolymer samples.

The mix design for the geopolymers is based on previous studies for the geopolymerisation of lunar and Martian simulants [4] [5] [11]. An important factor for the mix design is the factor representing the ratio between the liquid activator and the solid aluminosilicate material. The study by Montes et al. (2015) shows that the activator/aliminosilicate ratio is optimally 0.32 for a geopolymer composition based on simulated lunar regolith Lun-Cast-3D [11]. For this MGS-1 geopolymerisation study, the activator/aluminosilicate volume ratio is set at 0.3. This volume ratio was fixed for all experiments. Furthermore, the volume ratio of the amount of metakaolin to MGS-1 was empirically fixed at 0.2.

Besides the volume ratios of the activators and the solid aluminosilicate components, the influence of the concentration of the activators is important. Based on the study of Chakraborty (2019), it was determined to make 3 different concentrations (8M, 10M, 12M), of both NaOH and $LiOH.H_2O$ [5]. During the further progress of this research, based on the foregoing results, it was decided to also make an additional concentration of 6M for the $LiOH.H_2O$-based geopolymers.

To increase the reactivity of the simulated Mars raw material, the standard MGS-1 with average grain size of 122 µm was grinded by using Laarmann's LMBR500 Bottle Roller, for a duration of 6 hours [12]. This grinding device for the MGS-1 is shown in Figure 4. Mixing the MGS-1 reduces the average grain size from 122 µm to a lower fraction. By grinding the MGS-1 into finer powder, the surface area where the reactions take place will increase. Due to the higher surface area, there will be an increase in the frequency of chemical collisions. This results in a higher rate of reaction [13].

Figure 4: LMBR 500 Bottle Roller for grinding the MGS-1.

After the geopolymer mixtures have been fully assembled, mixed and compacted, they must be oven-cured for 1 day, 3 days, 7 days or 28 days at a constant temperature of 70 °C. The study by Chakraborty (2019) shows that curing geopolymer mixtures at room temperature shows less good results than oven curing. During that study, the geopolymers were cured in the oven at two different temperatures, which are 60 °C and 90 °C [5]. The decision to set the oven at a temperature of 70 °C is because this is a default temperature for the curing process of geopolymers. Rovnaník (2010) shows that metakaolin-based geopolymers gain the highest mechanical strength for oven curing at 60 °C and 80 °C [14]. Thanks to the reliable results already obtained from these previous studies on geopolymers, a constant curing temperature of 70 °C is used for the geopolymers in this study [11].

During the production of the geopolymers with $LiOH.H_2O$ as alkali activator, it was found that $LiOH.H_2O$ is not well soluble in the sodium silicate solution. This could be determined theoretically because of the lower solubility of lithium hydroxide. The solubility of lithium hydroxide is only 12.8 g per 100 g of water, and this at a temperature of 293.15 K [15]. In addition, sodium hydroxide, at the same temperature, has a solubility of no less than 111 g per 100 g of water. Hence, it was determined experimentally to add 5 g of NaOH to the $LiOH.H_2O$. This creates an exothermic reaction, whereby the heat produced will ensure that the $LiOH.H_2O$ dissolves more easily in the sodium silicate solution. This addition of sodium silicate will compensate for the poorly soluble character of lithium hydroxide. The improved solubility of the lithium hydroxide through adding 5 g of sodium silicate pellets is clearly visible by the fact that the poorly soluble lithium hydroxide substances actually start to dissolve. The large insoluble flakes begin to concentrate into smaller, soluble particles. This improved solubility is reflected in the appearance of the mixture, which appears more turbid than initially.

B. Analytical methodology

Fourier Transform Infrared Spectroscopy (FTIR) is used as a technique to analyse the vibrational energy in molecules [16]. The device that has been used in this research is PerkinElmer FTIR, as presented in Figure 5. While performing this analysis, the bonds between two atoms are studied at micro level. Finally, a graph will be obtained where the amount of transmission (in %) is displayed on the ordinate. The wavelength spectrum is shown on the abscissa. From an FTIR analysis, the infrared spectrum of adsorption or emission of a solid, liquid or gas can be determined. Based on the different peaks that can be observed, the functional groups in molecules can be identified.

Figure 5: PerkinElmer FTIR device.

C. Material testing

The MacBen compression test, as shown in Figure 6, is used to perform the mechanical characterisation of the geopolymers, in terms of compressive strength. This compression test is of the 2-cylinder 300 kN type, with digital automatic compression control. Depending on the test samples (cube or cylindrical geopolymers), other setting parameters must be configured to the device. Important setting parameters for the this test device are the rate at which the force increases, the start load, the final load and the surface area of the test specimen.

Figure 6: MacBen compression test for mechanical characterisation.

The effect of the use of the bottle roller on the average grain size of the Martian raw material is recorded with the Keyence laser microscope, as shown in Figure 7. This microscope uses a triple scanning approach, where scanning methods with the confocal laser or camera are used to measure objects. This allows a 3D representation of the object to be studied. By adjusting the magnification of the objective lens from 2.5x to 100x, a detailed image can be obtained of the grain distribution of MGS-1. Besides determining the mean grain size of MGS-1,

Figure 7: Keyence laser microscope for determining the effect of grinding MGS-1 and calcination of kaolinite.

this microscope is also used for the effect on the grain size after calcination of the kaolinite into metakaolin. Here, both kaolinite and metakaolin are studied at different scales relative to each other. From the analysis before and after the treatment of the material, an estimation can be made of the average grain size within a specific studied zone of the material. The effect of grinding MGS-1 and calcination of kaolinite is discussed in section III Results and discussion.

III. Results and Discussion

A. Compressive strength of geopolymers

The mechanical characterisation of the geopolymers is based on the compressive strength results. First, the results of the cube specimens are discussed, then the cylindrical ones. The results are presented as their mean value $\bar{x}$ from the set of three or six specimens tested, with their uncertainty factored in as one times the sample standard deviation s. The compressive strength f_c is thus defined as: $f_c = \bar{x} \pm s$.

In some cases, the compressive strength values are indicated in red. This indicates that one or more outliers were present in the data set of the measured values. These outliers were removed from the data set, in order to obtain representative values for the compressive strength. Prediction intervals are used to detect whether or not a measurement is an outlier, since it cannot be assumed that the measured values are normally distributed. Therefore, the use of prediction intervals is an objective way of making judgments about outliers from randomly distributed data.

Initially, the the compressive strength values for the cube NaOH-based geopolymers are shown in Table 2. It can be seen that the lowest 8M NaOH concentration performs the best of the three different concentrations, with an early developed strength with relatively high standard deviation of 4 MPa after 3 days, and then a decrease in strength after 7 days occurs. The other 10M and 12M NaOH samples achieve 64 % and 72 % respectively of the final strength of the 8M NaOH sample after 7 days. The samples formed with these two higher concentrations gradually increase in strength, with each an increment of 1 MPa as the curing time progresses to 3 and 7 days. It is also noted that these samples show a lower variability than the 8M NaOH concentration. As a result, it can be stated that these samples create a more reliable image in terms of strength.

Table 2: Compressive strength values for NaOH-based cube geopolymers.

sample	$f_{c,1d}$ $[MPa]$	$f_{c,3d}$ $[MPa]$	$f_{c,7d}$ $[MPa]$
8M NaOH - 70°C oven cured	**8 ± 2**	**16 ± 4**	**11 ± 2**
10M NaOH - 70°C oven cured	**5 ± 1**	**6 ± 2**	**7 ± 2**
12M NaOH - 70°C oven cured	**7.4 ± 0.7**	**7 ± 2**	**8 ± 1**

From Table 3, the $LiOH.H_2O$-based geopolymers show higher compressive strengths than the NaOH-based geopolymers. Initially, during the exploration phase, only geopolymers were made, composed of 8M, 10M and 12M $LiOH.H_2O$. It should be noted that the 10M $LiOH.H_2O$ samples show the highest compressive strength after 7 days, with an average compressive strength of 34 MPa. This geopolymer composition shows a substantially linear increase as function of curing time. The 8M $LiOH.H_2O$ concentration develops a high strength of 26 MPa, especially in the initial phase. After curing for 3 days, this strength drops to a value of 20 MPa. Besides the linear strength development of the 10M $LiOH.H_2O$ sample, the 12M $LiOH.H_2O$ samples show a curved trend for the increase in strength. Together with the 6M $LiOH.H_2O$ concentration, these geopolymer compositions develop the lowest strengths of the four different mixtures. The compressive strength for the 6M $LiOH.H_2O$ samples remains almost constant at a value of 10 MPa. It is also remarkable that the variability of the strong 8M and 10M $LiOH.H_2O$ samples is significantly higher than that of the 6M and 12M samples.

Table 3: Compressive strength values for $LiOH.H_2O$ + 5 g NaOH-based cube geopolymers.

sample	$f_{c,1d}$ $[MPa]$	$f_{c,3d}$ $[MPa]$	$f_{c,7d}$ $[MPa]$
6M LiOH.H2O + 5g NaOH - 70°C oven cured	**9 ± 2**	**10 ± 3**	**10 ± 2**
8M LiOH.H2O + 5g NaOH - 70°C oven cured	**26 ± 2**	**20 ± 4**	**20 ± 8**
10M LiOH.H2O + 5g NaOH - 70°C oven cured	**17 ± 2**	**23 ± 4**	**34 ± 7**
12M LiOH.H2O + 5g NaOH - 70°C oven cured	**7 ± 1**	**11.7 ± 0.5**	**16 ± 1**

By using the pellet press for the production of the cylindrical geopolymers, the results are expected to be more accurate. The reason for this is that the compaction can take place in a more controlled manner. Initially, the NaOH-based

geopolymers are investigated for their strength development over time. The results show that a low average compressive strength of 6 MPa is achieved after curing for 28 days. The cylindrical sample compressive strength value of 4 MPa, obtained after 7 days is only 36 % of the compressive strength obtained with the cube geopolymer samples.

A slightly increasing trend is observed in the strength development profile, but in absolute terms the compressive strength of the 8 M NaOH sample remains almost constant. As a result, it can be concluded that the compressive strength for this cylindrical geopolymer mixture is independent of curing time. In addition, there is a large degree of uncertainty in these results, due to the outliers in the data set after 1 day, 3 days and 28 days. For the compressive strength value after 1 day of curing, only one compressive strength value of 4 MPa could be maintained, since the other two compressive strength values were considered as outliers.

Table 4: Compressive strength values for NaOH-based cylindrical geopolymers.

sample	$f_{c,1d}$ [MPa]	$f_{c,3d}$ [MPa]	$f_{c,7d}$ [MPa]	$f_{c,28d}$ [MPa]
8M NaOH - 70°C oven cured	4	3.62 ± 0.01	4.0 ± 0.4	6 ± 3

It was rapidly established, during the exploration phase of this research with the cube geopolymer mixtures, that the $LiOH.H_2O$-based geopolymers showed a better strength development than the NaOH-based geopolymers. Therefore, the decision was taken to make the cylindrical geopolymer mixtures mainly with $LiOH.H_2O$ as alkali activator. For both the 6M and 8M $LiOH.H_2O$ + 5 g NaOH-based geopolymers, the evolution of the compressive strength was studied after 1 day, 3 days, 7 days and 28 days curing in the oven at 70 °C.

Both geopolymer mixtures develop the same compressive strength in the initial stage of curing. A compressive strength of 18 MPa is reached for both concentrations of $LiOH.H_2O$. Between 1 day and 3 days of curing, the largest jump in strength development is observed for both mixtures. After 3 days of curing, the strength increases slightly to 7 days of curing, the increase being only 1-2 MPa. When the geopolymers are further cured up to 28 days, a strong reduction in compressive strength is observed for both concentrations.

The 6M samples show the best average compressive strength after 28 days, with a value of 25 MPa. The trend of the compressive strength as a function of time is the same for both 6M and 8M samples. Compared to the evolution of compressive strength over time for the cube geopolymers with the same compositions, the 8M sample shows approximately the same trend for the compressive strength. The 6M sample shows a significantly better compression strength gradient for the cylindrical geopolymers than the cube geopolymers.

Table 5: Compressive strength values for $LiOH.H_2O$ + 5 g NaOH-based cylindrical geopolymers.

sample	$f_{c,1d}$ [MPa]	$f_{c,3d}$ [MPa]	$f_{c,7d}$ [MPa]	$f_{c,28d}$ [MPa]
6M LiOH.H2O + 5g NaOH - 70°C oven cured	18 ± 1	32.0 ± 0.3	33 ± 2	25 ± 7
8M LiOH.H2O + 5g NaOH - 70°C oven cured	18 ± 1	23 ± 5	25 ± 4	21 ± 4

With the cylindrical 6M $LiOH.H_2O$ + 5 g NaOH-based geopolymers, a compressive strength of a factor 3.3 times higher is registered than with the cube geopolymers of the same chemical composition.

B. FTIR analysis

The chemical characterisation of the different geopolymer mixtures is done by the analysis of the FTIR spectra. Initially, the FTIR spectra of the geopolymer precursors, metakaolin and MGS-1, are discussed. Subsequently, the different geopolymer mixtures are studied by the FTIR analysis. When analysing the different FTIR spectra, it is mainly important to characterise the different materials as a function of the peaks occurring in the wavelength spectrum [17].

Metakaolin is used as an additive for MGS-1 during geopolymerisation. The major peak in the amount of transmission is determined at wavelength of 1046 cm^{-1} . This wavelength represents the Si-O stretching vibrations. The broad adsorption bands on the IR spectrum at 793 cm^{-1} and 567 cm^{-1} refer to Si-O-Al vibrations and flexural vibrations, respectively.

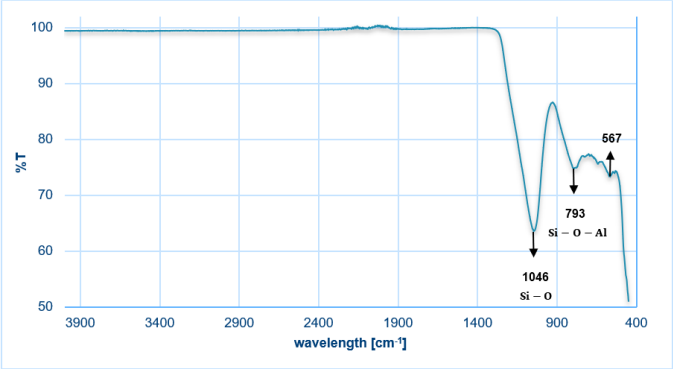

Figure 8: FTIR spectrum of metakaolin.

Since the simulated Mars raw regolith material MGS-1 is an aluminosilicate precursor, a similar strong peak to metakaolin is observed at wavelength of 1000 cm^{-1} in Figure 9. This wavelength refers to Si-O-Al asymmetric stretching vibrations within TO_4 tetrahedra typical of the amorphous aluminosilicates. The adsorption band at 1623 cm^{-1} refers to the bending vibrations of H-O-H. The peak at wavelength of 1440 cm^{-1} indicates atmospheric carbonation. Finally, the peak at 906 cm^{-1} refers to the symmetric Si-O bonds. As the amount of transmission decreases at low wavelengths, small peaks are observed at wavelength of 600 cm^{-1}. These peaks indicate the presence of silicates and aluminosilicate glasses in the raw MGS-1 regolith material.

From Figure 10, the NaOH-based geopolymers show almost the same pattern for the three different concentrations of 8M, 10M and 12M NaOH. A total of four different peaks can be observed in the FTIR diagram. The broad adsorption band at around 3342 cm^{-1} represent stretching vibrations of -OH groups and water molecules. The next peak is observed at a wavelength of 1640 cm^{-1}, which can be assigned to the bending vibrations of H-O-H. The peak at 1440 cm^{-1} corresponds to C-O stretching

vibrations from carbonate. Finally, the peak observed at 970 cm^{-1} represents the Si-O-Si asymmetric stretching vibrations.

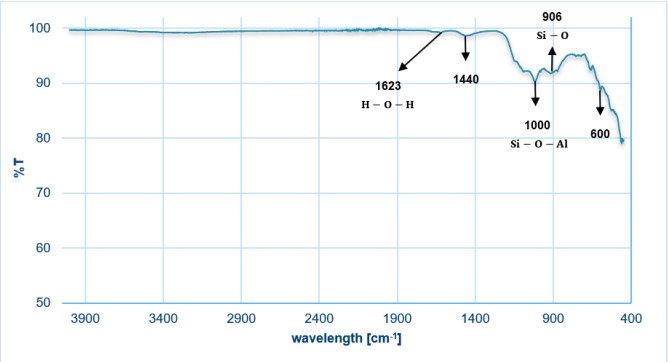

Figure 9: FTIR spectrum of MGS-1.

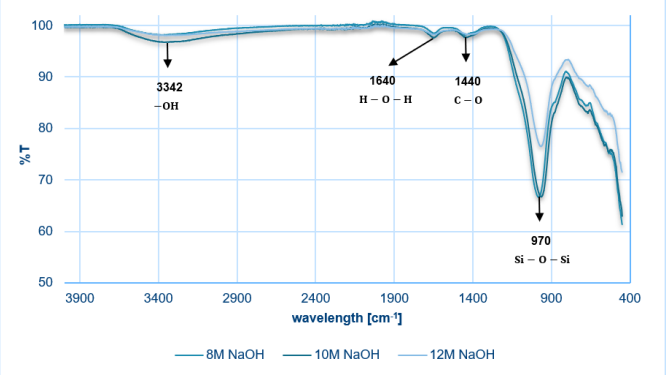

Figure 10: FTIR spectrum of NaOH-based cube geopolymers (1d cured).

In the $LiOH.H_2O$ + 5 g NaOH-based geopolymers, peaks are observed at wavelengths of 3379 cm^{-1}, 1648 cm^{-1} and 977 cm^{-1}. These observed peaks for the $LiOH.H_2O$ + 5 g NaOH-based geopolymer mixtures are related to stretching vibrations of -OH groups and water molecules, bending vibrations of H-O-H and Si-O-Si asymmetric stretching vibrations, respectively. Only little shifts in wavelengths are found for this geopolymer composition, compared to the NaOH-based geopolymers.

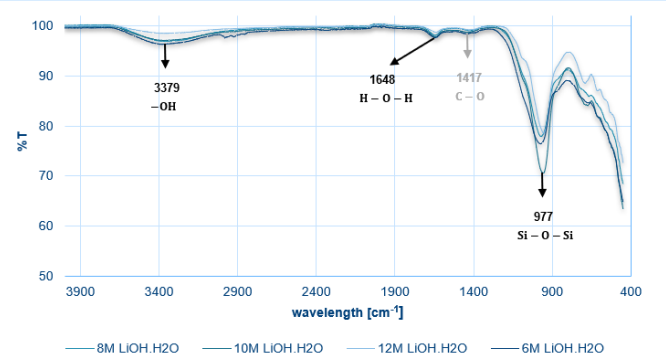

Figure 11: FTIR spectrum of $LiOH.H_2O$ + 5 g NaOH-based cube geopolymers (1d cured).

The biggest difference in the FTIR spectrum between the NaOH-based geopolymers and $LiOH.H_2O$ + 5 g NaOH -based geopolymers is the less pronounced peak at a wavelength of 1417 cm^{-1}. This indicates that the C-O stretching vibrations from carbonate are present to a lesser extent with LiOH. This implies that the $LiOH.H_2O$ + 5 g NaOH -based geopolymers have a shorter setting time and higher porosity [18]. As a result, the durability of NaOH-based geopolymers is expected to be better than that of $LiOH.H_2O$ + 5 g NaOH-based geopolymers. In addition, due to the shorter setting time of the $LiOH.H_2O$ + 5 g NaOH-based geopolymers, a higher early strength is expected compared to the NaOH-based geopolymers.

C. Effect of grinding and calcination on mean particle size

All the aluminosilicate-rich materials that are used in this research are investigated by the Keyence laser microscope. These materials are the rough MGS-1 regolith, the milled MGS-1, kaolinite and metakaolin. In each case a glass slide is used, where a suspension of the material to be tested in an alcohol solution was applied with the aid of a pipette. In this way, the most representative particle size distribution of the investigated material will be shown by using the Keyence laser microscope.

For the analysis with the Keyence laser microscope, the MGS-1 was studied at magnifications of 2.5x and 10x. These magnifications correspond to the scale of 300 µm and 100 µm.

When examining the microscopic images of the MGS-1 before grinding, it is clearly visible that there is a large variation between the different sizes of the grains in the material. Almost 40 % of the grains have a grain size of approximately 200 µm. All other grains have a grain size close to 100 µm. After grinding the MGS-1 with the Bottle Roller for 6 hours, it is clearly visible from Figure 13 that some large fractions of 200-250 µm remain, and that the average fraction has decreased to a grain size smaller than 63 µm. There are clearly much smaller grains present than was initially the case before grinding the MGS-1 regolith material.

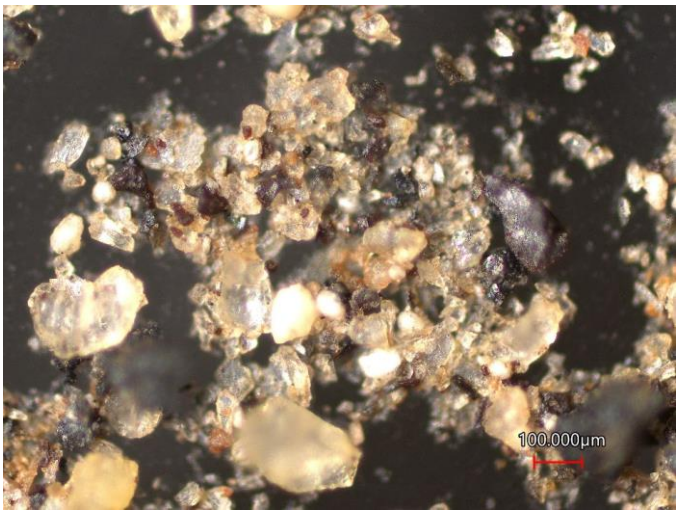

Figure 12: MGS-1 before grinding – scale bar 100 µm.

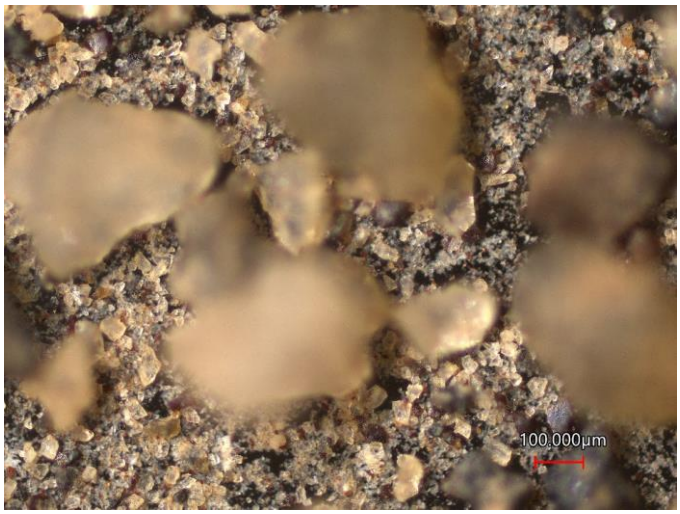

Figure 13: MGS-1 after grinding for 6 hours by Bottle Roller – scale bar 100 µm.

The effect of the calcination on the grain size of the original kaolinite additive is determined based on three different magnifications with the Keyence laser microscope, whereby magnifications of 2.5x, 10x and 50x are used. The reason for conducting the analysis here on a smaller scale is the fact that kaolinite is a clay mineral, and therefore consists of finer powder than is the case for the MGS-1.

No significant change in mean grain size before and after calcination can be observed from the microscopic images obtained at 50x magnification, in Figure 14 and Figure 15. It should also be noted here that the surface area of the grains after calcination is smaller due to the evaporation of water. From this analysis it can be concluded that calcination of kaolinite has no effect on the average particle size.

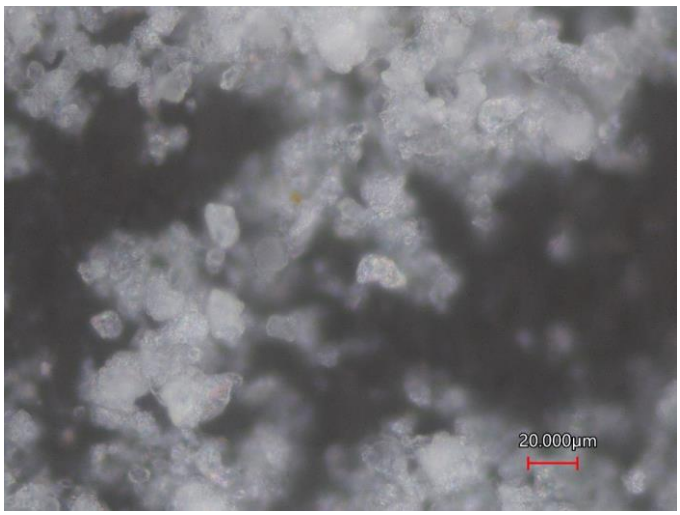

Figure 14: Kaolinite before calcination – scale bar 20 µm.

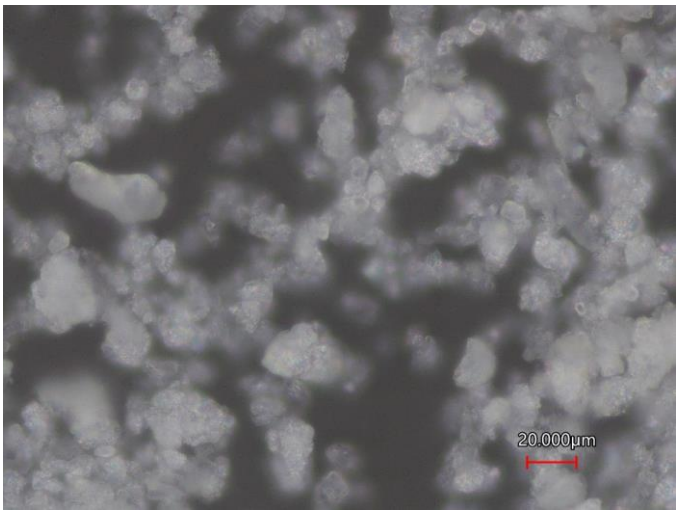

Figure 15: Metakaolin after calcination for 3 hours at 650 °C – scale bar 20 µm.

D. Most optimal geopolymer mixture

In order to make a judgment about the most optimal geopolymer mixture, the focus is on the cylindrical geopolymers. This is because they give more reliable results due to the uniform compaction with the pellet press. Among all tested geopolymer mixtures, the $LiOH.H_2O$ + 7.5 g NaOH-based geopolymers show the best results in terms of compressive strength. The strength development of these cylindrical geopolymers after 1 day, 3 days and 7 days is presented in Table 6, and graphically shown in Figure 16.

Table 6: $LiOH.H_2O$ + 7.5 g NaOH-based geopolymers (cylindrical samples).

sample	$f_{c,1d}$ $[MPa]$	$f_{c,3d}$ $[MPa]$	$f_{c,7d}$ $[MPa]$
6M LiOH.H2O + 7.5g NaOH - 70°C oven cured	**11 ± 2**	**21 ± 2**	**27 ± 5**
8M LiOH.H2O + 7.5g NaOH - 70°C oven cured	**19.7 ± 0.2**	**29 ± 1**	**30 ± 2**

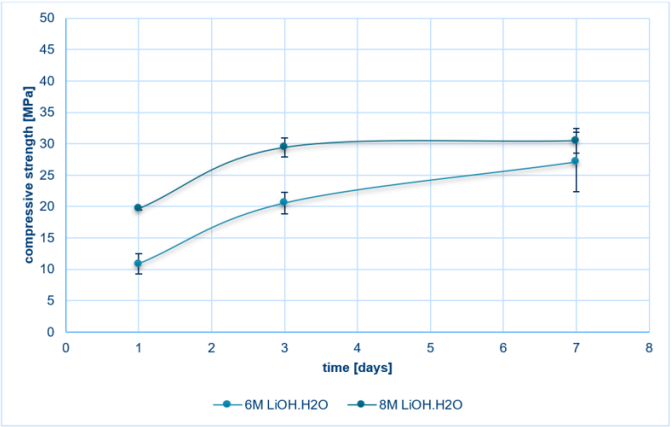

Figure 16: Most optimal geopolymer mixture; $LiOH.H_2O$ + 7.5 g NaOH-based geopolymers (cylindrical samples).

This good performance in terms of compressive strength can be observed for both the cube and cylindrical geopolymer mixtures. A total of two different concentrations were made of this $LiOH.H_2O$ + 7.5 g NaOH composition, both 6M and 8M. Both concentrations already give good early strength after 1 day, with compressive strengths of 11 MPa (6M $LiOH.H_2O$ + 7.5 g NaOH) and 20 MPa (8M $LiOH.H_2O$ + 7.5 g NaOH).

The increase in compressive strength is mainly perceived between 3 days and 7 days of curing at 70 °C. Finally, after 7 days, approximately the same strength is developed for both geopolymer mixtures, with a strength of 27 $\pm$ 5 MPa and 30 $\pm$ 2 MPa respectively for the 6M and 8M $LiOH.H_2O$ + 7.5 g NaOH-based geopolymers. When a specific selection is made of the best global geopolymer composition, the 8M $LiOH.H_2O$ + 7.5 g NaOH is declared as the winner. This geopolymer mixture develops an early strength, which means that it can be demoulded after a relatively short curing period. This early strength behaviour was already predicted from the FTIR analysis of the cube geopolymers, in section 5.3.3 of this Master's thesis. The C-O stretching vibrations from carbonate are present to a lesser extent with LiOH compared to NaOH. This implies that the $LiOH.H_2O$-based geopolymers have a shorter setting time and higher porosity compared to the NaOH-based geopolymers [18]. Due to the shorter setting time, a higher early strength is obtained, compared to the NaOH-based geopolymers. For use on Mars, this high early curing strength is an advantage, as structures can be built efficiently.

It can be said with certainty that the results for compressive strength of the most optimal geopolymer composition, namely $LiOH.H_2O$ + 7.5 g NaOH-based geopolymers, are reliable and representative. The representativeness of the measurement results is scientifically supported for the following four reasons:

1. The upward trend in the development of compressive strength is observed in both cube and cylindrical mixtures. The final strength for the same geopolymer compositions of the cube mixtures is also 22-23 MPa, while for the cylindrical mixtures it is 27-30 MPa.
2. Between the results for both the cube and cylindrical geopolymers, no outliers were identified by the prediction interval analysis. This implies that these geopolymers show statistically acceptable values for the increase in the compressive strength.
3. The variability of the results is limited. The measurement results of compressive strength for the 6M $LiOH.H_2O$ + 7.5 g NaOH-based geopolymers show a maximum standard deviation of 5 MPa. For the 8M $LiOH.H_2O$ + 7.5 g NaOH-based geopolymers, only a maximum sample standard deviation of 2 MPa is determined.
4. Each time three different samples were tested, eliminating as much as possible the random errors that can occur during the measurements.

From the statistical analysis, the most optimal geopolymer mixture is found as 8M $LiOH.H_2O$ + 7.5 g NaOH. The reason for the higher strength of the $LiOH.H_2O$-based geopolymers is because of the less pronounced C-O stretching vibrations from carbonate compared to the NaOH-based geopolymers. In the FTIR spectrum of the $LiOH.H_2O$-based geopolymers, a peak of 2924 cm^{-1} was observed in the cylindrical geopolymers, which can be attributed to C-H groups in the geopolymer matrix. This ensures that the mechanical strength of this geopolymer composition is better than the other geopolymers. In addition, lithium hydroxide is a strong base because it completely dissociates in an aqueous solution and produces a large number of OH^- ions.

IV. Conclusions

This research with the aim of developing a suitable geopolymer binder from in situ raw materials to build on Mars was a challenge for me. The research question is critically investigated by performing a combination of literature review and laboratory work.

Initially, it can be concluded that there are several challenges to make building and populating of the planet Mars possible. The extreme temperature variations, strong galactic cosmic rays and low pressure on Mars were examined. The materials for building on Mars must be able to withstand these extreme conditions. Geopolymers are used during this research because they require less water and energy than for the production of traditional Portland cement, and water is a scarce resource on Mars.

An innovative part of the research is that lithium hydroxide was used as activator for the geopolymerisation. Jones *et al*. (2020) showed that lithium hydroxide can provide good resistance to radiation [7]. To withstand the intense radiation on Mars, lithium hydroxide was used as alkali activator. For the investigation of simulated Martian raw regolith, lithium hydroxide has not previously been used to activate the geopolymerisation mechanism. Chen *et al*. (2012) conducted a study on the production of geopolymer bricks with 10M LiOH-based geopolymers [6]. A compressive strength of 9.4 MPa was measured after curing for 7 days at a temperature of 40 °C.

Compared to the average compressive strength of 30 MPa for the 8M $LiOH.H_2O$ + 7.5 g NaOH-based geopolymers and 34 MPa for the 10M $LiOH.H_2O$ + 5 g NaOH-based geopolymers, the compressive strengths reached in this research are 3 to 4 times higher than in the study Chen *et al*. (2012). Furthermore, hardly any studies were performed for the geopolymerisation with lithium hydroxide as alkali activator.

The results showed that the cube geopolymer samples are less reliable and representative in the results for the compressive strength. This is because a difficult uniform compaction could be performed for these geopolymer mixtures. The cylindrical geopolymer samples were compacted with the pellet press in four different layers, making the compressive strength results for these geopolymers more reliable than those of the cube geopolymer samples. The final conclusion from the laboratory tests is that $LiOH.H_2O$ + 7.5 g NaOH-based

geopolymers give the best results for compressive strength. Since lithium hydroxide achieved better results for compressive strength than sodium hydroxide, this is a positive and encouraging message to conduct further research with lithium hydroxide as activator.

The results of the laboratory work are satisfactory. When both the results of the cube and cylinder geopolymer samples are analysed, the same trends in final strength and strength development are found for the geopolymers based on 8M $LiOH.H_2O$ + 5 g NaOH, 6M $LiOH.H_2O$ + 7.5 g NaOH and 8M $LiOH.H_2O$ + 7.5 g NaOH. Since these representative results for the compressive strengths of both the cube and cylindrical geopolymer samples occur with the LiOH-based geopolymers, a strong geopolymer matrix is obtained.

The most optimal geopolymer mixture during this research is defined at 8M $LiOH.H_2O$ + 7.5 g NaOH. A combination of alkali activators lithium hydroxide and sodium hydroxide was added to a sodium silicate solution with chemical composition of 7.9 % Na_2O and 25.9 % SiO_2. Metakaolin was used as an additive for the simulated Mars raw regolith MGS-1 material. The volume ratio for the liquid activator/aluminosilicate material was set at 0.3. In addition, the volume ratio for the metakaolin/MGS-1 was fixed at 0.2.

The FTIR analysis for the highest compressive strength geopolymers show three distinct peaks according to the wavelength spectrum. The first two peaks at wavelengths of 3350 cm^{-1} and 1630 cm^{-1} are respectively related to the stretching vibrations of -OH groups and water molecules. The peak observed at wavelength of 967 cm^{-1} represents the Si-O-Si asymmetric stretching vibrations in the geopolymer mixture.

The use of lithium hydroxide as an alkali activator can certainly be further investigated. In this research, an impetus was already given to further research, in which better results are obtained for lithium hydroxide than for sodium hydroxide when added to sodium silicate.

V. Future research

This research can be seen as an exploration through the extensive field of interest in the world of geopolymers. A rough mix design was set up to vary as many different parameters as possible. It was important to discover the influence of the different parameters. The good results that were found in this research project may serve as an impetus for further research.

Acknowledgment

This study would not have been possible without promotor Prof. dr. Veerle Vandeginste and co-promotors Prof. Dr.-Ing. Jiabin Li and MSc Jiawei Tan. The authors would like to particularly thank Rudy Briers for the statistical analysis and interpretation of the data. During the laboratory research in the second semester, problems arose with the dimensioning of the cylindrical mould of the pellet press. Due to the good work of promotor Prof. dr. Veerle Vandeginste and Mrs. Joke Margodt, it was possible to contact the manufacturing company Laarmann. Eventually, this problem could be solved internally on the campus in Bruges. Dr. ing. Steven Fevery also deserves a word of thanks for helping by making the cylinders with the correct dimensions.

References

[1] Hecht, M., Hoffman, J., Rapp, D., McClean, J., SooHoo, J., Schaefer, R., ... & Ponce, A. (2021). Mars oxygen ISRU experiment (MOXIE). *Space Science Reviews*, *217*(1), 1-76.

[2] Dobrijevic, M., & Bertrix, I. (2022). Les satellites de Jupiter et la troisième loi de Kepler.

[3] Liu, J., Li, H., Sun, L., Guo, Z., Harvey, J., Tang, Q., ... & Jia, M. (2021). In-situ resources for infrastructure construction on Mars: A review. *International Journal of Transportation Science and Technology*.

[4] Alexiadis, A., Alberini, F., & Meyer, M. E. (2017). Geopolymers from lunar and Martian soil simulants. *Advances in Space Research*, *59*(1), 490-495.

[5] Chakraborty, S. (2019). *Geopolymerization of Simulated Martian Soil* (Doctoral dissertation, Tennessee Technological University).

[6] Chen, C., Li, Q., Shen, L., & Zhai, J. (2012). Feasibility of manufacturing geopolymer bricks using circulating fluidized bed combustion bottom ash. *Environmental technology*, *33*(11), 1313-1321.

[7] Jones, J. P., Jones, S. C., Billings, K. J., Pasalic, J., Bugga, R. V., Krause, F. C., ... & Brandon, E. J. (2020). Radiation effects on lithium CFx batteries for future spacecraft and landers. *Journal of Power Sources*, *471*, 228464.

[8] Rampe, E. B., Ming, D. W., Blake, D. F., Bristow, T. F., Chipera, S. J., Grotzinger, J. P., ... & Thompson, L. M. (2017). Mineralogy of an ancient lacustrine mudstone succession from the Murray formation, Gale crater, Mars. *Earth and Planetary Science Letters*, *471*, 172-185.

[9] Khalifa AZ, Cizer O, Pontikes Y et al. (2020) Advances in alkali-activation of clay minerals. *Cement and Concrete Research* 132: 106050

[10] Ilić, B., Radonjanin, V., Malešev, M., Zdujić, M., & Mitrović, A. (2016). Effects of mechanical and thermal activation on pozzolanic activity of kaolin containing mica. *Applied Clay Science*, *123*, 173-181.

[11] Montes, C., Broussard, K., Gongre, M., Simicevic, N., Mejia, J., Tham, J., ... & Davis, G. (2015). Evaluation of lunar regolith geopolymer binder as a radioactive shielding material for space exploration applications. *Advances in Space Research*, *56*(6), 1212-1221.

[12] Cannon, K. M., Britt, D. T., Smith, T. M., Fritsche, R. F., & Batcheldor, D. (2019). Mars global simulant MGS-1: A Rocknest-based open standard for basaltic martian regolith simulants. *Icarus*, *317*, 470-478.

[13] Sarraf-mamoory, R., Demopoulos, G.P. & Drew, R.A.L. Preparation of fine copper powders from organic media by reaction with hydrogen under pressure: Part II. The kinetics of particle nucleation, growth, and dispersion. *Metall Mater Trans B* 27, 585–594 (1996). https://doi.org/10.1007/BF02915656

[14] Rovnaník, P. (2010). Effect of curing temperature on the development of hard structure of metakaolin-based geopolymer. *Construction and building materials*, *24*(7), 1176-1183.

[15] Monnin, C., & Dubois, M. (2005). Thermodynamics of the LiOH+ H2O system. *Journal of Chemical & Engineering Data*, *50*(4), 1109-1113.

[16] Puligilla, S., & Mondal, P. (2015). Co-existence of aluminosilicate and calcium silicate gel characterized through selective dissolution and FTIR spectral subtraction. *Cement and Concrete Research*, *70*, 39-49.

[17] Wang, H., Li, H., & Yan, F. (2005). Synthesis and mechanical properties of metakaolinite-based geopolymer. *Colloids and Surfaces A: Physicochemical and Engineering Aspects*, *268*(1-3), 1-6.

[18] Wan-En, O., Yun-Ming, L., Li-Ngee, H., Abdullah, M. M. A. B., & Shee-Ween, O. (2020, June). The Effect of Sodium Carbonate on the Fresh and Hardened Properties of Fly Ash-Based One-Part Geopolymer. In *IOP Conference Series: Materials Science and Engineering* (Vol. 864, No. 1, p. 012197). IOP Publishing.

TABLE OF CONTENTS

List of figures

List of tables

List of symbols

a	Acceleration	[m/s²]
A	Area	[m²]
E	Young's modulus	[GPa]
E_e	Irradiance	[W/m²]
F	Force	[N]
f_c	Compressive strength	[MPa]
G	Electric conductance	[S]
I	Current	[A]
L	Length	[m]
m	Mass	[kg]
n	Amount of substance	[mol]
p	Pressure	[Pa]
P	Power	[W]
R	Resistance	[Ω]
t	Time	[s]
T	Temperature	[K]
U	Voltage	[V]
v	Velocity	[m/s]
V	Volume	[m³]
θ	Angle	[rad]
ρ	Density	[kg/m³]
γ	Specific weight	[N/m³]
ε	Strain	[mm/mm]
σ	Stress	[N/mm²]
λ	Wavelength	[m]

Abbreviations

ANFIS	Adaptive neuro-fuzzy interference system
ASR	Alkali silica reaction
ATR-FTIR	Attenuated Total Reflectance-Fourier Transform Infrared Spectroscopy
CRISM	Compact Reconnaissance Imaging Spectrometer Multispectral mapping
ESA	European Space Agency
FTIR	Fourier Transform Infrared Spectroscopy
GCRs	Galactic cosmic rays
GGBS	Ground granulated blast furnace slag
ICC	Isothermal Conduction Calorimetry
IPC	Inorganic polymer cement
ISRU	In situ resource utilisation
JSC-Mars	Johnson Space Center Simulant
MARIE	Mars Radiation Environment Experiment
MGS-1	Mars Global Simulant
MK	Metakaolin
MMS	Mojave Mars Simulant
MOXIE	Mars Oxygen In Situ Resource Utilisation Experiment
MRO	Mars Reconnaissance Orbiter
NASA	National Aeronautics and Space Administration
NMR	Nuclear Magnetic Resonance
OPC	Ordinary Portland Cement
PDF	Pair Distribution Function
RAD	Radiation Assessment Detector
RN	Rocknest
SEM	Scanning Electron Microscope
SEPs	Solar energetic particles

SF	Silica fume
TGO	Trace Gas Orbiter
WP	Work package
XRD	X-ray diffraction

1 INTRODUCTION

The aim of NASA (National Aeronautics and Space Administration) is to realise a permanent human presence on the Moon by 2024. As presented in Figure 1, the goal of NASA's ambitious project 'Journey to Mars' is to generate possible life on the planet Mars. When we want to live on Mars, residential buildings and infrastructure facilities are needed. There have already been many attempts to find other places in addition to Earth. Our planet Earth is subjected to a lot of challenges such as population increase, resource depletion, pollution and climate change.

The planet Mars (also called the Red Planet) seems to have potential to accommodate humans to live, since researchers have found water sources on this planet. In 2013, indications were obtained for the presence of flowing water. Measurements showed that during an evening a kind of salt layer forms in the top five centimeters of the soil, and this evaporated again in the morning (Thomas *et al*., 2019). NASA's first confirmation of the presence of water on Mars was given in 2015. Mars explorer Curiosity took measurements and discovered a source of flowing salt water along the mountain slopes on Mars during the summer period.

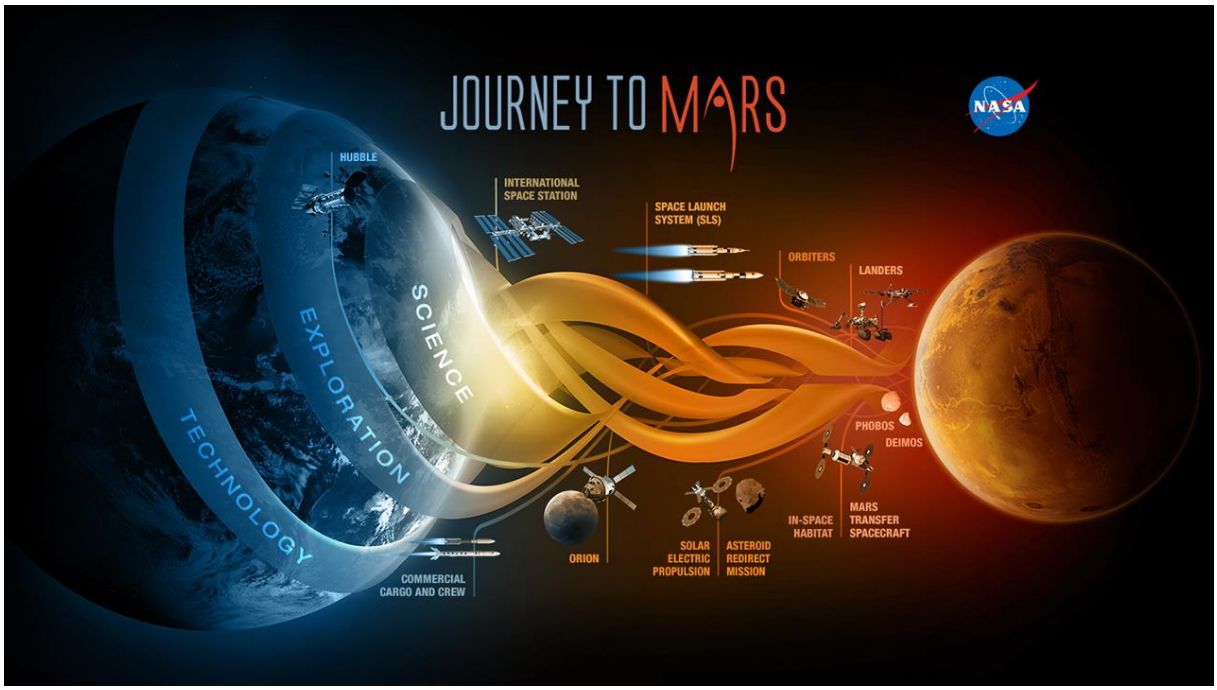

Figure 1: Journey to Mars. (NASA, 2014)

In December 2021, ExoMars TGO (Trace Gas Orbiter) has spotted significant amounts of water at the heart of Mars' Grand Canyon system, Valles Marineris (ESA, 2021). The water is hidden beneath Mars' surface, and can be detected by mapping the hydrogen in the uppermost meter of Mars' soil (Jakosky & Haberle, 1992). According to a recent study by Howell (2022), observations from NASA's MRO (Mars Reconnaissance Orbiter) show that liquid water flowed on Mars 2 billion years ago. This is much later than scientists once thought.

Scientists' biggest annoyance is that almost all water on Mars is in the form of ice. The water also exists in small quantities as vapor in the atmosphere. The only place where water ice is visible on the surface is the Arctic ice cap. Further research should prove whether there is still more water in the form of ice in the deep subsurface or as salt deposits, as shown in Figure 2.

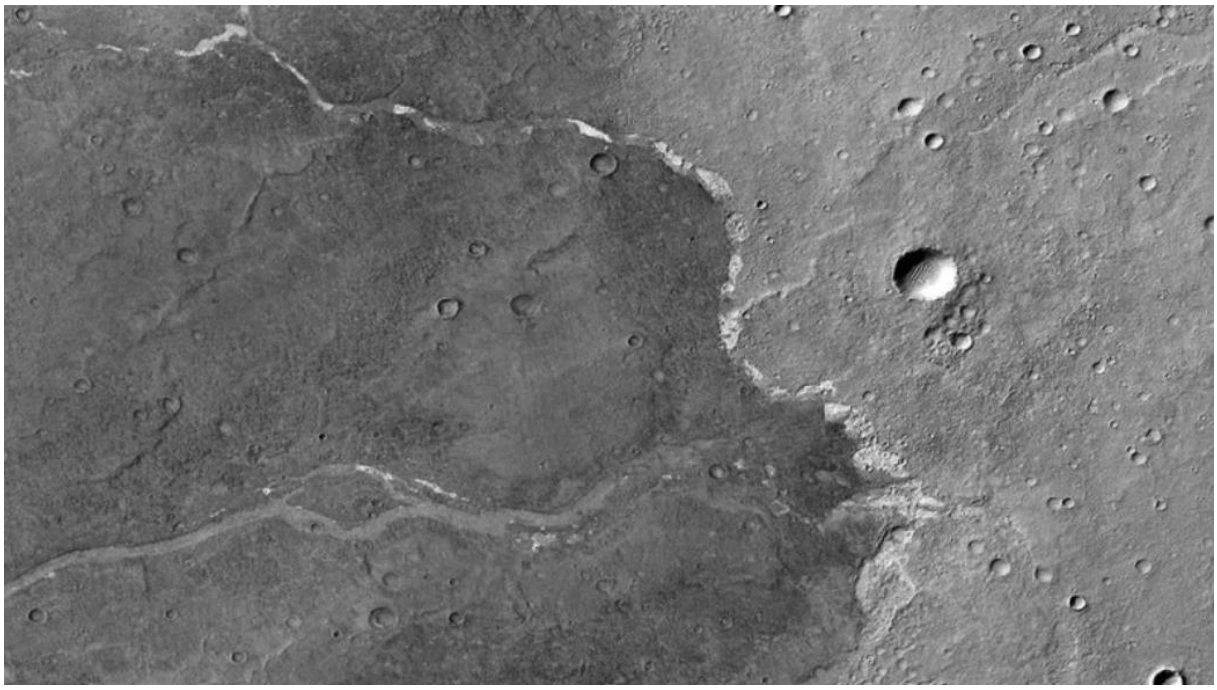

Figure 2: Bosporos Planum plain on Mars, from MRO. The white specks are salt deposits found within a dry channel, a clue to its watery past. (NASA/JPL-Caltech/MSSS, 2022)

The American Marsrover Perseverance has converted carbon dioxide into oxygen from Mars' carbon dioxide rich atmosphere (NASA, 2020). This Marsrover has landed at Jezero Crater on February 20th, 2021. His main job is to seek signs of ancient life and collect samples of rock and regolith for possible return to Earth. By using the MOXIE (Mars Oxygen In Situ Resource Utilisation Experiment) technology, on April 20th, 2021, Marsrover Perseverance produced oxygen from carbon dioxide in the Martian atmosphere by using solid oxide electrolysis. MOXIE heats Martian carbon dioxide to around 800 °C, this heating process separates oxygen and generates carbon monoxide as a by-product, as shown in Figure 3 (Hecht *et al*., 2021).

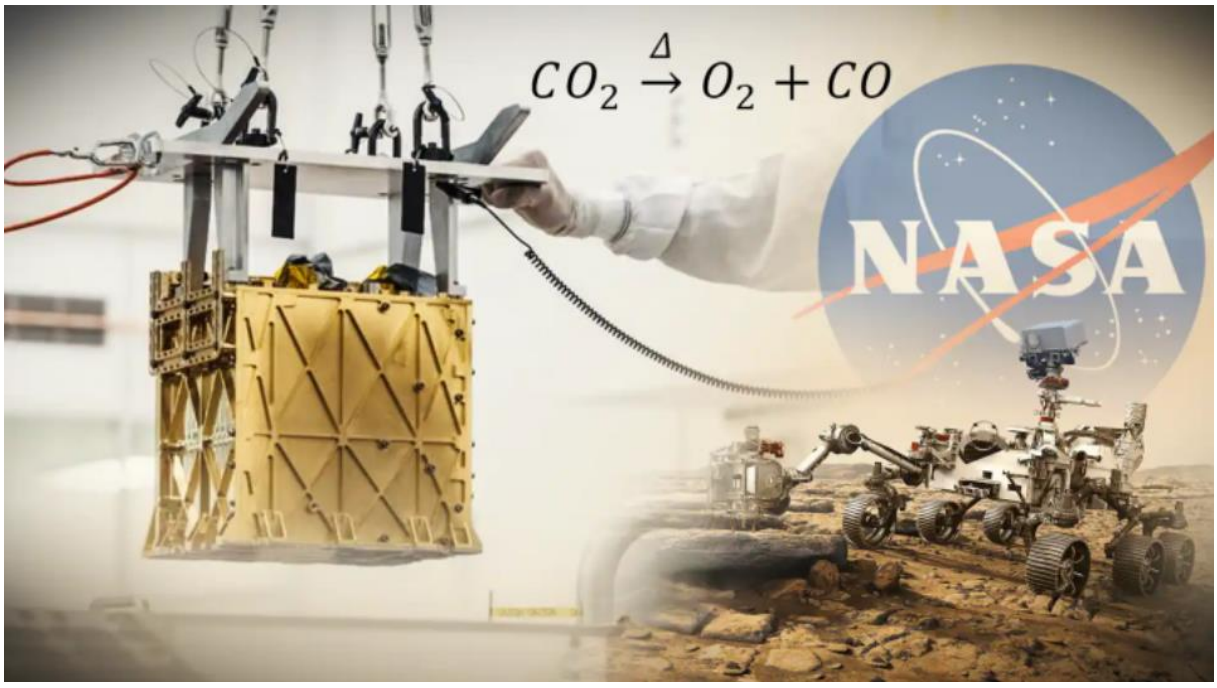

Figure 3: Converting carbon dioxide into oxygen by using MOXIE technology. (Menafin, 2022)

These technical innovations and recent findings are an indication of the possibility to generate oxygen on Mars. These developments could ensure the realisation of human life on Mars. To shield the oxygen from the carbon-rich atmosphere on Mars, oxygen needs to be produced in a restricted area, which is not in direct contact with the harmful atmosphere of the Red Planet.

To build such a restricted area on the planet Mars, building materials are needed appropriate for Mars' extreme environment. The distance between Earth and Mars varies from 54.6 million kilometers to 401 million kilometers, because of the different orbits from Mars and the Earth.

According to theory, the closest distance of 54.6 million kilometers would be reached if Mars is closest to the sun (perihelion) and Earth is at its furthest (aphelion). This has not yet happened in recorded history from NASA. The closest recorded distance to Mars was recorded in August 2003, when both were 56 million kilometers apart. Mars and Earth are furthest apart when they are both at aphelion and on opposite sides of the sun. In this case, they can be 401 million kilometers apart. The average distance between Earth and Mars is recorded as 225 million km (Dobrijevic & Bertrix, 2022). The Earth and Mars orbits are presented in Figure 4.

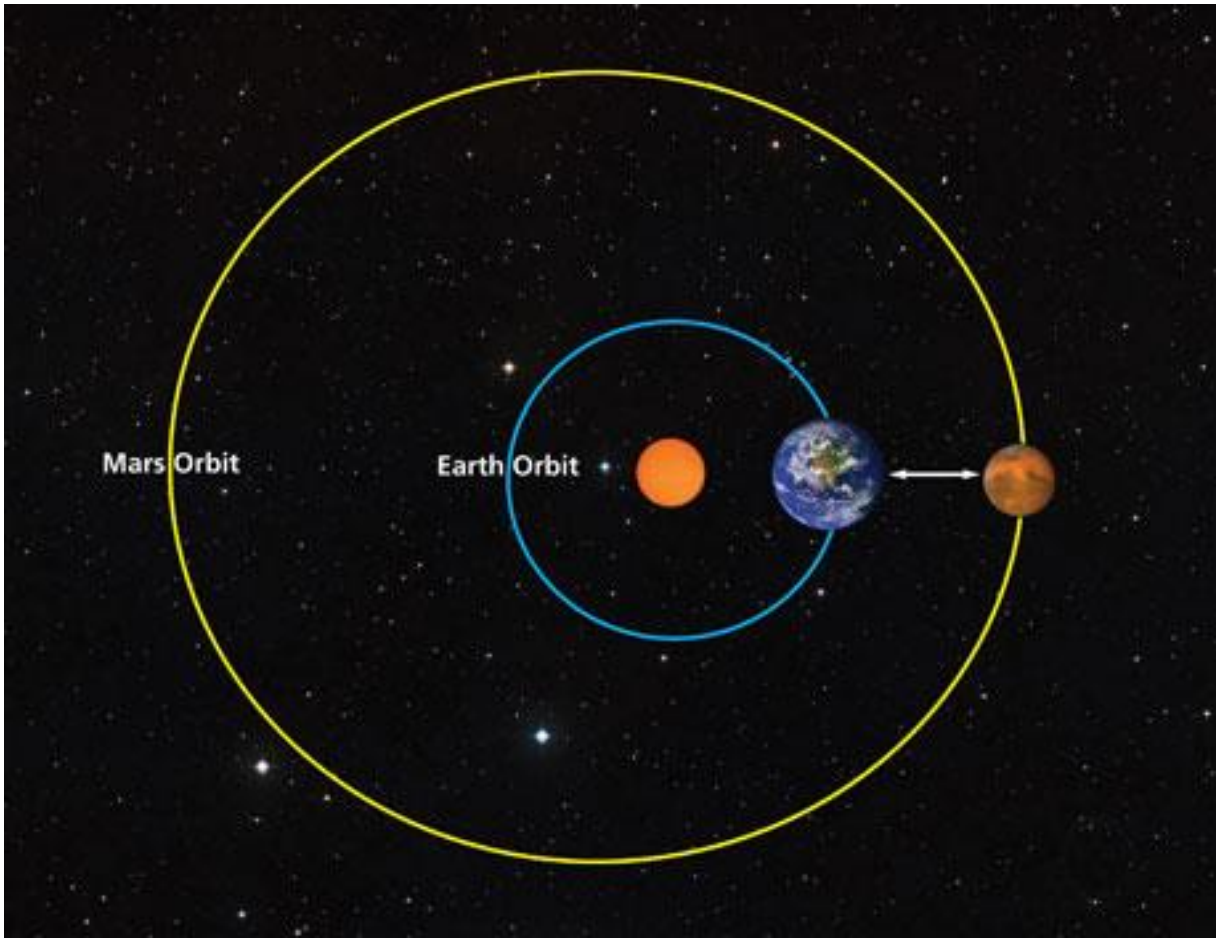

Figure 4: Earth and Mars orbits, respectively 365 and 687 days. (Sachan, 2012)

Due to the high cost of travel and the long trip to Mars, it is not economic to transport water, aggregates, binders, etc. from Earth to Mars because of the long distance between the two planets. To tackle this fundamental problem of high travelling cost, it is almost obligated to use the local materials or also called 'in situ materials'. In this Master's thesis research, the main focus is on the production of building materials using the local materials on Mars. Some important parameters for the design of new building materials for Mars are the environmental

conditions. These need to be investigated, because they differ completely from the conditions on Earth. Because of this reason, they will initially determine the material properties.

In the literature review of this Master's thesis, a distinction is made between the environmental conditions and geology of the planet Mars on the one hand. On the other hand, geopolymer properties and the geopolymerisation process will be investigated during this research project.

Extreme environmental conditions prevail on Mars. This makes the design of new building materials challenging. The average surface temperature is -63 °C with a maximum daily temperature difference of 60 °C (Liu *et al.*, 2021). These lower temperatures are a result of the fact that the planet Mars is further away from the sun than Earth. Also the pressure is only 0.7 % compared to the pressure on Earth, which means that there are almost vacuum conditions on Mars.

For all these reasons, several researchers are working on new ideas and ways of innovation to enable human life on the Red Planet. The goal of this research is to find a suitable geopolymer that is made from the local materials available on Mars. This research is based on the application of MGS-1, which is a Martian simulant from Gale Crater in Figure 5.

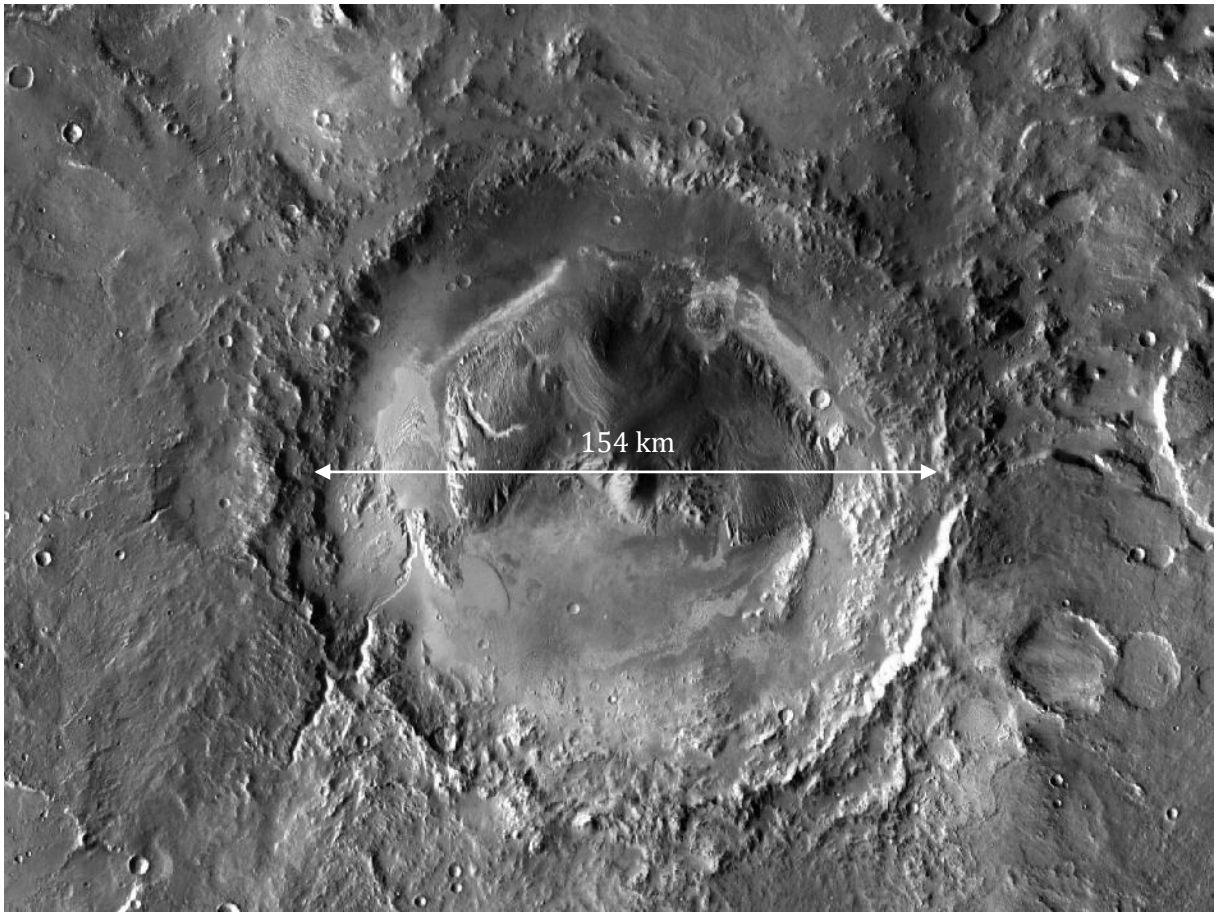

Figure 5: Gale Crater on Mars. (Edited from NASA/JPL-Caltech/ASU, 2012)

Geopolymers are chemical binders, formed by the alkali activation of an aluminosilicate source material. They are produced on Earth to operate as an ecological alternative for cement.

Geopolymer binders have the same setting and hardening behaviour as cement. In the case of geopolymers, less water and energy is needed to produce the geopolymer material. They can be produced based on waste or by-products from industry (Geopolymer Institute, 2022).

2 RATIONALE OF RESEARCH

2.1 Research context

The research of this Master's thesis is based on three different types of approaches: a social, ecological and scientific approach. These three topics form the basic drive of the research.

Starting from these three approaches, the underlying reasons and context of this research can be clarified. The social, ecological and scientific approach cannot be seen separately from each other, but they form a coherent whole. The global structure of the underlying reasons why this research is useful can be schematically presented, as in Figure 6. The explanations associated with the three different approaches are discussed further in this section.

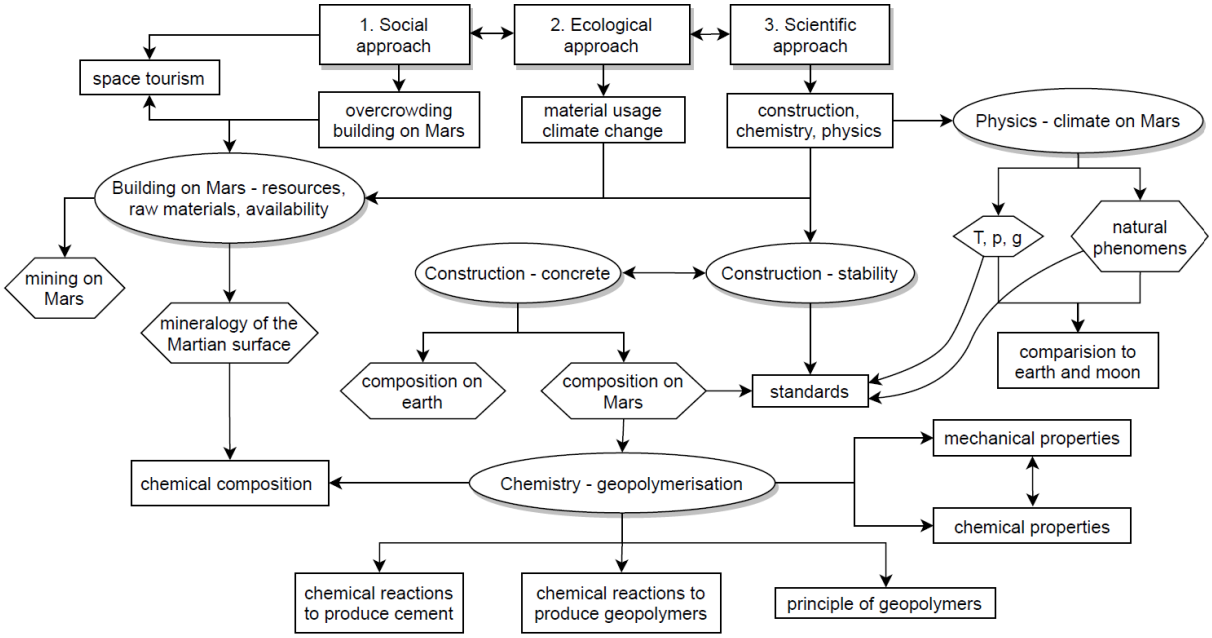

Figure 6: Schematic representation of research context.

2.1.1 Social approach

The ever-increasing population of the Earth challenges us to explore other ways of living. Not only the population growth, but also the increasing interest in space travel ensures that life on other planets will become more and more realistic. The planet Mars seems to be a good alternative to provide life for humanity, according to many researchers.

2.1.2 Ecological approach

The world population is producing more and more CO_2, causing the Earth to warm up at a rapid pace. Due to global warming, more and more natural disasters occur, such as floods, tornadoes, volcanic eruptions, earthquakes, etc. Therefore, this research is looking for sustainable materials, so that the use of traditional cement can be greatly reduced. The key of

this ecological point of view is that local resources need to be used on Mars. There is not much limestone available to make traditional cement like on Earth (Massachusetts Institute of Technology, 2007). Because of the fact that limestone is very limited on Mars, conventional concrete will not be the first choice as construction material. This is in contrast with the wide abundance of limestone on Earth.

Besides the fact that there is not enough limestone on Mars, the energy needed for reaching the high temperatures of 1300-1450 °C for the calcination of cement clinkers, cannot be achieved on Mars (see Figure 7). Therefore, new binding materials must be developed for the in situ raw materials available on Mars. Such alternative binder was discovered in the 1970s by the French scientist and engineer Prof. Joseph Davidovits, who is known as the father of 'geopolymers'.

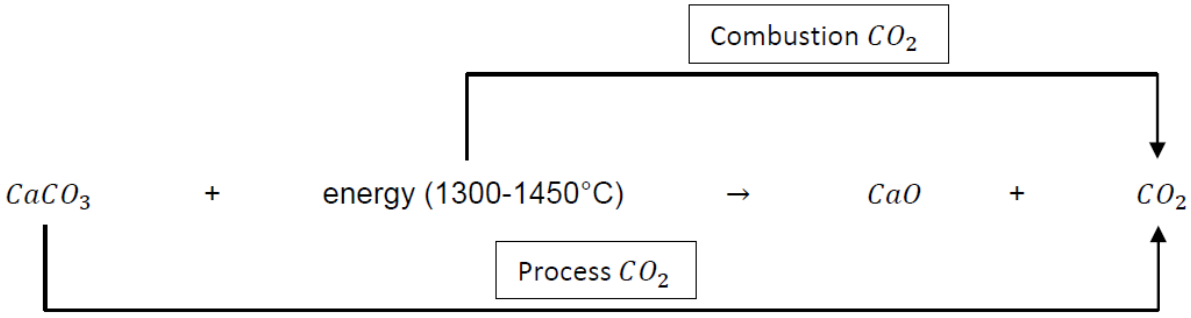

Figure 7: Calcination process of limestone for cement production.

The Red Planet has currently low temperatures, despite the fact that about 95 % of the atmosphere consists of CO_2. Adding some CO_2 to the atmosphere on Mars would not be a problem at all, on the contrary. Since it is very cold on Mars, an increase in temperature would be welcome.

The improvements and continuous innovation in technology and geopolymer science can be beneficial for the use of these geopolymers on Earth too. Due to several ecological problems on Earth, a more environmental friendly building material than conventional cement would be very welcome.

Therefore, the use of geopolymers on Earth is becoming more and more popular. Nowadays, there is large potential for geopolymer concrete applications for bridges, such as precast structural elements and decks, as well as the use of geopolymer-fiber composites (Aleem & Arumairaj, 2012). Due to its several advantages, geopolymer concrete is being introduced into the construction industry.

2.1.3 Scientific approach

Due to the differences in atmospheric conditions between Earth and Mars, the design of new materials for building on Mars will have to take this different conditions into account. Differences in temperature, gravity and pressure mean that new standards and regulations have to be drawn up. Due to the presence of new standards and regulations, reliable and safe building materials can be developed.

In addition to the stability of the structures to be built on Mars, the chemical background of the geopolymerisation reactions must be well understood. As a result, a chemical composition must be made of raw materials that can withstand the extreme conditions that occur on Mars.

2.2 Why building on Mars?

2.2.1 Population increase on Earth

The population in the world is currently (2020) growing at a rate of around 1.05 % per year (down from 1.08 % in 2019, 1.10 % in 2018, and 1.12 % in 2017). The current average population increase is estimated at 81 million people per year (Worldometer, 2021).

In addition to the rapidly increasing world population, there are higher risks of pandemics such as COVID-19. The political differences and economic crisis can create tensions between different societies, such as the war between Russia and Ukraine. This creates fear among some layers of the population about the attack with nuclear weapons. Furthermore, another danger is the impact of a meteorite on the Earth. For all these reasons, there is a greater drive from the human perspective to populate another planet, such as Mars (Petrescu *et al*., 2018). The evolution of the world population growth between 1700 and 2100 is given in Figure 8.

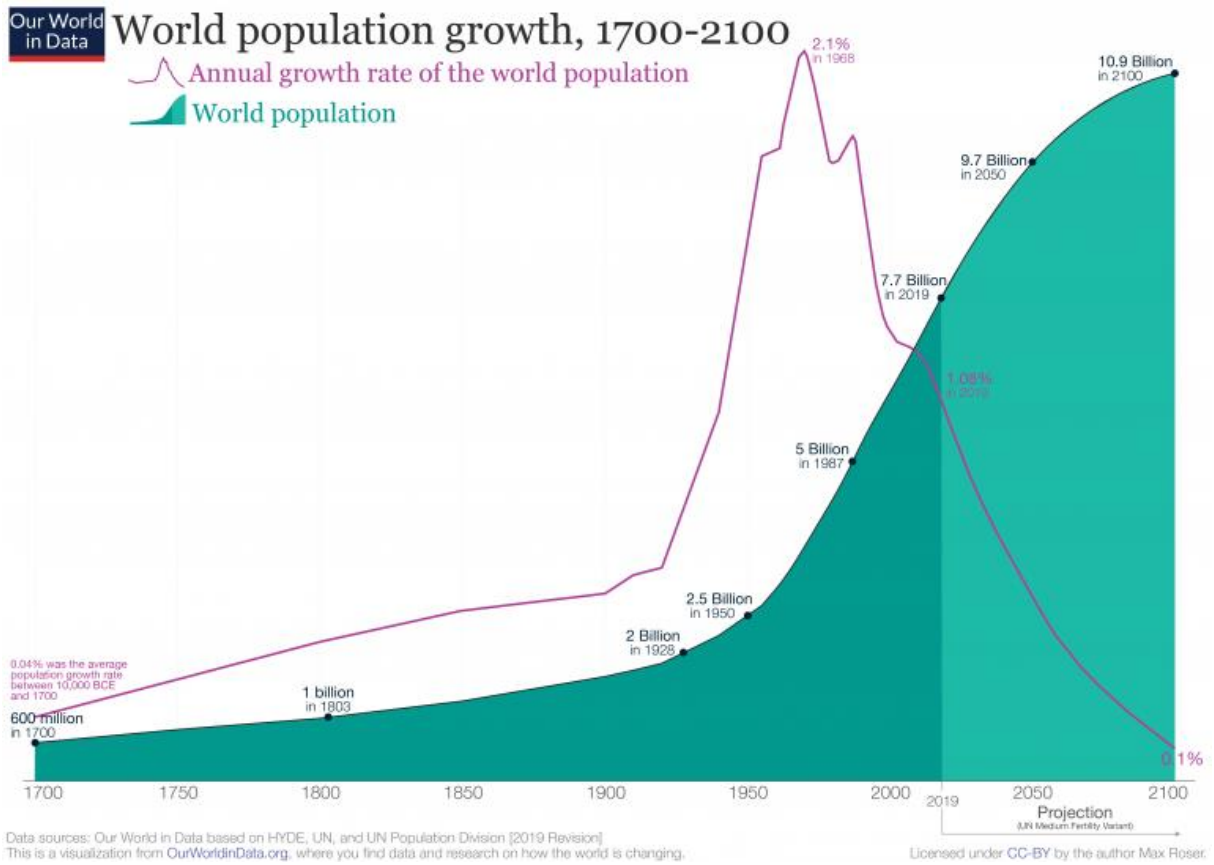

Figure 8: World population growth. (Roser *et al*., 2013)

2.2.2 Resource depletion on Earth

Resource depletion indicates that natural or renewable resources are being consumed faster than they can be replenished (Mittal & Gupta, 2015). This phenomenon is strongly catalysed by the current population explosion. Current patterns of use of energy and natural resources are proving unsustainable and urgently need to be restored. Developing countries abuse their

precious land on the basis of economic interests. An evolution in this way will lead to irreversible climate change and a decrease in economic growth due to social and ecological damage. Because global warming is still difficult to stop, life on the planet Mars can be seen as a second alternative.

2.2.3 Waste problems on Earth

The world is producing more and more, which means that the mountain of waste is increasing, literally as presented in Figure 9. Some countries can no longer manage the waste mountain. Global waste generation is strongly influenced by the degree of urbanisation, economic development and population growth (Kirchherr *et al.*, 2017). Due to an ever-increasing prosperity, more and more products and services are offered by companies. Due to the exchange of these products between different countries and continents, a world trade arises.

The manufacturing of new products follows a linear system in which different raw materials are used (Circular Economy Alliance, 2021). When these goods have reached their economic or technical life, they are thrown away. This system of linear economy generates 2.01 billion tons of waste worldwide every year. The average European produces approximately 5 tons of waste every year. Countries in East Asia, Pacific regions and regions in Europe and Central Asia are responsible for 43 % of global waste by volume (Christensen, 2011).

The amounts of waste produced cause nuisance to the environment and various organisms on Earth. A large part of it ends up in our seas and oceans, causing a disturbance of biodiversity. The pollution of the Earth by an increase in waste goes hand in hand with ecological problems. As a result, the world is increasingly moving from the linear economy model to a more advanced circular economy model.

Figure 9: Garbage problems on Earth. (Royte, 2006)

To stop the production of waste, it is becoming increasingly important to focus on the reuse and recycling of materials. As an example of a material in the construction industry that is difficult to recycle, cement quickly turns to our attention. In the construction sector, cement is an indispensable material for the production of concrete. Cement is crucial in the composition of concrete because it ensures the bonding of the various components, and is therefore mainly responsible for the strength development.

However, from an ecological point of view, cement is a culprit, since a lot of CO_2 is released during the production of cement. For example, it is generally known that the production of 1 ton of cement produces a total of 650-920 kg CO_2 emissions (Chakraborty, 2019). As much as seven percent of the global CO_2 emissions are due to the industrial process of cement production. Since this trend cannot simply be continued, research is being conducted into alternatives to cement as a binder. An example of this is the use of geopolymers, or the use of the so-called Supplementary Cementitious Materials (SCMs). Figure 10 shows the ternary diagram of $CaO - SiO_2 - Al_2O_3$, indicating the various SCMs available in current industry.

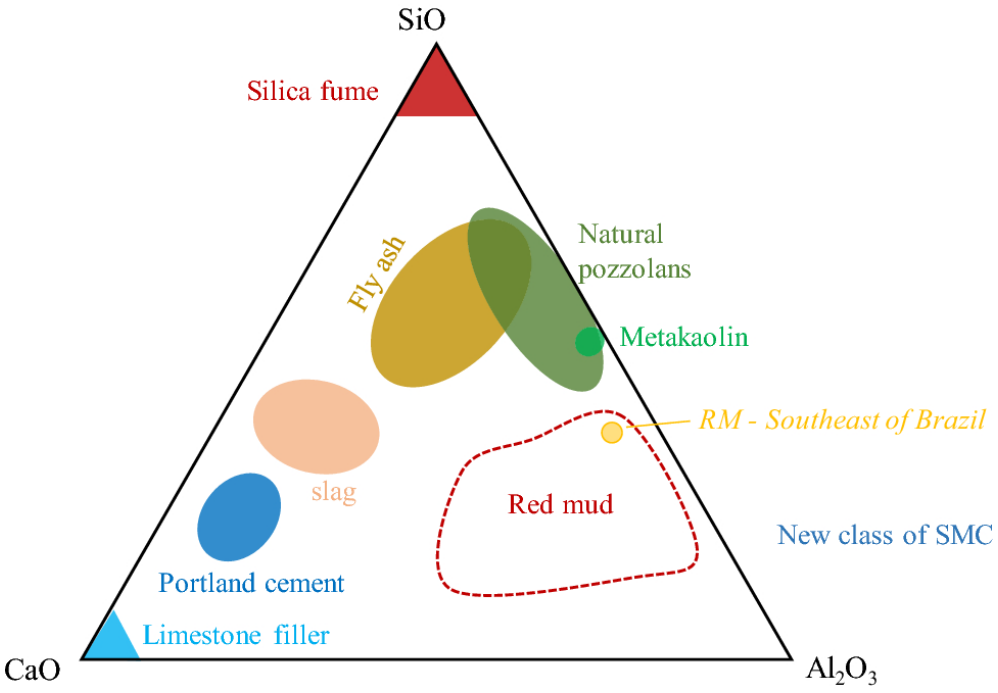

Figure 10: Ternary diagram of $CaO - SiO_2 - Al_2O_3$ for currently used SCMs compositions on Earth. (SpringerLink, 2022)

In addition, it is also possible to aim for the production of a green cement that meets ecological standards. For this, the focus must be on a circular model, in which all components in the cement production chain are linked to each other.

This sustainable model starts from the mining of the limestone and continues until the cement has reached end of life. At this point, the cement industry uses urban and industrial waste as fuel for the kiln. Saving on energy consumption through the reuse of waste to produce heat is an important factor in reducing the burden on the ecological cycle.

The recycling of the waste is an important step to close this circular model. Therefore, a waste recycle plant is used to fit the environmental regulations and be beneficial for the environment. This investment will be paid back relative quickly, making it a win-win both ecological and

economical aspects. By applying such a strategy of a circular economy model, a company can distinguish itself in the competitive market.

In Figure 11, a circular economy model for such a green cement production is given. The different steps in the optimised cement production process are presented. As already mentioned before, the important component in this cycle is the waste recycle plant, which closes the entire circular chain.

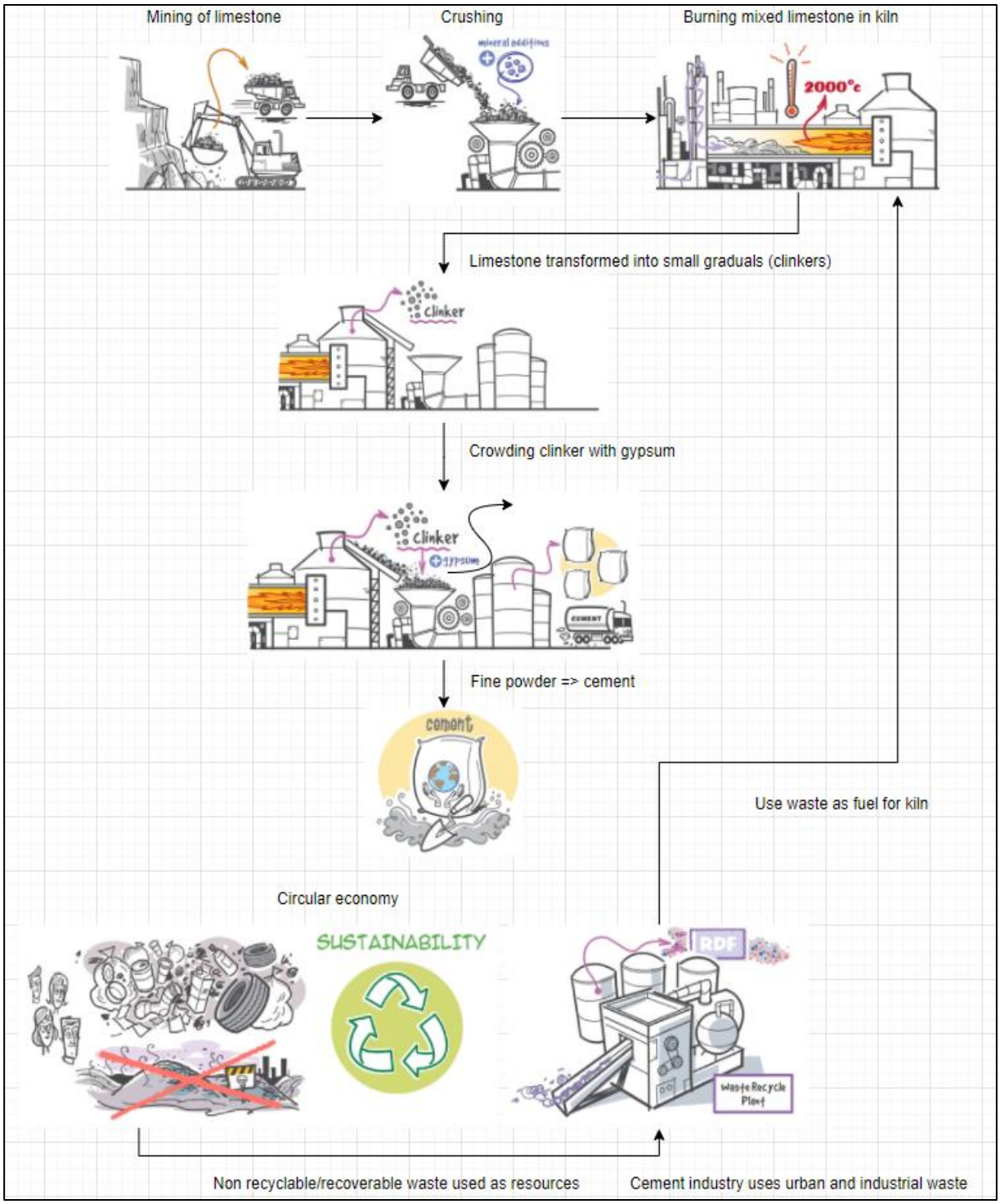

Figure 11: Cement production as a circular economy model.

2.2.4 Evidence of availability of water on Mars

The scientific studies and investigations that are happening on the planet Mars aim to look for traces of life, in the broad sense of the word, on the planet Mars (ESA, 2022). As already mentioned in the introduction, an important indication of life on the planet is the presence of water. Observations have shown that the amount of water on the planet Mars is mainly in the form of ice, or locked in the structure of abundant water-rich materials (Nazari-Sharabian *et al.*, 2020).

The main body of evidence for the presence of water on Mars is found in the ancient flow bed of the Gale Crater. This gives an indication of life on the planet, allowing planetary geologists to further investigate rocks, sediments and soils.

Through measurements with a gamma-ray spectrometer with the Mars Odyssey, on the surface of the planet, significant amounts of hydrogen molecules were detected on the planet. The current dry climate on the planet Mars makes organic life more difficult (Haberle *et al.*, 2017).

A study by Dass (2017) showed that there is a possibility for different organisms to grow on Mars. Experts identified two different types of fungi that can grow on Mars, namely mushrooms and basidiomycota. Fungi are an intriguing group of organisms, made up of millions of species. These are able to colonise in extreme environments (Carlile *et al.*, 2001), such as around the highly radioactive environment of Chernobyl (Dadachova *et al.*, 2007).

In addition, it was scientifically proven that these organisms can also survive in radiation-intensive environments of space stations (Novikova *et al*., 2009, 2016). Hence, experts are enthusiastically looking into the possibility of starting agricultural activities on Mars. Recent studies indicate that fungi can grow on predators (Cortesão *et al*., 2020).

2.2.5 Mars: most similar planet to Earth in the Solar System

According to ESA (2022) and several other researchers, Mars appears to be the most suitable planet for possible life in the Solar System, next to Earth. To compare the atmospheric conditions of Mars and Earth, the principles of flows and turbulence in the boundary layer of the atmospheric surface are important (Larsen *et al.*, 2002). For the most part, it appears that the surface layer turbulence and mean flow on Mars follow the same scaling laws as on Earth.

The largest micrometeorological discrepancies between the atmospheres of both planets are caused by the low air density of the Martian atmosphere. Due to the lower presence of water vapor on Mars, the share of atmospheric heat flux in the total surface energy decreases. This increases the temperature variation of the surface, resulting in larger heat and cold flows.

Because the wind speed shows the same characteristics as on Earth, this greater diabatic heat flux is supported by larger maximum values of the temperature. In addition, the higher kinematic viscosity yields a Kolmogorov scale on the order of 10 times that on Earth (Golitsyn, 1971). This phenomenon affects the transition between the rough and smooth flow characteristics. Dust storms are caused by local conditions and are more common when Mars is at its perihelion. Then, it is late spring-early summer in the Southern Hemisphere and the irradiation reaches a maximum value (Golitsyn, 1973).

The scaling laws between Mars and Earth have been validated by the analysis of a dataset of surface layer data from Mars, based on wind speed and temperature.

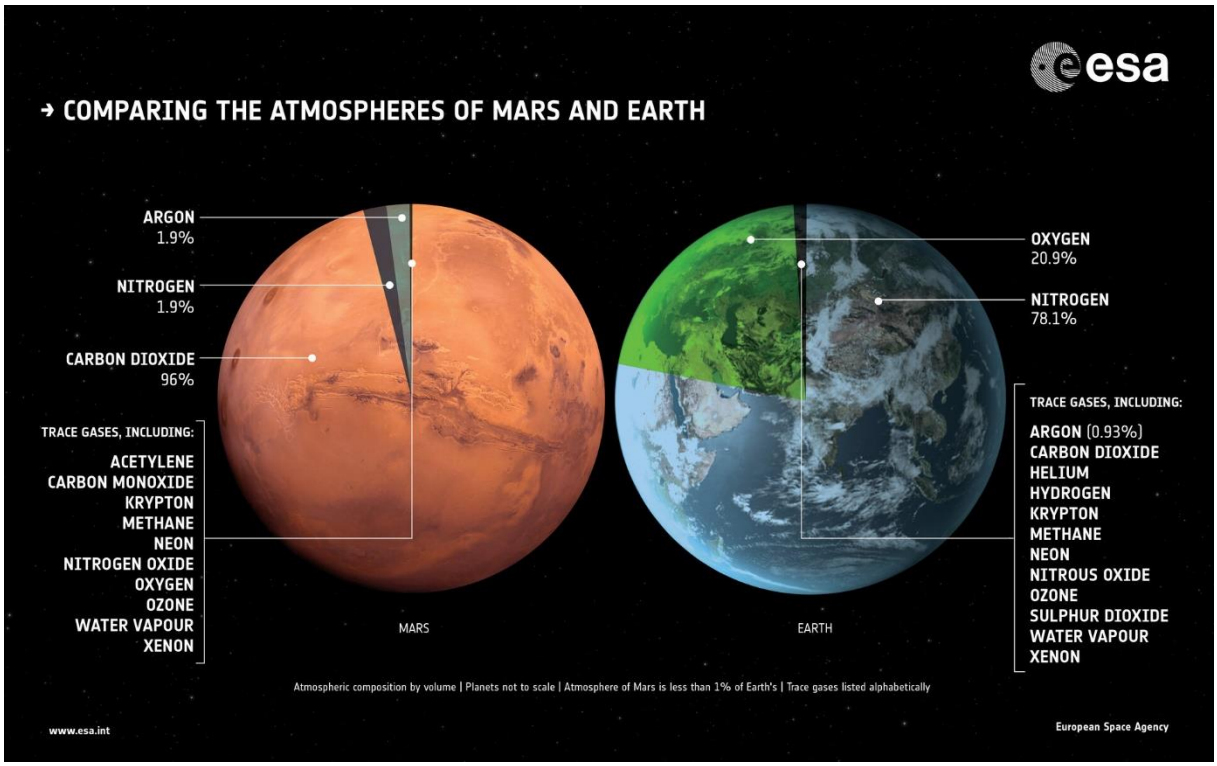

Figure 12: Comparison of the atmospheres of Mars and Earth. (ESA, 2022)

2.2.6 Use of local resources on Mars

Today, robotic missions are widely used to mitigate the risks and costs of human exploration on the planet (ESA, 2022). Before sending astronauts to Mars, the biological hazards in the soil stratigraphy must be well understood. It is difficult and therefore not realistic to take everything with us to survive the journey to our neighboring planet. For this reason, the focus is mainly on the use of resources that are available locally. The presence of liquid water is an important resource for human expeditions, both for consumption by astronauts and for use as fuel.

Various samples collected by robots can be used to evaluate where potential resources are available for the future human presence on the Red Planet. This research will mainly focus on the latter. In order to survive on the planet Mars, there must be the possibility of housing. Hence, sustainable building materials must be developed, based on in situ raw materials from Mars.

Various experiments can be carried out using simulated Mars raw regolith material to get a building material that has sufficient strength. That strength must be determined in such a way as to meet the structural stability requirements of structures. More specifically, this study will focus on the development of a suitable geopolymer for building on the planet Mars. This geopolymer is seen as a sustainable binder, which will be designed by using the in situ raw materials from the planet Mars. To make all this possible, first a qualitative study must be made of the geological composition of the soil on Mars. From this study, the amount of available resources and minerals on Mars can be obtained.

Finally, the final strength of the geopolymerisation will be analysed. From this, a judgment can be made whether this strength will meet the minimum stability requirements, and can thus be used in constructive applications.

2.3 Research objectives

2.3.1 Research question

Before the research can be started, a clear research aim needs to be identified. In order to devise a good and targeted strategy for the literature review, a clear research question was initially formulated:

"How can we develop a series of geopolymers from in situ Martian materials to build on Mars?"

Starting from this research question, the global research was divided into two main parts. On the one hand, the atmospheric conditions and materials that can withstand the extreme conditions that prevail on Mars are studied. Secondly, the composition and chemical basis of geopolymers is studied. The aim is to obtain a clear insight into the research objectives and what the outcome of the research should be. Eventually, a clear answer needs to be formulated to the research question. This can be found in the conclusion, section 7 of this research project.

2.3.2 Research goals

The general aim of the research project is to make geopolymer materials with simulated in situ raw materials that can meet the extreme conditions of Mars. The parameters will therefore have to be optimised for compositions and mixing ratios of alkaline liquids with raw materials and possible additives. The curing time and temperature will have to be adjusted to make a building material as suitable as possible.

2.3.3 Methodology

Various tasks will have to be performed during the research. In order to keep a good overview of the different parts of the research, the research question is divided into 5 work packages (WP). A clear planning can be set up on the basis of these work packages. This is of great importance in order to complete the research work within the stipulated period.

- WP 1: Literature review on geopolymers and materials for extreme conditions (temperature, radiation, formation process of geopolymers)
- WP 2: Characterisation of the simulated Mars raw material (MGS-1)
- WP 3: Design and synthesis of a range of geopolymers where different parameters are tested (composition, curing time, temperature, additives)
- WP 4: Characterisation of the synthesised geopolymers (chemical and mechanical)
- WP 5: Interpretation of the results, comparison with literature, writing of a thesis

The literature study and laboratory work in this research is divided into 2 major parts. The literature study takes place in the first semester. All important aspects of the planet Mars and geopolymers are studied in order to have the necessary knowledge for the mix design (WP 1, WP 2, WP 3). The mix design also takes place during the first semester, in order to start making the geopolymers (WP 3) at the start of the second semester. These are respectively mechanically and chemically characterized (WP 4), by the compression test and FTIR device. The interpretation of the results (WP 5) is done in the second part of the second semester.

2.4 Domains of research

The research on geopolymers to build on Mars is assigned to two specific domains. On the one hand, the domain of chemistry deals with the part on geopolymers and the associated reactions. On the other hand, the construction sector is also involved for the stability issues in this research project. In order to reach a consensus, good communication between various stakeholders will therefore be necessary. This can be defined as a good stakeholder management, which is explained in section 2.4.3 (Chinyio, 2022).

In this section, each of these two domains (chemistry and construction) reflects on their contribution to the research. In today's society it is becoming increasingly important to involve all stakeholders. In addition, the wishes and expectations of various parties must also be taken into account (Karlsen, 2002).

2.4.1 Chemistry

A large part of this research is based on chemical science. Initially, an attempt should be made to gain insight into the process of geopolymerisation. The important influence factors that determine the reaction products must be well understood before a mix design can be implemented. This requires a thorough knowledge of the composition of geopolymers. The most important parameter in the composition is the concentration of the alkali activator that will be added to the simulated Mars raw material. In addition, attention should also be paid to the ratio of the alkali activator to the aluminosilicate material. All influence factors will be investigated in the literature review, step by step.

In addition to the composition and the relative proportion of the different raw materials, the curing time and temperature must also be determined for the different geopolymer mixtures. The need for adding additives to the mixture will be apparent from the characterisation of the simulated Mars raw regolith material (WP 2).

All of the above factors will be derived from previous studies and already completed research on geopolymers. The part of chemical science in this study is estimated at 60 % of the total research time. In addition, the remaining 40 % is allocated to the construction sector and all other stakeholders involved in the project.

2.4.2 Construction

The construction sector also has a share in the research to a certain extent (Atkin, 2008). In order to be able to build on Mars, research must be carried out into a sufficiently load-bearing subsoil for the application of the foundations. The geopolymers made for building on the planet Mars must be able to withstand extremely low pressures, high temperature variations and sandstorms.

In first instance, this will require a good design of such structures, so there will have to be good communication and understanding between engineer and architect. In addition, the structural engineer has the task of providing building materials that achieve sufficient strength. Each player in the process has its own responsibility, and all the stakeholders together have a shared responsibility.

Standards and technical regulations will have to show what the minimum standards are for building materials to meet the atmospheric conditions of the planet Mars. Eventually, the

structural engineer will have ultimate responsibility for the stability of structures built on the planet Mars. The stock and availability of the various raw materials on the planet Mars must be sufficient to keep building realistic, both on social and economic aspects.

2.4.3 Interaction between different stakeholders

It soon becomes clear that there must be interaction between the various stakeholders. Finding a suitable building material for the planet Mars involves a lot of organisation, management and planning (Figure 13). For example, energy sources and machines are needed to make building possible. For successful completion of a construction project, the expectations of the stakeholders must be fulfilled during the entire life of the project (Cleland, 1995).

Figure 13: Stakeholder management cycle. (Darzin, 2022)

In addition to the construction and chemical sector, there are other parties that have to contribute to the realisation of this project. For example, the total world population must also be informed about the advantages of building on the planet Mars. A global approach through good communication will lead to a great chance of success. All this belongs to the completion of a project, whereby all parties are informed as much as possible. Developing and maintaining good relationships with all communities and stakeholders is crucial for a good stakeholder management.

Thoughtful stakeholder management involves investing time in identifying stakeholders and assessing their interests. This judgment will provide a strong basis for further developing the stakeholder management strategy. In this way, there is the greatest chance of success in effectively marketing this project to build on Mars, by the use of local resources.

3 LITERATURE REVIEW

3.1 Building on Mars

The goal of this research is to make it possible to set Mars as the next destination for human habitation. Building habitats on Mars requires good research and studies on the preparatory work. Similar to the infrastructure construction on the Earth, the technical issues of raw materials and circular economy, space habitation has to be addressed intensively before human inhabitation can become reality. Based on the history of Mars exploration missions and a series of current Mars exploration results, there is a lot of knowledge about the environmental conditions on Mars.

The most important information about the planet Mars is explained below. A crucial part for this Master thesis, is the focus on materials that can withstand the extreme environmental conditions on Mars. The importance and effect of temperature and pressure on geopolymers is taken into account for the design of a series of suitable geopolymers (Lui *et al*., 2021).

3.1.1 Introduction to the planet Mars

3.1.1.1 Background

Mars in the fourth planet in the solar system, while our planet Earth is the third one, in terms of relative distance from the sun (Figure 14). Due to the fact that the rotation period of Mars and the tilt of the rotational axis to the ecliptic plane are similar to those of Earth, its seasons are very similar to those of Earth (Ashbrook, 1953).

Through its similar behaviour to Earth, the planet Mars should be investigated for a possible place to live in the near future. The planet Mars has a unique topography and climate. Next to Earth, the planet Mars is most understood by humans. Nowadays, more than 30 probes had reached Mars and conducted detailed surveys on Mars to obtain a large amount of valuable data and images (Ziyuan & Fugen, 2011).

Figure 14: Solar system with planets Earth and Mars. (Graphic River, 2018)

3.1.1.2 History of exploration of Mars

The exploration of the planet started in the sixties when the Russian Soviet launched the first probe Mars 1960A, which failed but this marked the beginning of the human exploration of Mars. From the period between 1960s and 1990s, several Mars explorations took place in the United States and the Soviet (Ziyuan & Fugen, 2011).

The Mariner 9, part of NASA, successfully entered the orbit around Mars for the first time in 1971. With this achievement in the space history, the first high-resolution photographs were taken of the Red Planet. Some useful information was gained through NASA. Later in time, at the end of the 20th century, the Mars Pathfinder from the United States, was one of the most successful Mars exploration missions in history. With this mission, data was gained from in-depth analysis of the Martian atmosphere, climate, geology and the composition of the rocks and soils on Mars (Smith *et al*., 1997).

In the current 21st century, many countries have made or are still planning their programs towards Mars. In 2015, NASA issued its official plan for human inhabitation and colonisation of Mars. The name of this plan is 'Journey to Mars', as already explained in the introduction. For making this plan of the NASA to become reality, further research on the planet needs to be done. In 2016, China launched its first Mars exploration mission, and successfully delivered the Tianwen-1 into the Earth-Mars transfer orbit. This Chinese spacecraft successfully entered the Mars orbiter on February 10th, 2021. The mission objectives are the investigation of Martian surface geology and internal structure, and searching for current and past presence of water.

Table 1 gives an overview of the historical spacecrafts towards Mars by 2020. As of 2020, Mars is host to eight functional spacecraft: six in orbit, two on the surface and three on route (NASA, 2021).

Table 1: List of the current spacecraft towards Mars. (NASA, 2021)

Name	Location	Nationality	Launched Date	Status
Mars Odyssey	In orbit	United States	2001.04.07	Operational 2001-2025.
Mars Express	In orbit	ESA	2003.06.02	Operational 2003-2026.
Mars Reconnaissance Orbiter	In orbit	United States	2005.08.12	Operational
Mars Science Laboratory Curiosity	Surface	United States	2011.11.26	Operational
Mars Orbiter Mission	In orbit	India	2013.11.05	Operational
MAVEN	In orbit	United States	2013.11.18	Operational
ExoMars Trace Gas Orbiter	In orbit	ESA/Russia	2016.03.14	Operational
InSight	Surface	United States	2018.05.05	Operational
Al-Amal	En route	United Arab Emirates	2020.07.20	En route
Tianwen-1	En route	China	2020.07.23	En route
Perseverance rover	En route	United States	2020.07.30	En route

3.1.2 Mars environment

3.1.2.1 Topographical and geological information

Kamps *et al*. (2020) calculated the Martian surface type map based on Compact Reconnaissance Imaging Spectrometer Multispectral mapping (CRISM). Figure 15, made by Viviano-Beck *et al*. (2017), shows that the Martian surface mainly consists of dust covered region and southern highlands. The main landforms on Mars are plain, volcanos and mountains (Dundas *et al*., 2017).

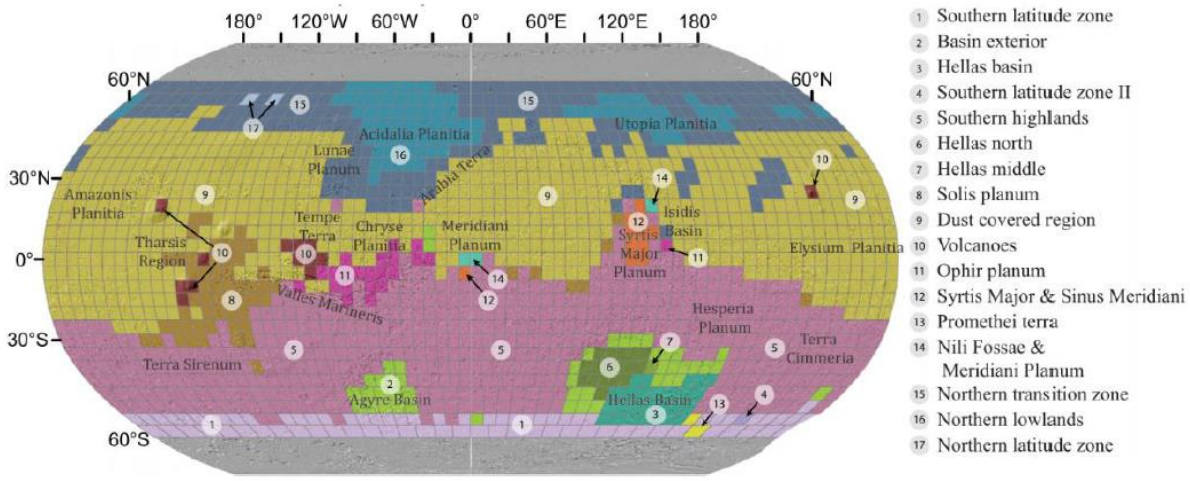

Figure 15: Global surface types based on hierarchical clustering analysis. (Viviano-Beck *et al*., 2017)

The Martian surface is rich to iron-bearing silicates, basaltic rock and carbon dioxide-ice. Beneath the Martian soil surface, this area is dominated by red dust, regolith and large chunks of rock (Golombek *et al*., 2020). Figure 16 shows the typical red surface view of Mars.

A study of the NASA (2017) suggested that the Mars surface may be too toxic for microbial life. The presence of perchlorates on Mars, which are composed of chlorine and oxygen, make it difficult to live on Mars because of the toxicity to human's health.

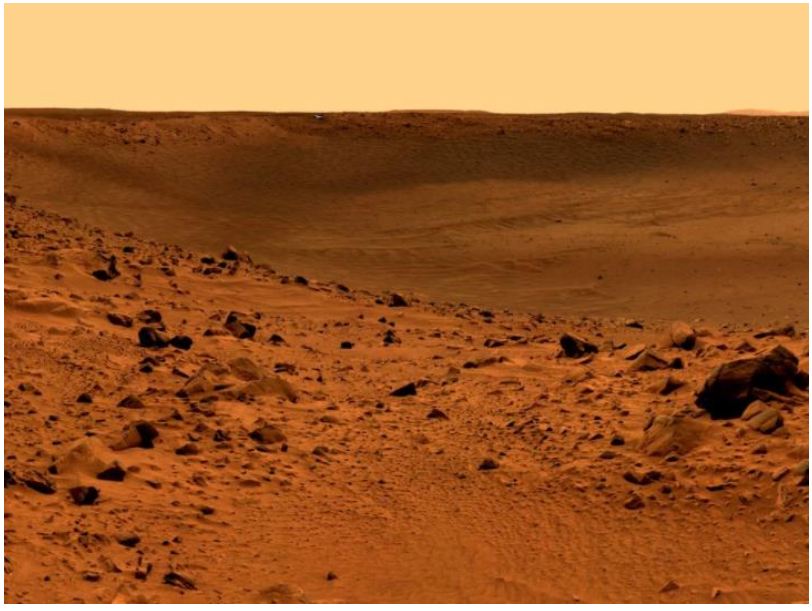

Figure 16: Landform of the Bonneville Crater on Mars. (NASA, 2017)

3.1.2.2 Atmospheric conditions

The atmosphere on Earth exists of 78 % of nitrogen (N_2) and 21 % of oxygen (O_2), and is very suitable to have good living conditions. When we compare the atmospheric composition from Earth to that of Mars, we get totally different values, as presented in Table 2. The atmosphere on Mars is composed of only 2.59 % of nitrogen (N_2) and 0.16 % of oxygen (O_2), while the largest proportion of gas consists of 95.1 % of carbon dioxide (CO_2). This CO_2 continuously transforms between dry ice and gas due to extreme temperature variations on the Red Planet.

Table 2: Major atmospheric compositions on Mars. (Liu *et al*., 2021)

Major atmospheric compositions	Mars (%)	Earth (%)
CO_2	95.1	M*
N_2	2.59	78.08
Ar	1.94	M*
O_2	0.16	20.95
CO	0.06	M*

The gravity on the surface of Mars is only 38 % of that of Earth. More gases are escaping on the planet Mars due to the lower gravity than on Earth. The small gravity on Mars results in a low average pressure of only 0.636 kPa, while on Earth the atmospheric pressure has a value of 101.325 kPa. As already mentioned in the introduction, the pressure on Mars is only 0.7 % of the pressure on Earth, this fact is the most significant difference between Earth and Mars (Williams, 2004). Due to the seasonal CO_2 condensation at the polar regions, the Martian pressure varies 20 % every year (Leovy, 2021).

Next to the atmospheric pressure difference between Earth and Mars, there is a large difference between the cosmic radiations too. Figure 17 shows an overview of the measured amount of cosmic radiation to the surface of Mars, by Mars Odyssey 2001 (Davies, 2016).

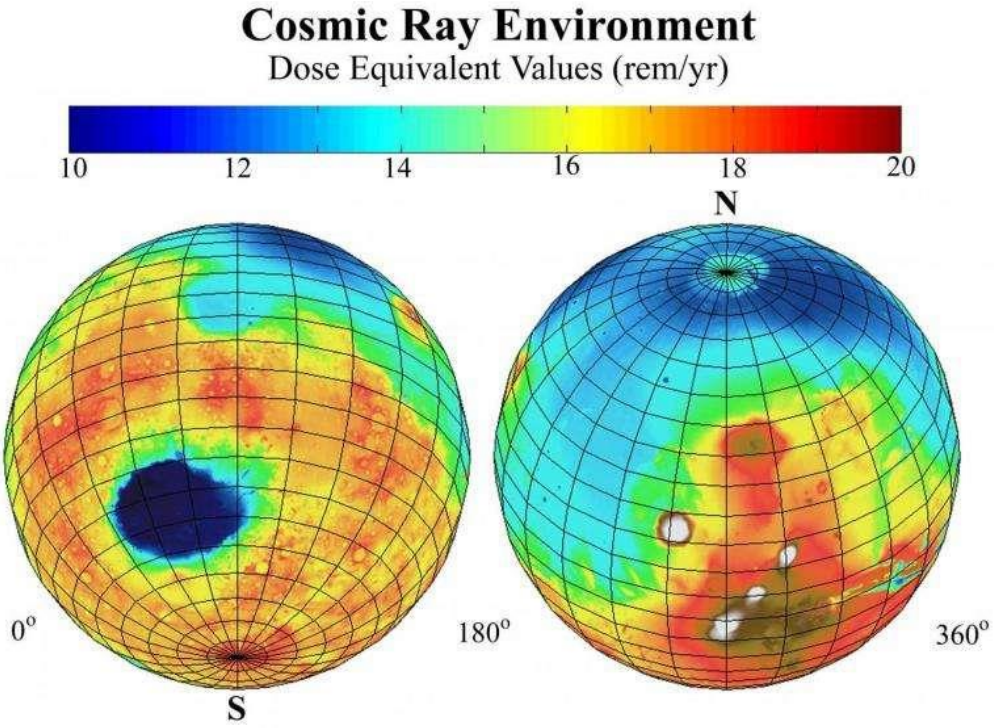

Figure 17: Large cosmic radiation on Mars. (NASA/Jet Propulsion Laboratory/JSC, 2002)

The annual average radiations on Mars are around 8 rads per year. Rad is the unit of absorbed ionising radiation per amount of matter (1 rad = 0.01 gray = 0.01 joule of energy absorbed per kilogram of weave). Compared to Earth, there is an average of 0.62 rads per year. This means that the cosmic radiations on Mars are about 13 times higher than on Earth (Davies, 2016).

3.1.2.3 Climate on Mars

The distance between the Earth and the Sun is approximately 158 million kilometers, while the distance from the Earth to Mars is between 55,8 and 400 million kilometers. The Earth gains 1361 W/m² solar radiation, while Mars gets only 586,2 W/m² (Leovy, 2001). The lower value for solar radiation on Mars is because of the further position relative to the Sun.

When comparing the temperatures, we can denote a large difference between Earth and Mars. Because of the lower solar radiation on Mars, the average temperature of Mars is significantly lower than on Earth. The average temperature on the surface of Mars is -63 °C with a daily maximum difference of 60 °C. The average temperature on Earth is 15 °C with a daily maximum difference of 30 °C (Johnson, 1965). The surface temperature on Mars can vary between -130 °C and 30 °C.

3.1.3 Soil types and composition

In situ resources are needed for an economical infrastructure construction process. Due to the large distance and high travelling cost between Earth and Mars, it is uneconomical to transport resources from Earth to Mars. A broader insight into the Martian soil stratigraphy is necessary to know which soil types are available to make building materials with a geopolymerisation process.

3.1.3.1 Martian soil

The Martian soil is, on the surface level, covered with a large amount of unconsolidated or weakly consolidated weathered material. At this moment, the definition of this material varies. The material includes mainly regolith, aeolian, sediment and dust (Certini *et al*., 2020). Martian soil, existing of rocks, can be applied as aggregates for construction materials. By combining these aggregates with a geopolymer binding material, geopolymer concrete can be composed by the use of in situ materials from Mars (Van Chanh, 2008).

3.1.3.2 Martian simulants

Martian soil can only be utilised on Mars after it is synthesised on Earth for testing and development. Therefore, researchers are focusing on simulating Martian soil based on the analysis from the various Mars spacecrafts (Lui *et al*., 2021). Different Martian simulants exist: JSC Mars-1, MMS and MGS-1 are commonly used to do research and laboratory work on Earth. In this research, the MGS-1 simulant from Gale Crater will be used.

3.1.3.3 Available metals on Mars

Mars is also called as the Red Planet due to its colour. This red colour refers to the availability of many metals in the Martian crust. From studies of Fairén *et al*. (2009) and Naser (2019) significant fractions on Si, Fe, S, Mg, Ca, Na, K and Al in the soil stratigraphy of Mars. These materials are not readily available on Mars and should be mined to produce metals (Naser & Chehab, 2018). In order to make building on Mars possible with metals such as steel, sufficient mining possibilities and equipment needs to be provided (Taylor *et al*., 2022).

3.1.4 Possible energy sources on Mars

In order to keep building on the planet Mars economically and technically feasible, available energy sources must be used. The main natural energy sources on Mars are solar and wind energy (Lui *et al.*, 2021). Next to these two energy sources, there are also many radioactive sources on Mars. In this paragraph, these three natural energy sources are highlighted.

3.1.4.1 Solar energy

With an average solar irradiance of 586.2 W/m² on Mars, compared to 1361 W/m² on Earth, there is certainly potential for installing solar panels to generate electrical energy (Leovy, 2001). However, these solar panels need to be protected against the violent sandstorms that can occur on Mars (Kass *et al.*, 2020). On the other hand, researchers believe that dust storms on the Martian surface would easily cover the solar panels (Stella & Herman, 2018). This would lead to a significant reduction in the efficiency of power generation. This problem could be tackled firstly by studying the application of solar energy in the desert on the Earth.

Due to the extremely varying atmospheric conditions on Mars, it will be of great importance to buffer the different forms of energy in energy storage systems, as shown in Figure 18. By storing the energy, the scarcity of energy can be intercepted as much as possible.

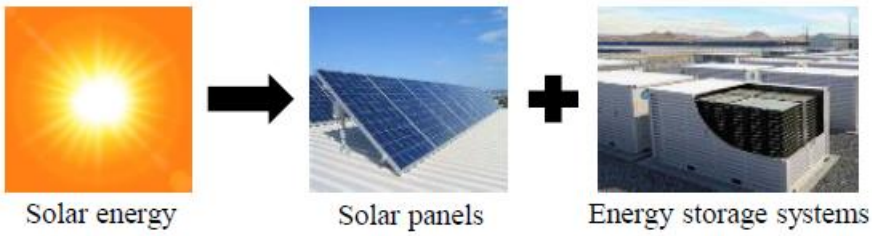

Figure 18: Solar energy on Mars. (Liu *et al.*, 2021)

3.1.4.2 Wind energy

Another possible energy source is the use of wind energy to generate electricity. Various Mars probes are measuring wind velocity on Mars, such as Viking, Mars Pathfinder and Curiosity. From the data obtained from the Mars probes, wind speeds of 2-7 m/s on the Martian surface were registered. During storms, wind speeds up to 40 m/s can be recorded (Pla-Garcia *et al.*, 2020). Due to differences in atmospheric pressure and temperature along the surface of Mars, huge dust storms can be developed. Dust and dust storms can seriously affect Mars exploration and solar energy utilisation, but on the other hand, they are also potential wind resources (Lui *et al.*, 2021).

The use of Martian wind energy is mainly to convert part of the kinetic energy of moving atmospheric particles into electricity, thermal energy or mechanical energy. Different in situ energy support strategies can be combined to realise a stable and continuous output of energy.

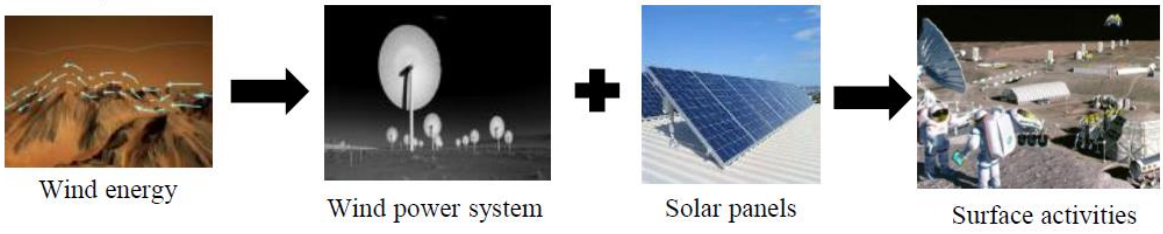

Figure 19: Wind energy on Mars. (Liu *et al.*, 2021)

3.1.4.3 Radiation energy and natural radioactive sources

Mars is highly exposed to cosmic rays (Saganti *et al*., 2004). Because there is no protective magnetic shell on Mars, and the planet is also made up of a thin atmosphere, radiation from space has an unobstructed path to Mars' surface. This radiation is very harmful to humans, but robots and machines are not hindered by these high-energy particles in space. For this reason, there is a potential for using this radiant energy as a natural energy source. Of course, it will be important to protect people against these radiations, by building highly insulated structures that can withstand these energetically charged particles in the Martian atmosphere.

The radiant energy can be used for the production of nuclear energy (Jones *et al*., 2019). In space, nuclear power systems can be applied from an energy conversion subsystem, which converts the nuclear heat into electrical energy. Figure 20 shows the conversion of nuclear energy to electrical energy. An isotopic thermoelectric generator is used for this. This device is a type of nuclear battery that uses a series of thermocouples to convert the heat released by the decay of a suitable radioactive material into electrical energy (Mesalam *et al*, 2019).

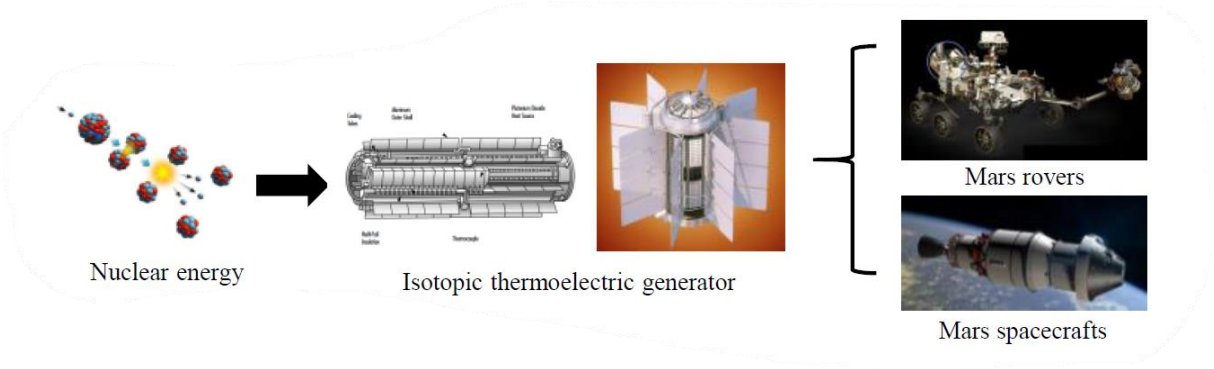

Figure 20: Conversion of nuclear energy into electrical energy for future Mars missions. (Liu *et al.*, 2021)

This generator makes use of the so-called Seebeck effect (Adachi *et al.*, 2013). This effect is known as the electromotive force (emf) that develops across two points of an electrically conductive material when there is a temperature difference between these two points. The advantage of such nuclear systems is that they provide a favourable option for missions requiring sustained energy. Many examples of nuclear-powered missions already exist, such as Curiosity Mars 2020 rover, Perseverance Mars 2021 rover, manned outposts, planetary orbiters in deep space and robotic space probes.

In order to demonstrate the feasibility of using nuclear energy, the radiations on Mars must first be determined objectively. This forms the basis for further scientific insights. When Mars Science Laboratory's Curiosity Mars rover landed on the surface of Mars in 2012, the Radiation Assessment Detector (RAD) instrument started measuring the natural radiation environment on the Martian surface. The radiation measurements have been started on August 7th, 2012. The device can measure radiation from two sources, galactic cosmic rays (GCRs) and solar energetic particles (SEPs) associated with solar flares and coronal mass ejections.

Figure 21 shows the measurements that have been made during the first 10 months after the landing of the rover on Mars (NASA, 2013). The ordinate axis represents the amount μGy per day, this is a unit of measure for the absorbed radiation dose. The abscissa represents the passage of time, with the several months at the bottom on the primary axis. The upper secondary axis shows the number of sols or Martian days since landing. The measured

radiations are mainly determined by the presence of galactic cosmic rays. These contribute to an average radiation dose of 210 μGy per day. The slight variations that can be observed are due to differences that occur in the shielding provided by the atmosphere between day and night. In total, four significant decreases were observed (sols 50, 97, 208 and 259) in the radiation spectrum, during the 10 measured months. These sudden declines are also known as Forbush declines. The reason for these sudden phenomena is due to the extra shielding from the radiations caused by interplanetary coronal mass ejections. These mass ejections are powered by the presence of sun activity. In the first 300 sols, the Radiation Assessment Detector observed only one particle event. This is indicated by the red circle on Figure 21. This peak corresponds to a dose rate of 261 μGy per day.

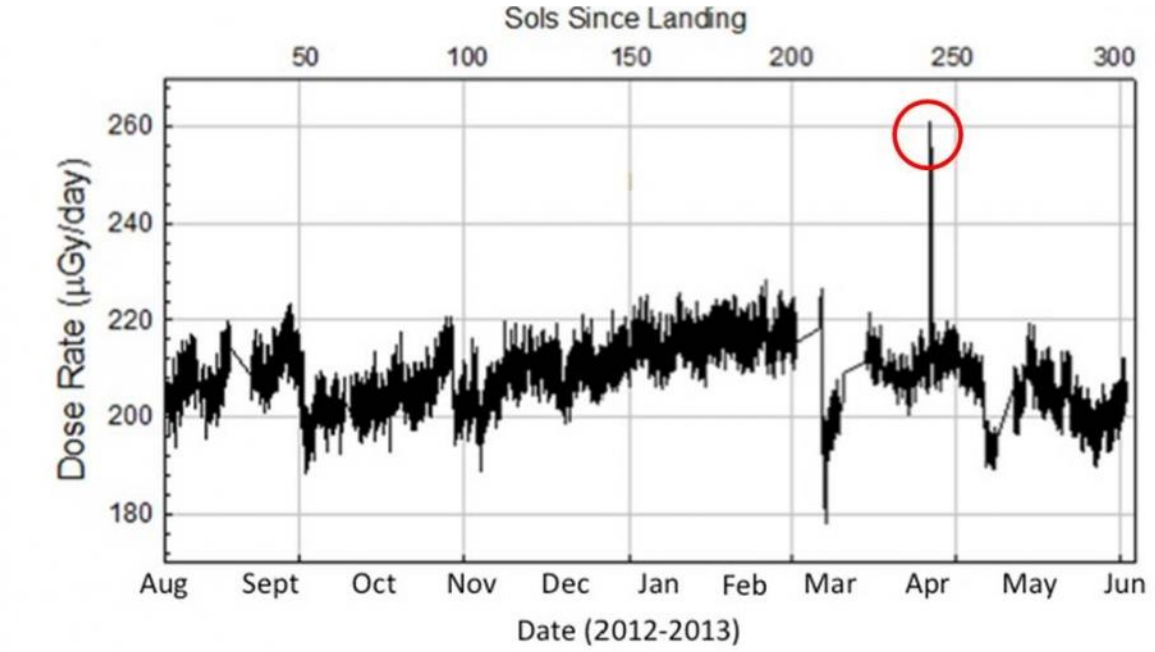

Figure 21: RAD measurements of cosmic ray and energetic particle radiation environment on the surface of Mars. (NASA/JPL-Caltech/SwRI)

An earlier study by Zeitlin *et al.* (2004) shows that the average radiation amount reaches a value of 238 μGy per day, over a range of 18 days in March 2002. These measurements were performed with Mars Radiation Environment Experiment (MARIE). MARIE is a charged-particle spectrometer consisting of silicon detectors and a Cerenkov detector. Measured dose rates range from 200 to 300 mSv per year. Sievert (Sv) represents the equivalent radiation to which a person is exposed in a given period, and is equal to 1 J/kg.

Compared to the radiation on Earth, muons produced by cosmic rays give a dose equivalent of 260 μSv per year at sea level. This is almost factor of 1000 lower than on Mars. These values apply to unprotected skin. Of course, due to the wearing of protective clothing and the presence of habitats, the actual doses will decrease in effective value. This high level of ionising radiation on the planet Mars initially poses a threat to the health of astronauts and potential humans who could populate the Red Planet. A study by Reyngold (2013) shows that the maximum allowed radiation exposure for NASA astronauts over their career is 1 Sv. In addition, this high degree of radiation on Mars appears to offer an advantage for the generation of electrical energy from nuclear sources. Compared to Earth, the radiation on Mars offers more future perspectives for the use of radiant energy in building processes on Mars. This radiant energy can be a useful natural energy source for controlling machines, such as 3D-printers.

3.1.5 Conceptual concrete structure model

From the fact of the high atmospheric differences between Earth and Mars, such as the cold temperatures and low pressures on Mars, it is necessary to design well-insulated constructions. The use of geopolymer foams offers food for thought due to the good thermal capacity (Novais *et al.*, 2020). The insulating effect of structures built on Mars is an important requirement that must be included in standards and guidelines of good practice. An example of such an insulated concrete structure developed by Reches (2019) is given in Figure 22.

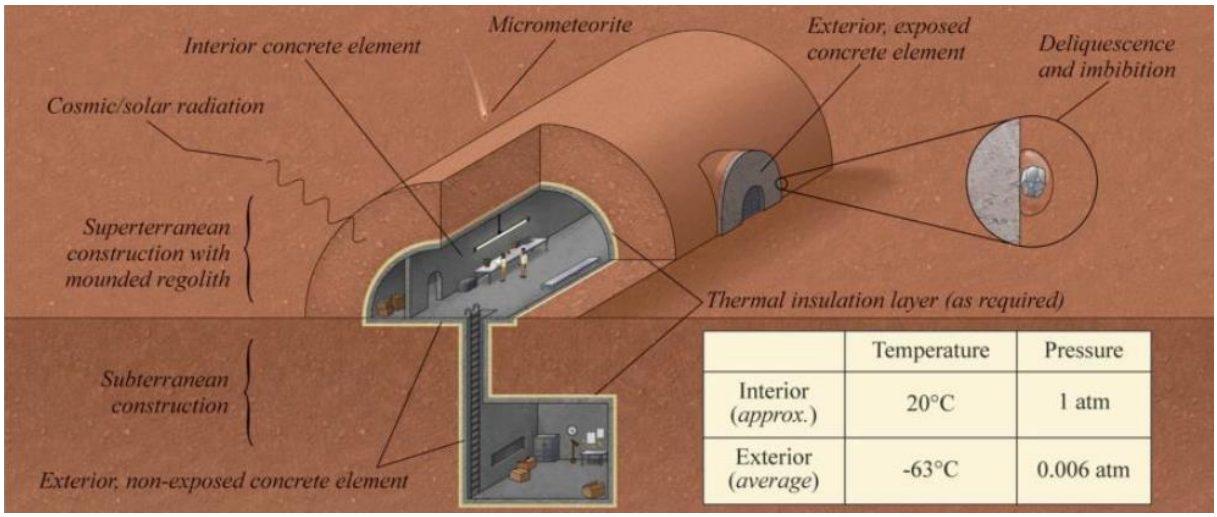

Figure 22: Structures made of concrete on the Martian surface. (Reches, 2019)

3.1.5.1 Durable materials

In situ raw materials from Mars are obtained from the surface of Mars, shallow underground layers and even deep underground spaces. Further research on material processing technologies needs to be done to ensure the strength under low pressure and temperature. The materials need to withstand the strong ultraviolet and solar radiation. The seismic and impact resistance of the building materials needs to be investigated by further research.

3.1.5.2 Intelligent construction technologies

The efficiency of energy conversion can be increased by the use of new technologies. Moreover, the space laser technology is widely studied to carry out the communication between the space shuttle and the ground. 3D printing can be applied to produce construction materials from in situ resources on Mars. Robots and automated management systems in Figure 23 are needed to carry out the intelligent construction process (Liu *et al.*, 2021).

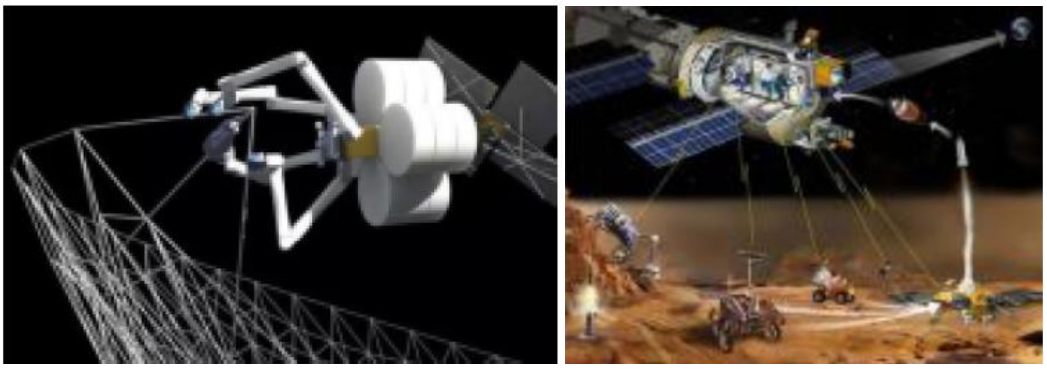

Figure 23: Intelligent construction technologies on Mars. (Liu *et al.*, 2021)

3.2 Geopolymers

3.2.1 Introduction to geopolymers

Before explaining the properties, applications and synthesis process of geopolymers, the history behind the development of geopolymers is important. Professor Joseph Davidovits is famous for his pioneering work on geopolymers. He is an internationally renowned French materials scientist and archeologist. Since 1979, he is Director of the Geopolymer Institute in France. Professor Davidovits is known as a world expert in low-temperature geosynthesis as well as in archeological science.

3.2.1.1 History of geopolymer technology

The term 'geopolymer' was coined in the 1970s by the French scientist and engineer Prof. Joseph Davidovits, and applied to a class of solid materials synthesised by the reaction of an aluminosilicate powder with an alkaline solution, called an activator (Davidovits, 1982, 1991, 2008). These materials were originally developed as high performing fire-resistant materials and for applications as coatings for fire protection for cruise ships (Talling, 2002). Other applications of these materials are found in more recent building infrastructures.

The synthesis of construction materials by alkaline activation of solid, non-Portland cement precursors was first demonstrated by Purdon in 1940. The majority of the historical background of geopolymers relates to the activation of blast furnace slags. The key distinction with geopolymers from the alkaline activation of slags, is that this produces a calcium silicate hydrate-based gel (Snell *et al*., 2017) with silicon present mainly in one-dimensional chains and some substitution of Al for Si and Mg for Ca, whereas the geopolymer gel is a normally three-dimensional alkali aluminosilicate framework structure (Duxson *et al*., 2007).

Palmo and Glasser published research into metakaolin geopolymers (Palmo & Glasser, 1992). These previous studies laid the groundwork for both broader and deeper studies of metakaolin geopolymers. This specific type of geopolymers are often used as a 'model system' by which the more commercially relevant fly ash-based materials may be better understood (Duxson *et al*., 2007).

Research into fly ash geopolymers has become of great importance in daily construction applications. Fly ash has been used in Portland cement concretes to enhance flow properties (Diamond, 1986) and to reduce the overall carbon footprint of concrete applications.

3.2.1.2 Geopolymer science

A geopolymer is defined as a solid and stable aluminosilicate material formed by alkali activation of a precursor that is usually supplied as a solid power (Davidovits, 2008). This kind of materials are not only referred to the term 'geopolymer', but has also been described as 'mineral monomers', 'inorganic polymers', 'alkali-bonded ceramics' and so on. The defining property of a geopolymer is that the binding phase comprises an alkali aluminosilicate gel, with aluminium and silicon linked in a three-dimensional tetrahedral gel framework that is relatively resistant to dissolution in water (MacKenzie, 2007 & Rees, 2007).

Initially, it must be said that geopolymers are known as a complex class of materials. The principal means of synthesising geopolymers is to combine an alkaline solution with a reactive aluminosilicate powder. The reactive aluminosilicate powder is most commonly fly ash (a by-product of coal combustion) or metakaolin (calcined kaolinite clay). This results in the formation

of a disordered alkali aluminosilicate gel phase. Embedded into this phase, are the unreacted solid precursor particles. The pore network of the gel contains the water that was used during mixing with the precursors (usually alkaline activating solution).

From studies of Provis in 2005, it has been shown that the geopolymeric gel binder displays structural similarities to zeolitic materials, observed on a nanometre length scale. Zeolites are a class of materials with a rationally designed pore system and active-sites distribution. They are primarily made of crystalline microporous zeolites, which can be accompanied by other secondary components to form composite materials (Masoumifard *et al*., 2018).

The structural analysis of geopolymers is straightforward, as they comprise a mixture of various X-ray amorphous phases, and are formed in a corrosive reaction environment. These geopolymers can be analysed by using 'challenging' techniques for characterization.

3.2.1.3 Geopolymer applications

Nowadays, geopolymers are becoming more and more popular in the world and also for space applications, like the research in this Master's thesis. The primary area of application of geopolymer technology is currently in the development of reduced-CO_2 construction materials.

Other applications for geopolymers include as a host matrix in waste encapsulation, as a low-cost ceramic and in fire protection of structures (Davidovits, 2018). The use of geopolymers in contemporary applications is gaining in importance. This new generation of cementitious materials has particular potential for use in fire-resistant fiber composites, concrete for infrastructure works and sealants (Almutairi *et al*., 2021). Further research for these applications should achieve the optimisation of the geopolymers.

Geopolymers can be seen as an ecological alternative to Portland-based cements. In many applications, geopolymers not only reduce greenhouse gas emissions, but also consume large volumes of industrial wastes such as fly ash, mine tailings and metallurgical slag (Majidi, 2009). Specifically in the construction sector, there is an increasing focus on the use of secondary raw materials and materials that can be reused. The unavoidable interest in using full or partial substitution of by-products as complementary pozzolanic materials is primarily due to the reduction of greenhouse gas emissions from cement production. Over the past decade, significant evolution and use of geopolymer concrete has been noted in the construction industry (Singh *et al*., 2015).

3.2.2 Inorganic polymer cements (IPC)

One of the main driving forces for the development of inorganic polymer technology is the potential of an alternative to Portland cement. Inorganic polymer cements (IPCs) can be synthesised by alkali-activation of a variety of materials including thermally activated clays, coal fly ash and blast furnace slag to produce a hardened material with mechanical properties that are suitable to replace the popular Portland cement (Duxson *et al*., 2007).

Inorganic polymer binders synthesised from the alkali-activation of metakaolin (thermally activated kaolinite) require large volumes of water to create workable pastes. Despite their high water demand, hardened metakaolin-based inorganic polymers can exhibit comparable mechanical properties to Portland cement (Davidovits, 1999). On the other hand, IPCs based on coal fly ash are of particular interest as they can display superior paste workability properties with less than a quarter of the water required to produce a metakaolin inorganic polymer paste. This may result in improved mechanical properties (Provis *et al*., 2007).

To determine the potential of an IPC to be a possible replacement for Portland cement, its compressive strength is usually determined by several mechanical compression tests.

3.2.2.1 Aluminosilicate glass chemistry

The reactive glassy phases present in low calcium coal fly ashes are those formed from the melting of clays present in the coal. The molten aluminosilicate droplets cool as they are carried out of the boiler and form amorphous and crystalline phases.

Phase separation occurs over most of the compositional range for aluminosilicate glasses, including the compositions likely to be present in coal fly ash. The molten particles will separate into two phases: a silica rich phase and an alumina rich phase. The most developed phase diagram for the alumina-silica composition is shown in Figure 24 (Pask, 1998).

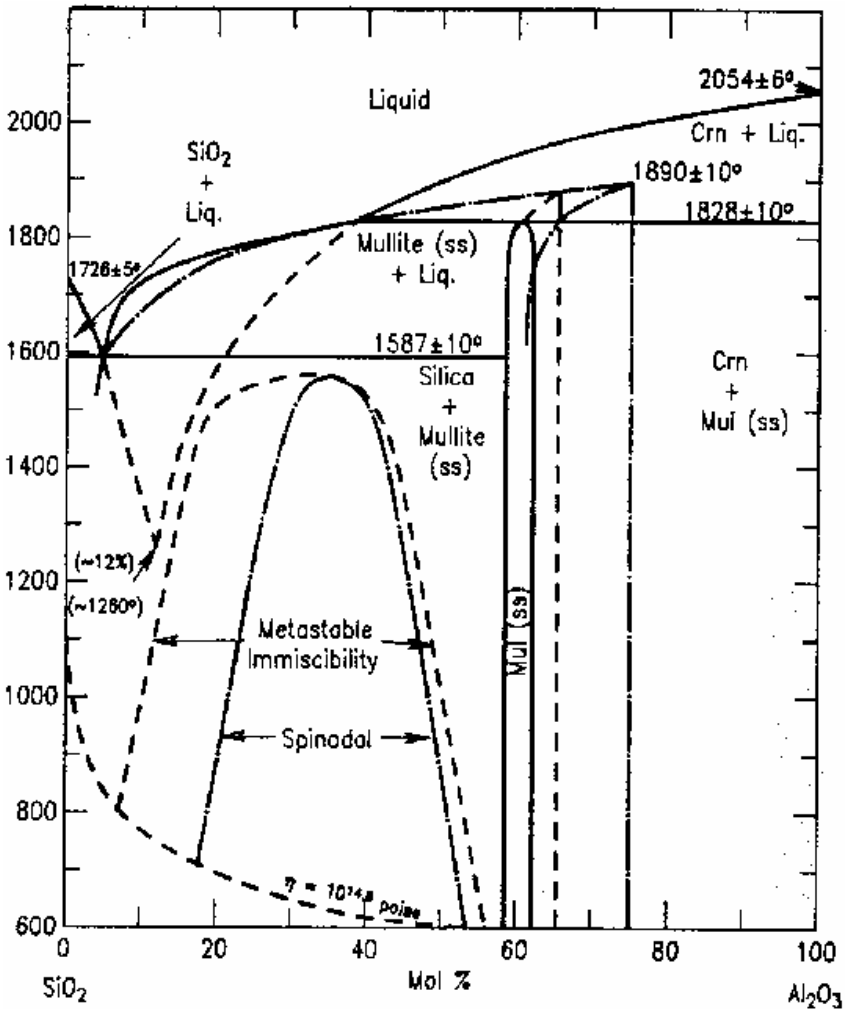

Figure 24: Phase equilibrium diagram for silica-alumina system. (Pask, 1998)

The alumina rich phase has a composition close to mullite, which is a rare silicate mineral formed from metamorphism of clay minerals. Unless rapid cooling rates are employed, a part of this phase or even the whole amount will crystallise (Johnson *et al*., 2001 & Li *et al*., 2002).

Alkali and alkali earth metal cations can have a significant impact on the behaviour of aluminosilicate melts. Aluminium can occur in tetrahedral coordination when an alkali cation is present, and these tetrahedra can substitute directly into the silica glass network. By an increasing alkali content within the melt, less and less phase separation will occur (Shelby, 2005).

3.2.2.2 Fly ash glass behaviour in IPC formation

IPCs are synthesised by dissolving aluminosilicate-rich phases from raw materials, also including coal fly ash. The major mineral constituents in Australian coals are the silicates. Kaolinite clays are generally predominant in the coals although illite and montmorillonite are also common. During the combustion of coal, the aluminosilicates will melt and mainly form spherical droplets of molten liquid.

The dissolution of different minerals and glasses has been well studied for many systems including the behaviour of silicate and aluminosilicate glasses under high alkaline conditions (Nordberg, 1964). When considering the dissolution behaviour, it is quite important to make the distinction between a crystalline and an amorphous material. Based on previous research, it has been stated that coal fly ashes contain more crystalline phases, such as quartz and mullite. These phases are considered unreactive (Craido *et al*., 2005 & Fernandez-Jiménez *et al*., 2006). This is because their rate of reaction in alkali-silicate solutions is considered to be extremely low when compared to amorphous materials.

Coal fly ashes are a complex multi-phase material and its behaviour during IPC formation is influenced by a wide range of factors. The ratio of silicon to aluminium in the reactive glass phases can vary between similar sources due to the crystallisation of mullite. A coal fly ash that cools slowly may crystallise large amounts of mullite, leaving little aluminium in the reactive glassy phases (Craido *et al*., 2005).

3.2.3 Geopolymer precursor design

This part focuses more on the design parameters for geopolymers. To make geopolymers, good raw materials are necessary. In fact, there are two classes of geopolymer synthesis, the generic two-part (solid source plus alkaline activator) geopolymer synthesis, and the one-part ‘just add water’ geopolymers.

The three most commonly used raw material classes used in geopolymerisation are slags, calcined clays and coal fly ashes. Each of these has been widely studied as a supplementary cementitious material (SCM) in Portland cement-based systems (Paris *et al*., 2016).

Calcined clays, such as metakaolin, have been relatively widely used in geopolymer synthesis. Their plate-like particle morphologies present tend to give an unfeasibly high water demand in geopolymer concrete applications.

3.2.3.1 Requirements of geopolymer precursors

Based on the concept of the real-world trade-off that a good product can be named as a ‘sweet spot’, it is necessary to take this into account. Price, reactivity, water demand and strength characteristics need to be optimized. These properties for a suitable material will be different for every geographic location, taking into account the properties and costs of the available raw materials, as well as the demands of the local market and environment. To give an example, chloride resistance is critical in marine climates, sulphate resistance in areas with acid sulphate soils, and freeze-thaw resistance is also critical.

For the research of geopolymers for the planet Mars, due to the extreme temperature variations from very low to moderate temperatures, these frost-thaw resistance should be guaranteed (Hos *et al*., 2002). In addition to the widely varying temperatures, these geopolymers must also be able to withstand the extremely low pressures and high radiation effects on the Red Planet.

3.2.3.2 Types of geopolymer precursors

Blast furnace slag (abbreviated GGBS, for 'ground granulated blast furnace slag') is broadly described as a mixture of poorly crystalline phases with compositions resembling gehlenite ($2CaO.Al_2O_3.SiO_2$) and akermanite ($2CaO.MgO.2SiO_2$), as well as depolymerized calcium silicate glasses. The degree of polymerisation largely controls reactivity.

The reactions of slag are dominated by small particles. Particles above 20 μm react very slowly, while particles below 2 μm react completely within approximately 24 hours in blended cements and in alkali-activated systems (He *et al*., 2004). It is stated that when using slag in geopolymerisation, careful control of particle size distribution can be utilised to control the strength development profile (Zhan *et al*., 2020).

Other geopolymer precursors are well-known as fly ashes. Fly ash consists of the remnant of clays, sand and organic matter present in coal. These compounds may melt in the furnace, but are then quenched rapidly in air to produce small, generally spherical glass particles. However, crystalline phases are also present, and heterogeneity is observed on both interparticle and intraparticle levels (Lam *et al*., 1998). Therefore, fly ash is a highly variable material that is dependent not only on impurities present in the coal prior to combustion, but also on the particulars of the combustion and quenching process. The fly ashes that are most widely used in geopolymer synthesis, are Class F (low in calcium) and Class C (higher in calcium) ashes.

3.2.3.3 MGS-1 simulant

The geopolymer precursors listed in the previous paragraph are not suitable to build on Mars, because of their low local availability. The synthesis of a geopolymer to build on Mars needs to start from in situ raw materials. As geopolymer aluminosilicate precursor for this research project, the MGS-1 simulant will be used, as shown in Figure 25.

Figure 25: MGS-1 simulant. (NASA/JPL-Coltech/MSSS)

The chemical composition of the MGS-1 Martian simulant is presented in Table 3 (Cannon *et al*., 2019). From this table with the chemical compositions of the MGS-1 simulant, we can conclude that this simulant is very rich in SiO_2 (50.8 w%), but has a much smaller amount of Al_2O_3 (8.9 w%) and CaO (3.7 w%) components. These three chemical components are important parameters for the geopolymer process and its efficiency.

The chemical composition proves the suitability to use this simulant material for the geopolymerisation with alkali activators. The exact amount of each of the compound will be discussed in the mix design method for geopolymers.

In designing and tailoring 'ideal' precursors for geopolymerisation to use these geopolymerised materials for building on the planet Mars, it is critical to be able to control the dissolution rates of the glassy phases present in the material. This can be achieved by optimisation of the network modifier (alkali or alkaline earth cation) content during precursor synthesis. The need for addition of alkali may be greatly reduced or even eliminated if the correct glass, or combination of glasses, can be selectively synthesised to enable a commercially viable one-part mix geopolymer.

The effect of the particle size of this geopolymer precursor needs to be taken into account for an efficient geopolymerisation process. The smaller the particles of the MGS-1 material, the higher the reaction rate due to the surface area of the particles that becomes higher. On the other hand, a higher water demand will be required for the geopolymerisation. From Cannon *et al.* (2019), the particle size distribution for the MGS-1 is given in Figure 26.

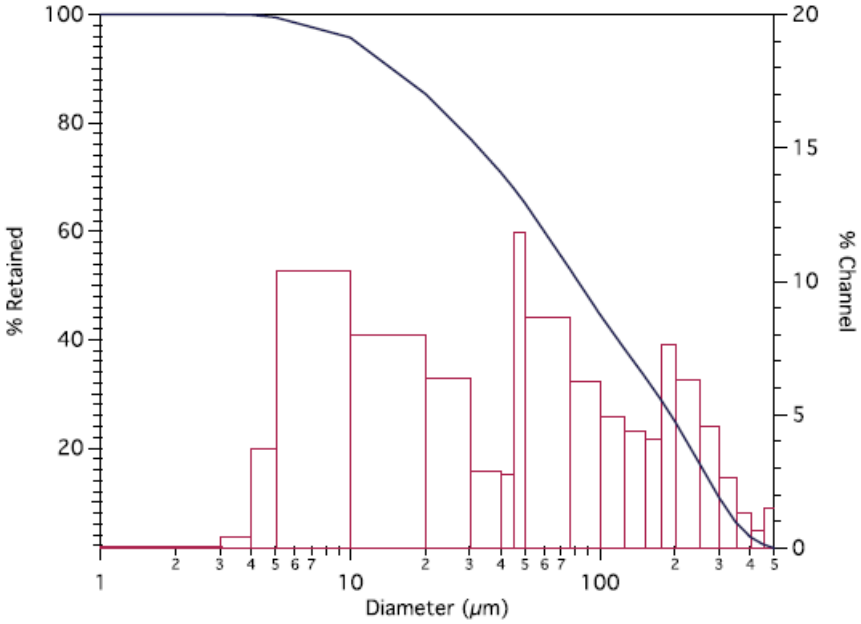

Figure 26: Particle size distribution for MGS-1. (Cannon *et al., 2019)*

The solid line on the particle size distribution shows the cumulative distribution, while the different bars show the fraction of grains in each of the channels. The mean grain size is 122 μm (Cannon *et al.*, 2019). From Webster *et al.* (2013) the whole particle sizes are described as percentages of the total volume in particles. From his study, less than 10 % of particles are in the range of 0.5-2 mm in diameter. Between 40 and 60 % of particles are sized between 100-150 μm. The last 30 to 50 % exists of finer grains than 100 μm.

Simulants based on MGS-1 are appropriate to use for a variety of scientific and engineering-based applications. In this research project, the MGS-1 is used to develop in situ resource utilisation technology (ISRU).

Unlike other simulants sourced from landscaping material, Mars Global Simulant is meant to be assembled ab initio from individual components to provide an accurate match to the mineralogy of Martian regolith. The physical, chemical, spectral and volatile properties of

prototype simulants based on MGS-1 are similar to measurements of Rocknest and other soils on Mars, and are an improvement over previous simulants (Cannon *et al*., 2019).

Table 3: Chemical composition of MGS-1. (Rampe *et al.*, 2017)

Oxide	MGS-1 (w%)
SiO_2	50.8
TiO_2	0.3
Al_2O_3	8.9
Cr_2O_3	0.1
FeO_T	13.3
MnO	0.1
MgO	16.7
CaO	3.7
Na_2O_3	3.4
K_2O	0.3
P_2O_5	0.4
SO_3	2.1

The MGS-1 Martian simulant is obtained from the Gale Crater on Mars (Bish *et al*., 2013). The average bulk density of this simulant is 1.29 g/cm³. Compared to some other well-known soils on Earth, this value of bulk density is on the lower end for typical soils. This lower value for MGS-1 can be compared to a soil with similar properties to clay.

Clayley soils have an average bulk density of 1.40 g/cm³, which value is close to the bulk density of MGS-1. Table 4 gives a better insight into some common bulk densities of soils on Earth. This table shows the different gradations of sandy and clayley materials, moving from bulk densities of 1.35 g/cm³ for clays, up to 1.65 g/cm³ for sands.

Table 4: Bulk densities of common soils on Earth. (Zeri *et al*., 2018)

Texture Class	Bulk Density (g cm^{-3})
Sand	1.65
Loamy sand	1.6
Sandy loam	1.55
Loam	1.5
Sandy clay loam	1.5
Silty clay loam	1.5
Silty loam	1.5
Clay loam	1.45
Silty clay	1.45
Sandy clay	1.4
Clay	1.35

3.2.4 Activating solution for geopolymers

In addition to the reactive solid components as geopolymer precursors, a chemical activator is needed to initiate the geopolymerisation process. The previously discussed aluminosilicate binder materials are activated by alkali hydroxides or silicates under high pH-conditions. The reaction product of this chemical reaction process will form the final geopolymer binder. The concentration of the alkali activators and the mass ratio of SiO_2 to Na_2O will determine the final properties and overall structure of the formed geopolymers.

3.2.4.1 Alkali hydroxide solutions

The alkali hydroxides most commonly used as activators in geopolymer synthesis are sodium and potassium. Aside from their obviously high corrosivity, the most important properties of concentrated hydroxide solutions that must be considered are viscosity and heat of dissolution. The graph in Figure 27 shows the variation of viscosity with concentration at 25 °C for each of the existing alkali hydroxides.

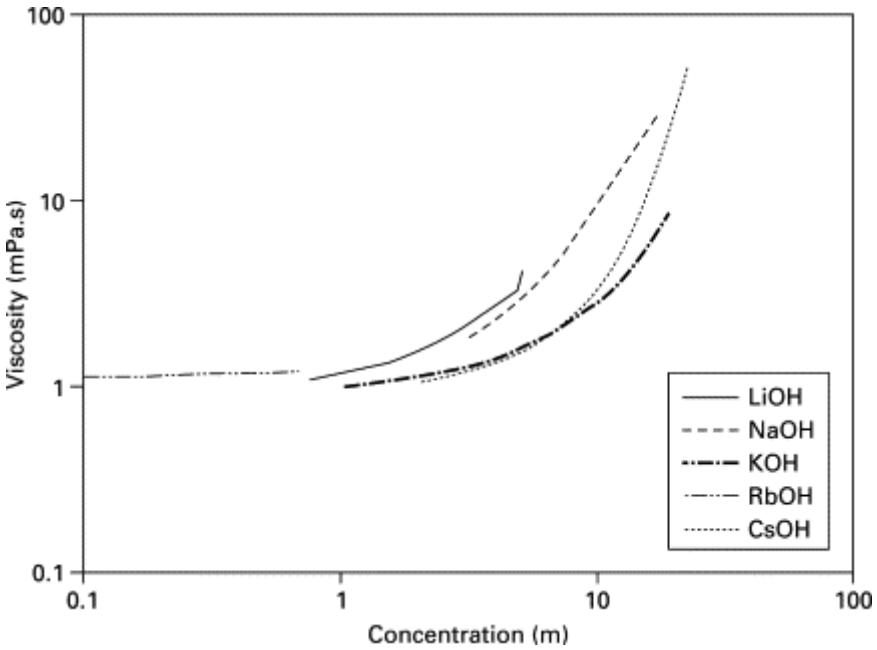

Figure 27: Viscosities of alkali hydroxide solutions as a function of concentration for LiOH, $NaOH$ and KOH (Laliberté, 2007), for $RbOH$ (Fricke, 1924) and for $CsOH$. (Sipos *et al*., 2000)

From the graph in Figure 27, it is clear that a consistent trend is followed by all the solutions depicted, with a gradual increase in viscosity up to about 1 M, at which point the viscosity does not differ markedly from that of water. After this observed gradual increase, there is a significant increase with steepness depending on the identity of the alkali cation. Note that both axes are not plotted linear, but logarithmic. All the commonly used alkali activators ($LiOH$, $NaOH$, KOH, $RbOH$ and $CsOH$) will be further discussed about their use and properties, such as solubility. The solubility, heat of dissolution and viscosity will determine the efficiency of the geopolymerisation reaction.

Before discussing the various alkali activators, the focus on the heat of dissolution is quite important. This heat of dissolution is indirectly correlated to the standard enthalpy of dissolution. Based on a study of Gurvich *et al.* (1996-1997), the standard reaction enthalpies are plotted in Figure 28. The study has been done on alkali activators with infinite dilution. In

fact, the actual heat released by dissolution into a highly concentrated solution will be slightly less than the considered infinite dilution.

The enthalpy of dissolution dominates the dilution effects, and this provides a useful estimate of the heat that will be released during the geopolymerisation process. The data of a study from Simonson *et al.* (1989) shows that the enthalpy of dissolution of $NaOH$ is only weakly dependent on the concentration at 25 °C. It does depend more on a significant difference in temperature.

Figure 28, from the study of Gurvich *et al.* (1996-1997) can be used to make the assumption that dissolving 10 moles of $NaOH$ into a litre of water releases 90 % of the heat that would be released in moving to infinite dilution. For $NaOH$ as alkali activator and a constant concentration of 10 M, the value of the standard enthalpy would be around 400 kJ. This amount of heat production will be enough to raise the temperature of the water in the solution to a sufficient level for geopolymerisation. In most cases, some heat will be lost to the surroundings and some part of the heat will be expended by evaporation of a part of the global solution.

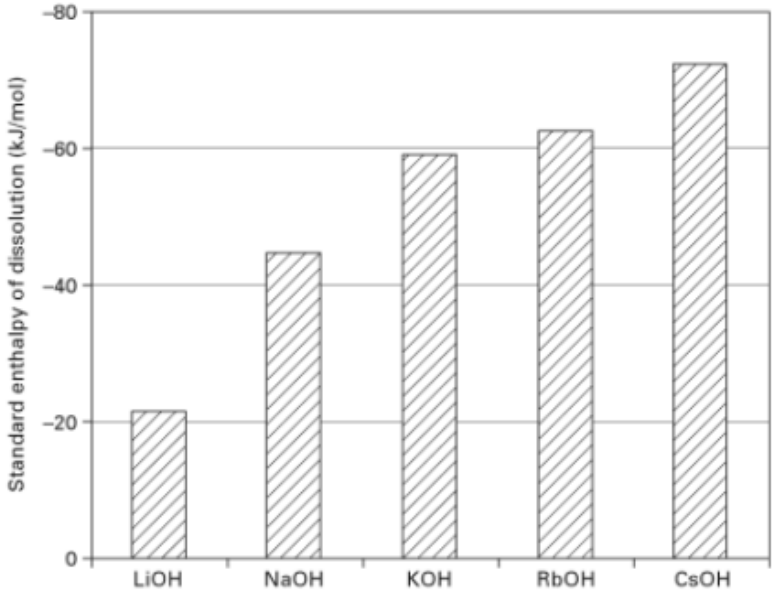

Figure 28: Distribution of standard enthalpies of dissolution for alkali activators to infinite dilution at 298,15 K. (Gurvich *et al*., 1996-1997)

As shown in Figure 28, the heat of dissolution increases with cation size. This means that solutions with high KOH concentrations will suffer a larger temperature rise than observed in $NaOH$-based solutions. The five most commonly used alkali activators for geopolymerisation are discussed below. For the research work in this Master's thesis, the alkali activators that have been used are $LiOH$ and $NaOH$. $NaOH$ is very commonly used as alkali activator, whereas $LiOH$ is seldom used as alkali activator. For this challenging research project for geopolymers on Mars, $LiOH$ seems to be an innovative and high potential material to set up the geopolymerisation process.

- **Lithium hydroxide ($LiOH$) and its radiation shielding behaviour**

$LiOH$ has the lowest solubility of the five alkali activators, with a value of 12.8 g of $LiOH$ per 100 g of water at 293.15 K (Monnin and Dubois, 2005). The use of $LiOH$ in geopolymers is either because it functions as an accelerator for geopolymerisation, analogous to its known

enhancement of colloid formation in silicate sols (Gaboriaud *et al*., 1999). In binders as cement, the primary role of Li^+ is to minimise degradation due to alkali-aggregate reaction in the presence of some reactive aggregates (Lumley, 1993). Research by Li *et al*. (2006) shows that alkali-aggregate reactions do not occur very often in geopolymers.

On Mars, the cosmic radiations are much higher than on Earth. As data was provided by the NASA's 2001 Mars Odyssey spacecraft with radiation measurement equipment, the Mars probe detected ongoing radiation levels which are 2.5 times higher than what astronauts experience on the International Space Station. 22 billion of galactic cosmic radiations are exposed to the planet Mars. This means an annual radiation level of 8 rads. For comparison to our planet Earth, humans in developed nations are exposed to 0.62 rads per year.

The human body can withstand a dose up to maximum 200 rads without permanent damage. Prolonged exposure to the kinds of radiation levels detected on Mars could lead to all kinds of health problems, such as acute radiation sickness, increased risk of cancer, genetic damage and even in the worst case it could lead to death. All these risks are presented in Figure 29.

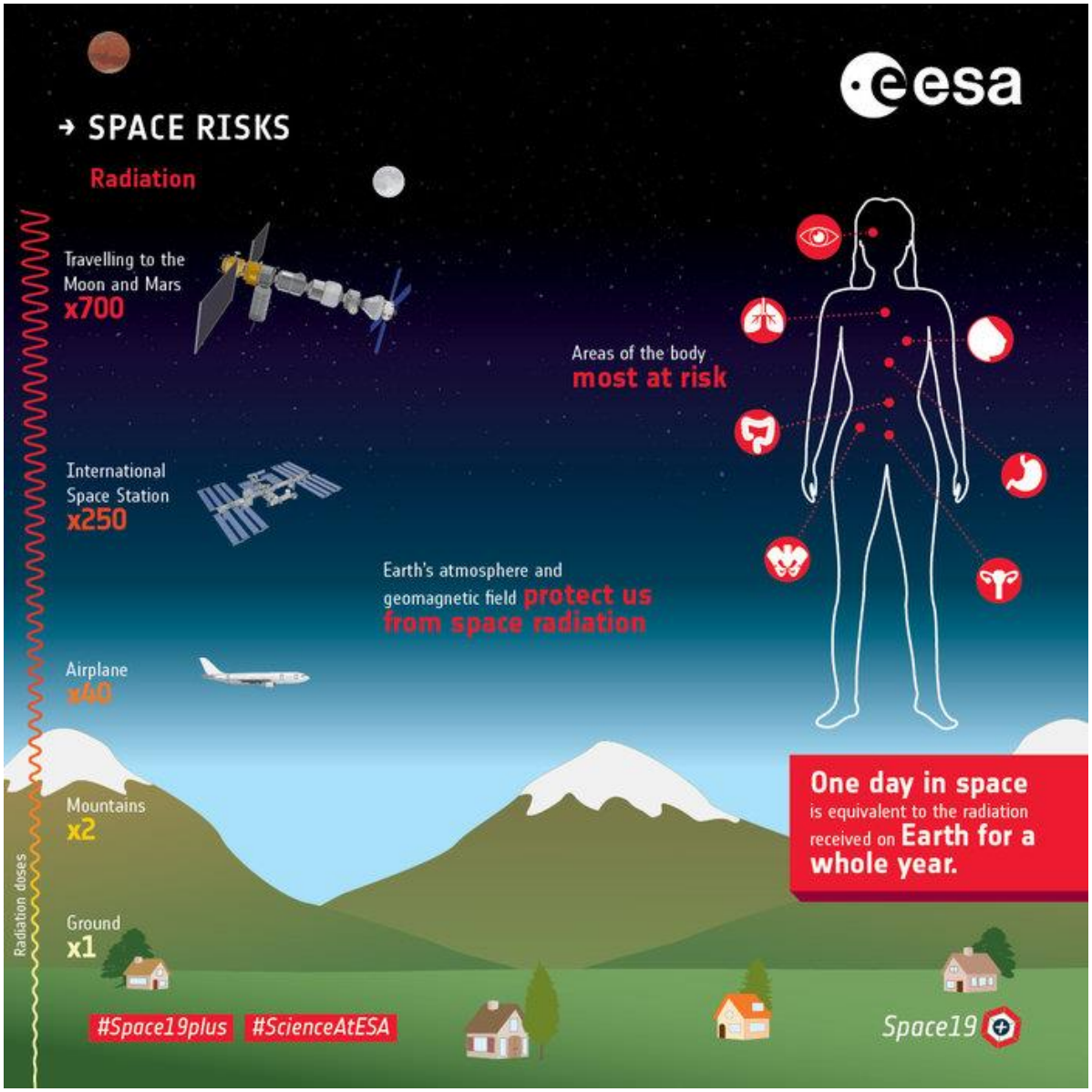

Figure 29: Importance of cosmic radiations on Mars, compared to other activities on Earth and in space. (ESA, 2019)

Figure 29 also shows the importance of the cosmic rays on Mars. This is especially important when preparing astronauts and humans for the long trip to Mars. Generally, one day in space corresponds to the radiation that a person on Earth would receive during a whole year.

Therefore, it is important to shelter ourselves from the strong galactic radiations. Therefore a material must be provided that can protect us when living on Mars can become reality. The use of $LiOH$ as a protection shield against the cosmic radiations is a good option.

Since $LiOH$ has a low molecular weight, the resistance against several radiations can be provided. As a recent study from Jones *et al*. (2020) proved that $LiOH$ can help by shielding a spacecraft on Mars against cosmic rays, this alkali activator can be used for making geopolymers to build on Mars.

- **Sodium hydroxide ($NaOH$)**

$NaOH$ is the most commonly used hydroxide activator in geopolymer synthesis. This alkali activator has the advantages in being cheap, reliable and widely available. These are the reasons why this alkali is widely used for geopolymerisation applications. $NaOH$ has a low viscosity and a good solubility of 111 g of $NaOH$ per 100 g of water at 293.15 K. Based on the phase diagram of $NaOH - H_2O$, provided in Figure 30, the solubility of $NaOH$ increases from 41.8 g/100 g to 337 g/100 g, with corresponding increase in temperature from 0 °C to 100 °C.

Between the temperature range of 0 and 25 °C, a complex sequence of solid hydrates is formed between concentrations of 30 and 50 wt% $NaOH$ (Pickering, 1893). The use of sodium hydroxide activators in geopolymers is well known to lead to the formation of observable zeolitic structures (Provis *et al*., 2005b). This happens particularly after extended periods of curing under moist conditions, or when exposed to a period of increased temperature.

A known issue in geopolymers activated with hydroxide solutions, is the formation of efflorescence (Zhang *et al*., 2013). Efflorescence is the formation of white sodium carbonate or bicarbonate crystals. In this process, the excess alkali reacts with atmospheric CO_2.

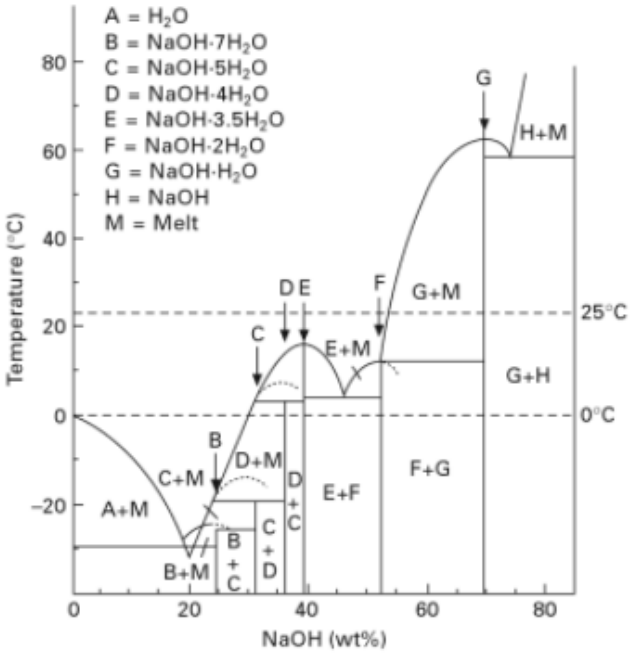

Figure 30: Phase diagram for $NaOH - H_2O$. (Cohen-Adad *et al*., 1960)

- **Potassium hydroxide (KOH)**

The solubility of KOH at 293.15 K is 112 g KOH per 100 g of water and does not dramatically decrease with decreasing the temperature (Pickering, 1893). Similar to sodium hydroxide, zeolite formation is also well-known to take place in KOH-activated geopolymers. Geopolymers are in fact similar to zeolites in chemical composition, but they reveal an amorphous structure. A study by Xu & Van Deventer (2000) generally found that minerals with a higher degree of dissolution show better compressive strength after geopolymerisation. The use of KOH instead of $NaOH$ promoted the geopolymerisation of all minerals, with a maximum compressive strength of 18 MPa being obtained. These good mechanical properties were established in the tectosilicate stilbite, after conditioning in KOH solution.

However, an important remark about KOH, is that crystallisation occurs less rapidly in KOH-activated metakaolin geopolymers than in $NaOH$-activated metakaolin geopolymers (Duxson *et al*., 2007).

- **Rubidium hydroxide ($RbOH$)**

Intensive research on the geopolymerisation process activated by $RbOH$ has not been conducted in detail. The main reasons are the high cost, low stability and relative scarcity of $RbOH$. The solubility of $RbOH$ has been obtained at a temperature of 293.15 K and has a value of 180 g $RbOH$ per 100 g of water (Wan *et al*., 2015). $RbOH$ has the second highest solubility in water, after $CsOH$, compared to the five alkali activators studied in this paragraph.

A study by Bernal *et al*. (2015) proves to be of interest for Mars' building research, as metakaolin geopolymers were analysed for dimensional stability at elevated temperature. Among other things, Rb silicate solutions were also used in this research context. Since temperatures can fluctuate widely on the surface of Mars, ranging from very low temperatures in the order of -130 °C to normal temperatures of 30 °C, it is important to investigate this shock effect from low to suddenly high temperatures. This research was based on X-ray diffraction of geopolymers produced with Na-, K-, Rb- and Cs-silicate solutions. After 5 years of curing, variations in structure and performance of the geopolymers were examined. From this study, it was found that the samples based on Rb- and Cs-silicate solutions showed no significant dimensional changes when exposed to a higher temperature.

Based on this new insights, increasing the radius of the alkali cation has a positive effect on the thermal stability of the metakaolin-based geopolymers. In addition, a highly densified and rigid structure is developed with long term curing conditions. Since not many studies have been performed for the geopolymerisation with $RbOH$, the research of Bernal *et al*. (2015) shows that this atom certainly has further potential for its use during geopolymerisation processes.

- **Caesium hydroxide ($CsOH$)**

$CsOH$ has been used in geopolymerisation in some instances, but predominantly in silicate-activated systems. The main use is in ceramic-type applications, where the higher thermal resistance and very low thermal expansion of aluminosilicates is desirable (Kriven *et al*., 2007). The solubility of $CsOH$ in water at 293.15 K is around 400 g $CsOH$ per 100 g of water (Kaneco *et al.*, 1999). From this fact, it can be stated that precipitation of $CsOH$ or its hydrates is unlikely to be problematic in geopolymer synthesis.

Other studies of Provis (2006) and Bell *et al*. (2008) show that the use of $CsOH$ as activator for aluminosilicate geopolymers provides very good X-ray contrast in a matrix of lighter elements such as Al and Si. According to Provis *et al*. (2008), $CsOH$ improves the geopolymerisation by forming a better metakaolin solution and the accelerated gel formation in the reaction process.

3.2.4.2 Alkali silicate solutions

Next to the commonly used alkali hydroxide solutions, geopolymers are often activated with alkali silicate solutions. Silicates are part of a family of anions consisting of Si or O. By using sodium hydroxide in high concentrations, replenished with silicate solutions, greater dissolution of the initial solid materials and hence higher compressive strength is achieved. Because of the enhanced solubility and chemical integrity, silicate solutions are used together with hydroxides for the production of geopolymers.

Several dissolution mechanisms exist for silicate compounds in the presence of hydroxides. By increasing the number of OH-groups, the energy barrier is reduced, which can promote the breaking of bonds. During the dissociation process of a water molecule, the hydrogen atom protonates a nearby silicate chain. This causes the OH-group to bond with a silicon atom and a water molecule pulls away the $Si - O - Si$ bridge. Eventually, the two silicates have been dissociated. The simplest dissociation mechanism is described as follows (Dupuis *et al*., 2020):

$$Si_2O_7H_6 + OH^- \rightarrow SiO_4H_4 + SiO_4H_3^-$$

Figure 31 shows the portion of the $Na_2O - SiO_2 - H_2O$ composition with crystallisation isotherms at 298.15 K (Baker *et al*., 1950). A study of Weldes & Lange (1969) shows that all compositions given for common commercially available sodium silicate solutions fall in the region in which precipitation of $Na_2SiO_3.9H_2O$ would be expected. Note that silica concentrations are plotted on logarithmic scale in Figure 31, to have a better presentation of the data at low silica content. For the purposes of the geopolymer activating solutions, the higher-silica region of the diagram is sufficient, as higher concentrations will be used.

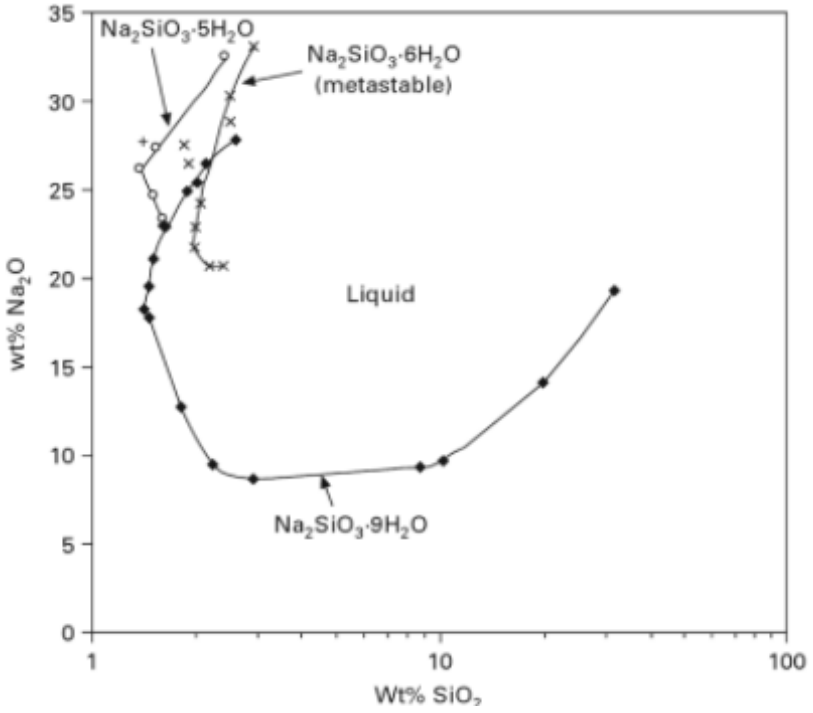

Figure 31: Crystallisation isotherms for hydrated sodium metasilicate phases at 25 °C and ambient pressure. (Baker *et al*., 1950)

From a study of Vail (1952), Figure 32 shows the fully ternary $Na_2O - SiO_2 - H_2O$ system at ambient temperature is provided. The diagram is divided in different regions to denote the properties and uses of materials obtained in each region. Each region of the diagram is briefly discussed. The regions that are most important in geopolymer synthesis are regions A and B.

Region A denotes the partially crystalline mixtures where generally many low-silica activating solutions are metastable compositions in this region. The most commercial silicate solutions fall in region B of the diagram. Solutions with composition in region C are highly prone to crystallisation, often hydrated sodium metasilicates. Region B tends to give inconveniently high viscosities, which is not sufficient for geopolymerisation at ambient conditions (Vail, 1952).

Lithium silicate solutions are researched by Vail (1952) and Weldes & Lange (1969). From that study, it became clear that lithium silicate preparation is hindered by the low solubility of hydrated lithium metasilicate phases, particularly at increased temperature.

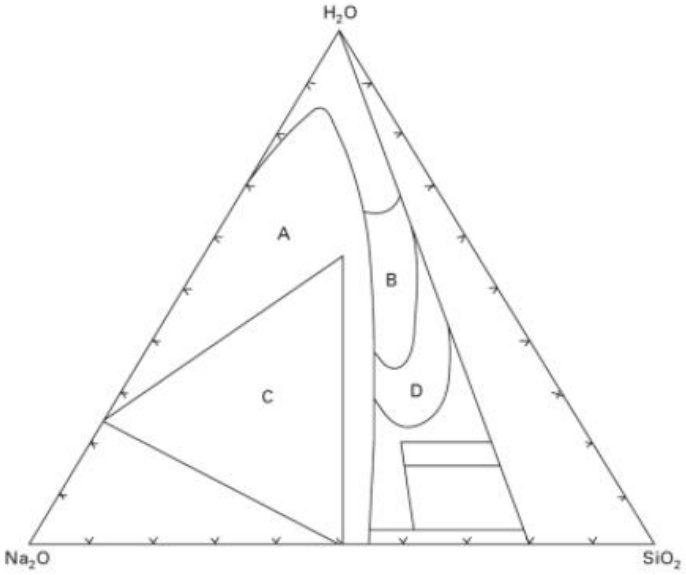

Figure 32: Compositional regions leading the different type of product in the $Na_2O - SiO_2 - H_2O$ system. (Vail, 1952)

Where sodium and potassium silicates are usually prepared by direct dissolution into water of glasses of appropriate composition, lithium silicate is instead generated by the dissolution of amorphous silica into aqueous $LiOH$ (Iler, 1979). Compared to hydroxide solutions, most silicate activating solutions used in geopolymerisation are buffered at pH varying from 11 to 12. The most commonly used hydroxide, which is $NaOH$, has a pH value between 13 and 14.

3.2.4.3 Effect of alkali concentration and curing conditions on mechanical properties

A study by Tuyan *et al*. (2018) investigated the effect of the alkali activator concentration and curing conditions on the consistency and strength of claystone powder-based geopolymers. The results of the study show that the optimum alkali activator concentration was achieved at a mass ratio of SiO_2/Na_2O of 1.6 and Na_2O content of 10 % by weight. The maximum compressive strength of 36.2 MPa was determined by curing for 5 days at 90 °C.

Another study by Livi & Repette (2017) on fly ash-based geopolymers generally found an improve in mechanical strength by increasing molecular concentration and curing temperature. The strongest geopolymer mixture was obtained with a 16 M $NaOH$-solution and a curing temperature of 85°C. This resulted in a final compressive strength of 21.4 MPa.

A recent research by D'Elia *et al*. (2020) investigated the effect of varying activating solution concentration of 4, 6 and 8 M $NaOH$ on mechanically and thermally pretreated carbonate-high illite clay strength development. Mixtures were prepared with an alkali solution/clay mass ratio of 0.55 and cured at room temperature in a climate chamber. The results of the study show that the mixtures prepared with higher concentrations of 6 or 8 M $NaOH$ exhibit a more compact matrix than those prepared with 4 M $NaOH$. Using the 6 M $NaOH$ solution yields a binder with a compressive strength of 20 MPa after only 2 days, and a strength of 30 MPa after 28 days.

3.2.4.4 Effect of composition of silicate solution on viscosity and density

Figure 33 presents the viscosities of sodium silicate solutions as a function of its composition, showing data obtained from Vail (1952). To compare the commonly used sodium silicate solutions to potassium silicate solutions, Figure 34 represents the viscosities of potassium silicate solutions with varying composition, also obtained from data of Vail's research (1952).

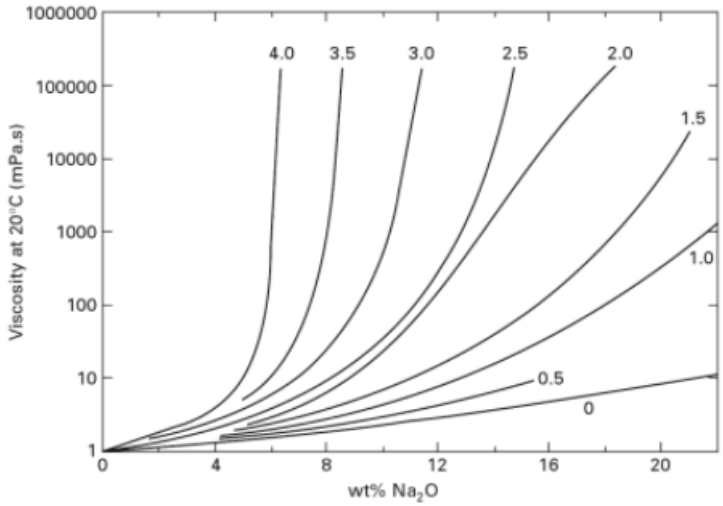

Figure 33: Viscosities of sodium silicate solutions with mass ratio SiO_2/Na_2O, indicated on the curves. (Vail, 1952)

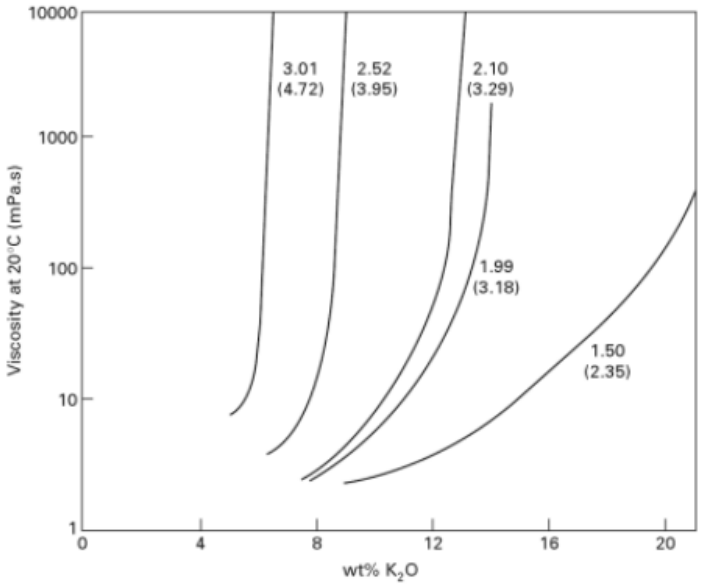

Figure 34: Viscosities of potassium silicate solutions with mass ratio SiO_2/K_2O, indicated on the curves. (Vail, 1952)

From the data of Figures 33 and 34, an important remark is that viscosities of the alkali silicate solutions are plotted on logarithmic scale. With increasing silica content (this means a higher SiO_2/K_2O ratio), the viscosity increases dramatically. Potassium silicate solutions show a significantly lower viscosity than sodium silicates of comparable composition. This is rather an important value for laboratory study of geopolymers, where the higher cost of potassium silicate solutions is less important than in commercial production of geopolymers.

Yang *et al*. (2008b) showed that the viscosity of sodium silicate solutions decreases significantly with increasing temperature. However, the solubility of some sodium metasilicate phases begins to decrease at elevated temperature (Vail, 1952), meaning that heating is not a guaranteed way to ensure or accelerate the dissolution of solid precursors during preparation of a geopolymer activating solution.

A study by Favier *et al*. (2014) was performed on the flow properties of metakaolin-based geopolymers. This study proves that these geopolymers can be described as Newtonian fluids. The colloidal interactions between the metakaolin particles are negligible, and it is mainly the hydrodynamic effects that control the rheological behaviour. The viscosity of geopolymers is mainly controlled by the high viscosity of the suspension of the alkaline silicate solution. An important remark is that the viscosity of the final geopolymers is not determined by the contribution of direct contacts between metakaolin grains, but by the composition of the alkaline liquids. Vail also highlighted that starting from a given density and viscosity of a silicate solution, these physical properties are sufficient to calculate its composition without need for a chemical analysis of the silicate solution.

Figure 35 shows the variation of sodium silicate solution density as a function of its composition, depending on the amount of silica (SiO_2) and sodium (Na_2O). The density of the alkali silicate solution is directly related to the microstructure of the geopolymer to be formed. Hereby, a denser alkali silicate solution will ensure that the matrix is more densely packed. This will increase the cohesion forces between the different grains in the geopolymer matrix, which will significantly increase the ultimate strength of the geopolymer.

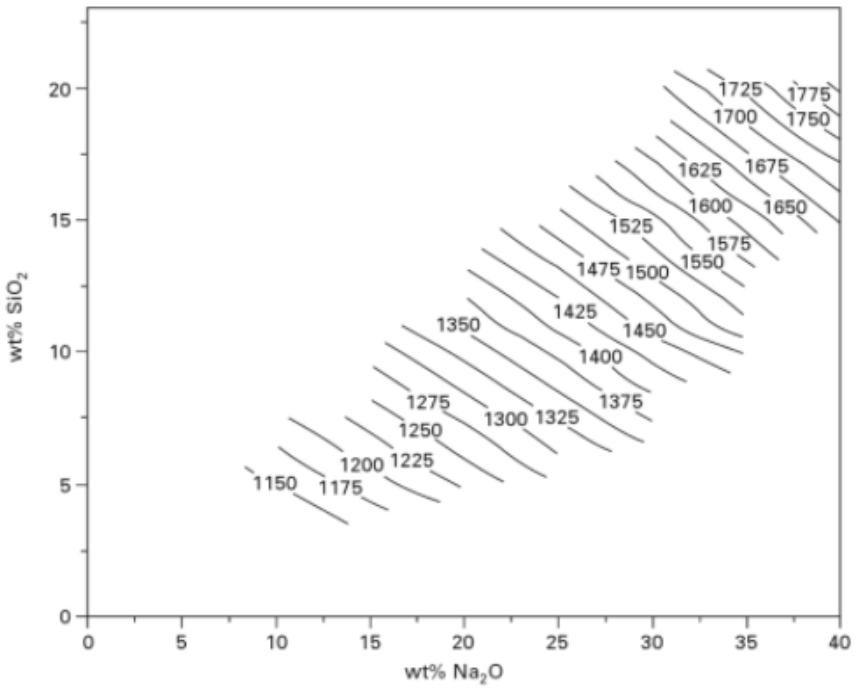

Figure 35: Density of sodium silicate solutions as a function of its composition. (Vail, 1952)

Figure 35 shows that especially the amount of silica will have an important influence on the final density of the sodium silicate solution. A less strong gradient in silica is required to generate the same change in density as with sodium. For the design of the geopolymers, the amount of silica and sodium can be determined. In this way, an accurate estimate can be made of the expected density of the final geopolymer.

For the research in this Master's thesis, sodium silicate is used as alkali silicate solution. Sodium and potassium silicates and hydroxides are the most commonly used activating solutions, with sodium-based solutions being less expensive. Nevertheless, potassium-based solutions represent more favourable phase behaviour.

3.2.5 Comparison between geopolymers and OPC

Compared to Ordinary Portland cement (OPC), geopolymers are more environmentally friendly because they can reduce carbon emissions. Due to lower temperatures required to produce geopolymers, the 3D structure of geopolymers and OPC can be compared to each other. A study by Mo *et al*. (2014) on the geopolymerisation of metakaolin-based geopolymers shows that the best mechanical properties are obtained at a curing temperature of 60 °C. Compared to the manufacture process of Portland cement, the curing temperature is no less than 1300-1450 °C.

Figure 36 shows the 3D structures of both geopolymer (left) and OPC (right). The geopolymer matrix clearly shows a three-dimensional network. Since Al^{3+} of $(AlO_4)^{-1}$ is a fourfold coordination, Na^+ compensates for the excess negative charge (Lahoti *et al*., 2019). The water as a catalyst generally does not participate in the geopolymerisation. In addition, the water of the calcium silicate hydrate gel ensures calcium silicate hydrate ($C-S-H$) to be formed.

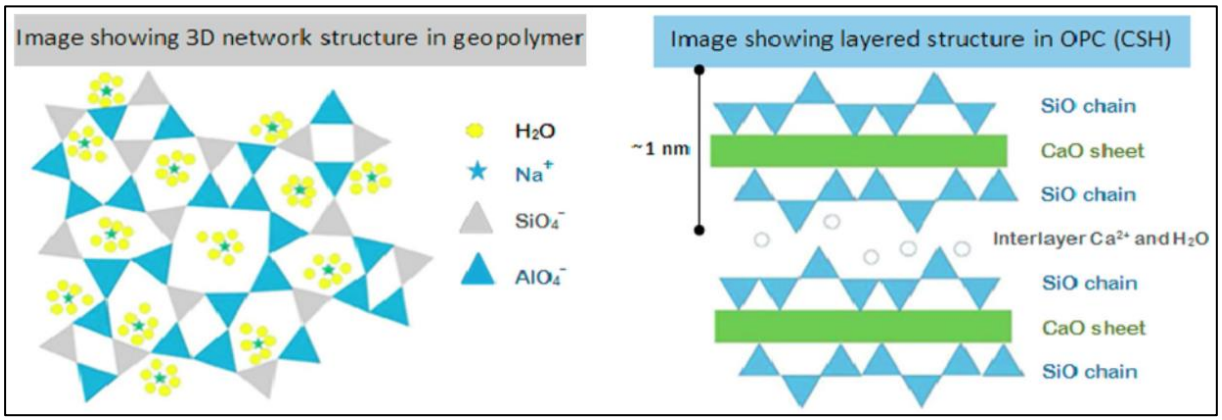

Figure 36: Schematic molecular structure of geopolymer in contrast to OPC. (Lingyu et al., 2021)

Where the geopolymerisation provides a three-dimensional network, the curing of OPC will result in a layered structure (Saleh & Eskander, 2020). This is due to exothermic hydration reactions of the cement components with water molecules. Portland cement contains four main components, namely C_3S, C_2S, C_3A and C_4AF. Both silicates C_3S and C_2S require almost the same amount of water for hydration. C_3A reduces the temperature of burning of clinker and facilitates the combination of lime and silica, while C_4AF is more stable because it produces less heat compared to C_3A.

Calcium hydroxide is formed from the C_3S-hydration, and is more than twice that obtained from C_2S hydration. The reaction rate of C_3A is faster than that of the calcium silicates, therefore

gypsum ($CaSO_4.2H_2O$) is added to cement clinker. During the hydration reactions, the following four reactions take place between the different cement components and water molecules:

$$C_3S + 6H_2O \rightarrow C_3S_2.3H_2O + 3Ca(OH)_2$$

$$C_2S + 4H_2O \rightarrow C_3S_2.3H_2O + 3Ca(OH)_2$$

$$C_3A + 6H_2O \rightarrow C_3A.6H_2O$$

$$4C_4AF + 2Ca(OH)_2 + 10H_2O \rightarrow C_3A.6H_2O + C_3F.6H_2O$$

The strength of geopolymers is based on polymerisation, while the strength of OPC comes from the hydration of Portland cement (Škvára *et al*., 2006). The hardening mechanisms of geopolymers and OPC are significantly different from each other. In fact, there are currently geopolymers that achieve higher strengths than OPC.

For example, the study of Atiş *et a*l. (2015) shows that geopolymers based on class F fly ash and $NaOH$ as activating medium achieve a compressive strength of 120 MPa. For this geopolymer design, the boundary conditions are the following: alkali activation with 14 % $NaOH$, and curing of 115 °C for only 24 hours.

In Figure 37, the ternary diagram for $SiO_2 - Al_2O_3 + Fe_2O_3 - CaO$ is presented. This represents the possible aluminosilicate precursors that can be used for geopolymerisation reactions. The left part of the diagram mainly shows the precursors for OPC, which reach their strength by hydration reactions. This mainly consists of components rich in CaO, such as ground granulated blast furnace slag (GBFS). On the right side of the diagram, the main precursors that can be used for geopolymers are shown. These mainly contain components rich in Al_2O_3 and SiO_2, such as metakaolin (MK).

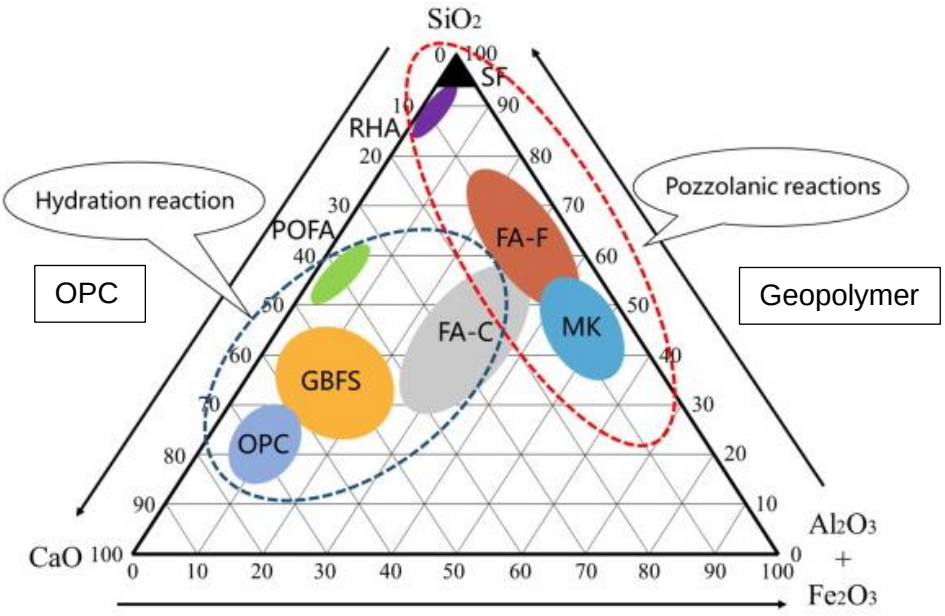

Figure 37: $SiO_2 - Al_2O_3 + Fe_2O_3 - CaO$ ternary diagram. (Chen *et al*., 2021)

3.2.6 Metakaolin geopolymers

In the research for synthesising several geopolymers to build on the planet Mars, kaolinite will be used as an additive, next to the MGS-1 simulant as aluminosilicate geopolymer precursor.

The use of kaolinite as an additive to MGS-1 was determined from the fact that mineral species such as kaolinite have been identified around the Gale Crater (Xue & Jin, 2013). In addition to kaolinite, other mineral species such as chlorites, smectite, jarosite, and northupite were detected. The diversity of the clay minerals in Gale Crater suggests the variation of aqueous change. The presence of iron sulfate mineral jarosite, formed by the oxidation of iron sulfides in acidic environments, shows the experience of acidic sulfur rich state in Gale history.

The importance and principle of metakaolin geopolymers need to be well-understood before starting the design process for making the geopolymers. More specifically, in this part the formation, structure and properties of metakaolin geopolymers are further discussed and evaluated.

3.2.6.1 Metakaolin

Metakaolin itself is a relatively complex material that can be generated by a heating process of kaolinite. Metakaolin is generated by the calcination of kaolinite clay at temperatures ranging from 500-800 °C, depending on the purity and crystallinity of the precursor clay (MacKenzie *et al*., 1985). Metakaolin is also used as a pozzolanic additive to Portland cement concretes, or is activated by mixing with lime (Sabir *et al*., 2001).

The main disadvantage of the use of metakaolin-based geopolymers is that the very high surface area and plate-like particle shape of the metakaolin mean that the water demand of a reacting metakaolin mix is very high. The layered structure of kaolinite is shown in Figure 38. Due to the very high surface area and plate-like particle shape of metakaolin, difficulties such as drying shrinkage and cracking can develop. These failure mechanisms occur due to the excess water leaving the hardened geopolymer over a period of time.

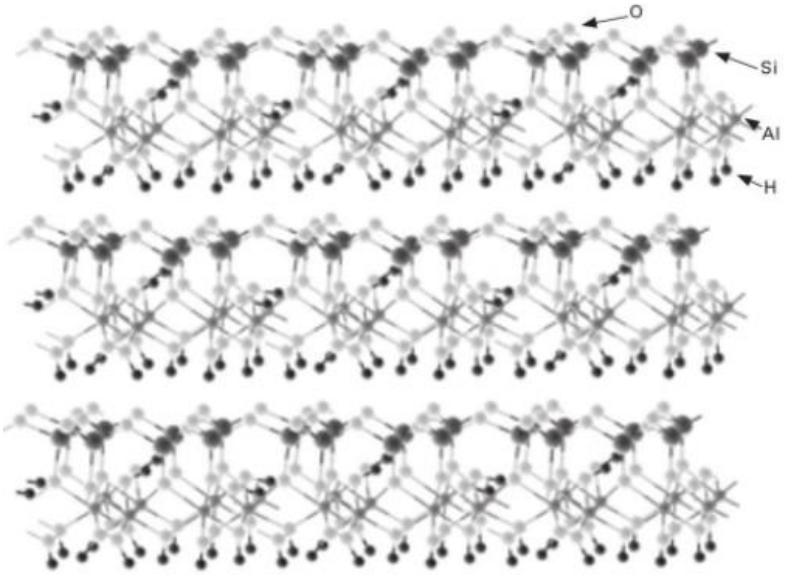

Figure 38: Layered structure of kaolinite. (MacKenzie *et al*., 1985)

In addition, the effect of efflorescence is higher in metakaolin geopolymers than in fly ash-based geopolymers, due to the higher alkali content of these materials. In literature, metakaolin-based geopolymers are often used as a model system to explain the geopolymerisation reactions of other geopolymers. Since metakaolin is an anhydrous aluminosilicate material made from calcined natural kaolinite $Al_2Si_2O_5(OH)_4$, its chemical stability is high. During the dihydroxylation process, water is lost and a natural amorphous and disordered structure will be formed, as shown in Figure 39 (Paiva *et al.*, 2016).

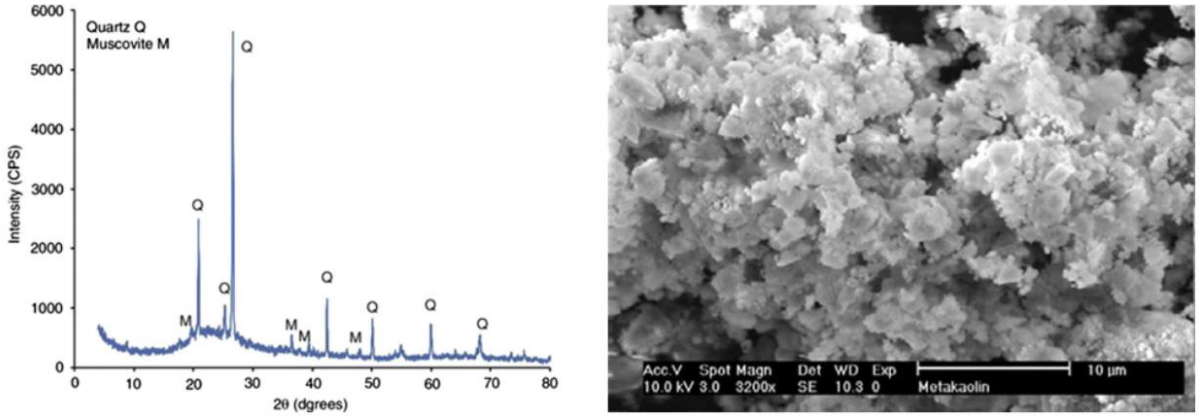

Figure 39: X-ray diffraction (left) and SEM (right) of metakaolin. (Lingyu *et al.*, 2021)

As can be observed from Figures 38 and 39, the structure of metakaolin appears disordered to X-ray analysis, although the fact that it is derived by the removal of hydroxyl groups from the layered kaolinite structure means that some degree of ordering must remain. This is observed by electron diffraction (Lee *et al*., 2003), and also in the fact that the dihydroxylation process is at least partially reversible (Rocha & Klinowski, 1990).

In essence, metakaolin consists of alternating buckled silicate and aluminate layers, with the silicon in 4-coordination and the aluminium in a mixture of 4-, 5- and 6-coordination. It is generally accepted that the key to the reactivity of metakaolin is the strain in the bonding network induced by thermal dihydroxylation (Davidovits, 2008). The metakaolin sources used in geopolymerisation differ very significantly in particle size, purity and in the crystallinity of the kaolinite from which they were derived.

The K_α diffractogram of Metastar 402 is shown in Figure 40. Metastar 402 is a commercial metakaolin. All sharp peaks are attributed to a slight muscovite impurity. The broad peaks at 15°-35° 2θ are characteristic of the metakaolin structure.

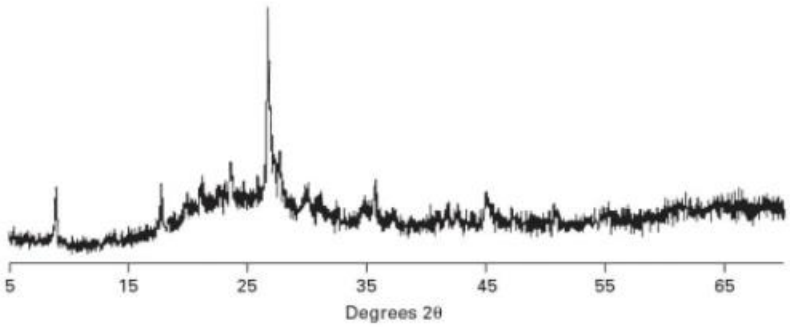

Figure 40: K_α diffractogram of a commercial metakaolin. (Metastar 402, Imerys, UK)

3.2.6.2 Formation of metakaolin geopolymers

The formation process of metakaolin geopolymers can be divided into 4 main parts. The insight into this process is crucial for the understandings in reaction rate and potential reaction products.

1. Alkaline attack on the metakaolin structure results in the release of silicate and aluminate species into solution, with 5- and 6-coordinated Al being converted to 4-coordination upon dissolution (Duxson *et al*., 2005). It has been stated that the initial release of Al may be more rapid than that of Si (Weng & Sagoe-Crentsil, 2007).

2. Interactions between the small dissolved species, and also involving any silicate initially supplied by the activating solution, lead to the transformation of aluminosilicate oligomers.

3. Dissolution proceeds to the point where the concentration of dissolved aluminate is sufficiently high to destabilise the silicate solution, and precipitation of dissolved species activates the formation of a gel. Note that the dissolution continues while gelation is occurring, meaning that the coating of gel on the particle surfaces will impact the dissolution process by hindering mass transport (Feng *et al*., 2004).

4. Geopolymer gel grows to the point where the reacting slurry solidifies. The time taken for this depends strongly on the mix design, as well as the presence of any contaminants. Setting can occur directly or it can take some time, depending on the mix design and the curing environment. Reaction processes continue for some time after the point of setting, as is evident from ongoing strength development and also the growth of X-ray observable zeolitic crystallites in some samples (Duxson *et al*., 2007).

In the case of metakaolin geopolymers, the achievable extent of reaction for the conversion of metakaolin to geopolymer gel, is in many circumstances quite high. This is particularly the case if samples are cured in sealed moulds at slightly elevated temperature for some period of time (Provis *et al*., 2005).

3.2.6.3 Nanostructure of metakaolin geopolymers

Nuclear Magnetic Resonance (NMR) spectroscopy has proven to be a technique of significant value in the investigation of metakaolin geopolymers in particular. The study of NMR spectroscopy on fly ash geopolymers is often problematic due to the presence of iron in many fly ashes. As from the data provided by the X-ray diffractograms of geopolymers synthesised with different alkali activators, the results are shown in Figure 41. Geopolymers synthesised by mixing metakaolin with (a) sodium hydroxide solution and (b-e) sodium silicate solutions with mole ratios SiO_2/Na_2O of 0.5, 1, 1.5 and 2, respectively.

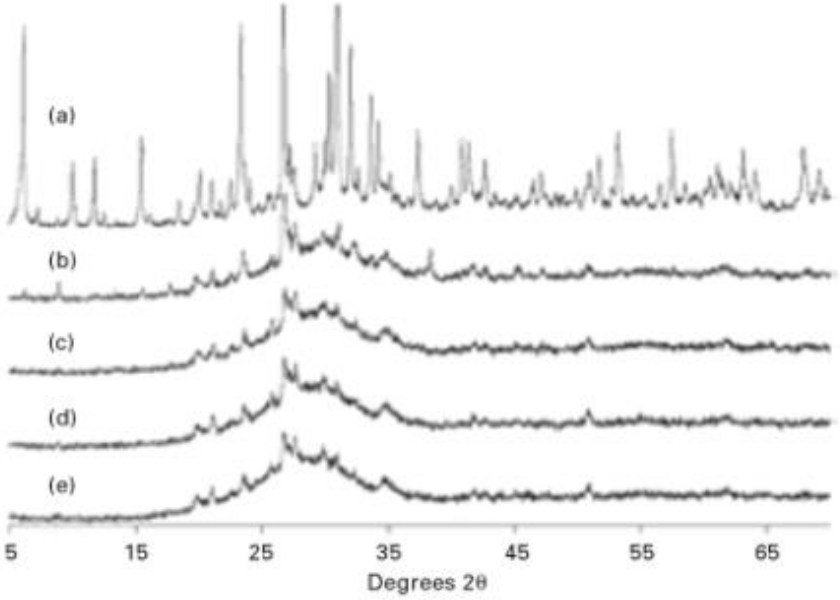

Figure 41: X-ray diffractograms of geopolymers synthesised by mixing metakaolin with alkali activators. (Duxson, 2006)

The small sharp peaks common to all samples are due to the muscovite impurity in the metakaolin. Sample (a), which is activated with sodium hydroxide solution, shows the formation of appreciable crystallinity in the form of faujasite and minor contributions from other zeolites. Sample (b) shows slight crystallinity (Duxson, 2006).

Figure 42 presents the NMR spectra of the same samples as discussed from the previous Figure 41. The importance of this visualisation is because of detailed analysis of peak positions and width provides insight into the extent of ordering and Si/Al substitution in the geopolymer frameworks (Duxson *et al*., 2005).

Substitution of Al into the silicate network results in a less negative chemical shift (Engelhardt & Michel, 1987), and it is clear that, as expected, geopolymers synthesised with a higher Si/Al ratio show a greater extent of Al substitution and a lower distribution of connectivity types Q^4 (tetrahedral Si surrounded by 4 $-OAl$ bonds and (4-n) $-OSi$ bonds).

The extent of framework disorder (Si/Al ordering violation) was higher in K-aluminosilicate geopolymers than in Na-aluminosilicate geopolymers. Comparison of the NMR spectra of Na and K of mixed-alkali geopolymers at low Si/Al ratio and early age shows that K^+ is preferentially incorporated into the gel while Na^+ remains solvated for longer (Duxson *et al*., 2005c-2006).

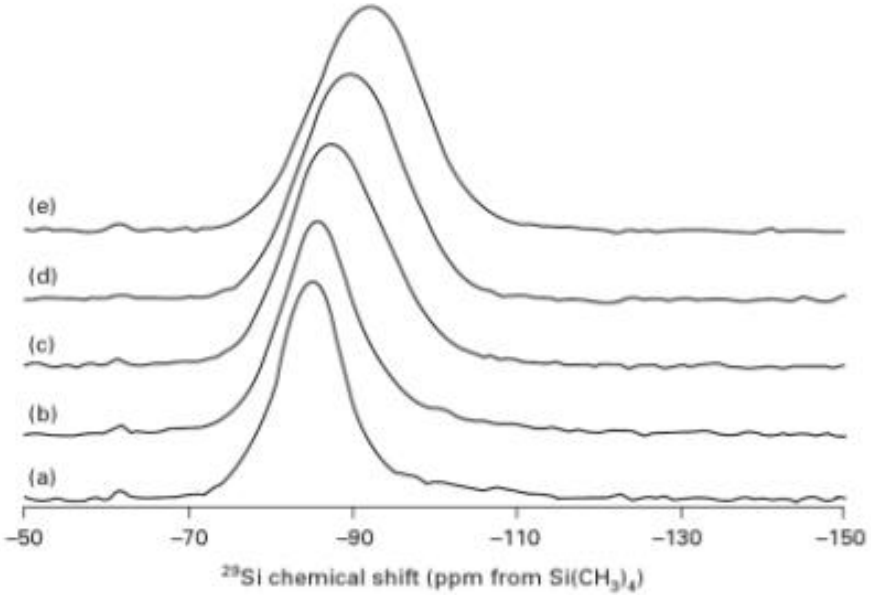

Figure 42: NMR spectra of geopolymers synthesised by mixing metakaolin with alkali activators. (Duxson, 2006)

Next to the results obtained from the NMR data, recent work using X-ray Pair Distribution Function (PDF) analysis, has shown that even in samples which appear 'amorphous' to standard X-ray diffractometry, there is a significant extent of short-range order.

From Figure 43, it is possible to conclude that while comparing the short-range atomic ordering in a caesium aluminosilicate geopolymer with a model pollucite structure, there are very marked similarities between both Cs-geopolymer and crystalline pollucite.

The main short-range difference between the two structures appears to be a slight shift in position of the Cs^+ atom upon crystallisation. However, more significant differences start to occur at longer length scales as the extent of ordering in the geopolymer decreases (Bell *et al*., 2008).

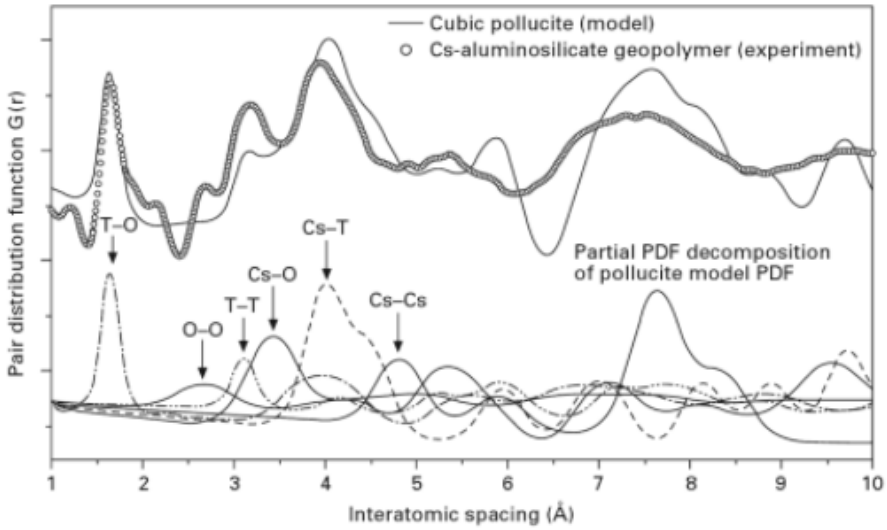

Figure 43: Comparison of the Pair Distribution Functions (PDFs) of cube pollucite and caesium geopolymer. (Bell *et al*., 2008)

3.2.6.4 Microstructure of metakaolin geopolymers

The primary importance of the microstructural details of geopolymers is two-sided. Firstly, the mechanical strength of the binder is clearly related to its composition. This can be correlated to the details of the reaction process by analysis of the binder microstructure (Duxson *et al*., 2005b). Secondly, the pore network of the geopolymer binder will play a highly significant role in determining its durability. The main degradation mechanism involves attack by aggressive reagents (Bassil *et al*., 2008). The data in Figure 44 shows a clear optimum in strength at high silica content, more specific at Si/Al ratio of 1.90. The compressive strength of metakaolin geopolymers increases linearly by approximately 400 % from Si/Al ratio of 1.15 to Si/Al ratio of 1.90, before decreasing until Si/Al ratio of 2.15. The maximum compressive strength achieved for metakaolin geopolymers at Si/Al ratio of 1.90 is 75 MPa, as shown in Figure 44.

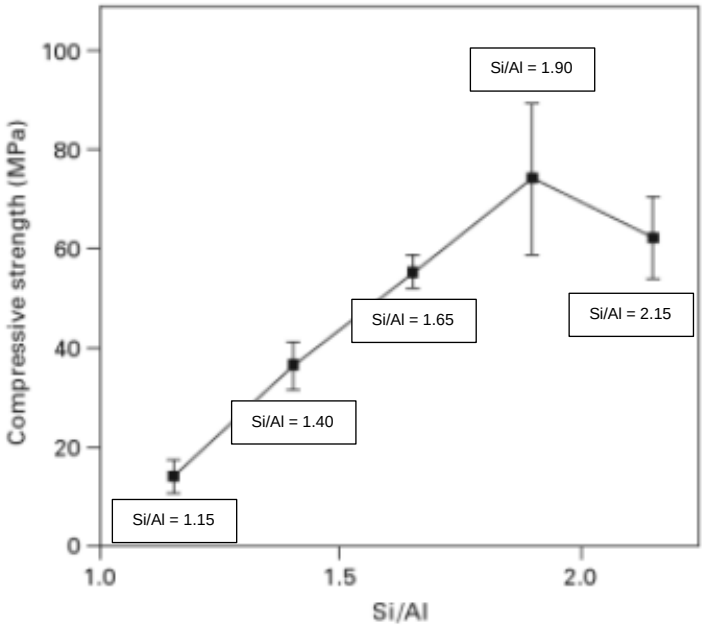

Figure 44: Compressive strengths of geopolymers from the reaction of metakaolin with NaOH activator with varying Si/Al ratios. (Edited from Duxson *et al*., 2005b)

The images of Figure 45 show a rough, disconnected binder structure at low silica content for images (a) and (b). While increasing the amount of silica in the solution, the rough disconnected binder structure transforms into a smoother, more homogeneous binder (Duxson *et al*., 2005 & Duxson, 2006).

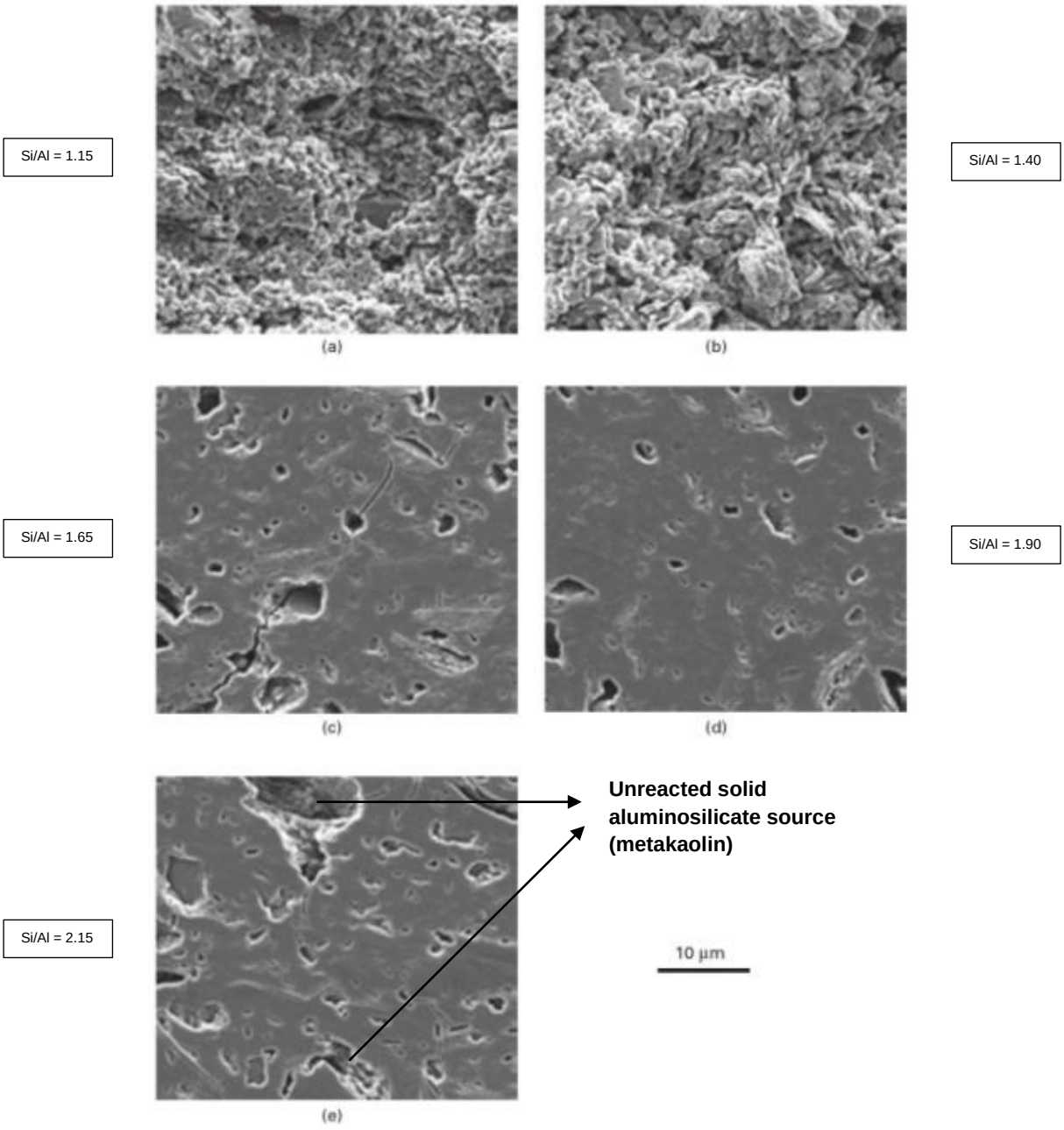

Figure 45: Microstructure of geopolymers synthesised by mixing metakaolin with alkali activators sodium hydroxide and sodium silicate. (Edited from Duxson, 2006)

While still increasing the silica content after having reached the optimum strength will lead to a decrease in strength due to a highly homogeneous gel which is very porous. The microstructure at $\mathrm{Si/Al}$ = 2.15 with reduced strength shows the unreacted solid aluminosilicate source as solid particles, as indicated with arrows on image (e).

Due to the understanding of the structure and chemistry of metakaolin, we can analyse the interactions between the disordered layered structure of metakaolin and the alkaline activating solutions. From this research, a better insight is gained into the microstructure of metakaolin.

3.2.7 Geopolymer reaction synthesis

Experimental studies have confirmed that polymerisation entails an increase in the molecular weight of silica, implying the condensation of silanol groups (Glukhovsky, 1967):

$$\equiv \mathrm{SiOH} + \mathrm{HOSI} \equiv \rightarrow \mathrm{SiOSi} \equiv + \mathrm{H_2O}$$

The term polymerisation is used in a loose sense, in which the condensation of $\mathrm{Si(OH)}$ units may generate larger units either by enlarging the size of spherical particles or by increasing the number of particles comprising the aggregate. Spherical particle formation take place under certain conditions, while particle aggregation and the concomitant formation of viscous sols or gels require a different set of conditions. These two types of polymerisation may occur simultaneously (Glukhovsky, 1967).

3.2.7.1 Conceptual model of polymerisation

Glukhovsky (1967) proposed a general model to describe the mechanisms that govern the alkali activation of aluminosiliceous materials. His model divides the geopolymerisation process into three main stages: 'destruction – coagulation', 'coagulation – condensation' and 'condensation – crystallisation'. These three main stages for the polymerisation process are explained in this paragraph, with the occurring reaction equations.

1. **Destruction – Coagulation**

The first disaggregation process is based on severing the $\mathrm{Me-O}$, $\mathrm{Si-O-Si}$, $\mathrm{Al-O-Al}$ and $\mathrm{Al-O-Si}$ bonds in the starting material. Reactivity conditions can only be attained if the ionic force is varied by adding electron donor ions with the covalent $\mathrm{Si-O-Si}$ and $\mathrm{Al-O-Al}$ bonds. The addition of electron donor ions can be seen as alkaline metals, to raise the pH. The $\mathrm{OH^-}$ ions initiate the rupture of the $\mathrm{Si-O-Si}$ bonds:

$$\equiv\mathrm{Si{-}O{-}Si}\equiv + \mathrm{OH^-} \Rightarrow \equiv\mathrm{Si{-}O{-}Si}\equiv \Rightarrow \equiv\mathrm{Si{-}OH} + {}^{-}\mathrm{O{-}Si}\equiv$$
$$\qquad\qquad\qquad\qquad\quad |$$
$$\qquad\qquad\qquad\qquad\quad \mathrm{OH^-}$$

This takes place by the action of the $\mathrm{OH^-}$ redistributing the electron density around the silicon atom and rendering the $\mathrm{Si-O-Si}$ bond more susceptible to rupture. The degree of silicon dihydroxylation may rise to more than two or three units, forming intermediate complexes that decompose into silicic acid $\mathrm{Si(OH)_4}$ as well as oligomeric, anionic species containing $\equiv\mathrm{SiO^-}$ groups (Glukhovsky, 1967).

The presence of alkaline metal cations neutralises the resulting negative charge. As the hydroxyl groups affect the $\mathrm{Al-O-Si}$ bond, the aluminates in the alkaline solution form complexes, predominantly $\mathrm{Al(OH)_4^-}$ (Radnai *et al.*, 1998). The $\mathrm{-Si-O-Na^+}$ complexes, which are stable in alkaline media, create conditions suitable for the transport of the reacting structural units and the development of the coagulated structure.

2. **Coagulation – Condensation**

In the second stage, accumulation enhances the contact among the disaggregated products, forming a coagulated structure where polycondensation takes place.

The condensability of silicic acid rises with high pH values, at which it is slightly dissociated or in a molecular state. Therefore, pH > 7, the disaggregation of the $\mathrm{Si-O-Si}$ bond gives rise

to a hydroxylated complex, $Si(OH)_4$, which condenses to form a new $Si-O-Si$ bond and generate the following dimer:

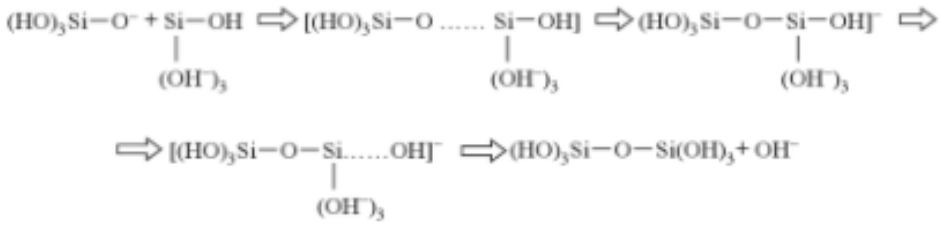

This reaction is catalysed by the OH^- ion. The clusters formed by the polymerisation of orthosilicic acid may grow in all directions, generating colloidal particles (Davidovits, 2008).

3. Condensation – Crystallisation

The model of Duxson *et al*. (2007) incorporates the two stages that govern zeolite synthesis:

- Nucleation stage in which the aluminosilicates dissolve in the alkaline medium, favouring the formation of zeolite precursors. This stage is heavily dependent upon kinetic and thermodynamic parameters.
- Several nuclei are reaching a critical size and crystals begin to develop. This process is known as 'crystal nucleation', which starts from liquid or solution phase to evolve into macroscopic crystals by the further process of crystal growth (Gavezzotti, 2021).

The conceptual model in Figure 46 gives an overview of the various stages, comprising the transformation of a source of aluminosilicates into an alkaline inorganic polymer. An important remark is that these stages are occurring simultaneously into a heterogeneous process.

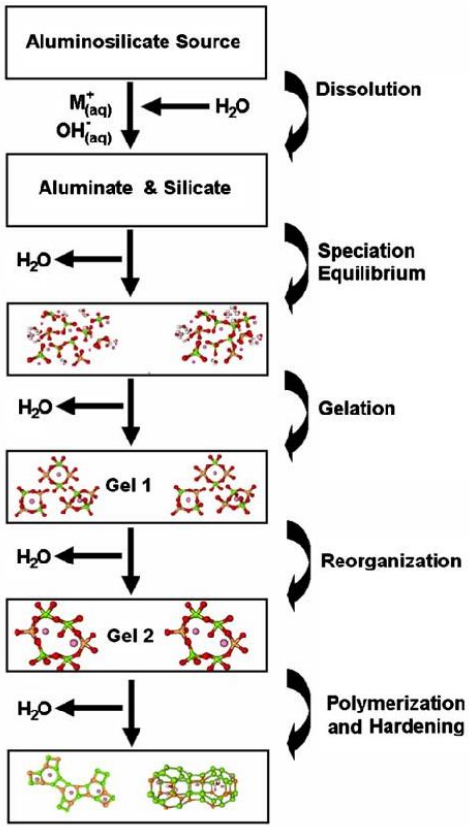

Figure 46: Conceptual model for geopolymerisation. (Duxson *et al*., 2007)

Initially there is contact between the solid particles and the alkaline solution which causes the vitreous or amorphous component of these particles to dissolve. There occurs a release of aluminates and silicates, as monomers. In a next step, these monomers react to form dimers, which in turn react with other monomers to form trimers, tetramers, etc.

When the solution is reaching a saturation point, an aluminosilicate gel precipitates. Initially, this is an aluminium-rich gel (denoted as Gel 1 in Figure 46). As the reaction process progresses, more $Si-O$ groups in the initial solid source dissolve, which lead to an increase of the silicon concentration. This provokes the gradual increase of the proportion of silicon in the zeolite precursor gel (denoted as Gel 2 in Figure 46).

These structural reorganisation processes determine the final composition of the polymer as well as pore microstructure and distribution in the material. These are critical factors in the development of many physical properties of the resultant product (Fernandez-Jimenez *et al*., 2006 & Sofi *et al*., 2007).

Nowadays, this gel is known to be a product containing large numbers of zeolite-like nanocrystals. Zeolite formation calls for a minimum amount of liquid and crystallisation takes some time (Barrer, 1982).

3.2.7.2 Rate of reaction

The development of a detailed understanding of reaction kinetics is critical to the accurate control and tailoring of geopolymer setting rates. This is an important parameter to predict which products will be formed during the geopolymerisation process.

As in the case of a $C-S-H$ geopolymer gel, many factors affect the structural and chemical composition of alkaline aluminosilicate gel. Figure 47 shows the structure of a $N-A-S-H$ geopolymer gel, which is the main reaction product of the alkali-activated aluminosilicates.

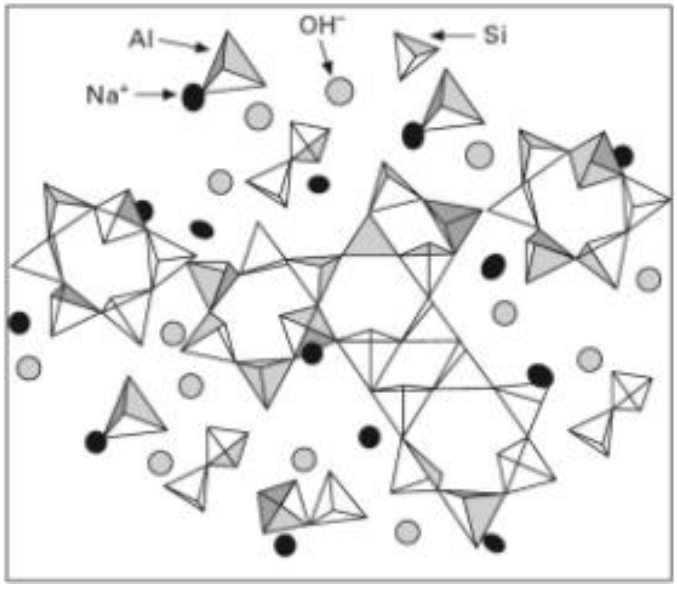

Figure 47: 2D-model of the structure for $N-A-S-H$ geopolymer gel. (Craido, 2007)

Figure 48 represents the reaction mechanism of a study conducted by Lin *et al*. (2020). Hereby, the effect of Na_2SiO_3 solution/ $NaOH$ solution as mass ratio and SiC sludge amount of metakaolin-based geopolymers was determined during the performance of geopolymerisation. The results show that since the Na_2SiO_3 solution/$NaOH$ solution is low, a sufficient amount of OH^- is needed to increase the solubility and inhibit the polycondensation reaction phase.

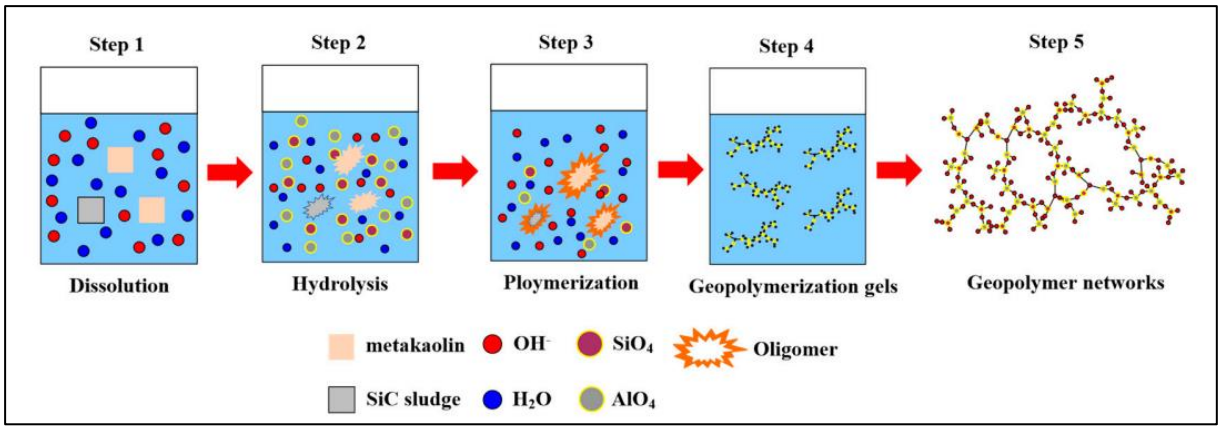

Figure 48: Geopolymerisation process with SiC sludge (SiCS). (Lin *et al*., 2020)

3.2.8 Geopolymer reaction measurement techniques

Understanding reaction rates necessitates the development of analytical techniques capable of measuring the rate of geopolymer gel network growth. In this section, different experimental and computational techniques to study repolymerisation kinetics are explained. In particular, the determination of aluminosilicate gel network growth rates and elucidation of some of the many factors affecting geopolymer kinetics are studied.

3.2.8.1 In situ infrared spectroscopy

In order to chemically analyse the reaction process and the reaction products formed, the technique of in situ infrared spectroscopy can be used. Infrared spectroscopy provides a sensitive probe of the structure of the hardened geopolymer. The technique of Attenuated Total Reflectance-Fourier Transform Infrared Spectroscopy (ATR-FTIR) is used to measure the relative concentration changes of the main functional groups involved in the early stages of the geopolymer gel formation (Rees *et al*., 2007), by analysis of the different peaks in Figure 49.

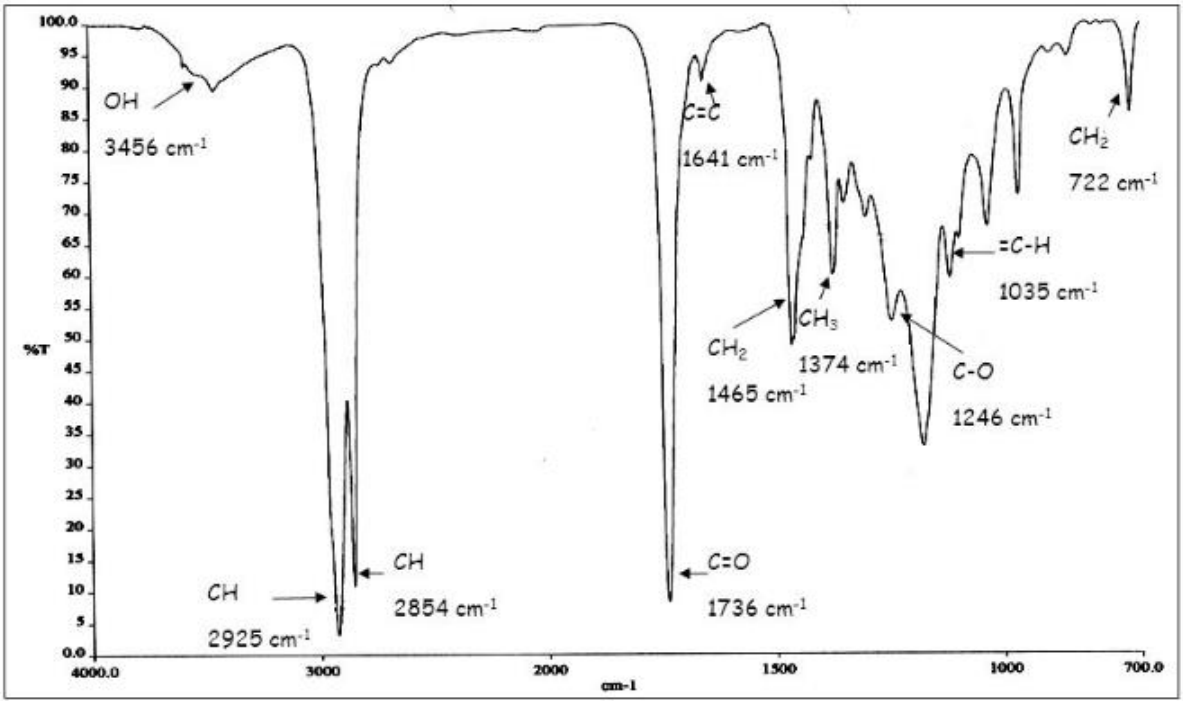

Figure 49: FTIR analysis chart. (Niom, 2022)

Infrared spectroscopy measures the adsorption of infrared radiation by chemical bonds in a material. Functional groups in molecules tend to adsorb IR radiation in the same frequency range regardless of the structure of the rest of the molecule that the functional group is in. This correlation between the structure of a molecule and the frequencies at which it adsorbs IR radiation enables identification of the structure of unknown molecules (Simmons, 1999).

3.2.8.2 Calorimetry

Palomo and some other researchers have studied the effect of various parameters including reaction temperature and calcium addition through isothermal conduction calorimetry (ICC). The researchers were looking for a link between heat release data and final mechanical strength of the geopolymeric products. From the study, a correlation was found between the reaction rate and alkali cations for metakaolin-based geopolymerisation systems (Rahier *et al*., 1996). The conclusion was that the overall extent of reaction in metakaolin-based geopolymers depends only to a limited degree on the identity of the alkali cations present in the case of Na, K, and mixtures of them (Duxson *et al*., 2005 & Provis *et al*., 2005).

A study by Nath *et al*. (2016) was conducted through ICC to study the reaction kinetics in the early stage of geopolymerisation. Fly ash particles were subjected to an alkali activation with 10 M $NaOH$ solution in a ratio of 2:1. Kinetic parameters such as activation energy and reaction rate were retrieved from the heat development data of the geopolymerisation. In the early stages of geopolymerisation, nucleation was considered the main reaction mechanism. This reaction follows the first-order reaction kinetics. Finally, an apparent activation energy of 100 kJ/mol was measured for this reaction process.

Another interesting study by Aupoil *et al*. (2019) studied the interplay between silicate and hydroxide ions during the geopolymerisation process of metakaolin with sodium hydroxide. The impact of the alkalinity on the reactivity of metakaolin was assessed using ICC. After the metakaolin brought in contact with the alkali activator, hydroxide ions are gradually released into the solution during the condensation of aluminosilicates. These released hydroxide ions can then in turn dissolve metakaolin again. This generates a chain reaction and a circular mechanism. Due to the fact that silicate solutions allow the reaction to take place at lower hydroxide concentrations, the final reaction path is directed to geopolymers and not to zeolites.

3.2.8.3 Rheology

Various researchers have used rheological techniques to monitor the setting kinetics of geopolymers based on fly ash and metakaolin (Rahier *et al*., 1996). The shear-dependent rheology of geopolymers provides the basis for their use as a Portland cement replacement. When considering construction technologies such as 3D printing of geopolymer concrete, the rheology of geopolymers will be one of the main influencing factors on the quality of the final construction. In 2012, a study was conducted on the rheological properties of geopolymers (Romagnoli *et al*., 2012). The effects of temperature, curing time and alkali concentration on the fundamental rheological parameters were determined. The study shows that rheological parameters have been shown to be very sensitive to chemical changes in the studied system.

Another study by Panda *et al*. (2018) investigated the evolution of the yield stress and thixotropy of fly ash-based geopolymers, with the possibility of 3D printing. The use of SCMs such as ground granulated blast furnace slag (GGBS) and silica fume (SF) influence the early strength development and freshness properties of the geopolymer system, respectively. The feasibility of the 3D printing process is evaluated by analysis of viscosity and shape retention after printing. In order to make an objective comparison between the rheological properties of

Portland cement and metakaolin-based geopolymers, a study conducted by Favier *et al*. (2013) on the differences between these two binders. From the results of this study, it was established from a macroscopic point of view that geopolymers are more viscous liquids than Portland cement. The viscosity of the mixture is ten to a hundred times higher than water, making it currently not suitable for use in 3D printing processes. This requires further research into methods to increase the yield strength of geopolymers.

3.2.8.4 Diffraction techniques

The use of diffraction techniques to analyse geopolymerisation kinetics is greatly complicated by the fact that this reaction process involves conversion from one X-ray amorphous phase into another. X-ray diffraction techniques for the analysis of the formation of crystalline zeolites within geopolymers has been used as a probe of the reaction progress in systems cured at higher temperatures (Loanrewaju, 2002 & Lloyd, 2008). A detailed understanding of the reaction kinetics is critical to the nature of the products formed. Because geopolymerisation is a multi-stage process, many standard analytical techniques can provide only limited information (Provis & Rees, 2009).

In the geopolymerisation process, one X-ray amorphous material such as metakaolin must first be converted to another amorphous material, the geopolymer gel. By applying more complex techniques, such as FTIR spectroscopy or X-ray diffractometry, important insights can be gained at nanoscale of geopolymer products.

3.2.8.5 Nuclear magnetic resonance (NMR)

Rahier *et al*. (2007) used NMR to probe kinetics in the very early stages of geopolymer formation. Nuclear magnetic resonance spectroscopy is a useful tool to study normal and pathological biomedical processes in weaves. This technique detects local magnetic field around atomic nuclei. By applying an external magnetic field, as indicated in Figure 50, an energy transfer is possible between base energy to a higher energy level. The intramolecular magnetic field around an atom will change the resonance frequency, which provides detailed information about the electronic structure of the molecule and its individual functional groups.

The understanding of the reaction kinetics will provide the opportunity to control and tailor the setting rate of geopolymers. This will also provide a significant degree of control over the geopolymeric products that are going to be formed.

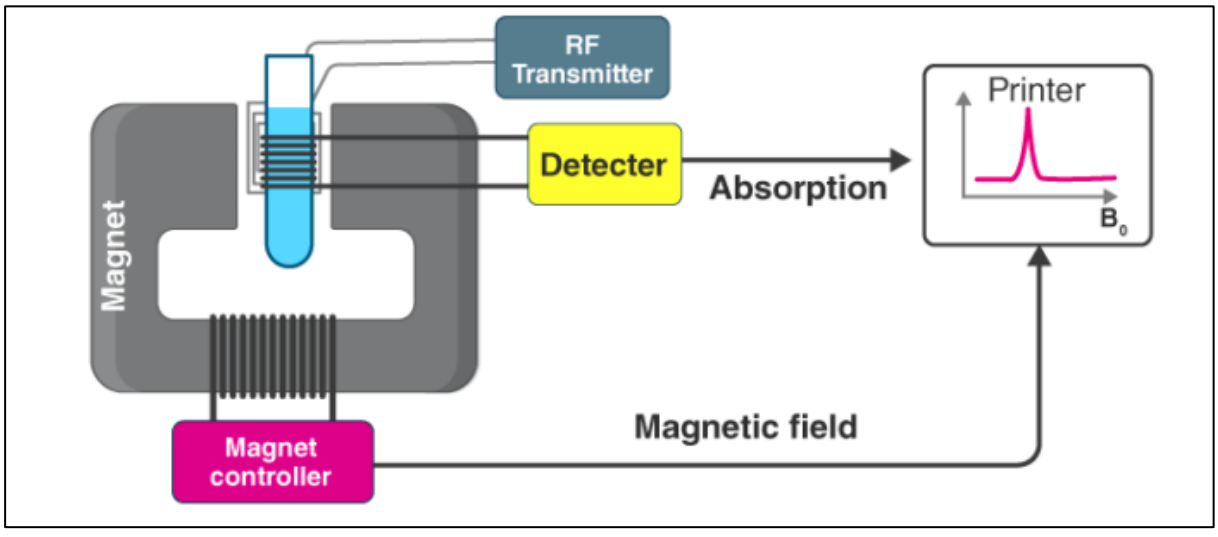

Figure 50: Nuclear magnetic resonance spectroscopy. (Aryal, 2022)

3.3 Durability of geopolymers against extreme conditions

The durability of geopolymers is quite important to withstand the extreme conditions on the planet Mars. On Mars, there are two extreme parameters of environmental conditions that need to be controlled and be taken into account for the geopolymer design and material choice. This two extreme parameters are the very low pressure of 0.636 kPa on Mars, and the extreme temperature variations on Mars, varying between -130 °C and 30 °C on Mars' surface. A study by Lambertin *et al*. (2013) shows that the influence of radiation on metakaolin-based geopolymers does not pose any significant sustainability problems.

This research investigated the effects of gamma radiation on metakaolin-based sodium activated geopolymers. The influence of gamma radiation on the microstructure of sodium geopolymer was investigated by means of porosity measurements and an analysis of the distribution function of X-ray particles. After the irradiation of the geopolymers, only a change in pore size distribution and structural relaxation was observed.

The durability of any material is related to its mineralogical composition and microstructure. The factors that will influence the durability of geopolymers are weight loss, compressive strength, variations in volume and mechanisms of attack. From a rational analysis of the durability of geopolymers and Portland cement, it can be stated that geopolymers have a durable behaviour similar to that of Portland cement (Gourley & Johnson, 2005).

3.3.1 High temperature and fire resistance

Different authors have studied the behaviour of alkali-activated aluminosilicates at high temperature, and there is general agreement that geopolymers show better fire resistance than Portland cement mortars or concrete.

Previous investigations by Davidovits *et al.* (1991, 1994, 1999) reported very good heat resistance properties of materials prepared using sodium silicate, potassium silicate and metakaolin. Those materials have thermal stability up to 1200-1400 °C. Barbosa and MacKenzie (2003) found that increased amounts of water or sodium silicate could reduce the thermal resistance of geopolymer material when exposed to fire. Rickard *et al*. (2015) studied the microstructure of two different geopolymer mixtures. One geopolymer had a dense microstructure with a high degree of reactivity, while the other geopolymer had little or no reaction due to the large amount of fly ash. Due to the large amount of fly ash, this second geopolymer has difficulties with strength, due to the porous geopolymer matrix.

In Figure 51, the strong geopolymer can be clearly seen on the left, while the lower strength geopolymer can be recognised on the right. As a result of macro cracks and damage caused by desiccation, the left-hand strong geopolymer undergoes more strength losses, decreased thermal performance and increased dimensional instability. In contrast, the right-hand, less strong geopolymer, is more resistant to high temperatures.

This confirms the statement of Barbosa and MacKenzie (2003) about the reduced thermal resistance at higher silicate concentrations. Due to higher silicate concentrations, a denser geopolymer matrix is reached, as a result of which the strength of the geopolymer will increase significantly. This will significantly increase the risk of macro cracks due to heat, which poses a risk to the durability of the geopolymer. Since there are no surface temperatures higher than 30 °C on Mars, but strong temperature variations may occur, it is important to consider the effect of sudden temperature increases in the design of geopolymers.

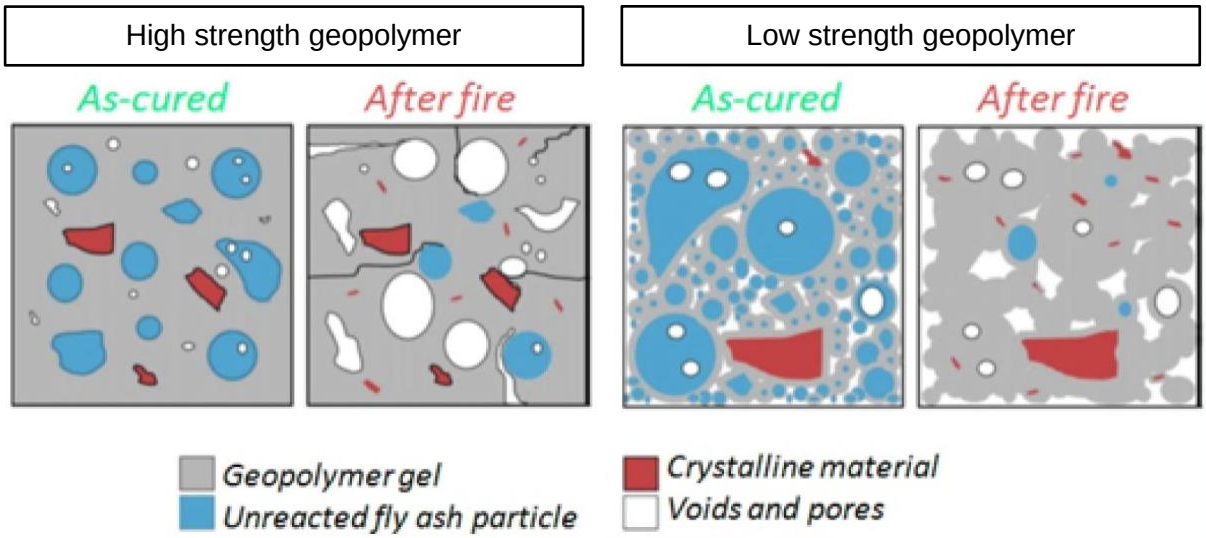

Figure 51: Schematic depiction of microstructure changes in geopolymer paste upon firing. (Edited from Rickard, 2015)

3.3.2 Alkali silica reaction

The alkali-silica reaction (ASR) is a chemical process involving alkaline oxides from cement, and reactive silica present in aggregates (Swamy, 1992). The reaction causes damage due to the formation of expansive reaction products. This process depends on the presence of potentially reactive aggregate, the existence of alkalis, Ca-rich phases and humidity. The absence of any of these factors reduces or may even prevent the ASR process and consequent damage due to expansion.

Figure 52 shows the three different phases in the ASR process (Pan *et al*., 2012). Initially, a break occurs in the siloxane network, which is caused by the attack of hydroxyl ions, such as Na^+ en K^+. The second step in the process is the expansion of alkali silica gel through the adsorption of free surrounding water. In order to allow this phase in the reaction process to continue, the following three conditions must be met: presence of reactive granules, sufficient concentration of alkalinity and a relative humidity of at least 80 % in the pores.

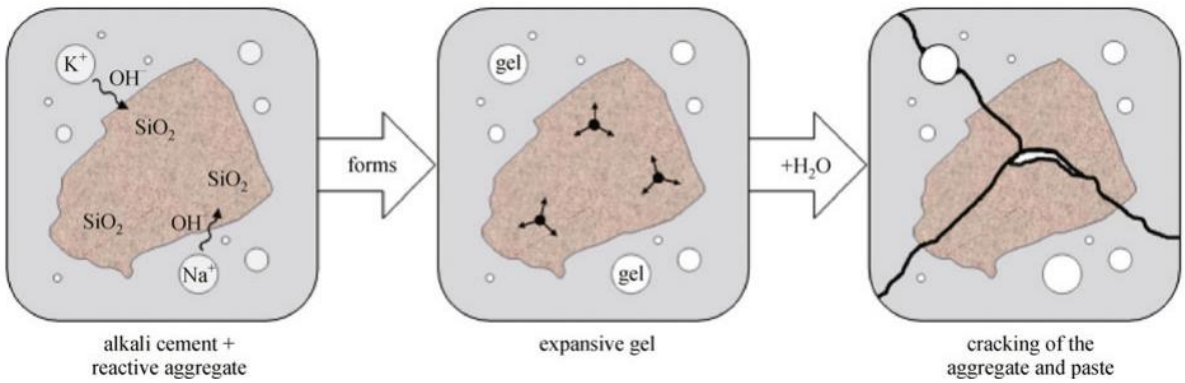

Figure 52: Alkali silica reaction process. (Pan *et al.*, 2012)

When the hydrated alkali-silica gel is formed, it reacts with calcium ions contained in the aluminosilicate material. Finally, in the third and final stage, the ASR products will expand due to the adsorption of moisture. This expansion will create internal stresses in the geopolymer

matrix, causing the granulates and surrounding geopolymer paste to crack. As a result, the strength of the geopolymers will decrease considerably over time.

Gourley and Johnson (2005) indicate that any ASR that is likely to occur in geopolymer mortars will take place during the original dissolution and condensation polymerisation process, while the material is still in gel form. Such reactions provide paste-aggregate chemical bonding.

3.3.3 Sulphate attack

Palomo *et al.* (1999) reported that mortars made with alkali-activated metakaolin show very good stability when immersed in various types of aggressive solutions, such as deionized water, sodium sulphate solution and sulphuric acid. Bakharev (2005) showed that alkaline activated pastes and mortars perform satisfactory when exposed to sulphates and seawater. No differences were observed in gel composition or microstructure of geopolymers after contact with saline solutions, which is a mixture of sodium chloride (or salt) and water.

From the research of Bakharev (2005) on the resistance of geopolymer materials to acid attack, the performance of geopolymers against exposure to sulfuric acid was investigated too. A general trend was observed that geopolymer specimens exposed to sulfuric acid solutions became very porous and fragile. This porous character can be seen on the right side of Figure 53, where there is a significantly larger volume of voids and openings present.

From SEM observations, it could be perceived that new crystals were formed with geopolymers activated by sodium silicate. These newly formed crystals in the geopolymer matrix ensure that there is an increased natural resistance against all kinds of chemical attack mechanisms. The molecules in the structure will be better ordered, resulting in increased strength properties. This will have a positive effect on the internal cohesion interactions between different particles in the geopolymer matrix.

Geopolymers activated with sodium hydroxide, mainly amorphous structures are observed after two months of exposure to sulfuric acid solutions. Due to the attack of this sulfuric acid solution, the geopolymer structure will undergo a transformation from crystalline to amorphous structure.

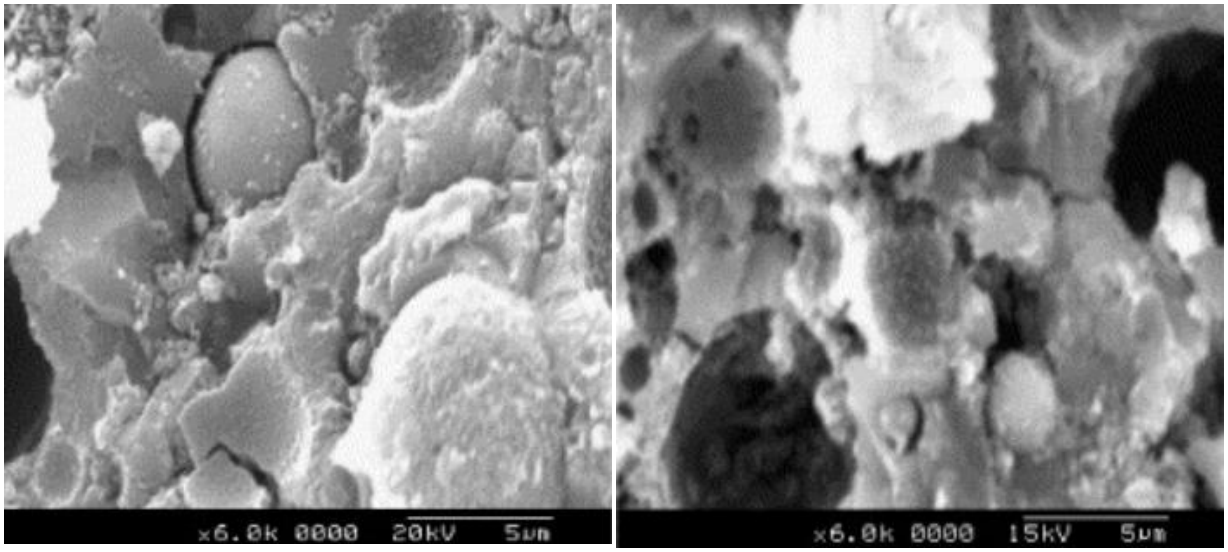

Figure 53: SEM images of sodium hydroxide activated geopolymer samples before (left) and after (right) two months in 5 % sulfuric acid solution. (Bakharev, 2005)

3.3.4 Acid attack

An interesting property of geopolymer binders is the high resistance to acidic media. The resistance of alkali activated metakaolin or fly ash to chemical attack by acids such as nitric, sulphuric or hydrochloric has been claimed to be far better than that of Portland cement mortar or concrete. Davidovits *et al.* (1999) indicates that metakaolin-based geopolymers show only 7 % mass loss when samples are immersed in a 5 % sulphuric acid solution for 4 weeks.

Figure 54 represents the effect of acetic attack on the durability of class F fly ash-based geopolymers (Bakharev, 2005). Before the sodium and potassium activated geopolymers were exposed to the acetic acid solution, a crystalline appearance was observed. After exposure to a 5 % acetic acid solution for two months, the geopolymers activated by sodium hydroxide and sodium silicate showed a porous character.

On the contrary, geopolymers that were activated by a combination of sodium and potassium hydroxide, no porous structure was observed, but an amorphous character could be seen. The change from this crystalline to amorphous character is shown in Figure 54. On the left, the sodium and potassium activated geopolymer is shown before it was exposed to the 5 % acetic acid solution, while on the right the same geopolymer is shown after two months exposure to the 5 % acetic acid solution.

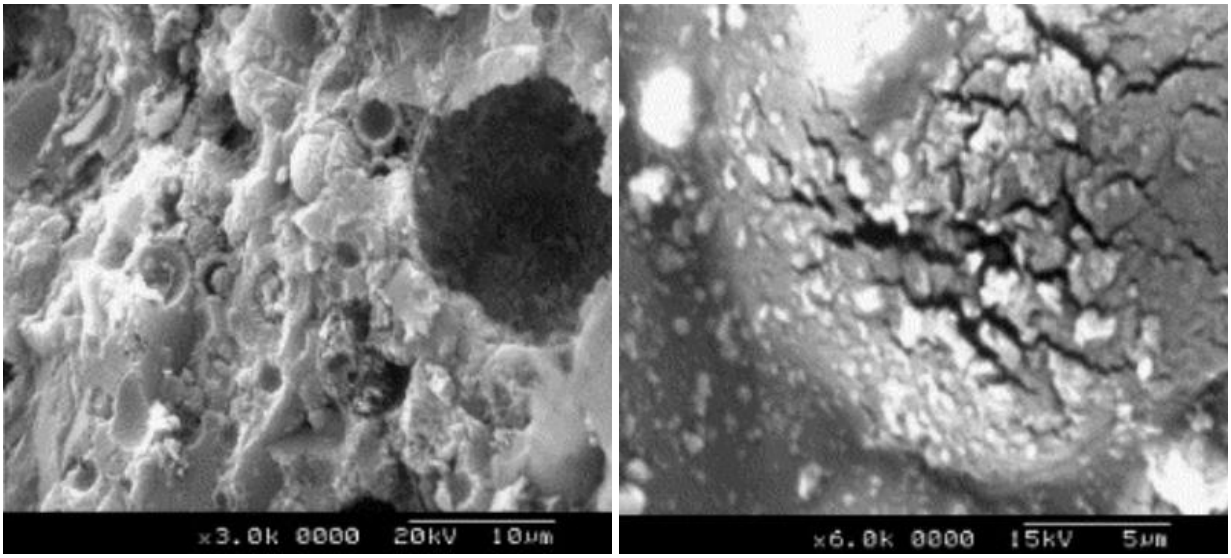

Figure 54: SEM images of sodium and potassium hydroxide activated geopolymer samples before (left) and after (right) two months in 5 % acetic acid solution. (Bakharev, 2005)

3.3.5 Frost attack

The resistance to freezing and thawing mainly depends on the degree of saturation and the pore structure of the hardened material. Škvára (2007) indicates that geopolymer binders based on fly ash possess excellent frost resistance.

For alkali-activated fly ash concrete with sodium silicate, the mass of the sample body did not change to any practical extent during the freezing and defrosting cycles taking place in an aqueous environment.

4 METHODOLOGY

In the methodology, a broader focus is placed on laboratory testing equipment and the mix design of geopolymers. This section can be seen as a link between the theoretical background in the literature review and its practical implementation for this research project.

4.1 Experimental methodology

4.1.1 Alkali activators: $NaOH$ and $LiOH.H_2O$

In order to find an answer to the research question, a start was made by setting up a good methodology and planning. Important factors from the literature review on geopolymers were used to implement the mix design for the geopolymers. The choice of composition and concentrations for the alkali activators was based on a study on the geopolymerisation of another simulated Martian raw material, namely MMS-1 (Chakraborty, 2019). To achieve an optimal geopolymer composition, two different alkali activators were used. Initially, a series of geopolymers were made, based on sodium hydroxide ($NaOH$). The literature review showed that many geopolymers have already been made with this chemical product. Therefore, the use of $NaOH$ is a reliable choice. In addition to the geopolymers with $NaOH$ as an alkali activator, geopolymers were also made based on lithium hydroxide monohydrate ($LiOH.H_2O$).

From a study by Jones *et al*. (2020), it seems that $LiOH.H_2O$ can withstand the cosmic rays that occur on the planet Mars. This is due to the low density of this alkali activator. In the past, no geopolymers were made with this activator, which is why in this research extra attention is paid to the geopolymer composition with $LiOH.H_2O$. These two alkali activators will be dissolved in a sodium silicate solution until the desired concentrations are reached. The simulated Mars regolith MGS-1 will then be added to this sodium silicate solution.

4.1.2 MGS-1 as precursor and kaolinite as additive

Based on Table 5, provided by Rampe *et al*. (2017), it appears that this raw material from Mars is very rich in SiO_2 (50.8 w%), but consists to a lesser extent of Al_2O_3 (8.9 w%) and CaO (3.7 w%). These last two components are also important to obtain a good geopolymerisation.

To increase the amount of Al_2O_3, the decision was made to add clay mineral kaolinite $Al_2O_3.2SiO_2.2H_2O$ to MGS-1. Because kaolinite itself does not show the highest reactivity, it was decided to convert this kaolinite into metakaolin (Khalifa *et al.*, 2020). This is done by putting the kaolinite in a furnace for a certain period of time at a certain constant temperature. The process that takes place during the conversion of kaolinite to metakaolin is called calcination. Due to the heating process of kaolinite, the water between the atoms evaporates. This process changes the internal atomic structure of kaolinite and forms an amorphous aluminosilicate $Al_2O_3.2SiO_2$ (Ilić *et al.*, 2010). The reaction occurring during this process of dihydroxylation can be represented by the following chemical equation:

$$Al_2O_3.2SiO_2.2H_2O \xrightarrow{\text{heating at } 650\ ^\circ C} Al_2O_3.2SiO_2 + 2.H_2O\uparrow$$

Table 5: Chemical composition of Rocknest (RN) and MGS-1. (Rampe *et al.*, 2017)

Bulk major element chemistry for Rocknest (RN) and the MGS-1 simulant.

Oxide	RN bulk[a]	Calc. MGS-1[b]	RN amorph.[c]	Calc. MGS-1 amorph.[b]	MGS-1 prototype
SiO_2	43.0	48.3	34.2	47.0	50.8
TiO_2	1.2	0.2	2.1	0.6	0.3
Al_2O_3	9.4	9.5	5.4	7.0	8.9
Cr_2O_3	0.5	0.1	1.4	0.2	0.1
FeO_T	19.2	16.9	23.0	21.0	13.3
MnO	0.4	0.1	1.2	0.2	0.1
MgO	8.7	12.1	4.0	9.9	16.7
CaO	7.3	6.7	4.4	4.5	3.7
Na_2O	2.7	2.6	3.3	1.0	3.4
K_2O	0.5	0.1	1.4	0.3	0.3
P_2O_5	1.0	0.2	2.7	0.6	0.4
SO_3	5.5	3.2	13.9	7.7	2.1
Cl	0.7	0.0	2.0	0.0	–
SUM	100.1	100.0	99.9	100.0	100.0

To establish the temperature and duration of heating the kaolinite for the experiments, values obtained from literature review were used. A study by Ilić *et al.* (2010) shows that a temperature of 650 °C, for 90 minutes, is the most economical solution to allow the calcination of the kaolinite to take place.

In order to obtain a complete reaction, and also to obtain a higher reactivity of the metakaolin, it was decided to set the furnace at 650 °C for 180 minutes. A mass of 50 g of kaolinite was weighed in each case, in order to convert this into metakaolin, which serves as an additive for the Martian regolith MGS-1.

4.1.3 Moulds for the geopolymers

4.1.3.1 Cube geopolymer samples

The geopolymers will be produced in two different shapes: a cube and cylindrical shape. The cube moulds consist of six different cubes of 20x20x20 mm, as shown in Figure 55. After preparing the geopolymer mixture, it was manually applied in the different cube openings. Because the compaction has a major influence on the results of the compressive strength, these cubes were pressed with a pestle each time by a tapping movement. This was optimised during the research by making the tapping movement increasingly uniform for all cubes. Due to the optimisation of the compaction process, by applying an equal amount of strokes to the pestle, the user-dependent errors were reduced as much as possible.

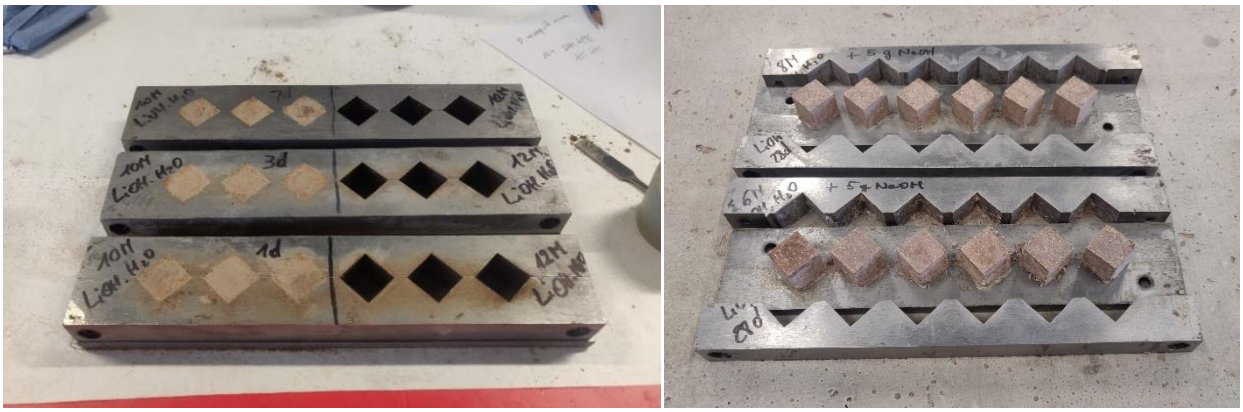

Figure 55: Cube moulds.

After the cube moulds were completely filled and compacted, a plastic film was applied before being placed in the oven at a constant temperature of 70 °C, as in Figure 56. The reason for applying the film is to prevent water evaporation during the curing process of the geopolymers.

Figure 56: Oven at 70 °C for curing process of geopolymers.

These cube moulds were used to make a comparison with the measurement results from other studies, such as the study by Chakraborty (2019). An additional reason for using these moulds is because of problems with the delivery of the pellet press for making cylindrical geopolymer samples. The manufacturer made two mistakes in the dimensioning of the cylindrical moulds.

4.1.3.2 Cylindrical geopolymer samples

In addition to make the geopolymers in cube moulds, cylindrical moulds were also used. The pellet press of the company Laarmann was used for this. The great advantage of this device is the uniform compression force that can be applied to the geopolymer mixture. To make uniform cylindrical mixtures with equal mass and height, the required amount of geopolymer mixture to add to the mould was weighed behorehand. The pellet press performs compaction in 4 equal layers, each time up to an imposed compression force of 0.25 tons. The dimensions of the different cylinders were fixed at a diameter of 20 mm, and a height of 40 mm.

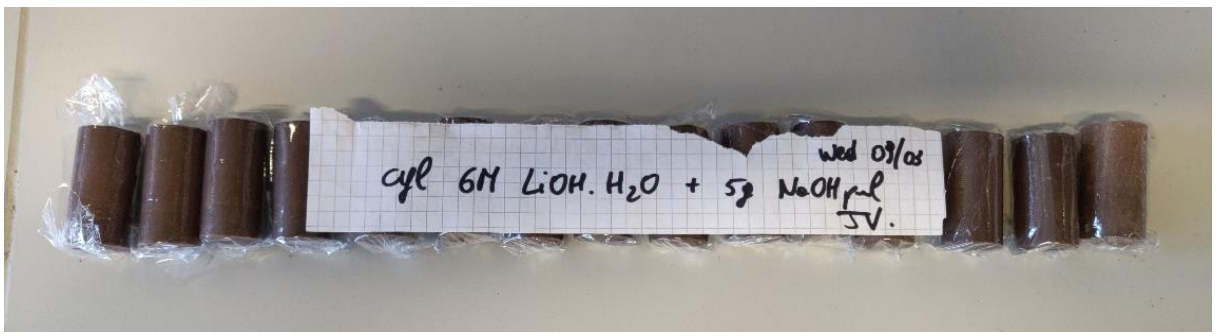

Figure 57: Cylindrical geopolymer samples of 6M $\mathbf{LiOH.H_2O + 5\ g\ NaOH}$.

The device for the compaction of the cylindrical samples is presented in Figure 58. By filling the cylindrical mould in 4 layers, a force was exerted on the geopolymer mixture in each case. This was accomplished by the lower cylindrical part moving upwards by a smooth movement. When the force of 0.25 tons is reached for each case, the compaction is stopped automatically.

Figure 58: Pellet press for compaction of cylindrical geopolymer samples.

The pellet press that is used during this research has a range from 200 kg to 5 tons of compression force. The applied kilogram force of 0.25 tons or 250 kg corresponds to the following compressive pressure during the compaction of each of the four layers:

$$\sigma = \frac{\mathrm{F}}{\mathrm{A_{cylinder}}} = \frac{250\ \mathrm{kg} \times 9.81\ \mathrm{m/s^2}}{\frac{\pi \times (0.020\ \mathrm{m})^2}{4}} = 7.81 \times 10^6\ \mathrm{N/m^2} = 7.81\ \mathrm{MPa}$$

During the compaction of each cylindrical layer, a compressive force of 7.81 MPa is applied. This is done in 4 different layers in order to obtain the best possible degree of compaction. In this way, as much air as possible is removed between the pores of the geopolymer mixture.

4.1.4 Mix design of the geopolymers

The mix design and the different important influence parameters were determined from the studies of Montes *et al.* (2015), Alexiadis *et al.* (2017) and Chakraborty (2019). An important factor for the mix design is the factor representing the ratio between the liquid activator and the solid aluminosilicate material. Montes *et al.* (2015) shows that the activator/aliminosilicate ratio is optimally 0.32 for a geopolymer composition based on simulated lunar regolith Lun-Cast-3D. For this MGS-1 geopolymerisation study, the activator/aluminosilicate volume ratio is set at 0.3, based on an extensive literature review. This volume ratio was fixed for all

experiments, so as to implement a simple mix design. Furthermore, the volume ratio of the amount of metakaolin to MGS-1 was empirically fixed at 0.2. After some meetings with PhD researcher Jiawei Tan, guideline values for a good geopolymer mixture were given. In total, there are three important ratios for geopolymers (Tan, 2022):

$$Na_2O/\text{binder} = 0.04 - 0.09$$

$$H_2O/\text{binder} = 0.05 - 0.3$$

$$Na_2O/SiO_2 = 1 - 2$$

Besides the volume ratios of the activators and the solid aluminosilicate components, the influence of the concentration of the activators is important. Based on the study of Chakraborty (2019), it was determined to make 3 different concentrations (8M, 10M, 12M), of both $NaOH$ and $LiOH.H_2O$. During the further progress of this research, based on the foregoing results, it was decided to also make an additional concentration of 6M for the $LiOH.H_2O$-based geopolymers.

An example for a mix design calculation of a geopolymer mixture consisting of 8M $NaOH$ is shown below (where: mass in g, volume in ml). These values are valid for a total geopolymer volume of 100 ml. These mix design calculations are done by use of Microsoft Excel.

For	100	ml					
	8	M NaOH	10	M NaOH	12	M NaOH	
$V_{alumino}$	70.00	ml	70.00	ml	70.00	ml	
m_{MGS-1}	**72.24**	g	**72.24**	g	**72.24**	g	
m_{kaolin}	**36.68**	g	**36.68**	g	**36.68**	g	
$V_{activator}$	30.00	ml	30.00	ml	30.00	ml	
V_{NaOH}	**4.51**	ml	**5.63**	ml	**6.76**	ml	
$V_{Na_2SiO_3}$	**25.49**	ml	**24.37**	ml	**23.24**	ml	
m_{NaOH}	9.60	g	12.00	g	14.40	g	
$m_{Na_2SiO_3}$	34.16	g	32.65	g	31.14	g	

Figure 59: Mix design calculations for 8M, 10M and 12M NaOH-based geopolymers.

- ✓ For 100 ml geopolymer mixture (8M $NaOH$):

$$m_{NaOH} = n_{NaOH}.M_{NaOH} = 8\ \text{mol/l} \times 39.997\ \text{g/mol} \times \frac{100\ \text{ml}}{1000\ \text{ml}} = 31.998\ \text{g}$$

- ✓ Calculation of volumes for solid aluminosilicate and liquid activator:

$$\frac{\text{liquid activator}}{\text{aluminosilicate}} = 0.3\ (\text{volume ratio})$$

$$V_{aluminosilicate} = (1 - 0.3) \times 100\ \text{ml} = 70\ \text{ml}$$

$$V_{activator} = 0.3 \times 100\ \text{ml} = 30\ \text{ml}$$

- ✓ Calculation of volumes of $NaOH$ and Na_2SiO_3:

$$V_{NaOH} = \frac{m_{NaOH}}{\rho_{NaOH}} \times 0{,}3 = \frac{31.998\ \text{g}}{2.13\ \text{g/cm}^3} \times 0.3 = 4.51\ \text{ml}$$

$$V_{Na_2SiO_3} = 30\ ml - V_{NaOH} = 30\ ml - 4.51\ ml = 25.49\ ml$$

✓ Calculation of mass of $NaOH$ and Na_2SiO_3:

$$m_{NaOH} = \rho_{NaOH} \times V_{NaOH} = 2.13\ g/cm^3 \times 4.51\ ml = 9.60\ g$$

$$m_{Na_2SiO_3} = \rho_{Na_2SiO_3} \times V_{Na_2SiO_3} = 1.34\ g/cm^3 \times 25.49\ ml = 34.16\ g$$

✓ Calculation of mass of MGS-1 and metakaolin:

$$\frac{\text{metakaolin}}{\text{MGS} - 1} = 0.2\ (\text{volume ratio})$$

$$m_{MGS-1} = \rho_{MGS-1} \times V_{aluminosilicate} \times (1 - 0.2) = 1.29\ g/cm^3 \times 70\ ml \times (1 - 0.2) = 72.24\ g$$

$$m_{metakaolin} = \rho_{metakaolin} \times V_{aluminosilicate} \times 0.2 = 2.62\ g/cm^3 \times 70\ ml \times 0.2 = 36.68\ g$$

When composing the geopolymer mixtures, it is important to weigh the mass amount of metakaolin, and not the amount of kaolinite. Suppose the amount of kaolinite is weighed in advance, then there would be an underestimation of the amount of Al_2O_3 in the geopolymer mixture. The underlying reason for this is that during the dihydroxylation process, when kaolinite is converted into metakaolin, an average mass reduction of 6 g takes place on a total weighed mass of 50 g of kaolinite. This mass reduction can be explained by the fact that a certain amount of water evaporates during the conversion of kaolinite into metakaolin:

$$Al_2O_3.2SiO_2.2H_2O \xrightarrow{\text{heating at } 650\ ^\circ C} Al_2O_3.2SiO_2 + 2.H_2O \uparrow\ (\text{water evaporation})$$

4.1.5 Mixing, compacting, grinding and curing of geopolymers

For the mix design, concentration calculations for Na_2SiO_3 were performed. Initially, the mass percentage could be determined, from which the volume percentage could also be determined by the density of the Na_2SiO_3 solution. The sodium silicate solution used in this research has a chemical composition of 7.9 % Na_2O and 25.9 % SiO_2. The mass and volume percentages can be determined according to the following calculations, considering a solution of 100 ml of sodium silicate.

✓ On 100 ml solution:

$$7.9\ g\ Na_2O \rightarrow n = \frac{7.9\ g\ Na_2O}{61.98\ g/mol} = 0.1275\ mol\ Na_2O$$

$$25.9\ g\ SiO_2 \rightarrow n = \frac{25.9\ g\ SiO_2}{60.08\ g/mol} = 0.4311\ mol\ SiO_2$$

✓ Chemical reaction:

$Na_2O + SiO_2 \rightarrow Na_2SiO_3$ with Na_2O as limiting factor

$0.1275\ mol\ Na_2O + 0.4311\ mol\ SiO_2 \rightarrow 0.1275\ mol\ Na_2SiO_3$

✓ Determining w% and V%

$$\frac{0.1275\ mol\ Na_2SiO_3}{100\ ml\ solution} = \frac{1.275\ mol\ Na_2SiO_3}{l\ solution} = \frac{1.275\ mol \times 122.06 \frac{g}{mol}\ Na_2SiO_3}{l\ solution}$$

$$\textbf{mass percentage w\%} = \frac{155.6\ \text{g}\ Na_2SiO_3}{\text{l solution}} = \frac{\frac{155.6\ \text{g}}{1340\ \text{g/l}}\ Na_2SiO_3}{\text{l solution}} = \mathbf{11.6\ w\%\ Na_2SiO_3}$$

$$\textbf{volume percentage V\%} = \frac{11.6\ \text{g}\ Na_2SiO_3/100\ \text{g solution}}{1.34\ \text{g/cm}^3} = \mathbf{8.66\ V\%\ Na_2SiO_3}$$

After the alkali activator and the aluminosilicate mixture are brought together, they must be mixed for a certain period of time. This was done with the aid of a kitchen mixer, whereby a time regime of 3 minutes mixing time per 200 ml of geopolymer mixture was determined experimentally. A uniform mixture was used for each geopolymer mixture, making the results more reliable and therefore less user-dependent. Figures 60 and 61 show the mixing and compaction process of the cube-shaped geopolymers.

Figure 60: Preparation of geopolymer mixtures.

Figure 61: Manual compaction of the cube geopolymer samples during research work.

A challenge during the production of the geopolymers was the supply and processing of enough raw materials to make these geopolymers. The main raw materials that require the appropriate preparation are the simulated Martian regolith (MGS-1) and the metakaolin ($Al_2O_3.2SiO_2.2H_2O$).

To increase the reactivity of the simulated Mars raw material, the standard MGS-1 with average grain size of 122 μm (Cannon *et al.*, 2019) was grinded by using Laarmann's Bottle Roller, for a duration of 6 hours. This grinding device for the MGS-1 is shown in Figure 62. Mixing the MGS-1 reduces the average grain size from 122 μm to a lower fraction. By grinding the MGS-1 into finer powder, the surface area where the reactions take place will increase. Due to the higher surface area, there will be an increase in the frequency of chemical collisions. This results in a higher rate of reaction (Sarraf *et al.*, 1996).

The method used during the filling of the cylinder is as follows: half of the total mass of spheres in the Bottle Roller is the total mass of MGS-1 to be added. Specifically, this means for a total mass of 963.4 g of spheres in the cylinder, a total of 471.7 g of MGS-1 must be added in the cylinder. This guideline must be followed to obtain a fine enough powder of MGS-1.

In addition to grinding the MGS-1 more finely, a sufficient amount of metakaolin must also be produced. For this purpose, a suitable amount of kaolinite must be placed for 180 minutes in the furnace at 650 °C to create metakaolin.

Figure 62: Bottle Roller for grinding the MGS-1 simulant.

After the geopolymer mixtures have been fully assembled, mixed and compacted, they must be cured for a certain time in the oven at a constant temperature of 70 °C, as shown in Figure 63. The study by Chakraborty (2019) shows that curing geopolymer mixtures at room temperature shows less good results than oven curing. During that study, the geopolymers were cured in the oven at two different temperatures, which are 60 °C and 90 °C.

The decision to set the oven at a temperature of 70 °C is because this is a default temperature for the curing process of geopolymers. Rovnaník (2010) shows that metakaolin-based geopolymers gain the highest mechanical strength for oven curing at 60 °C and 80 °C. Thanks to the reliable results already obtained from these previous studies on geopolymers, a constant curing temperature of 70 °C is used for the geopolymers in this research (Montes *et al.*, 2015).

Figure 63: Cube and cylindrical geopolymer samples in oven at curing temperature of 70 °C.

4.1.6 Research progress and solubility issues

The production of the geopolymers started on Monday, February 14th, 2022, and ended on Tuesday, March 22nd, 2022. Because of the tight timing, a time schedule was made in Microsoft Excel. Due to this structured time schedule, a good overview was kept, day after day, when production and testing of the geopolymers needs to be done. Proud to be said that all the laboratory work could be completed in the first part of the second semester.

Figure 64: Cube (left) and cylindrical (right) geopolymer samples, before curing.

In order to be able to compare the results of the compression tests of the geopolymers with traditional Portland cement (Holcim CEM I 52.5R HES), a number of cube cement mixtures were also produced. During the production of the geopolymers with $\mathrm{LiOH.H_2O}$ as alkali activator, it was found that $\mathrm{LiOH.H_2O}$ is not well soluble in the sodium silicate solution. This could be determined theoretically, as this lower solubility was already mentioned in the

literature review. In section 3.2.4 from the literature review of geopolymers, it was mentioned that the solubility of lithium hydroxide is only 12.8 g per 100 g of water, and this at a temperature of 293.15 K. In addition, sodium hydroxide, at the same temperature, has a solubility of no less than 111 g per 100 g of water.

From this data, we can conclude that lithium hydroxide only has a solubility of 11.5 % relative to sodium hydroxide. The effect of the low solubility of lithium hydroxide in the sodium silicate solution is shown in Figure 65, on the left side, where flakes of lithium hydroxide have been formed. These solid substances are detrimental to the production of geopolymers.

Hence, it was determined experimentally to add 5 g of $NaOH$ to the $LiOH.H_2O$. This creates an exothermic reaction, whereby the heat produced will ensure that the $LiOH.H_2O$ dissolves more easily in the sodium silicate solution. This addition of sodium silicate will compensate for the poorly soluble character of lithium hydroxide. The improved solubility of the lithium hydroxide through adding 5 g of sodium silicate pellets is shown in Figure 65, on the right side. Here, it is clear that the initially poorly soluble lithium hydroxide substances actually start to dissolve. The large insoluble flakes begin to concentrate into smaller, soluble particles. This improved solubility is reflected in the appearance of the mixture, which appears more turbid than initially.

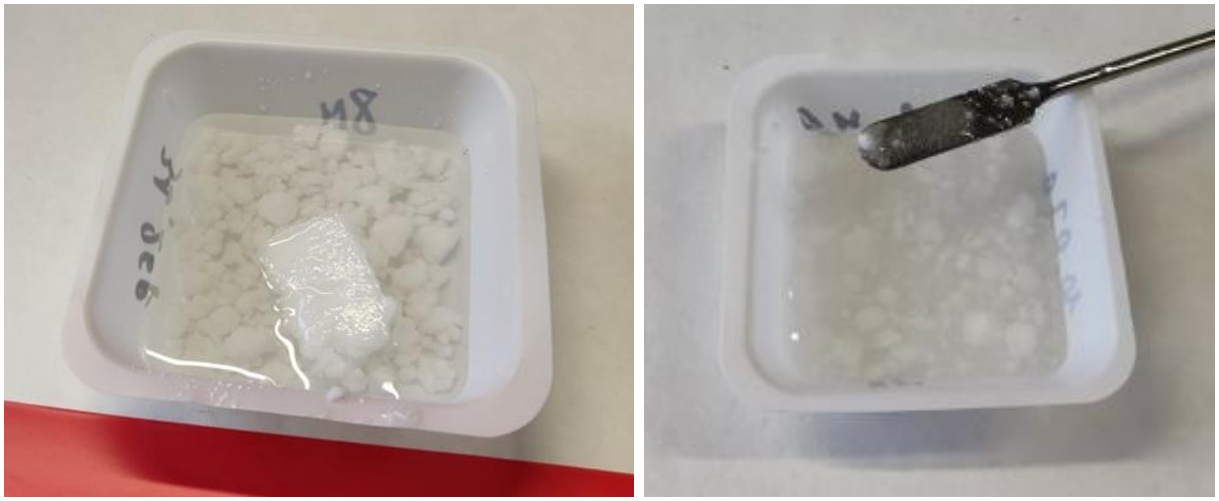

Figure 65: Bad solubility of lithium hydroxide in sodium silicate solution (left), sufficient solubility of lithium hydroxide in sodium silicate solution after adding 5 g of $NaOH$ (right).

After a critical reflection on the results of the first three weeks of laboratory testing on Friday, March 4th, 2022, it was found that the cube geopolymer mixtures with a concentration of 8M show the best results. In addition, it is also remarkable to note that the geopolymers based on $LiOH.H_2O$ as alkali activator show better results in compressive strength than those based on $NaOH$. As a result, it was decided to mainly focus on $LiOH.H_2O$ as activator in the production of the cylindrical geopolymer mixtures. In addition to the 8M $LiOH.H_2O + 5\,g\,NaOH$ experiments are also carried out with a lower concentration of 6M $LiOH.H_2O + 5\,g\,NaOH$, to identify the influence of lower alkali concentration. The rationale for this choice of the lower concentrations was that 8M $LiOH.H_2O + 5\,g\,NaOH$ geopolymers showed the best test results.

An overview of the planning schedule with the different geopolymer mixtures made during this research is presented in bullets below. This schedule was strictly followed-up in order to maintain the efficiency of the production of geopolymers. However, this planning was flexibly adapted to the mix design of the geopolymers, based on a critical reflection on previous results.

- Monday, February 14th, 2022

  9 cube geopolymers of 8M NaOH
  9 cube geopolymers of 10M NaOH

- Tuesday, February 22nd, 2022

  9 cube geopolymers of 12M NaOH
  9 cube geopolymers of 8M $\mathrm{LiOH.H_2O} + 5\ \mathrm{g\ NaOH}$

- Tuesday, March 1st, 2022

  9 cube geopolymers of 10M $\mathrm{LiOH.H_2O} + 5\ \mathrm{g\ NaOH}$
  9 cube geopolymers of 12M $\mathrm{LiOH.H_2O} + 5\ \mathrm{g\ NaOH}$

- Wednesday, March 2nd, 2022

  6 cube geopolymers of 6M $\mathrm{LiOH.H_2O} + 5\ \mathrm{g\ NaOH}$
  6 cube geopolymers of 8M $\mathrm{LiOH.H_2O} + 5\ \mathrm{g\ NaOH}$

- Monday, March 7th, 2022

  18 cube geopolymers of 6M $\mathrm{LiOH.H_2O} + 5\ \mathrm{g\ NaOH}$

- Wednesday, March 9th, 2022

  15 cube geopolymers of 6M $\mathrm{LiOH.H_2O} + 5\ \mathrm{g\ NaOH}$
  15 cube geopolymers of 8M $\mathrm{LiOH.H_2O} + 5\ \mathrm{g\ NaOH}$

- Thursday, March 10th, 2022

  6 cube cement mixtures of Holcim CEM I 52.5R HES

- Monday, March 14th, 2022

  2 cylindrical geopolymers of 8M NaOH

- Tuesday, March 15th, 2022

  9 cube geopolymers of 6M $\mathrm{LiOH.H_2O} + 2.5\ \mathrm{g\ NaOH}$
  9 cube geopolymers of 8M $\mathrm{LiOH.H_2O} + 2.5\ \mathrm{g\ NaOH}$

  9 cylindrical geopolymers of 6M $\mathrm{LiOH.H_2O} + 2.5\ \mathrm{g\ NaOH}$
  9 cylindrical geopolymers of 8M $\mathrm{LiOH.H_2O} + 2.5\ \mathrm{g\ NaOH}$

❖ Wednesday, March 16th, 2022

15 cylindrical geopolymers of 8M NaOH

❖ Monday, March 21st, 2022

12 cube cement mixtures of Holcim CEM I 52.5R HES

Figure 66: Portland cement CEM I 52.5R HES cube samples.

❖ Tuesday, March 22nd, 2022

9 cube geopolymers of 6M $\mathrm{LiOH.H_2O} + 7.5\ \mathrm{g\ NaOH}$
9 cube geopolymers of 8M $\mathrm{LiOH.H_2O} + 7.5\ \mathrm{g\ NaOH}$

9 cylindrical geopolymers of 6M $\mathrm{LiOH.H_2O} + 7.5\ \mathrm{g\ NaOH}$
9 cylindrical geopolymers of 8M $\mathrm{LiOH.H_2O} + 7.5\ \mathrm{g\ NaOH}$

Figure 67: Prepared cylindrical and cube geopolymer samples.

The planning schedule for performing the compression tests and the FTIR analysis was made through different timelines, as is shown in Figure 68. The green time bars represent the $NaOH$-based geopolymer mixtures. The yellow time bars represent the $LiOH.H_2O$-based geopolymer mixtures with addition of $NaOH$, to obtain better solubility. Curing times were set at 1 day, 3 days, 7 days and 28 days. In the first phase of the research, during the first three weeks, the main focus was on the evolution of the compressive strength according to short term curing conditions (1 day, 3 days and 7 days).

Further into the research, based on a critical analysis after three weeks, it was decided to carry out the 28 day curing on the geopolymers which have significant potential in developing their long term strength. Especially the geopolymers that showed the best results during these first weeks were subjected to this longer curing time. In this way, through an initial exploratory study in the first three weeks, specific further research can be done into the geopolymer with the best mechanical and chemical properties.

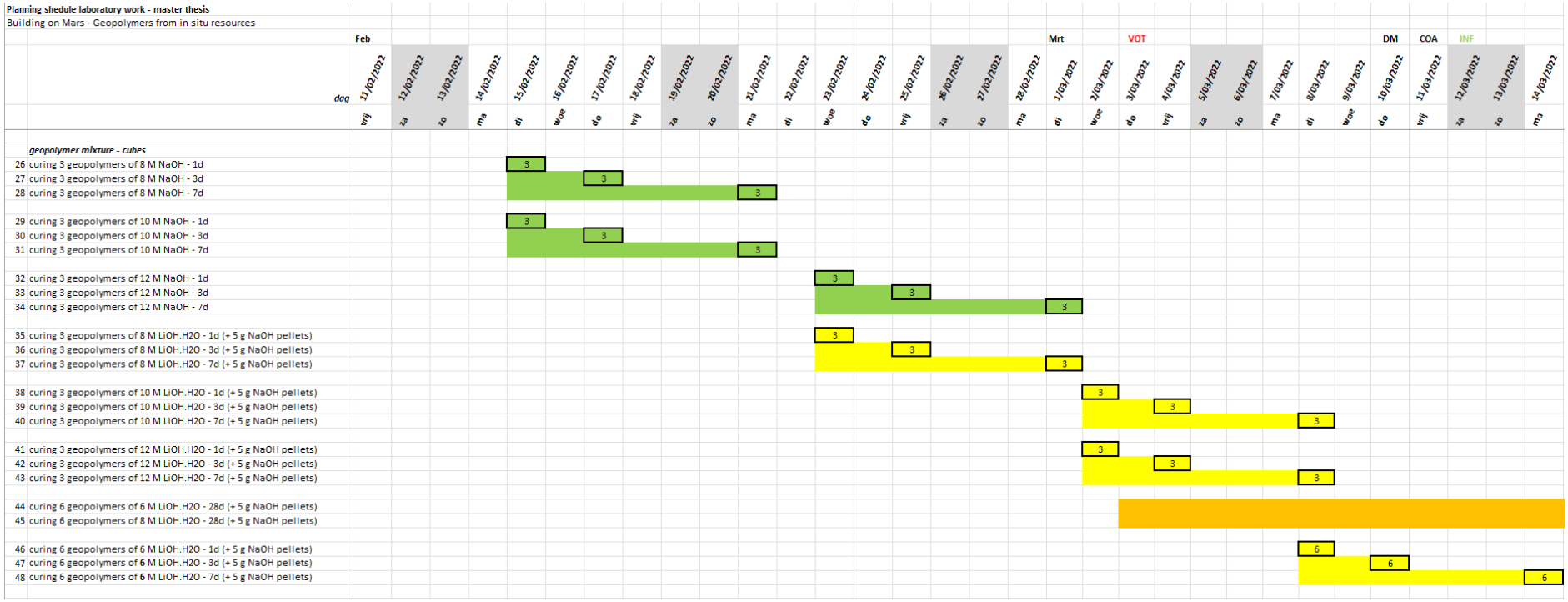

Figure 68: Planning schedule for production of geopolymers, during first phase of laboratory work.

4.2 Analytical methodology

4.2.1 FTIR principle

Fourier Transform Infrared Spectroscopy (FTIR) is frequently used as a technique to analyse the vibrational energy in molecules (Puligilla *et al.*, 2015). The device that has been used in this research project is PerkinElmer FTIR, as presented in Figure 69. While performing this analysis, the bonds between two atoms are studied at micro level. Finally, a graph will be obtained where the amount of transmission (in %) is displayed on the ordinate. The wavelength spectrum is shown on the abscissa. From an FTIR analysis, the infrared spectrum of adsorption or emission of a solid, liquid or gas can be determined. Based on the different peaks that can be observed, the functional groups in molecules can be identified.

Figure 69: PerkinElmer FTIR device.

The working principle of the FTIR method can be explained by the different emission spectra of light (Garcia-Lodeiro *et al.*, 2011). As indicated in Figure 70, a fine beam of infrared light is emitted onto the sample. Subsequently, the molecules present in the sample adsorb certain characteristic frequencies of infrared light. Based on the frequencies of the light, the characterisation of the functional groups in the geopolymer binder can be made.

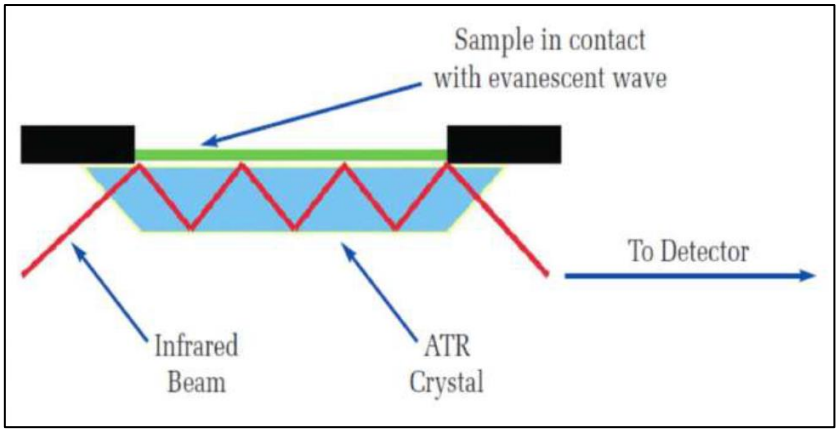

Figure 70: Working principle of FTIR. (Madavarapu, 2014)

For the geopolymers, the infrared spectrum of adsorption or emission can be determined by grinding into very fine powder. The raw measurement data is ultimately converted into the actual spectrum by an internal Fourier transform. From this chemical analysis of the geopolymers, a relationship will be figured out between the compressive strength and the internal composition of the geopolymers. Finally, a judgment can be made about the suitability of the final geopolymer to offer as a possible building material for the planet Mars. Finding this appropriate building material is in fact the goal of this research.

4.2.2 Learning outcomes during research process

During the research process to obtain a suitable geopolymer, several problems were identified during the implementation of the theoretical background into practice. This section clarifies the main limitations, and more important, the way in which these limitations have been dealt with.

4.2.2.1 No optimal compaction method for cube geopolymer samples

During the first phase in the research process, the compaction of the cube geopolymers was done manually by pressing the mixture simple by finger. The problem that arose with this, however, is that the degree of compaction of the different geopolymers will not be uniformly distributed. This was also found in the fluctuation of the compressive strength results of the cube geopolymers. The solution devised for this is to beat the plastic cap evenly with a pestle through a manual tapping motion, in order to compact the geopolymers in a consistent way.

From experimental experience, a standard method of ten strokes per layer to be compacted was established. In order to obtain a high compaction accuracy, and also to eliminate user-dependent errors as much as possible, the cube geopolymers are compacted in ten successive layers. This results in a total of 100 compaction strokes per cube geopolymer. Because this method is a very labour-intensive process for cube geopolymers, preference is given to the pellet press. The cylindrical geopolymers can hereby be mechanically compacted through a cylinder force, acting on the geopolymer mixture. By using cylindrical geopolymers, the test results become more reliable due to the lower reliance on user-dependent operations. Figure 71 shows the manually compacted cube geopolymers, with the pestle and plastic cap as compaction tools, visible at the top left of the figure.

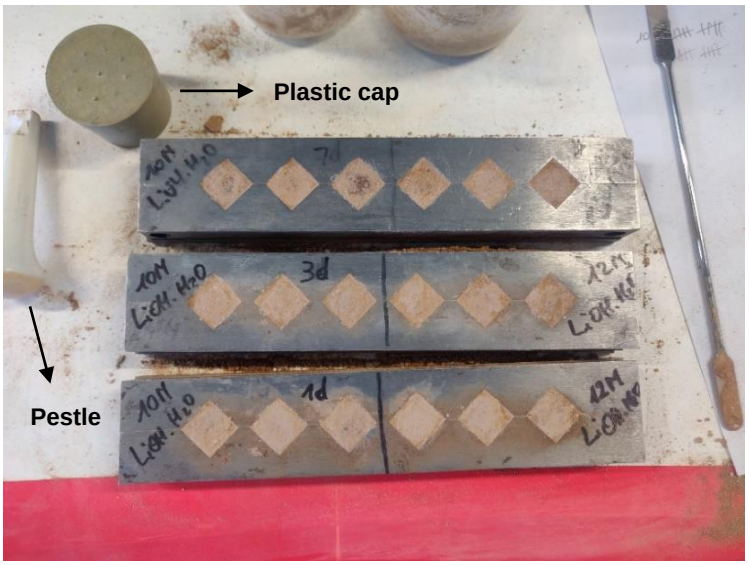

Figure 71: Manually compacted cube geopolymer samples.

4.2.2.2 No uniform mixing time for geopolymers

It soon became clear in the research design that certain standard methods must be applied. This makes it able to consequently compare the results of the laboratory work afterwards. One of those standards lies in the fact that a uniform mixing time of the various components for the geopolymer mixture must be applied. It was established experimentally that a mixing time of three minutes per 200 ml geopolymer volume to be produced should suffice.

By continuously applying this uniform mixing procedure, the reliability of the various results is improved. This means that a qualitative comparison can be made between the different results from the laboratory tests. The critical reflection of these test results can be found in section 6.

4.2.2.3 Bad solubility of $LiOH.H_2O$ in sodium silicate solution

When the geopolymers were produced by alkali activator NaOH, an exothermic reaction was observed in which quite a lot of heat was released. The exothermic process enhanced the solubility of NaOH in the sodium silicate solution. This results in a complete reaction process where the reaction products are entirely developed.

As previously mentioned in paragraph 4.1.6, during the second week of production of the geopolymers based on $\mathrm{LiOH.H_2O}$, problems were detected for the solubility of $\mathrm{LiOH.H_2O}$ in the sodium silicate solution. Lithium is unique among the alkali metals because it has the smallest atomic radius to possess the single valence electron in this group of alkali metals. In addition, lithium has a comparatively large hydrated radius and polarising power compared to the other alkali metals (Federico et al., 2009). Due to the low density of lithium, no exothermic reaction is initiated after dissolution in the sodium silicate solution.

If no further actions are taken to increase the solubility of $\mathrm{LiOH.H_2O}$ in the sodium silicate solution, white lumps are formed. To solve this problem, the reaction process was activated by adding a small amount of NaOH pellets. As a good standard, 5 g NaOH pellets are added to increase the solubility of $\mathrm{LiOH.H_2O}$ in the sodium silicate solution, as shown in Figure 72. This action has a positive effect on the formation of the reaction product, because a combination of two alkali activators is used to activate or catalyse the geopolymerisation mechanism.

Figure 72: Increased solubility of $\mathrm{LiOH.H_2O}$ in $\mathrm{Na_2SiO_3}$ solution by 5 g NaOH pellets catalysation.

4.2.2.4 Different heights for cylindrical samples

During the production of the cylindrical geopolymers by using the pellet press, it was found that the cylindrical samples differ in height. The reason for this is easy to understand because

different masses are added to the several layers that are compacted. To counter this problem, the exact amounts of geopolymer mixture per layer are calculated.

An example of such a calculation for the production of cylindrical geopolymers, activated by a concentration of 8M $NaOH$, is shown in Figure 73.

1 cylinder	12566	mm³	8	M NaOH	
	1.26E-05	m³			
	0.0126	l	19.19	g geopolymer mixture	
	12.6	ml	**4.80**	g/layer (compaction in 4 layers)	
	12.6	**cm³**			
				6.40	g/layer (compaction in 4 layers)

Figure 73: Calculation of mass to be added per compaction layer.

$$\text{added mass per layer} = \sum(m_{MGS-1}; m_{metakaolinite}; m_{NaOH}; m_{Na_2SiO_3}) \times \frac{V_{cylinder}}{V_{mixe\ design}}$$

$$\textbf{added mass per layer} = (72.24 + 36.68 + 9.60 + 34.16)\ g \times \frac{12.6\ ml}{100\ ml} = \mathbf{4.80\ g}$$

An experimentally determined correction factor is applied to this calculated amount, so that the cylinder obtains an exact height of 40 mm. The reason for applying this correction is that the air inclusions that are removed during compaction are not included in this calculation method.

During the compaction process of the cylindrical geopolymers in four successive layers, the air gradually leaves the geopolymer mixture. This process brings the grains closer together into a denser matrix and increases the density of the mixture. This means that the occupied volume of the geopolymer becomes smaller for the same mass. As shown in Figure 74, a larger mass of geopolymer mixture will therefore be necessary to maintain the same volume.

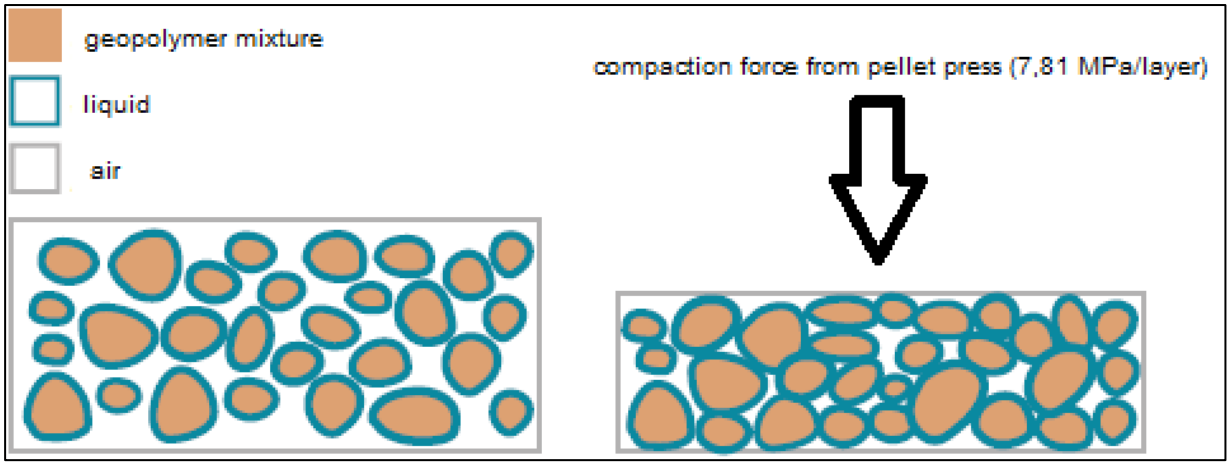

Figure 74: Compaction of geopolymer with pellet press. (Edited from Cafre, 2022)

4.2.2.5 Excessive use of demoulding oil

During the production of the first geopolymer mixtures, an excessive amount of demoulding oil was applied to the cube moulds. The reason for this was that the moulds were not opened before the oil was applied. This was also observed when these cubes were demoulded for performing the compression tests. This was clearly visible in the cube geopolymers due to the low manual compaction by finger, as well as the excessive amount of demoulding oil applied.

The solution to this problem is to open the cube moulds before applying the oil and evenly apply the demoulding oil by making a smoothing motion. However, this problem does not arise with the cylindrical geopolymers, because they can be demoulded immediately after production. Due to the high compaction force applied on the cylinder, strong cohesive forces are created in the internal structure of the geopolymer. Finally, one coherent cylindrical core is formed, and these cylindrical geopolymers can be easily pressed out of the mould, by applying a compression force with the pellet press.

The problem with the demoulding oil, however, arose in the initial phase of the laboratory experiments. This was quickly established through continuous feedback and critical attitude to the obtained measurement results. Figure 75 shows the excess use of the demoulding oil on the cube geopolymers. At the bottom of the cubes, the large amount of demoulding oil is clearly visible due to the dark colour.

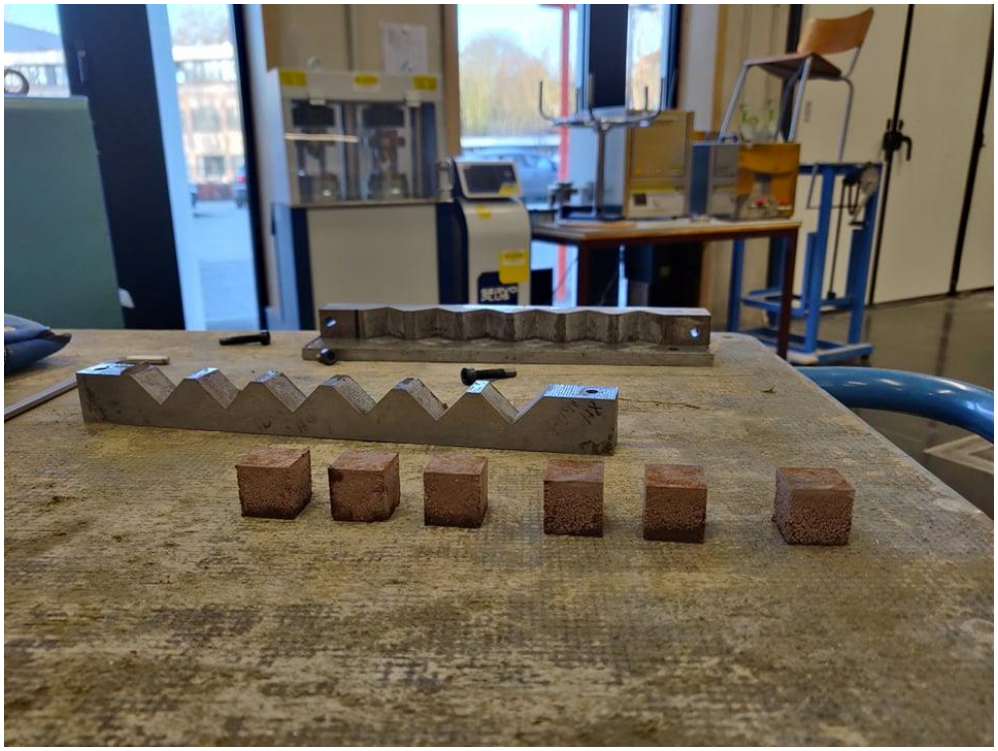

Figure 75: Excessive use of demoulding oil on the cube geopolymer samples.

4.2.3 Quality management during research process

The production and test cycle in the research procedure was characterised by an internal customer-supplier relationship. The aim is to comply as much as possible with the quality spiral and the principle of integral quality management during this research (Vervenne, 2020).

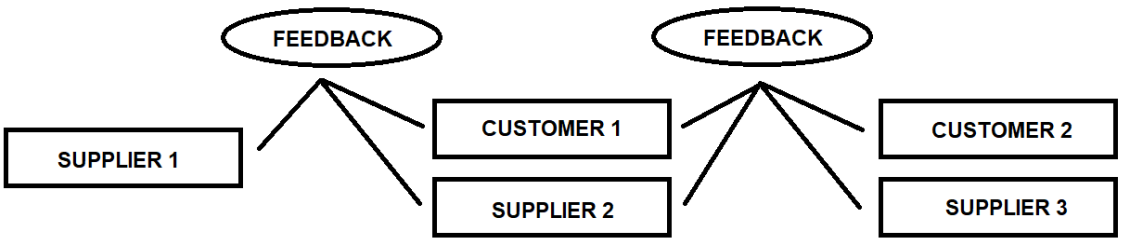

Figure 76: Internal consumer-supplier relationship during research.

4.3 Material testing

4.3.1 Compression tests

The MacBen compression test, as shown in Figure 77, is used to perform the mechanical characterisation of the geopolymers, in terms of compressive strength. This compression test is of the 2-cylinder 300 kN type, with digital automatic compression control. Depending on the test samples (cube or cylindrical geopolymers), other setting parameters must be configured to the device. Important setting parameters for the this test device are the rate at which the force increases, the start load, the final load and the surface area of the test specimen.

Figure 77: MacBen compression test for mechanical characterisation.

4.3.1.1 Cube geopolymer samples

The settings of the compression test for the cube geopolymers are listed below. The value of the final load is set to 20 % by default. This means that, as soon as there is a greater decrease in load than 20 % of the previous load increment, the device will automatically end the compression test and finally show the highest compressive strength value registered.

- Test description: IGNAC3 PRISMA
- Rate: 1.000 kN/s
- Start load: 1.000 kN
- Stop load: 20 %
- Area: 400.000 mm²

4.3.1.2 Cylindrical geopolymer samples

For the cylindrical geopolymers, the setting parameters remain the same, except for the surface of the sample. The area of the cylindrical samples can be calculated by:

$$A_{cyl} = \frac{\pi \times D^2}{4} = \frac{\pi \times (0.020\ \mathrm{m})^2}{4} = 314 \times 10^{-6}\ \mathrm{m}^2 = 314\ \mathrm{mm}^2$$

- Test description: IGNAC3 PRISMA
- Rate: 1.000 kN/s

- ❖ Start load: 1.000 kN
- ❖ Stop load: 20 %
- ❖ Area: 314.159 mm²

4.3.2 Other used devices during the research process

4.3.2.1 FTIR

The chemical characterisation of the geopolymers was done using the PerkinElmer FTIR device. Different peaks were registered at the corresponding wavelengths from an infrared spectrum. The degree of adsorption of the infrared light in the material will provide insight into the vibrational energy of the atoms, internal to the structure of the geopolymers. This analytical technique is typically used for materials analysis. Molecular vibrations in covalent bonds or functional groups can be observed in this way, depending on the adsorption of IR radiation at certain frequencies (Eurolab, 2020).

By performing the FTIR analysis, the geopolymers with good mechanical properties can be linked to their actual composition. This allows an attempt to establish a relationship between the mechanical and chemical properties of the geopolymers. The working principle of the FTIR has already been described in section 4.2.1.

4.3.2.2 Bottle roller

The LMBR500 Bottle Roller in Figure 78 only has the function to transform the simulated Mars raw material MGS-1 into finer powder. This increases the reactivity of the aluminosilicate material, because of the higher surface area of the particles. For a detailed description of the increased reactivity, reference is made to section 4.1.5. By using the bottle roller, the original grain structure was converted into fine powder. The effect of treating the MGS-1 with the bottle roller is also visible with the naked eye. To qualitatively capture this difference in grain size, the effect of the bottle roller treatment was examined on microscopic level by use of the Keyence laser microscope.

Figure 78: LMBR500 Bottle Roller for grinding the MGS-1 simulant.

4.3.2.3 Keyence laser microscope

The effect of the use of the bottle roller on the average grain size of the Martian raw material is recorded with the Keyence laser microscope, as shown in Figure 79. This microscope uses a triple scanning approach, where scanning methods with the confocal laser or camera are used to measure objects. This allows a 3D representation of the object to be studied. By

adjusting the magnification of the objective lens from 2.5x to 100x, a detailed image can be obtained of the grain distribution of MGS-1. Besides determining the mean grain size of MGS-1, this microscope is also used for the effect on the grain size after calcination of the kaolinite into metakaolin. Here, both kaolinite and metakaolin are studied at different scales relative to each other. From the analysis before and after the treatment of the material, an estimation can be made of the average grain size within a specific studied zone of the material. The effect of grinding MGS-1 and calcination of kaolinite is discussed in section 6.2, in the critical reflection of the results.

Figure 79: Keyence laser microscope for determining the effect of grinding MGS-1 and calcination of kaolinite.

Glass slides are used to determine a representative mean grain size, as shown in Figure 80. First, the granular powders are suspended in an alcohol solution in glass tubes. After they have been mixed adequately, they are brushed over the glass slides in order to obtain the most uniform possible approximation of the grain distribution. Because alcohol has the natural property to evaporate in ambient air, only the grains remain on the glass slides after ten minutes of waiting.

In Figure 80, the glass slides of metakaolin, kaolinite, MGS-1 rough material and MGS-1 milled are shown from left to right. The most important point of attention when preparing the glass slides, is that no excessive amount is sprinkled over the glass slides. If an excessive amount of suspended material is used, a microscopic analysis of grain size becomes difficult, since the

different grains are no longer distinguishable from each other. In that case, the grains are in a dense matrix, as can be seen on the second glass slide in Figure 80. The difference is clearly visible between the first and second glass slide, where a more suitable amount of suspended material of metakaolin has been applied to the first glass slide.

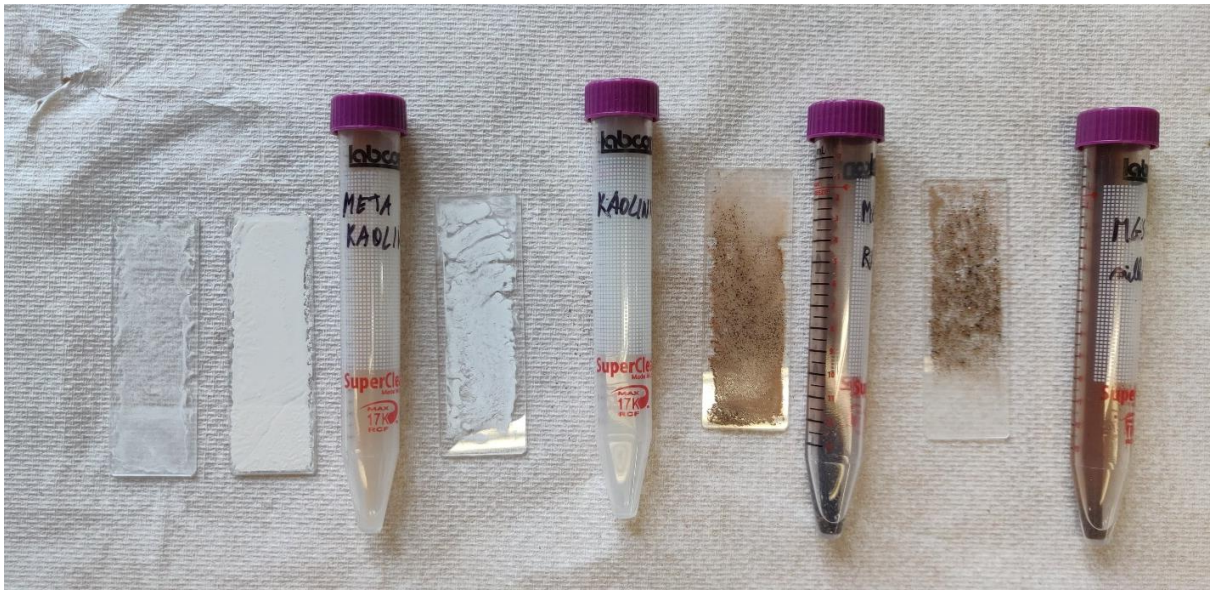

Figure 80: Glass slides and tubes for microscopic analysis of particle size.

4.3.2.4 Pellet press

The most important operation in making the geopolymers is the compaction or densification of the geopolymer mixture. From the very beginning, attention was paid on this during the preliminary study of the research. The importance of sufficient compaction was clearly emphasised from constructional knowledge about conventional concrete production. The better the compaction can be done, the better the strength of the mixture will become because the air abandons the mixture. The compaction of the cubes had to be done in a systematic, but manual way. However, this method is not ideal due to the user-dependent influence on the results.

The pellet press from company Laarmann was used for the production of the cylindrical geopolymers. This device has already been introduced and discussed in section 4.1.3.2., whereby referring to Figure 58. Due to the uniform compaction, the compressive strength results are more reliable and there will be fewer outliers in the results to be expected. For the analysis and critical reflection of the compressive strength results, preference is therefore given to the more reliable cylindrical geopolymers.

4.3.2.5 Oven and furnace: curing and dihydroxylation

An oven and a furnace are required for the careful and efficient execution of the experiments. The oven was set at a continuous temperature of 70 °C for the curing process of the geopolymers on 1 day, 3 days, 7 days and 28 days. This oven has already been described in sections 4.1.3.1 and 4.1.5. The furnace is needed to convert the kaolinite into metakaolin. This calcination process requires a constant temperature of 650 °C for 3 hours. Due to the almost ten times higher temperature, the furnace must have much more power than the oven. In addition, some patience must be exercised before the furnace is at the right temperature. A warm-up time of 30 minutes to move from room temperature to the desired temperature of 650 °C for calcination of kaolinite, is needed.

4.4 General test setup

The primary objective of this research was to determine an optimum mix design for the geopolymerisation of simulated Mars regolith MGS-1. Essentially, three different concentrations (8M, 10M and 12M) were analysed of $NaOH$ and $LiOH.H_2O$. The mix design and testing of the geopolymers took place in two different phases, which are chronologically spread over time: an exploration and implementation phase.

The exploration phase took place during the first three weeks of the second semester. This phase can be seen as an exploration through the geopolymer properties by varying concentrations of the alkali activators. The purpose of this phase is to draw a rough conclusion from the observed results. The best results are retained for further research in the second implementation phase. This second phase followed after an initial analysis of the results, starting from the fourth week of the second semester until the end of Easter holidays.

4.4.1 Exploration phase

During the first three weeks of geopolymer production, only cube geopolymers were made, according to the next compositions:

- 8M $NaOH$
- 10M $NaOH$
- 12M $NaOH$
- 8M $LiOH.H_2O + 5\ g\ NaOH$
- 10M $LiOH.H_2O + 5\ g\ NaOH$
- 10M $LiOH.H_2O + 5\ g\ NaOH$

4.4.2 Implementation phase

After the first feedback moment on March 4th, 2022 between the mix design and the evaluation of the results, a second set of mixtures was made. In this second series, both cube and cylindrical geopolymers were made. The main focus during the implementation phase was on the cylindrical geopolymers, as the pellet press was ready for use on March 2nd, 2022. Due to the good results of the geopolymers with the alkali activator $LiOH.H_2O$, most of the cylindrical geopolymers were made with $LiOH.H_2O$ as the activating medium. Based on the best results from the first three weeks of testing, the following mix designs were performed:

- 8M $NaOH$
- 6M $LiOH.H_2O + 5\ g\ NaOH$
- 8M $LiOH.H_2O + 5\ g\ NaOH$
- 6M $LiOH.H_2O + 2.5\ g\ NaOH$
- 8M $LiOH.H_2O + 2.5\ g\ NaOH$
- 6M $LiOH.H_2O + 7.5\ g\ NaOH$
- 8M $LiOH.H_2O + 7.5\ g\ NaOH$

After the geopolymers have cured according to the prescribed time, they are subjected to the compression test. After this test has been carried out, the geopolymer material is recovered and a fraction of the geopolymer is very finely ground into powder. This powder is then used for the FTIR analysis.

5 RESEARCH RESULTS

All test results for the various measured compressive strengths and FTIR spectra are objectively presented below in tables and graphs. The observed trend is objectively described for each different geopolymer mixture. Its interpretation and critical analysis can be found under the critical reflection and conclusions of this Master's thesis. The general trend of the compressive strength as a function of time is shown through a best-fitting curve. The purpose of this section is to provide a clear overview of the results of the laboratory work performed. An important note is that the statistical analysis has already been performed on the results presented in this section. For the background of the statistical analysis, reference is made to section 6. For the presentation of all measured data, reference is made to the appendices.

5.1 Statistical background

The error bars displayed at the different data points indicate the sample standard deviation s, or the variability around the mean value. This will mainly be an indication for the reliability of the measurements. Generally, we let $x_1, x_2, \ldots, x_n$ denote sample values in the statistical approach (Statistics for Engineers, 2013).

The **sample variance**, denoted by $\mathbf{s}^2$, is given by: $s^2 \approx \sigma^2 = \sum_{i=1}^{n} \frac{(x_i - \bar{x})^2}{n-1}$

The **sample standard deviation**, denoted by $\mathbf{s}$, is the positive square root of s^2: $s = \sqrt{s^2}$

The standard deviation is a measure of variability. Large variability in a statistical data set produces relatively large values for $(x - \bar{x})^2$, and thus a large sample variance. The quantity $n - 1$, which is the best approach for σ^2, is called 'the degrees of freedom' associated with the variance estimate, where n represents the number of elements in the data set.

Thus for a considered statistical problem, the sample along with inferential statistics allows us to draw conclusions about the whole population, where elements of probability are used. And on the other hand, elements in probability allows us to draw conclusions about characteristics of hypothetical data taken from the population, based on known features of the population. This fundamental relationship between probability and statistical interference is shown schematically in Figure 81.

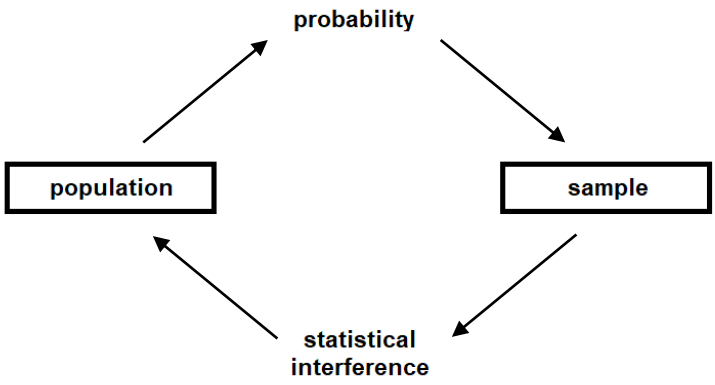

Figure 81: Relationship between probability and statistical interference.

5.2 Compressive strength of geopolymers

The mechanical characterisation of the geopolymers is based on the compressive strength results. First, the results of the cube specimens are discussed, then the cylindrical ones. The results are presented as their mean value $\bar{x}$ from the set of three or six specimens tested, with their uncertainty factored in as one times the sample standard deviation s. The compressive strength f_c is thus defined as: $f_c = \bar{x} \pm s$.

In some cases, the compressive strength values are indicated in red. This indicates that one or more outliers were present in the data set of the measured values. These outliers were removed from the data set, in order to obtain representative values for the compressive strength. The methodology for determining whether or not a measurement is an outlier is described in section 6.1. Prediction intervals are used for this, since it cannot be assumed that the measured values are normally distributed. Therefore, the use of prediction intervals is an objective way of making judgments about outliers from randomly distributed data.

5.2.1 Cube samples

Table 6: NaOH-based geopolymers.

sample	$f_{c,1d}$ $[MPa]$	$f_{c,3d}$ $[MPa]$	$f_{c,7d}$ $[MPa]$
8M NaOH - 70°C oven cured	**8 ± 2**	**16 ± 4**	**11 ± 2**
10M NaOH - 70°C oven cured	**5 ± 1**	**6 ± 2**	**7 ± 2**
12M NaOH - 70°C oven cured	**7.4 ± 0.7**	**7 ± 2**	**8 ± 1**

Initially, the trend of the compressive strength for the NaOH -based geopolymers is shown. It can be seen that the lowest 8M NaOH concentration performs the best of the three different concentrations, with an early developed strength with relatively high standard deviation of 4 MPa after 3 days, and then a decrease in strength after 7 days occurs.

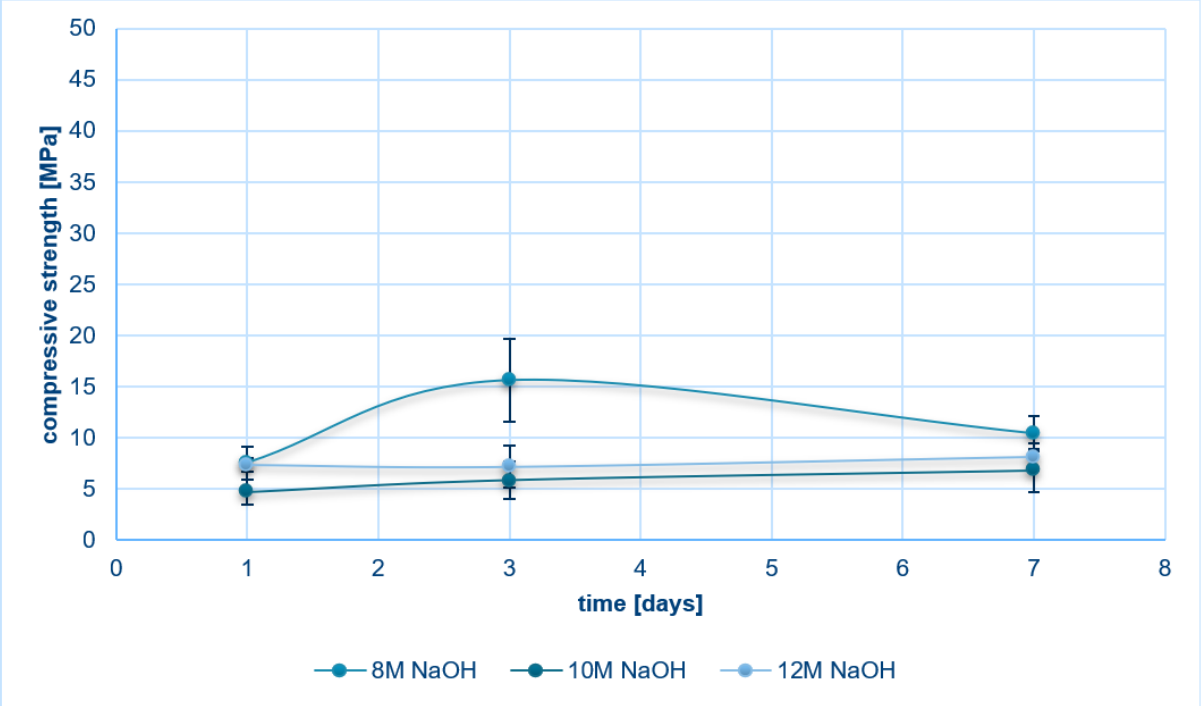

Figure 82: **NaOH-based geopolymers.**

The other 10M and 12M $NaOH$ samples achieve 64 % and 72 % respectively of the final strength of the 8M $NaOH$ sample after 7 days. The samples formed with these two higher concentrations gradually increase in strength, with each an increment of 1 MPa as the curing time progresses to 3 and 7 days. It is also noted that these samples show a lower variability than the 8M $NaOH$ concentration. As a result, it can be stated that these samples create a more reliable image in terms of strength.

Table 7: $LiOH.H_2O + 5$ g NaOH-based geopolymers.

sample	$f_{c,1d}$ $[MPa]$	$f_{c,3d}$ $[MPa]$	$f_{c,7d}$ $[MPa]$
6M LiOH.H2O + 5g NaOH - 70°C oven cured	**9 ± 2**	**10 ± 3**	**10 ± 2**
8M LiOH.H2O + 5g NaOH - 70°C oven cured	**26 ± 2**	**20 ± 4**	**20 ± 8**
10M LiOH.H2O + 5g NaOH - 70°C oven cured	**17 ± 2**	**23 ± 4**	**34 ± 7**
12M LiOH.H2O + 5g NaOH - 70°C oven cured	**7 ± 1**	**11.7 ± 0.5**	**16 ± 1**

The $LiOH.H_2O$-based geopolymers show higher compressive strengths than the $NaOH$-based geopolymers. Initially, during the exploration phase, only geopolymers were made, composed of 8M, 10M and 12M $LiOH.H_2O$. It should be noted that the 10M $LiOH.H_2O$ samples show the highest compressive strength after 7 days, with an average compressive strength of 34 MPa. This geopolymer composition shows a substantially linear increase as function of curing time. The 8M $LiOH.H_2O$ concentration develops a high strength of 26 MPa, especially in the initial phase. After curing for 3 days, this strength drops to a value of 20 MPa.

Besides the linear strength development of the 10M $LiOH.H_2O$ sample, the 12M $LiOH.H_2O$ samples show a curved trend for the increase in strength. Together with the 6M $LiOH.H_2O$ concentration, these geopolymer compositions develop the lowest strengths of the four different mixtures. The compressive strength for the 6M $LiOH.H_2O$ samples remains almost constant at a value of 10 MPa. It is also remarkable that the variability of the strong 8M and 10M $LiOH.H_2O$ samples is significantly higher than that of the 6M and 12M samples.

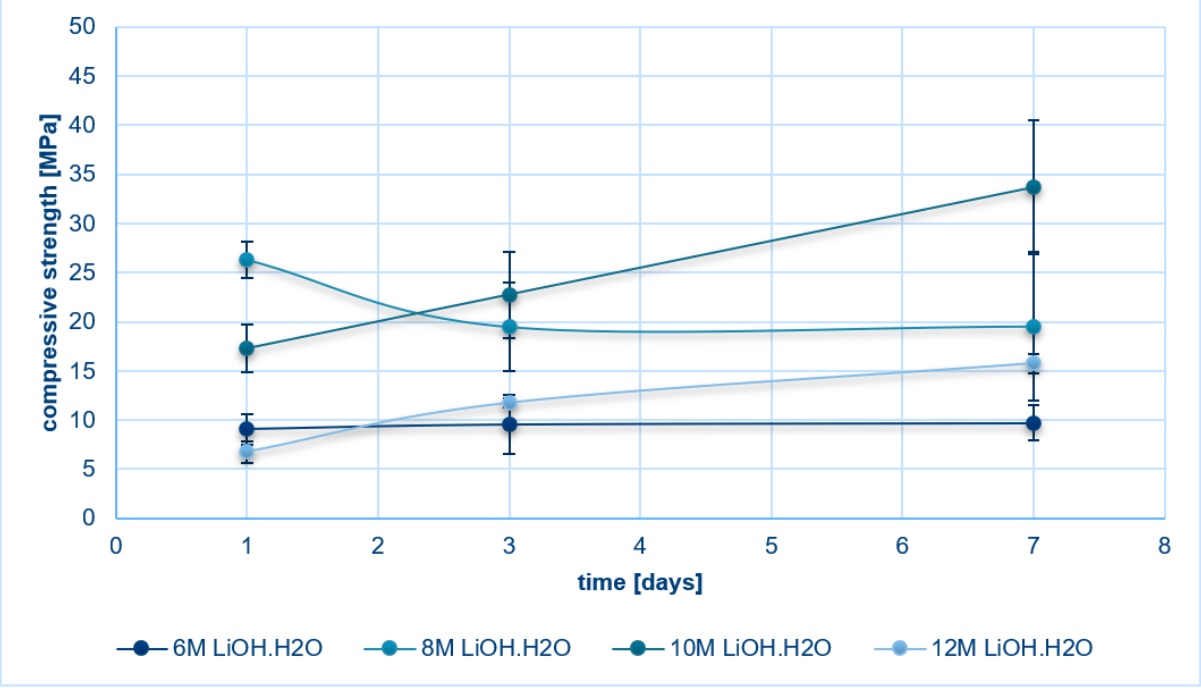

Figure 83: $LiOH.H_2O + 5$ g NaOH-based geopolymers.

Table 8: $LiOH.H_2O + 2.5$ g NaOH-based geopolymers.

sample	$f_{c,1d}$ $[MPa]$	$f_{c,3d}$ $[MPa]$	$f_{c,7d}$ $[MPa]$
6M LiOH.H2O + 2.5g NaOH - 70°C oven cured	**2.92 ± 0.02**	**2.8 ± 0.3**	**4.0 ± 0.3**
8M LiOH.H2O + 2.5g NaOH - 70°C oven cured	**7 ± 1**	**10 ± 1**	**10 ± 3**

The influence of the added concentration of activating $NaOH$ pellets was investigated by initially decreasing the mass of $NaOH$ from 5 g to 2.5 g in the lithium hydroxide solution. As with the results of $LiOH.H_2O + 5$ g $NaOH$-based geopolymers, a significantly higher strength is found for the 8M concentration of the $LiOH.H_2O + 2.5$ g $NaOH$ -based, compared to the lower 6M concentration. This while the compressive strength of the 6M concentration $LiOH.H_2O$ is only 40 % of the strength of the higher 8M concentration samples.

The strength development for both geopolymer mixtures is gradual, with the lower 6M samples mainly developing its strength between 3 days and 7 days of curing. The higher 8M samples mainly develop strength between 1 day and 3 days of curing. In addition, it is also established that the variability on the 8M $LiOH.H_2O$ samples is higher than the 6M samples. It should be mentioned here that the 6M $LiOH.H_2O$ geopolymers show outliers (red values), which makes that the representativeness of the results decreases. Overall, a reduction in compressive strength occurs by decreasing the concentration of $NaOH$. This decrease due to the reduced concentration is estimated at no less than 50 %.

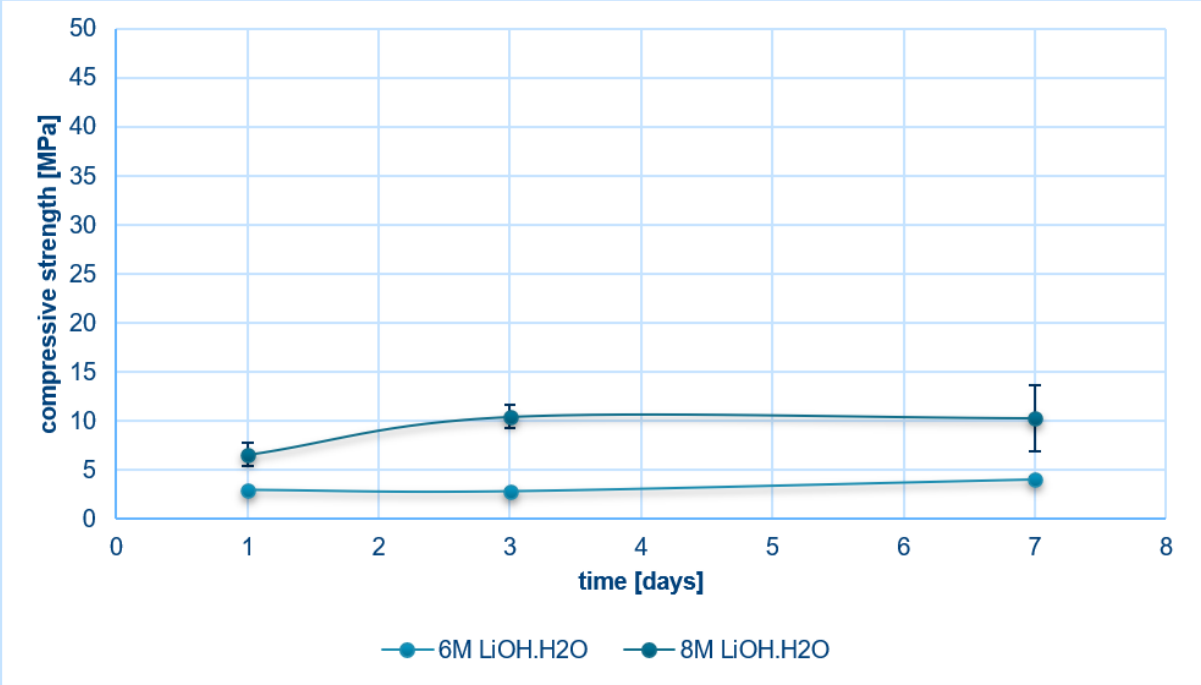

Figure 84: $LiOH.H_2O + 2.5$ g NaOH-based geopolymers.

Table 9: $LiOH.H_2O + 7.5$ g NaOH-based geopolymers.

sample	$f_{c,1d}$ $[MPa]$	$f_{c,3d}$ $[MPa]$	$f_{c,7d}$ $[MPa]$
6M LiOH.H2O + 7.5g NaOH - 70°C oven cured	**20 ± 2**	**28 ± 2**	**22 ± 5**
8M LiOH.H2O + 7.5g NaOH - 70°C oven cured	**4 ± 1**	**6 ± 1**	**23 ± 3**

Because lowering the concentration of $NaOH$ has a negative influence on the ultimate strength development of the geopolymers, the influence of an increase in the concentration of added

$NaOH$ pellets is studied. The next two geopolymer mixtures studied consist of the same concentrations of 6M and 8M $LiOH.H_2O$, but with an increased $NaOH$ concentration by adding 7.5 g $NaOH$ pellets to both geopolymer mixtures. Generally, it should be mentioned that the final compressive strength after 7 days of both geopolymers of 6M and 8M $LiOH.H_2O$ is almost the same, which has a value of 22-23 MPa.

These values for the compressive strengths are higher than the compressive strengths obtained when 5 g $NaOH$ pellets were added to the alkali activator solution. They are not only higher in strength, but they fluctuate in close proximity after curing for 7 days, which was not the case for the $LiOH.H_2O + 5$ g $NaOH$-based geopolymers. There, the compressive strength of the 6M concentration is approximately half the compressive strength of the 8M concentration, while the compressive strengths are almost the same with addition of 7.5 g $NaOH$ pellets to the $LiOH.H_2O$ solution.

The variability on the compressive strength results of the 6M $LiOH.H_2O$ concentration is about half greater than that of the 8M $LiOH.H_2O$ concentration. The strength development between the two concentrations is also completely different. For example, with the 6M $LiOH.H_2O$ concentration, an average compressive strength of 20 MPa is obtained after 1 day of curing, after which it increases to 28 MPa after 3 days, before decreasing again to a value of 22 MPa after 7 days. The increase in strength for the 8M $LiOH.H_2O$ concentration shows a continuously increasing trend as strength is especially developed between 3 days and 7 days of curing.

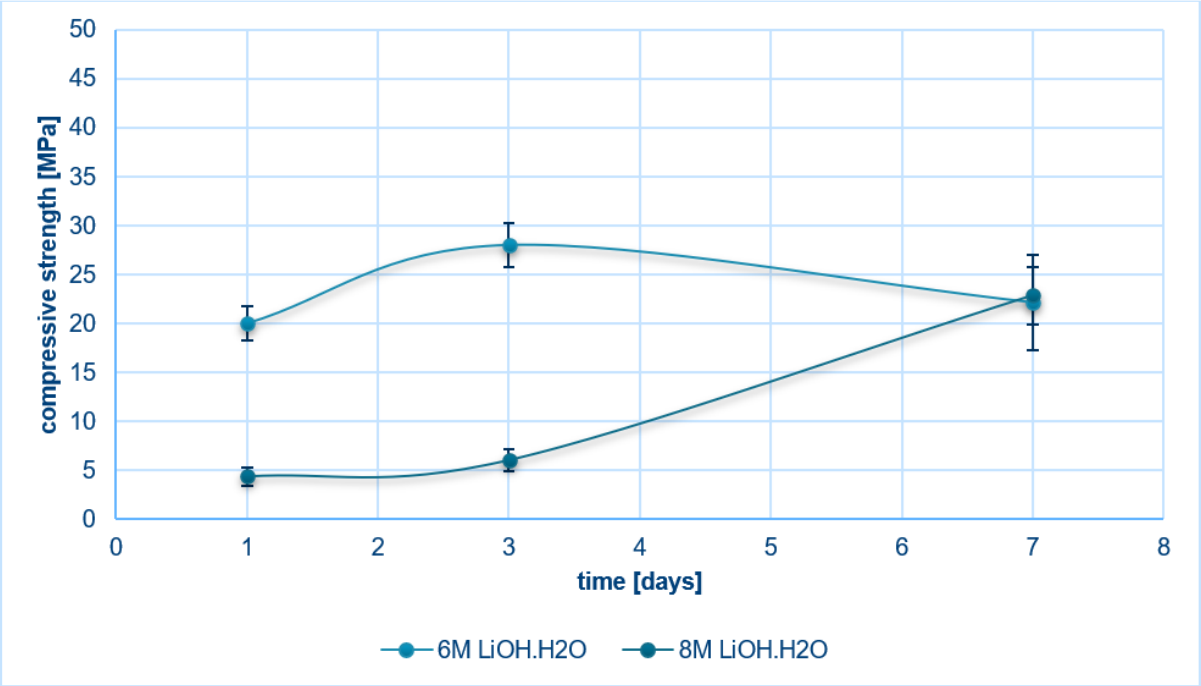

Figure 85: $LiOH.H_2O + 7.5$ g $NaOH$-based geopolymers.

Table 10: $LiOH.H_2O + 5$ g $NaOH$-based geopolymers (28d cured).

sample	$f_{c,1d}$ $[MPa]$	$f_{c,3d}$ $[MPa]$	$f_{c,7d}$ $[MPa]$	$f_{c,28d}$ $[MPa]$
6M LiOH.H2O + 5g NaOH - 70°C oven cured	**9 ± 2**	**10 ± 3**	**10 ± 2**	**25 ± 2**
8M LiOH.H2O + 5g NaOH - 70°C oven cured	**26 ± 2**	**20 ± 4**	**20 ± 8**	**22 ± 3**

The compressive strength results of the well-performing geopolymer formulations are further investigated in long term analysis (curing for 28 days), during the implementation phase of the

research. For this purpose, six similar geopolymer mixtures were prepared in each case, the compressive strength being determined after 28 days. For the low 6M $\mathrm{LiOH.H_2O} + 5\ \mathrm{g\ NaOH}$ concentration geopolymers, a significant increase in compressive strength of the samples was observed between 7 days and 28 days of curing, while for the higher 8M $\mathrm{LiOH.H_2O} + 5\ \mathrm{g\ NaOH}$ concentration only a small increase in strength of only 2 MPa was determined. At the 6M concentration, a geopolymer mixture was even established with a compressive strength of no less than 53 MPa. This high compressive strength was removed from the data set after statistical analysis with prediction intervals because it was cataloged as an outlier.

In general, it can be concluded that the developed strength of the 6M $\mathrm{LiOH.H_2O} + 5\ \mathrm{g\ NaOH}$ concentration samples after 28 days is 14 % higher than the 8M concentration. This can be said with a degree of certainty, as the variability on the results is limited to a maximum of 3 MPa after 28 days. For the 8M concentration, there is especially great uncertainty in the results after curing for 7 days, with a standard deviation of as much as 8 MPa being measured.

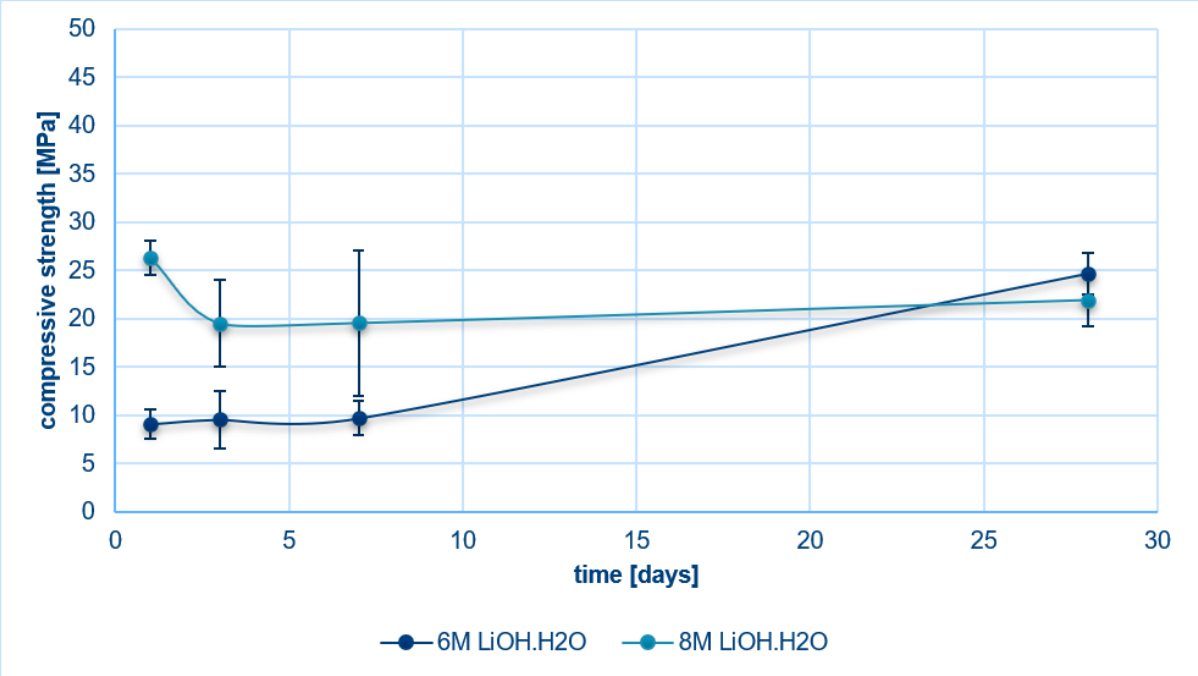

Figure 86: $\mathrm{LiOH.H_2O} + 5\ \mathrm{g\ NaOH}$-based geopolymers (28d cured).

Table 11: Comparison to CEM I 52.5R HES (28d cured).

sample	$f_{c,1d}\ [MPa]$	$f_{c,3d}\ [MPa]$	$f_{c,7d}\ [MPa]$	$f_{c,28d}\ [MPa]$
Holcim CEM I 52.5R HES - 70°C oven cured	**78 ± 4**	**72 ± 11**	**71 ± 2**	**92 ± 8**

In order to make a comparison with the reference material Portland cement, mixtures were also made according to the same liquid/binder ratio of 0.3, as volume ratio. These cement mixtures were subjected to the same curing parameters, both for curing time and temperature. It can soon be concluded that the cement mixtures achieve a considerably higher compressive strength than the geopolymer mixtures.

The variability on the results is also remarkably higher for cement than geopolymers, with a maximum of no less than 11 MPa after curing in the oven for 3 days. The developed strength first decreases gradually as a function of time, with an average strength reduction of 7 MPa after curing for 7 days. After curing for 28 days, an increase in strength is observed again to 92 MPa. This increase in compressive strength is clearly noticeable, but there is an uncertainty

in the results since the variability is no less than 8 MPa. This is also evident from the large error bar, at the data point of the measured compressive strength after 28 days of curing.

When comparing the compressive strengths of the geopolymers and cement relative to each other, on average a 6.8 times higher early (curing for 1 day) strength is achieved for cement, compared to all produced cube geopolymers in this research. After increasing the curing time, this relative difference becomes smaller and smaller. An increase in curing time from 1 day to 28 days, results in a 43 % stronger geopolymer, relatively. This means that geopolymers become relatively stronger compared to classic Portland cement, as the curing time increases.

To calculate the factor for the relative difference in strength between the cement mixtures and geopolymer mixtures after different curing times (1d, 3d, 7d and 28d), the quotient of the compressive strength of the cement and the average compressive strength of the geopolymers is determined. This can be represented symbolically by: $\Delta f_{c,x\ days} = \frac{f_{c,cement}}{f_{c,geopolymer,mean}}$

- Difference in early stage strength development - after <u>1 day</u>: cement **6.84x** stronger

$$\Delta f_{c,1\ day} = \frac{78\ MPa}{(8+5+7.4+9+26+17+7+2.92+7+20+4+9+26)\ MPa/13}$$

- Difference in early stage strength development - after <u>3 days</u>: cement **5.48x** stronger

$$\Delta f_{c,3\ days} = \frac{72\ MPa}{(16+6+7+10+20+23+11.7+2.8+10+28+6+10+20)\ MPa/13}$$

- Difference in early stage strength development - after <u>7 days</u>: cement **4.73x** stronger

$$\Delta f_{c,7\ days} = \frac{71\ MPa}{(11+7+8+10+20+34+16+4.0+10+22+23+10+20)\ MPa/13}$$

- Difference in late stage strength development - after <u>28 days</u>: cement **3.91x** stronger

$$\Delta f_{c,28\ days} = \frac{92\ MPa}{(25+22)\ MPa/2}$$

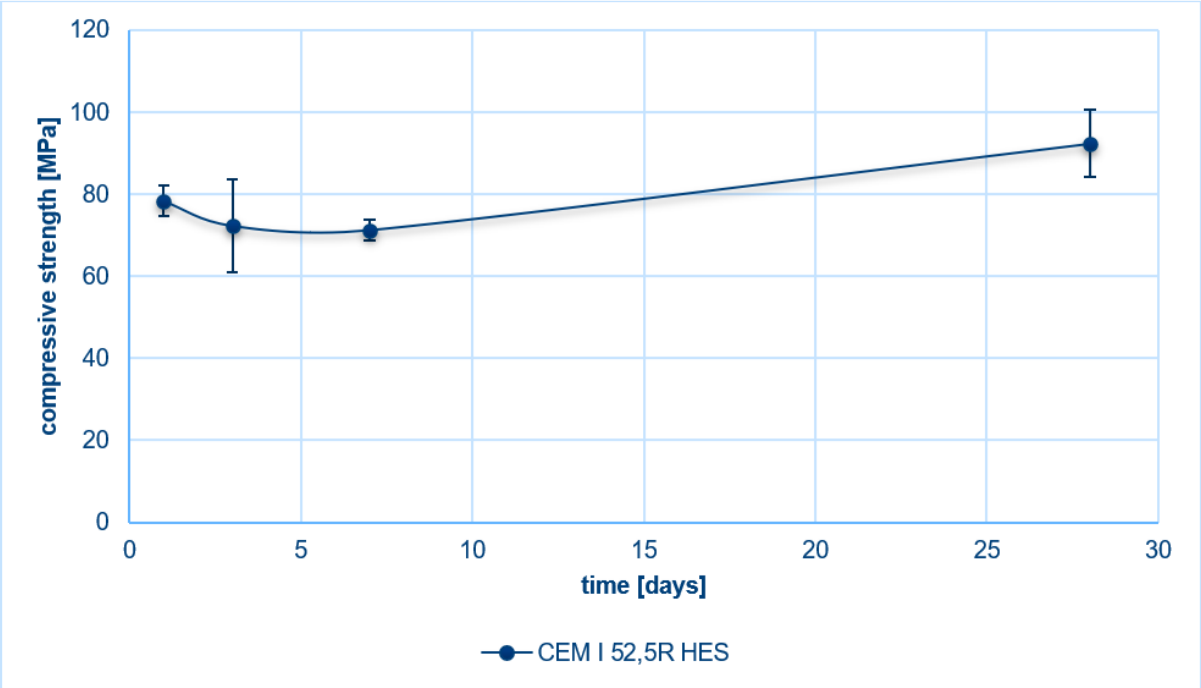

Figure 87: Comparison to CEM I 52.5R HES (28d cured).

5.2.2 Cylindrical samples

Table 12: $NaOH$-based geopolymers (28d cured).

sample	$f_{c,1d}\ [MPa]$	$f_{c,3d}\ [MPa]$	$f_{c,7d}\ [MPa]$	$f_{c,28d}\ [MPa]$
8M NaOH - 70°C oven cured	4	3.62 ± 0.01	4.0 ± 0.4	6 ± 3

By using the pellet press for the production of the cylindrical geopolymers, the results are expected to be more accurate. The reason for this is that the compaction can take place in a more controlled manner. Initially, the $NaOH$-based geopolymers are investigated for their strength development over time. The results show that a low average compressive strength of 6 MPa is achieved after curing for 28 days. The cylindrical sample compressive strength value of 4 MPa, obtained after 7 days is only 36 % of the compressive strength obtained with the cube geopolymer samples.

A slightly increasing trend is observed in the strength development profile, but in absolute terms the compressive strength of the 8 M $NaOH$ sample remains almost constant. As a result, it can be concluded that the compressive strength for this cylindrical geopolymer mixture is independent of curing time. In addition, there is a large degree of uncertainty in these results, due to the outliers in the data set after 1 day, 3 days and 28 days. For the compressive strength value after 1 day of curing, only one compressive strength value of 4 MPa could be maintained, since the other two compressive strength values were considered as outliers.

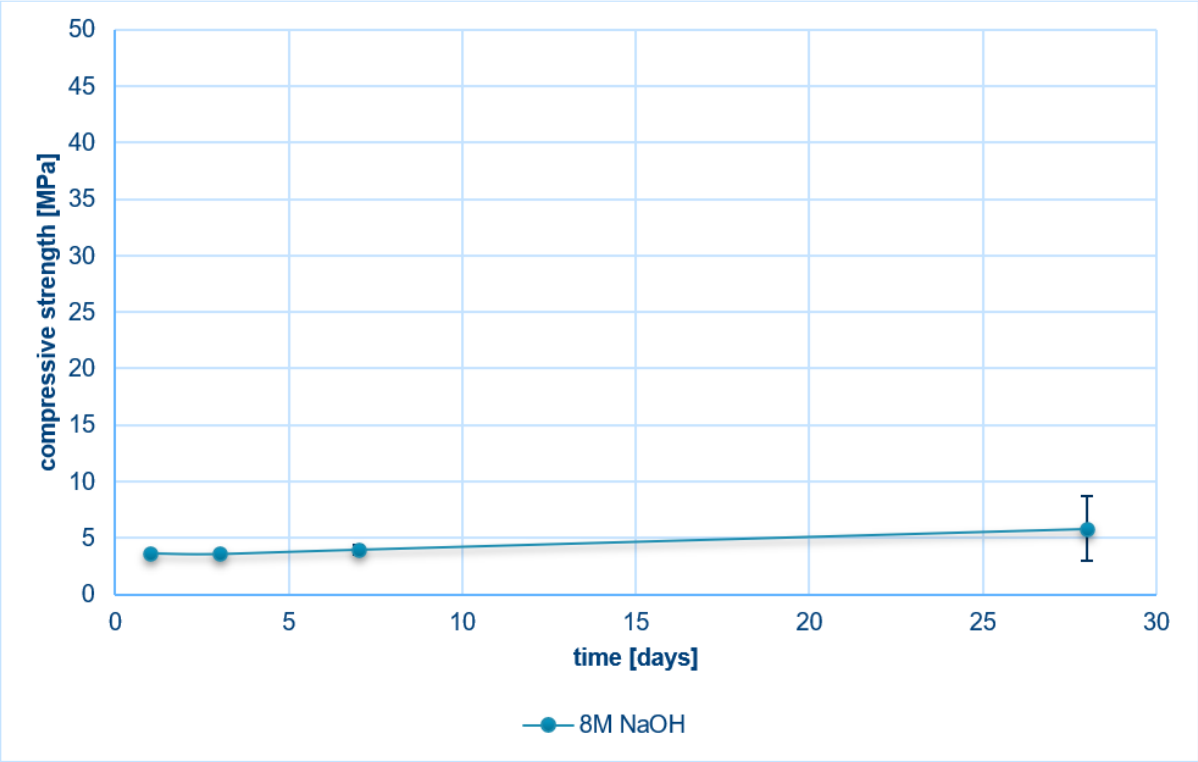

Figure 88: $NaOH$-based geopolymers (28d cured).

Table 13: $LiOH.H_2O + 5$ g $NaOH$-based geopolymers.

sample	$f_{c,1d}\ [MPa]$	$f_{c,3d}\ [MPa]$	$f_{c,7d}\ [MPa]$	$f_{c,28d}\ [MPa]$
6M LiOH.H2O + 5g NaOH - 70°C oven cured	18 ± 1	32.0 ± 0.3	33 ± 2	25 ± 7
8M LiOH.H2O + 5g NaOH - 70°C oven cured	18 ± 1	23 ± 5	25 ± 4	21 ± 4

It was rapidly established, during the exploration phase of this research with the cube

geopolymer mixtures, that the $LiOH.H_2O$-based geopolymers showed a better strength development than the $NaOH$-based geopolymers. Therefore, the decision was taken to make the cylindrical geopolymer mixtures mainly with $LiOH.H_2O$ as alkali activator. For both the 6M and 8M $LiOH.H_2O + 5\ g\ NaOH$-based geopolymers, the evolution of the compressive strength was studied after 1 day, 3 days, 7 days and 28 days curing in the oven at 70 °C.

Both geopolymer mixtures develop the same compressive strength in the initial stage of curing. A compressive strength of 18 MPa is reached for both concentrations of $LiOH.H_2O$. Between 1 day and 3 days of curing, the largest jump in strength development is observed for both mixtures. After 3 days of curing, the strength increases slightly to 7 days of curing, the increase being only 1-2 MPa. When the geopolymers are further cured up to 28 days, a strong reduction in compressive strength is observed for both concentrations.

The 6M samples show the best average compressive strength after 28 days, with a value of 25 MPa. The trend of the compressive strength as a function of time is the same for both 6M and 8M samples. Compared to the evolution of compressive strength over time for the cube geopolymers with the same compositions, the 8M sample shows approximately the same trend for the compressive strength. The 6M sample shows a significantly better compression strength gradient for the cylindrical geopolymers than the cube geopolymers. With the cylindrical 6M $LiOH.H_2O + 5\ g\ NaOH$-based geopolymers, a compressive strength of a factor 3.3 times higher is registered than with the cube geopolymers of the same chemical composition.

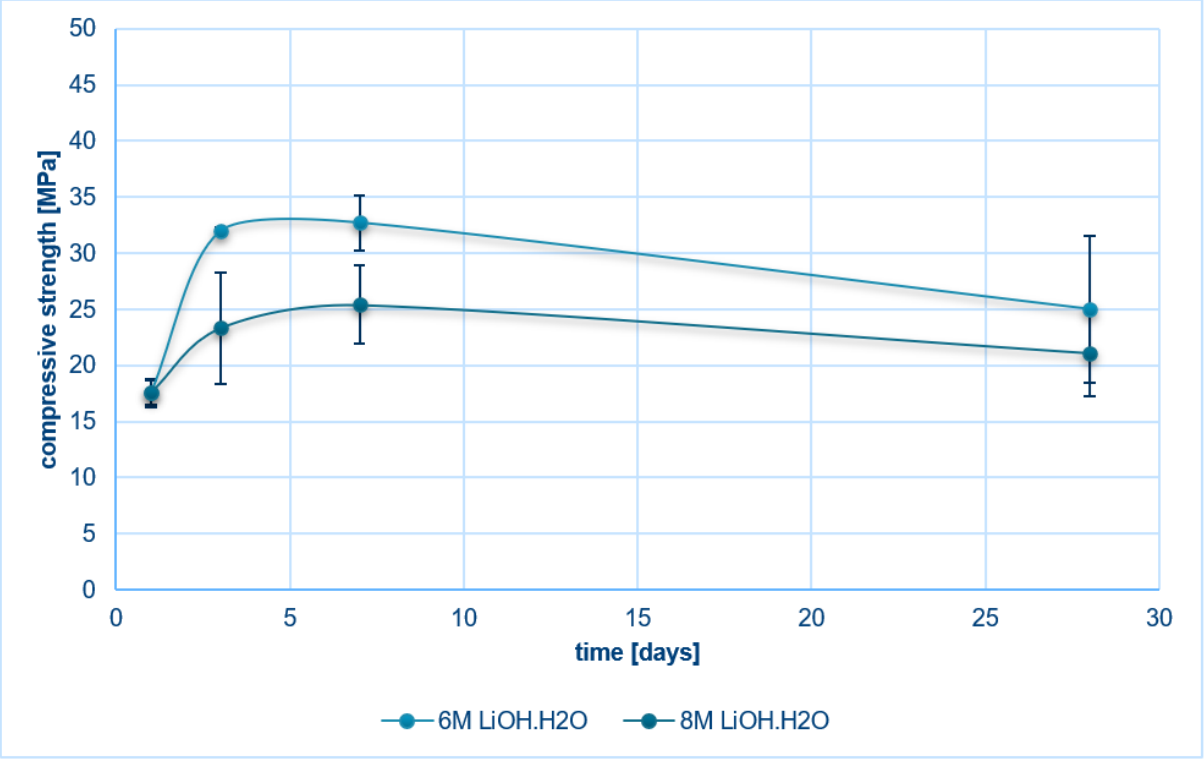

Figure 89: $LiOH.H_2O + 5\ g\ NaOH$-based geopolymers.

Table 14: $LiOH.H_2O + 2.5\ g\ NaOH$-based geopolymers.

sample	$f_{c,1d}\ [MPa]$	$f_{c,3d}\ [MPa]$	$f_{c,7d}\ [MPa]$
6M LiOH.H2O + 2.5g NaOH - 70°C oven cured	**4.2 ± 0.6**	**7 ± 1**	**11 ± 1**
8M LiOH.H2O + 2.5g NaOH - 70°C oven cured	**18 ± 3**	**28 ± 4**	**24 ± 2**

The reduction in concentration of the $NaOH$ pellets by decreasing the amount of added mass from 5 g to 2.5 g in the lithium hydroxide solution has a negative effect on the strength development for the 6M $LiOH.H_2O$ samples. On the other hand, the reduction of the sodium hydroxide concentration has a positive effect on the strength development of the higher 8M $LiOH.H_2O$ concentration samples.

The compressive strength for the 6M concentration sample increases almost linearly with time, with a small gradient. Thus, the evolution of the strength is gradual for this geopolymer composition, with a final mean compressive strength of 11 MPa after 7 days of curing. This variation in compressive strength is 2.8 times as strong as the variation in compressive strength for cube geopolymers with the same composition.

In addition, the 8M samples show a significantly better progress of increase in compressive strength than the lower 6M concentration samples. Initially a compressive strength of 18 MPa has developed after curing for 1 day. Between 1 day and 3 days of curing, a strong increase in compressive strength of 10 MPa occurs, resulting in a mean compressive strength value of 28 MPa after 3 days. The compressive strength of the cylindrical geopolymers is 2.8 times greater than that of the cube geopolymers after curing for 3 days. Subsequently, a slight decrease of 4 MPa occurs between the 3 day and 7 day curing. This decrease was also observed in the evolution of the compressive strength of the $LiOH.H_2O + 5\ g\ NaOH$-based geopolymers.

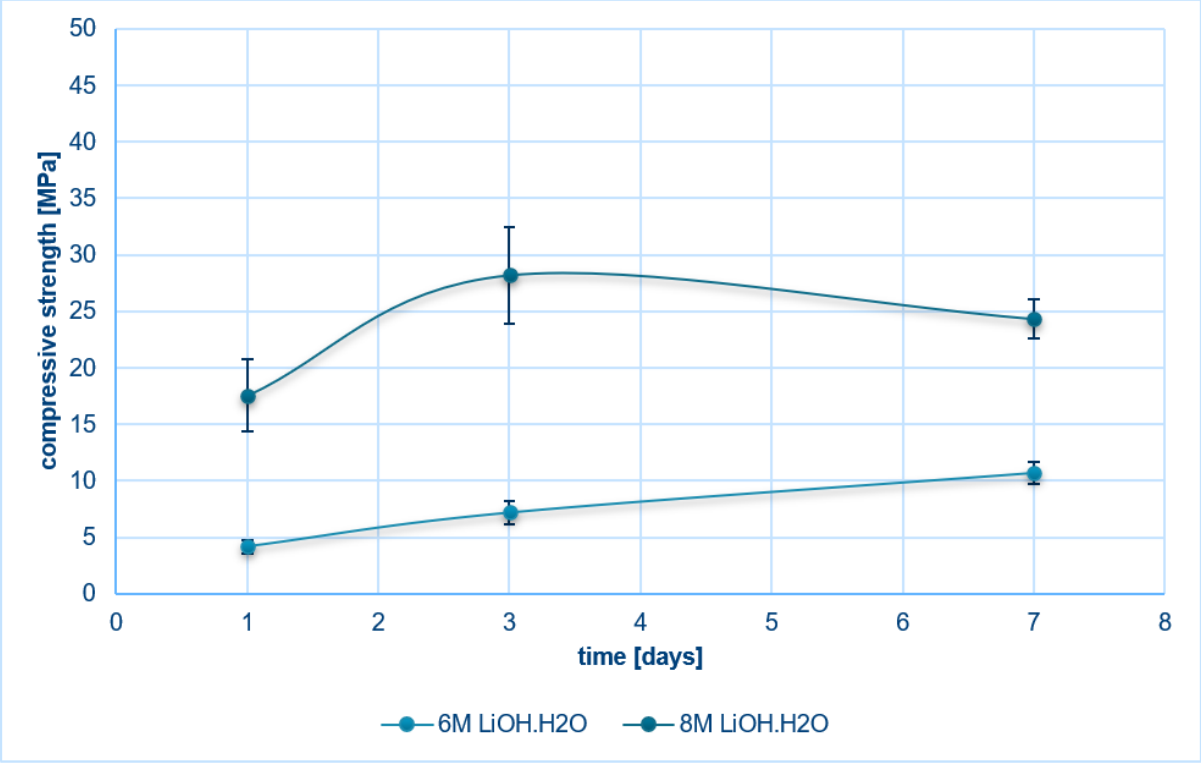

Figure 90: $LiOH.H_2O + 2.5\ g\ NaOH$-based geopolymers.

Table 15: $LiOH.H_2O + 7.5\ g\ NaOH$-based geopolymers.

sample	$f_{c,1d}\ [MPa]$	$f_{c,3d}\ [MPa]$	$f_{c,7d}\ [MPa]$
6M LiOH.H2O + 7.5g NaOH - 70°C oven cured	**11 ± 2**	**21 ± 2**	**27 ± 5**
8M LiOH.H2O + 7.5g NaOH - 70°C oven cured	**19.7 ± 0.2**	**29 ± 1**	**30 ± 2**

By increasing the concentration of the $NaOH$ pellets in the lithium hydroxide solution, a strong evolution of the strength over time is observed for both the 6M and 8M $LiOH.H_2O + 7.5\ g\ NaOH$-based geopolymers. In general, the strength development of the higher 8M concentration samples is the best, with a compressive strength of 30 MPa after curing for 7 days. The lower 6M concentration samples show almost the same evolution of strength development, with a compressive strength of 27 MPa being obtained after 7 days.

The strength development for both concentrations has a parabolic shape as a function of time. A small variability can also be established for the 8M concentration, with a maximum of 2 MPa. In addition, the lower 6M concentration samples show a higher variability over time, with a maximum value of 5 MPa.

Compared to the cube geopolymers with the same composition, a better strength development is obtained after 1 day and 3 days for the 8M concentration. Even after curing for 7 days, a higher compressive strength is obtained for both the 6M and 8M concentrations, compared to the cube geopolymers. On average, a 26 % higher compressive strength is obtained compared to the cube geopolymers. Moreover, compared to all previous geopolymers, these geopolymer compositions finally achieve the highest compressive strengths.

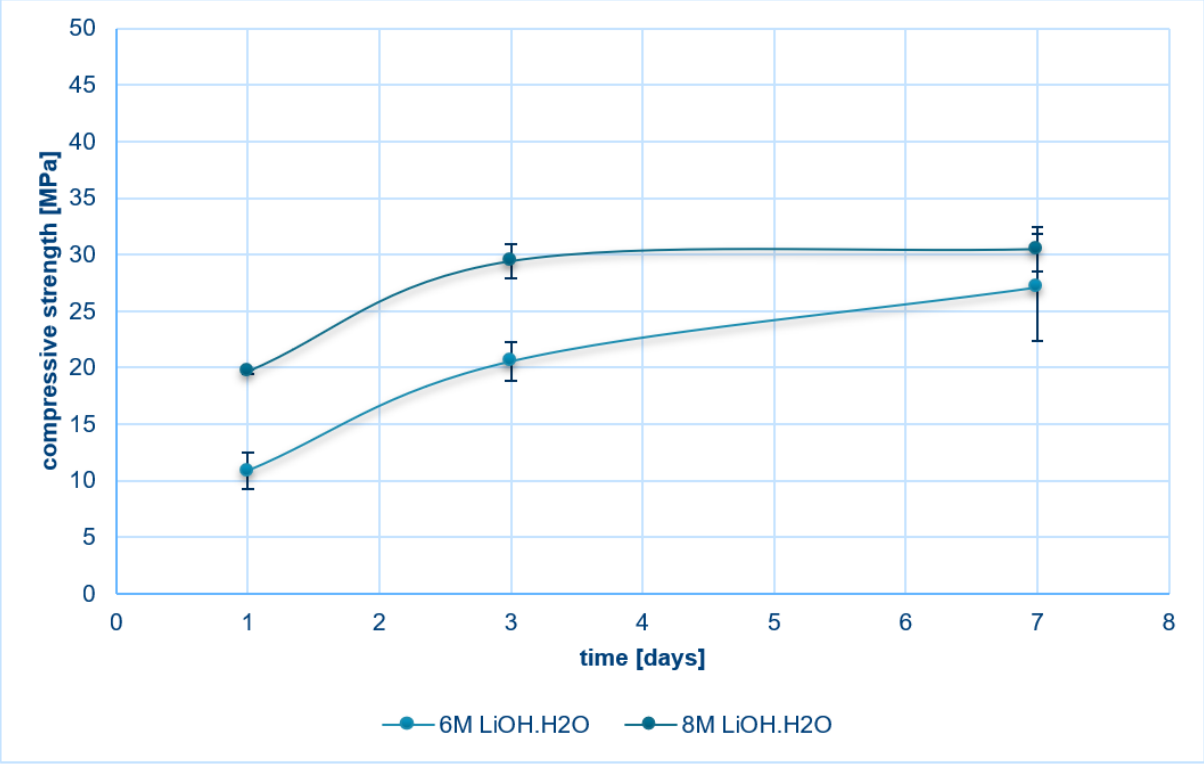

Figure 91: $LiOH.H_2O + 7.5\ g\ NaOH$-based geopolymers.

5.3 FTIR analysis

The chemical characterisation of the different geopolymer mixtures is done by the analysis of the FTIR spectra. Initially, the FTIR spectra of the geopolymer precursors, metakaolin and MGS-1, are discussed. Subsequently, the different geopolymer mixtures are studied by the FTIR analysis, starting with the cube geopolymers and ending with the cylindrical geopolymers. When analysing the different FTIR spectra, it is mainly important to characterise the different materials as a function of the peaks occurring in the wavelength spectrum (Wang *et al*., 2005).

5.3.1 Metakaolin

Metakaolin is used as an additive for MGS-1 during geopolymerisation. The major peak in the amount of transmission is determined at wavelength of 1046 cm^{-1}. This wavelength represents the $\mathrm{Si}-\mathrm{O}$ stretching vibrations. The broad adsorption bands on the IR spectrum at 793 cm^{-1} and 567 cm^{-1} refer to $\mathrm{Si}-\mathrm{O}-\mathrm{Al}$ vibrations and flexural vibrations, respectively.

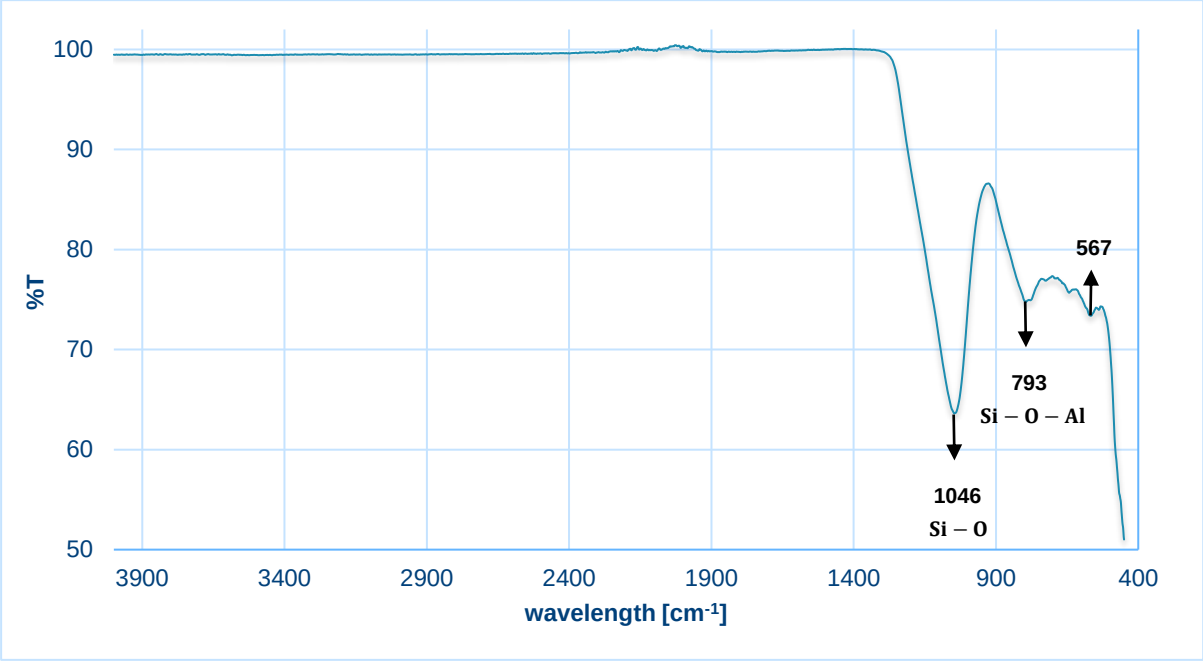

Figure 92: FTIR spectrum of metakaolin.

5.3.2 MGS-1

Since the simulated Mars raw regolith material MGS-1 is an aluminosilicate precursor, a similar strong peak to metakaolin is observed at wavelength of 1000 cm^{-1}. This wavelength refers to $\mathrm{Si}-\mathrm{O}-\mathrm{Al}$ asymmetric stretching vibrations within TO_4 tetrahedra typical of the amorphous

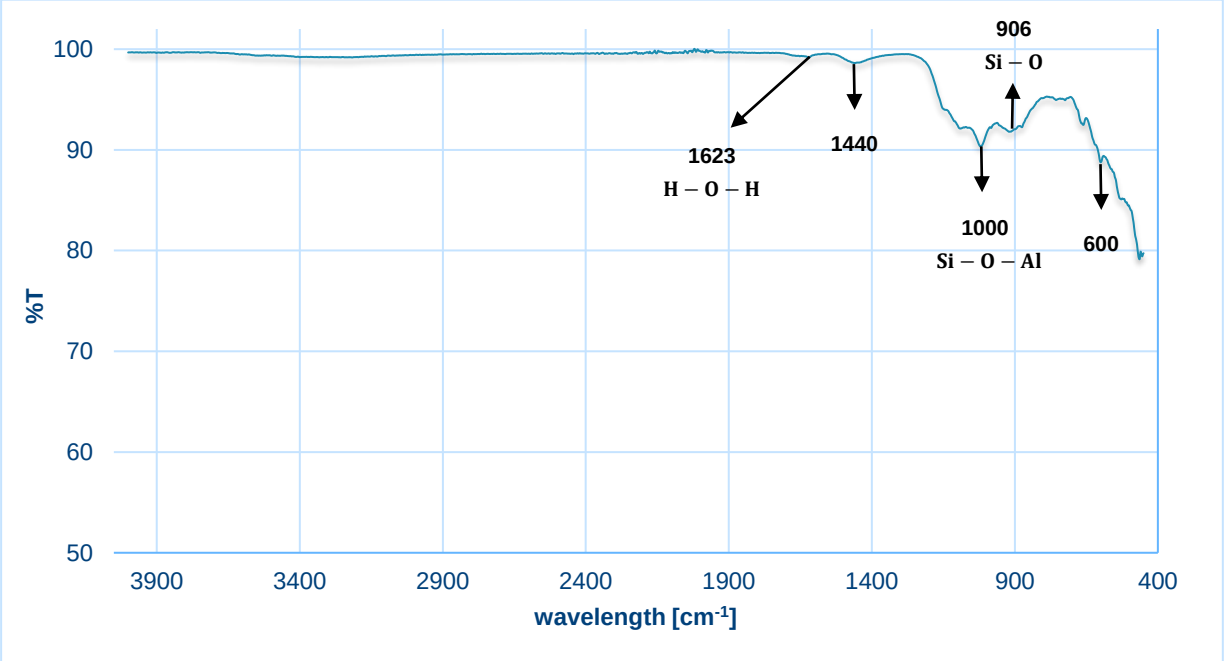

Figure 93: FTIR spectrum of MGS-1.

aluminosilicates. The adsorption band at 1623 cm^{-1} refers to the bending vibrations of $H-O-H$. The peak at wavelength of 1440 cm^{-1} indicates atmospheric carbonation. Finally, the peak at 906 cm^{-1} refers to the symmetric $Si-O$ bonds. As the amount of transmission decreases at low wavelengths, small peaks are observed at wavelength of 600 cm^{-1}. These peaks indicate the presence of silicates and aluminosilicate glasses in the raw MGS-1 regolith material.

5.3.3 Cube samples

The $NaOH$-based geopolymers show almost the same pattern for the three different concentrations of 8M, 10M and 12M $NaOH$. A total of four different peaks can be observed in the FTIR diagram. The broad adsorption band at around 3342 cm^{-1} represent stretching vibrations of $-OH$ groups and water molecules. The next peak is observed at a wavelength of 1640 cm^{-1}, which can be assigned to the bending vibrations of $H-O-H$.

The peak at 1440 cm^{-1} corresponds to $C-O$ stretching vibrations from carbonate. Finally, the peak observed at 970 cm^{-1} represents the $Si-O-Si$ asymmetric stretching vibrations.

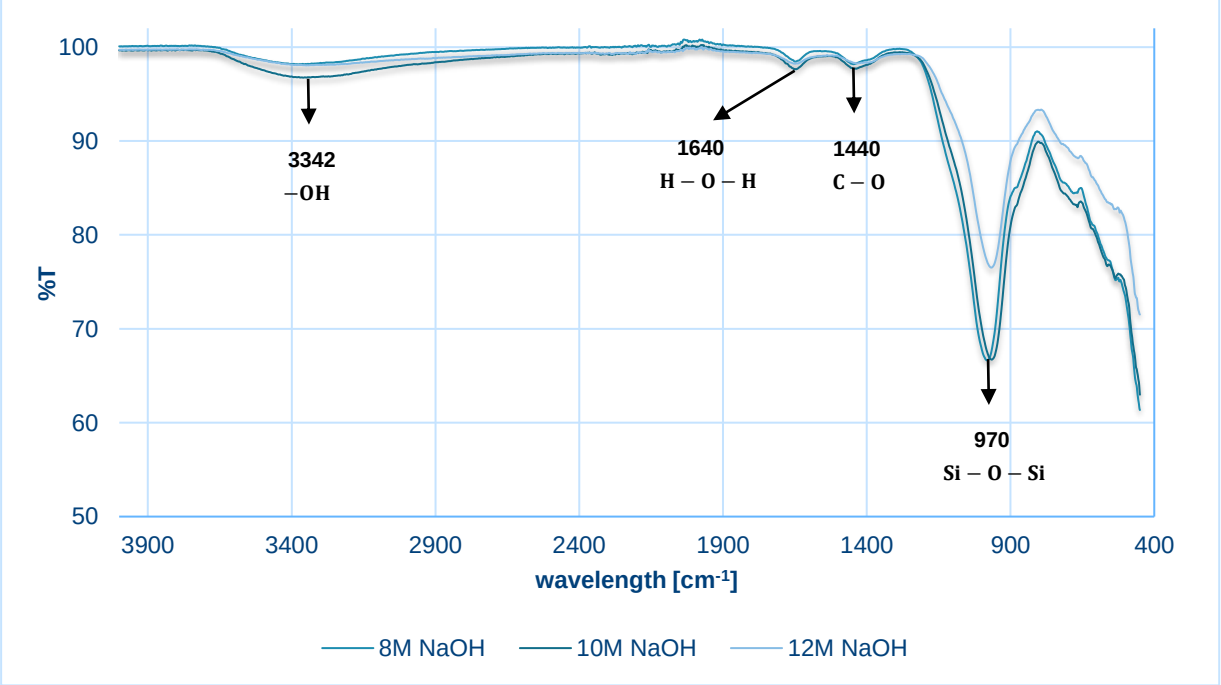

Figure 94: FTIR spectrum of $NaOH$-based geopolymers (1d cured).

During the geopolymerisation, the aluminosilicate rich precursors MGS-1 and metakaolin are converted into a geopolymer gel. There are clear differences in the FTIR spectrum before (Figure 92 and Figure 93) and after (Figure 94) the geopolymerisation. The shifting of the main band of 1000 cm^{-1} to smaller wavelengths suggests the silica solubilisation and polycondensation processes (Montes *et al*., 2015). This transformation in the wavelength spectrum is typical for geopolymerisation.

Moreover, the disappearance of the bands at around 600 cm^{-1} points out the consumption of silicates or aluminosilicates glasses (Lee & Van Deventer, 2003). During the process of geopolymerisation, the band at 3342 cm^{-1} is created due to the stretching vibrations of $-OH$ groups. This band is created during the formation of geopolymer gel (Arioz *et al*., 2013).

In the $\mathrm{LiOH.H_2O + 5\ g\ NaOH}$-based geopolymers, peaks are observed at wavelengths of 3379 $\mathrm{cm^{-1}}$, 1648 $\mathrm{cm^{-1}}$ and 977 $\mathrm{cm^{-1}}$. These observed peaks for the $\mathrm{LiOH.H_2O + 5\ g\ NaOH}$-based geopolymer mixtures are related to stretching vibrations of $-\mathrm{OH}$ groups and water molecules, bending vibrations of $\mathrm{H-O-H}$ and $\mathrm{Si-O-Si}$ asymmetric stretching vibrations, respectively. Only little shifts in wavelengths are found for this geopolymer composition, compared to the NaOH-based geopolymers.

The biggest difference in the FTIR spectrum between the NaOH-based geopolymers and $\mathrm{LiOH.H_2O + 5\ g\ NaOH}$-based geopolymers is the less pronounced peak at a wavelength of 1417 $\mathrm{cm^{-1}}$. This indicates that the $\mathrm{C-O}$ stretching vibrations from carbonate are present to a lesser extent with LiOH. This implies that the $\mathrm{LiOH.H_2O + 5\ g\ NaOH}$-based geopolymers have a shorter setting time and higher porosity (Wan-En et al., 2020). As a result, the durability of NaOH-based geopolymers is expected to be better than that of $\mathrm{LiOH.H_2O + 5\ g\ NaOH}$-based geopolymers. In addition, due to the shorter setting time of the $\mathrm{LiOH.H_2O + 5\ g\ NaOH}$-based geopolymers, a higher early strength is expected compared to the NaOH-based geopolymers.

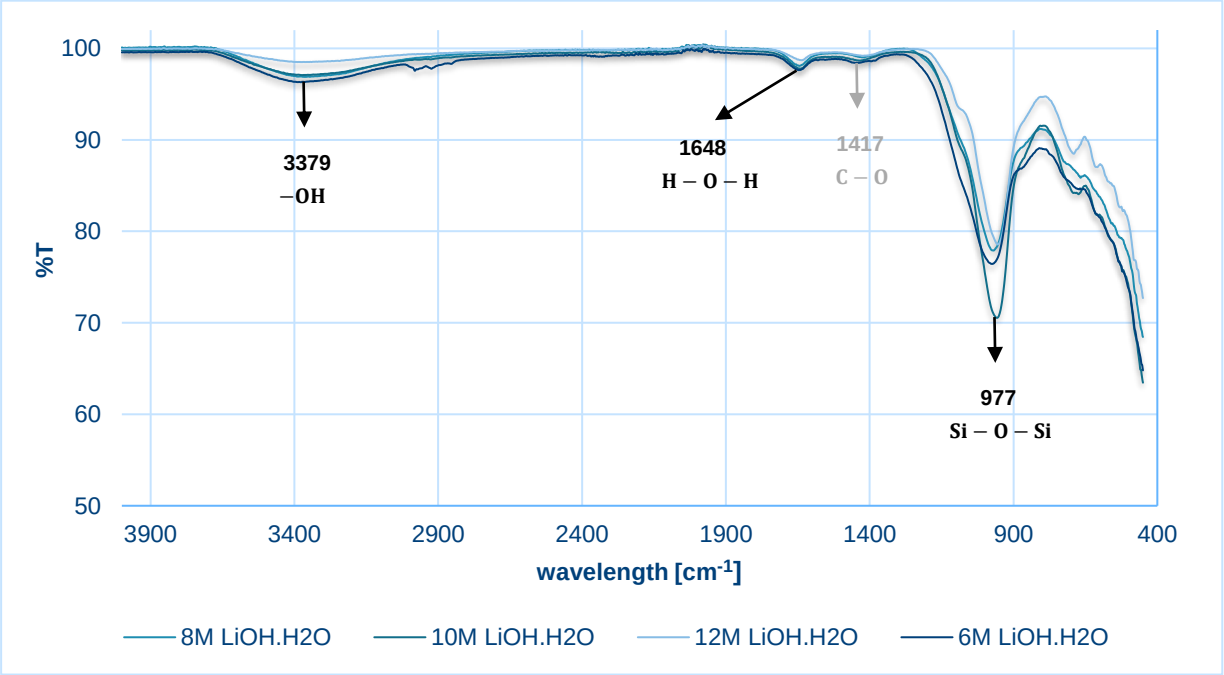

Figure 95: FTIR spectrum of $\mathrm{LiOH.H_2O + 5\ g\ NaOH}$-based geopolymers (1d cured).

For both the $\mathrm{LiOH.H_2O + 2.5\ g\ NaOH}$-based geopolymers and $\mathrm{LiOH.H_2O + 7.5\ g\ NaOH}$-based geopolymers, three nearly the same peaks are observed. For the $\mathrm{LiOH.H_2O + 2.5\ g\ NaOH}$-based geopolymers, strong peaks are detected at wavelengths of 3340 $\mathrm{cm^{-1}}$, 1635 $\mathrm{cm^{-1}}$ and 972 $\mathrm{cm^{-1}}$. These observed peaks for the $\mathrm{LiOH.H_2O + 2.5\ g\ NaOH}$-based geopolymer mixtures are related to stretching vibrations of $-\mathrm{OH}$ groups and water molecules, bending vibrations of $\mathrm{H-O-H}$ and $\mathrm{Si-O-Si}$ asymmetric stretching vibrations, respectively.

The difference between the FTIR spectra of $\mathrm{LiOH.H_2O + 2.5\ g\ NaOH}$-based geopolymers and $\mathrm{LiOH.H_2O + 7.5\ g\ NaOH}$-based geopolymers is noticeable at the adsorption band of 1416 $\mathrm{cm^{-1}}$. A clear peak can be noted here with the $\mathrm{LiOH.H_2O + 2.5\ g\ NaOH}$-based geopolymers. This peak indicates the $\mathrm{C-O}$ stretching vibrations from carbonate in the geopolymer matrix. The general lower transmittance for $\mathrm{LiOH.H_2O + 2.5\ g\ NaOH}$-based geopolymers means that there is a high population of bonds which have vibrational energies to the incident light (Nahm, 2015). From Figure 96, this means that there are more $-\mathrm{OH}$ groups and $\mathrm{Si-O-Si}$ bonds present in

the lower 6M $LiOH.H_2O + 2.5\ g\ NaOH$-based geopolymers than the higher 8M $LiOH.H_2O + 2.5\ g\ NaOH$-based geopolymers.

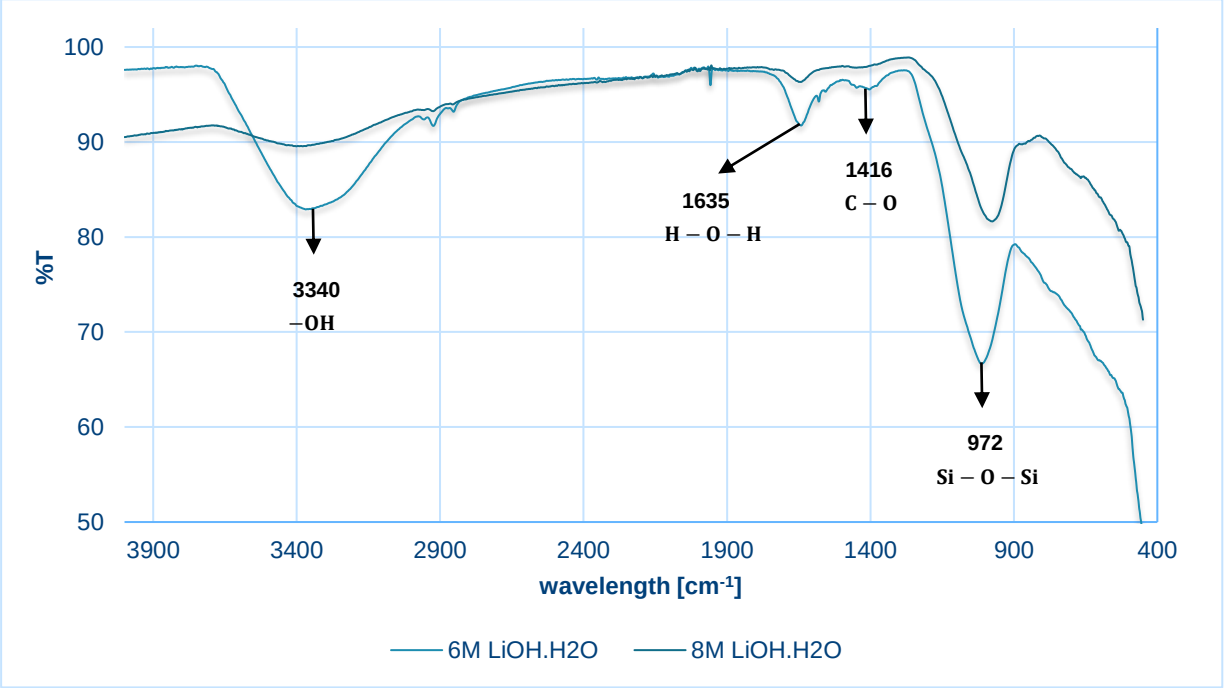

Figure 96: FTIR spectrum of $LiOH.H_2O + 2.5\ g\ NaOH$-based geopolymers (1d cured).

The peaks at wavelength of 3352 cm^{-1} and 1627 cm^{-1} represent vibration of $-OH$ groups and water molecules, while the peak at 972 cm^{-1} corresponds to the $Si-O-Si$ asymmetric stretching vibrations. Similar to the $LiOH.H_2O + 5\ g\ NaOH$ -based geopolymers, there is registered a lower amount of transmittance than the $LiOH.H_2O + 2.5\ g\ NaOH$ -based geopolymers. From this observation, it can be concluded that the 6M $LiOH.H_2O + 2.5\ g\ NaOH$-based geopolymers possess the largest amount of $-OH$ groups and $Si-O-Si$ bonds of all studied $LiOH.H_2O$-based geopolymers, since the most IR light is adsorbed for that case.

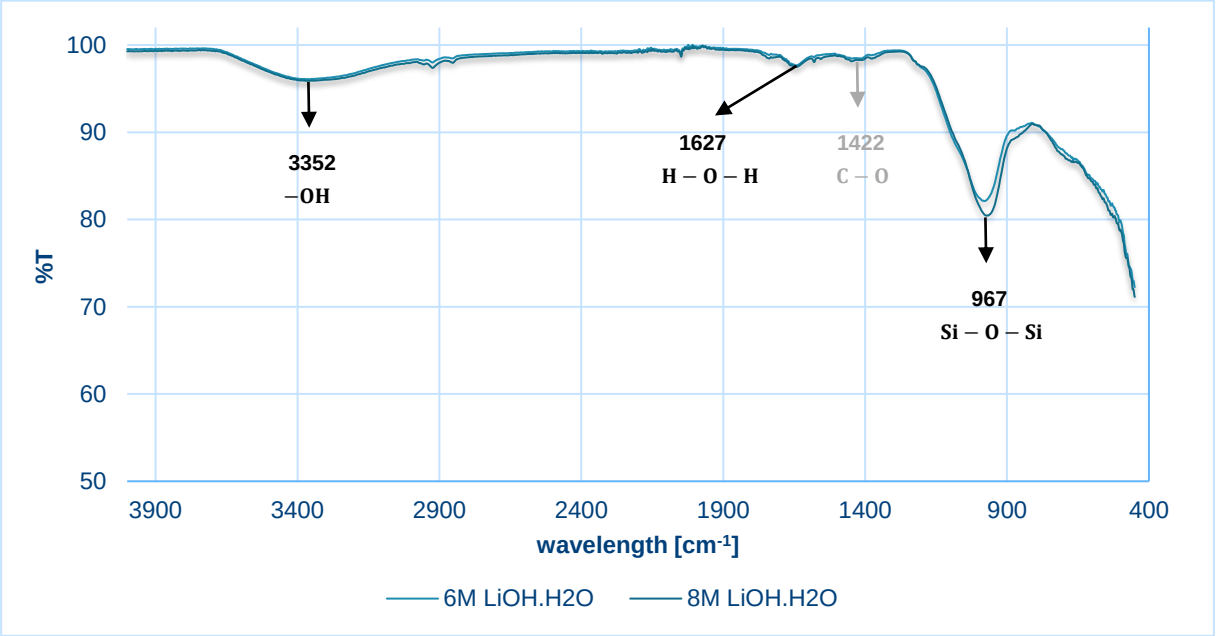

Figure 97: FTIR spectrum of $LiOH.H_2O + 7.5\ g\ NaOH$-based geopolymers (1d cured).

A different FTIR spectrum is obtained for the cube mixtures based on Portland cement. The peaks at the high low wavelengths are less pronounced for cement than they were for geopolymers. For these Portland cement mixtures peaks are observed at wavelengths of 3632 cm^{-1}, 2966 cm^{-1}, 1739 cm^{-1}, 1366 cm^{-1}, 1217 cm^{-1} and 951 cm^{-1}. These peaks are indicated in Figure 98.

The first peak at wavelength of 3632 cm^{-1} correspond to CH, which is formed as silicate phases in the hydrated cement (Yaseen *et al*., 2019). The peak at 2966 cm^{-1} falls in the range of 2900-3400 cm^{-1}, correspond to the $\mathrm{O-H}$ stretching vibrations in the water molecules. The water band peak is located at 1739 cm^{-1}. This peak indicates the $\mathrm{H-O-H}$ bending vibrations of the adsorbed water molecules. The peak at 1366 cm^{-1} refer to asymmetric stretching. This gives rise to a sharp and broad IR peak.

The last two peaks are located at 1217 cm^{-1} and 951 cm^{-1}. The weak band at wavelength of 1217 cm^{-1} corresponds to SO_4^{2-} vibration in sulphates. Furthermore, the peak at 951 cm^{-1} corresponds to asymmetric $\mathrm{Si-O}$ stretching vibrations. This indicates limited polymerisation in $\mathrm{C-S-H}$.

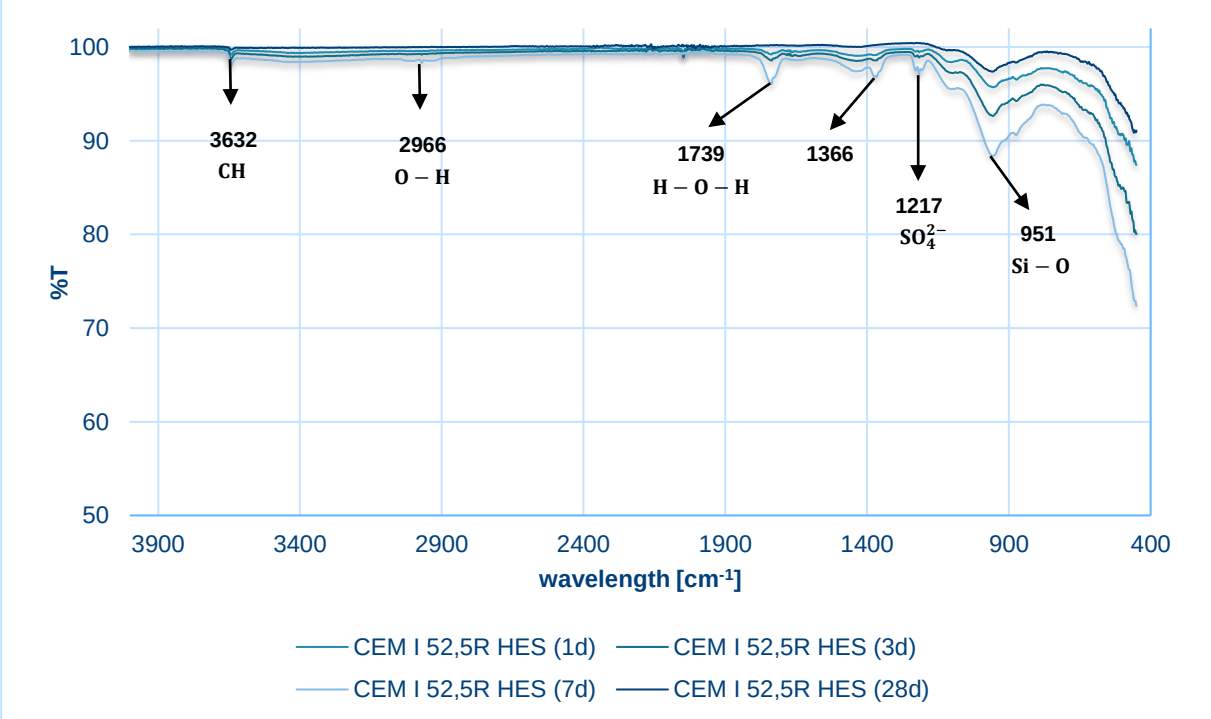

Figure 98: FTIR spectrum of CEM I 52.5R HES (1d, 3d, 7d and 28d cured).

The main difference between the cement mixtures and geopolymer mixtures is the number of adsorbed IR wavelengths. The cement mixtures adsorb certain wavelengths to a greater extent, where geopolymers do not exhibit these bonds. Due to the higher number of bonds present in cement, it is expected that it will also achieve the greatest compressive strength, compared to the geopolymers. Especially the bonds in the range of 900-1400 cm^{-1} determine the ultimate strength. This is because the bonds of the active components of the cement and geopolymers can be found here. For cement, the main components in this range are calcium, silicon, aluminium and iron. For geopolymers, the main components contain traces of aluminosilicate minerals. Geopolymers are mainly known for their high early strength, low shrinkage and sulphate resistance (Davidovits, 1994). This is because the SiO_2 and $\mathrm{Al}_2\mathrm{O}_3$ components in geopolymers exhibit better durability properties than $\mathrm{Ca(OH)}_2$ in cement.

5.3.4 Cylindrical samples

The cylindrical geopolymers are in turn subjected to an FTIR analysis. After it has been derived from the cube geopolymers that each time three or four peaks form at approximately the same wavelengths, an analogous analysis can be performed for the cylindrical geopolymers. Both the $NaOH$-based geopolymers and $LiOH.H_2O + 5\ g\ NaOH$-based geopolymers exhibit almost the same behaviour as the cube geopolymers, when subjected to an FTIR analysis. As presented in Figure 99 and Figure 100, only small shifts in wavelength occur, compared to the cube geopolymers of the same composition.

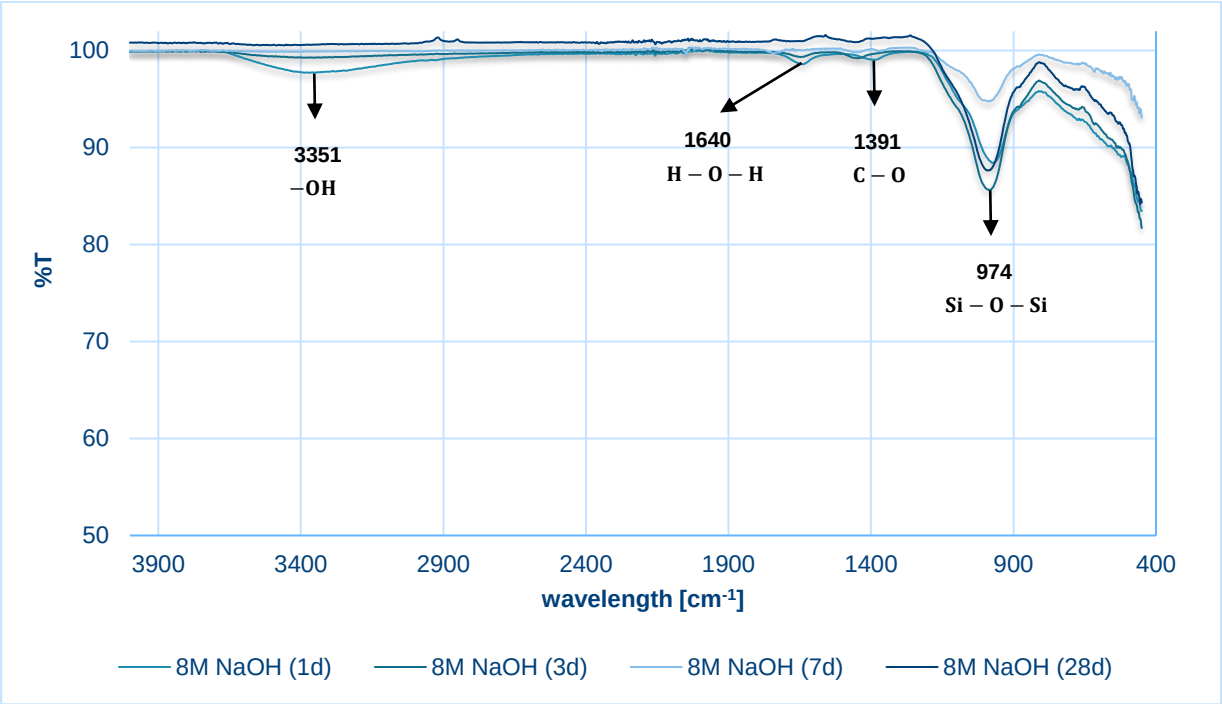

Figure 99: FTIR spectrum of $NaOH$-based geopolymers (1d, 3d, 7d and 28d cured).

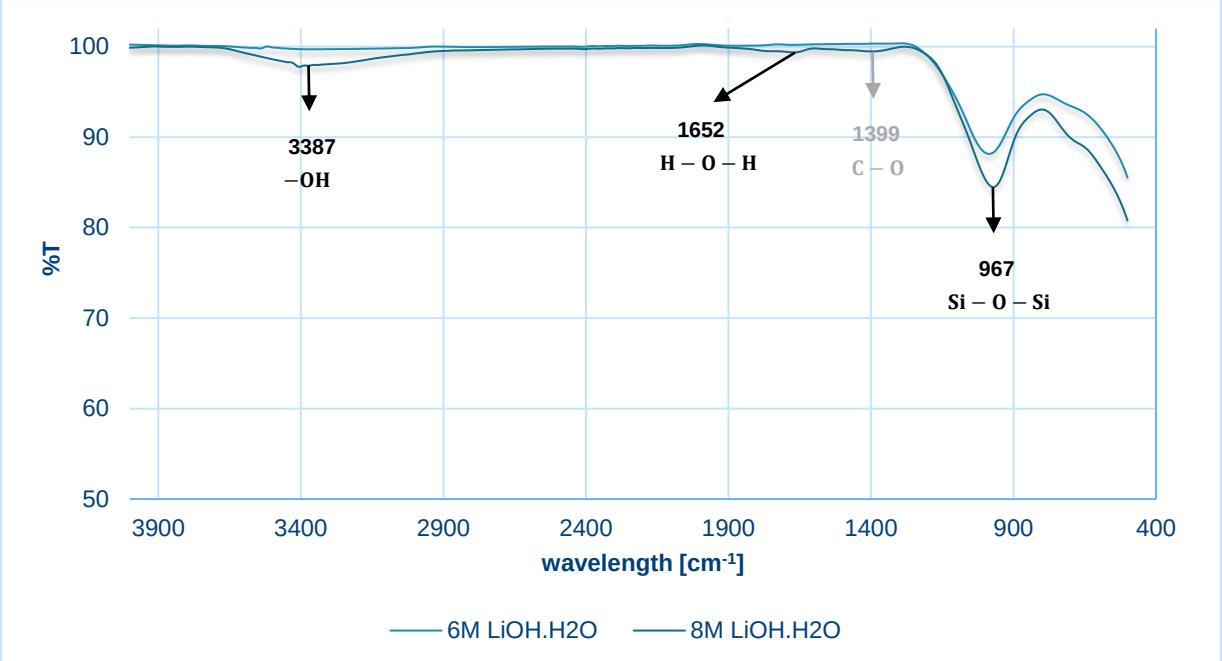

Figure 100: FTIR spectrum of $LiOH.H_2O + 5\ g\ NaOH$-based geopolymers (1d cured).

For the $\mathrm{LiOH.H_2O + 2.5\ g\ NaOH}$-based geopolymers, peaks are observed at wavelengths of 3325 $\mathrm{cm^{-1}}$, 1629 $\mathrm{cm^{-1}}$ and 975 $\mathrm{cm^{-1}}$. These peaks represent respectively the stretching vibrations of $-\mathrm{OH}$ groups and water molecules, bending vibrations of $\mathrm{H-O-H}$ and $\mathrm{Si-O-Si}$ asymmetric stretching vibrations.

The main difference compared to the cube geopolymers of the same composition is that the peaks are less pronounced, especially for the peak at 1430 $\mathrm{cm^{-1}}$. This implies that there are less $\mathrm{C-O}$ stretching vibrations from carbonate in the geopolymer matrix, compared to the cube $\mathrm{LiOH.H_2O + 2.5\ g\ NaOH}$-based geopolymers.

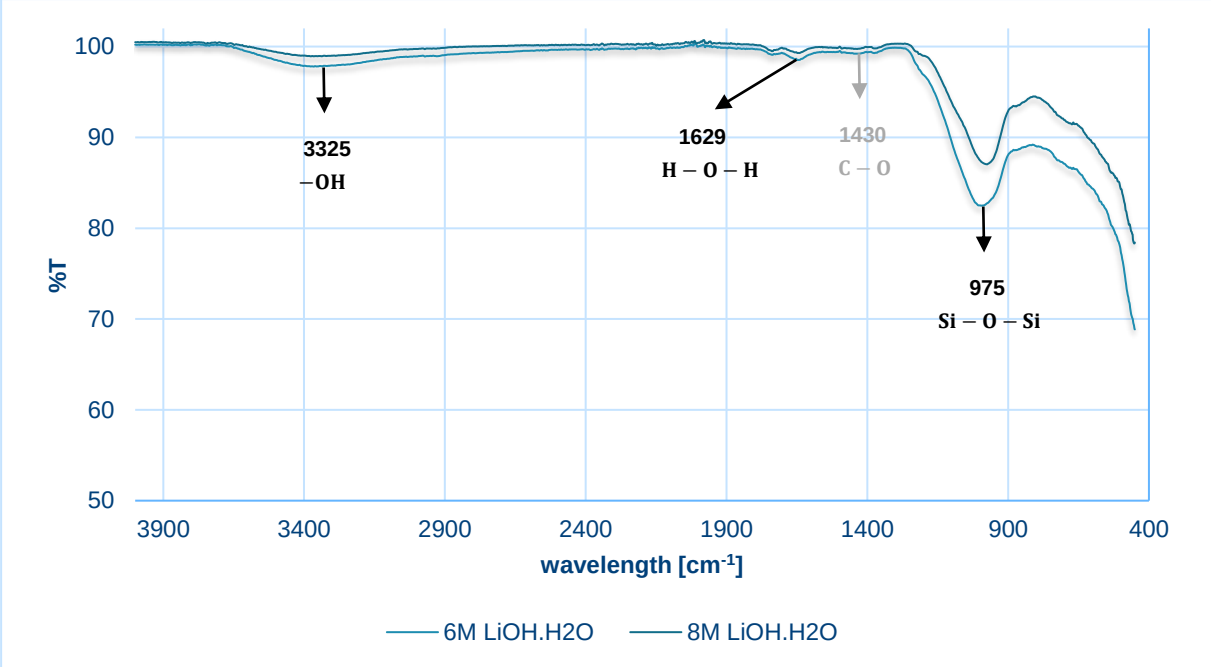

Figure 101: FTIR spectrum of $\mathrm{LiOH.H_2O + 2.5\ g\ NaOH}$-based geopolymers (1d cured).

In the FTIR diagram of the $\mathrm{LiOH.H_2O + 7.5\ g\ NaOH}$-based geopolymers, several smaller peaks are observed between the vibration of $-\mathrm{OH}$ groups and the bonds of water. Compared to the other geopolymer compositions, an additional peak is observed at wavelength of 2924 $\mathrm{cm^{-1}}$. The peaks at 3341 $\mathrm{cm^{-1}}$ and 1646 $\mathrm{cm^{-1}}$ are respectively related to the stretching vibrations of $-\mathrm{OH}$ groups and water molecules. The peak at 967 $\mathrm{cm^{-1}}$ represent the $\mathrm{Si-O-Si}$ asymmetric stretching vibrations in the geopolymer mixture. The smaller peak at 1427 $\mathrm{cm^{-1}}$ is attributed to $\mathrm{C-O}$ stretching vibrations from carbonate. This band is related to the presence of sodium carbonate by the reaction of alkali metal hydroxides with atmospheric carbon dioxide.

As presented in Figure 102, the additional peak at wavelength of 2924 $\mathrm{cm^{-1}}$ can be attributed to $\mathrm{C-H}$ groups (Huang *et al*., 2018). This peak is caused by the interaction of atmospheric carbon dioxide and hydrogen atoms in the formation of these $\mathrm{LiOH.H_2O + 7.5\ g\ NaOH}$-based geopolymers. This functional group can be found in many organic compounds. Because this geopolymer composition is the only one to clearly display this peak, this geopolymer can exhibit different mechanical properties than the other geopolymer compositions.

Due to the different bonds that arise between the different atoms during the geopolymerisation process, a denser geopolymer matrix is obtained. This results in a better cohesion of the geopolymer matrix. Subsequently, these $\mathrm{LiOH.H_2O + 7.5\ g\ NaOH}$-based geopolymers have potential to develop the highest compressive strength. Since no significant differences from

the FTIR results occur, it is expected that no extreme differences in the mechanical properties between the different geopolymer compositions will occur.

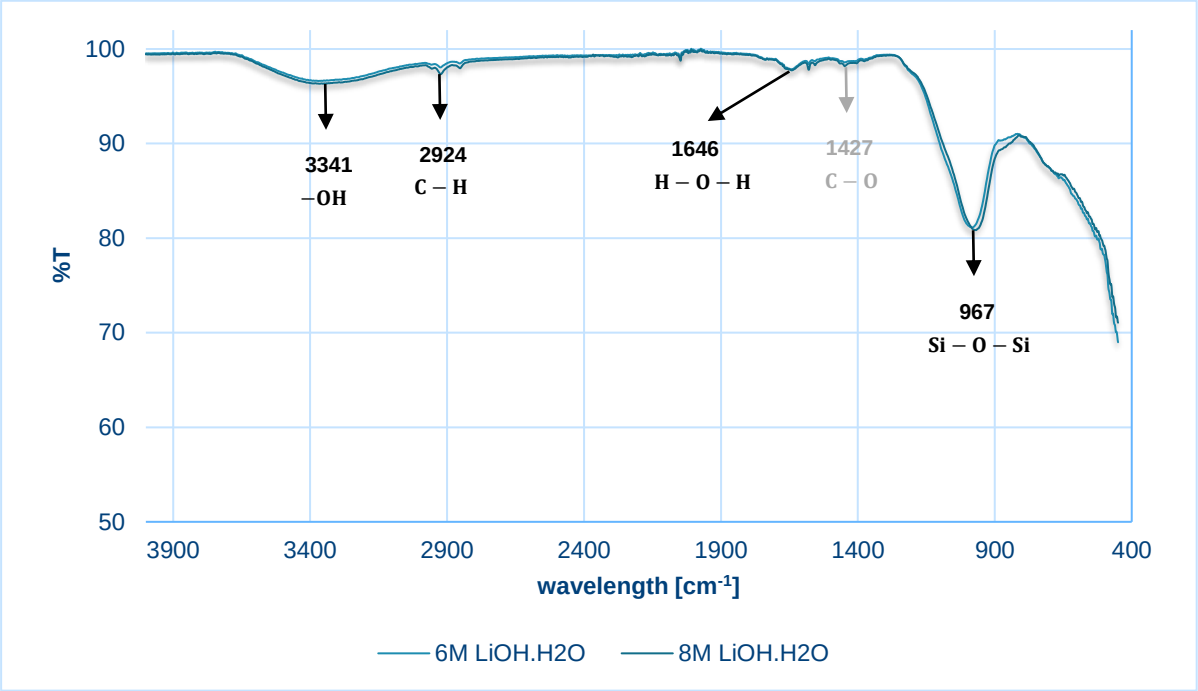

Figure 102: FTIR spectrum of $LiOH.H_2O + 7.5$ g NaOH-based geopolymers (1d cured).

6 CRITICAL REFLECTION

6.1 Prediction interval for outlier detection

6.1.1 Statistical background

To determine from the data set of measured values for compressive strength whether a value is an outlier, the classical normal distribution cannot be applied. This is because the measurement results are not normally, but randomly distributed for this research. A statistical test that does take into account randomly distributed data, is the application of a **prediction interval**. Based on at least two measured values, the prediction is made between which limits the next measured value must be in order not to be cataloged as an outlier. A prediction interval is an estimate of a range in which a future observation will fall, with a certain defined probability, given what has already been observed.

The scientific background for a prediction interval is the **Student distribution** or **t-distribution**. This t-distribution is a probability distribution that is a derivative of the normal distribution. This is related to the distribution of the scaled sample mean of a random sample from a normal distribution. This distribution is described by the test statistic T of the t-test. Let Z be a standard normal random variable and V a chi-squared random variable with v degrees of freedom. If Z and V are independent, then the distribution of the random variable T, where

$$T = \frac{Z}{\sqrt{V/v}}$$

is given by the density function $h(t)$:

$$h(t) = \frac{\Gamma[(v+1)/2]}{\Gamma(v/2)\sqrt{\pi v}} \times (1 + \frac{t^2}{v})^{-(v+1)/2} \quad , \quad -\infty < t < +\infty.$$

With Γ is defined as gamma function $\Gamma(\alpha)$, which represents the gamma distribution $f(x;\alpha,\beta)$:

$$\Gamma(\alpha) = \int_0^{\infty} x^{\alpha-1}\, e^{-x}\, dx \quad , \quad \alpha > 0$$

$$f(x;\alpha,\beta) = \begin{cases} \dfrac{1}{\beta^{\alpha}\Gamma(\alpha)} x^{\alpha-1} e^{-x/\beta} & , \quad x > 0 \\ 0 & , \quad \text{elsewhere} \end{cases}$$

The random variable T is known as the **t-distribution** with v degrees of freedom (Walpole *et al.*, 2013). In deriving the equation of this distribution, it is assumed that the samples are selected from a normal population. Although this would seem to be a very restrictive assumption, it can be shown that nonnormal populations possessing nearly bell-shaped distributions will still provide values of T that approximate the t-distribution very closely. This is why the use of prediction intervals is appropriate for this research, as the results come from a population that is randomly distributed.

Let $X_1, X_2, \ldots, X_n$ be independent random variables that are all normal with mean μ and standard deviation σ. From these random variables, the **sample mean** $\bar{X}$ can be defined as:

$$\bar{X} = \frac{1}{n} \times \sum_{i=1}^{n} X_i$$

and the **sample variance** S^2:

$$S^2 = \frac{1}{n-1} \times \sum_{i=1}^{n} (X_i - \bar{X})^2.$$

Then, the random variable $T = \frac{\bar{X}-\mu}{S/\sqrt{n}}$ has a t-distribution with $v = n - 1$ degrees of freedom. This **t-distribution** can be represented as in Figure 103, with the number of degrees of freedom v as dependence. The abscissa shows the variable x, while the ordinate shows the probability P(x). This t-distribution is represented in Figure 103 for degrees of freedom v equal to 1, 2, 5 and infinity.

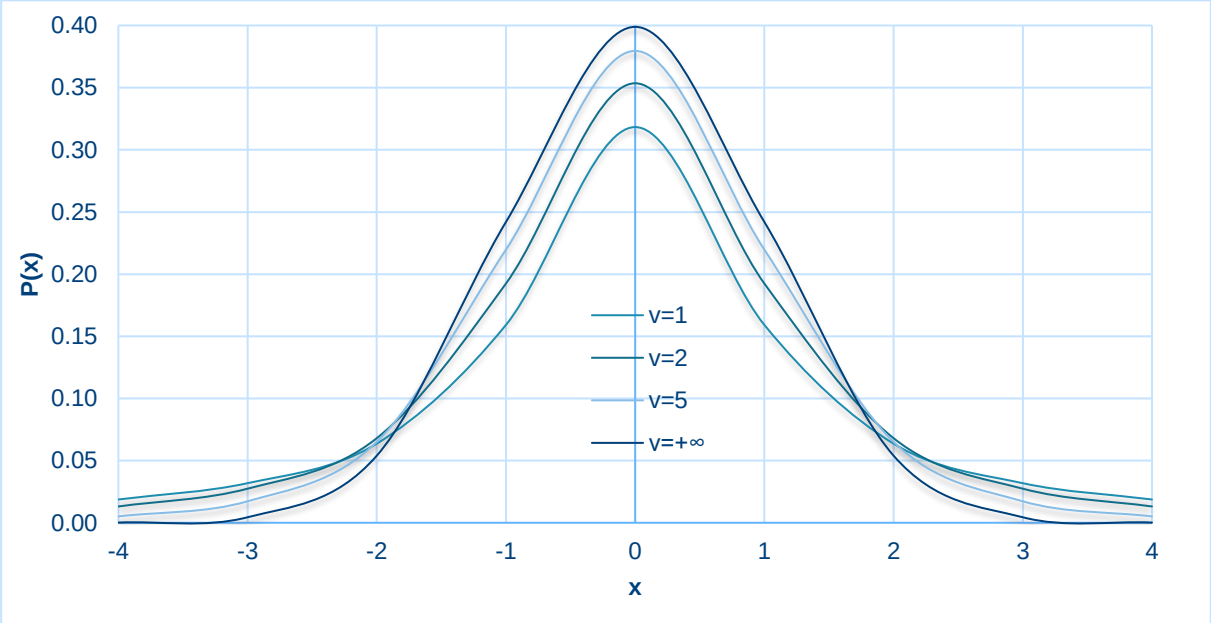

Figure 103: T-distribution as statistical background for prediction interval.

For a normal distribution of measurements with unknown mean μ and unknown variance σ^2, a $100(1-\alpha)\%$ **prediction interval** of a future observation x_0 is:

$$\bar{x} - t_{\alpha/2} \times s \times \sqrt{1 + 1/n} < x_0 < \bar{x} + t_{\alpha/2} \times s \times \sqrt{1 + 1/n}$$

where $t_{\alpha/2}$ is the t-value with $v = n - 1$ degrees of freedom, leaving an area of $\alpha/2$ to the right.

with variance σ^2: $\sigma^2 \approx s^2 = \frac{1}{n-1} \sum_{i=1}^{n} (x_i - \bar{x})^2$

and standard deviation s: $s = +\sqrt{s^2}$

6.1.2 Application of prediction interval for outlier detection

The prediction interval produces a bound that covers a future single observation with probability $1 - \alpha$ if it comes from the population from which the sample was drawn. As a result, a methodology for outlier detection involves the rule that an observation is an outlier if it falls outside the prediction interval computed without including the questionable observation in the sample. In general, a significance level of 5 % is applied, i.e. $\alpha = 0.05$. In other words, this is the maximum error allowed.

For the measurement results of the compressive strengths, the prediction interval was applied to the measurement values that appear to be suspiciously far from the others. In this way, it can be determined in a scientifically supported way which values are outliers, and which are not. Due to the application of prediction intervals, the interpretation of the results can be carried out in the most objective way possible.

This is specifically applied to the cube compressive strength measurements of the six tested 6M $\mathrm{LiOH.H_2O} + 5\ \mathrm{g\ NaOH}$-based geopolymers after 28 days curing at 70 °C, as shown in Table 16. It should be mentioned here that the first measured compressive strength of 52.973 MPa clearly deviates from the other five measured values. When the sample mean and sample standard deviation are determined from the other five measurements, this strongly deviating compressive strength of 52.973 MPa is relatively 2.15 times greater than the average measured compressive strength. Hence, it is certainly advisable in this case to check this value as a possible outlier, or aberrant observation.

Table 16: Compressive strengths of 6M $\mathrm{LiOH.H_2O} + 5\ \mathrm{g\ NaOH}$-based geopolymers (28d).

30/03/2022	sample	$F_{max}\ [kN]$	$f_c\ [MPa]$	
	6M LiOH.H2O + 5g NaOH 28d 70°C - sample 1	21.189	52.973	
	6M LiOH.H2O + 5g NaOH 28d 70°C - sample 2	10.293	25.733	
	6M LiOH.H2O + 5g NaOH 28d 70°C - sample 3	8.988	22.470	
	6M LiOH.H2O + 5g NaOH 28d 70°C - sample 4	8.914	22.285	
	6M LiOH.H2O + 5g NaOH 28d 70°C - sample 5	10.835	27.088	
	6M LiOH.H2O + 5g NaOH 28d 70°C - sample 6	10.302	25.755	
		$f_{c,mean}\ [MPa]$	**24.67**	25 ± 2
		σ	2.16	
		3σ	6.48	
		$f_{c,min}\ [MPa]$	22.51	
		$f_{c,max}\ [MPa]$	26.83	

First the value $\mathrm{t_{n-1},\frac{\alpha}{2}}$ must be determined using the inverse t-distribution. To determine this value, the number of degrees of freedom v and the significance level α must be known. In this case, the prediction interval is calculated based on the measured values of samples 2 to 6. In addition, a maximum allowed error of 5 % is commonly used. In other words, the significance level is $\alpha = 0.05$. For this case, the number of degrees of freedom is $\mathrm{v} = \mathrm{n} - 1 = 5 - 1 = 4$.

From the previously obtained data:

$$\mathbf{t_{n-1},\frac{\alpha}{2}} = \mathrm{t_{5-1},\frac{0.05}{2}} = \mathbf{2.78}$$

This value represents the boundary on the horizontal axis of the t-distribution, with $\frac{\alpha}{2}$ area to the right of this boundary. This representation is shown graphically in Figure 104.

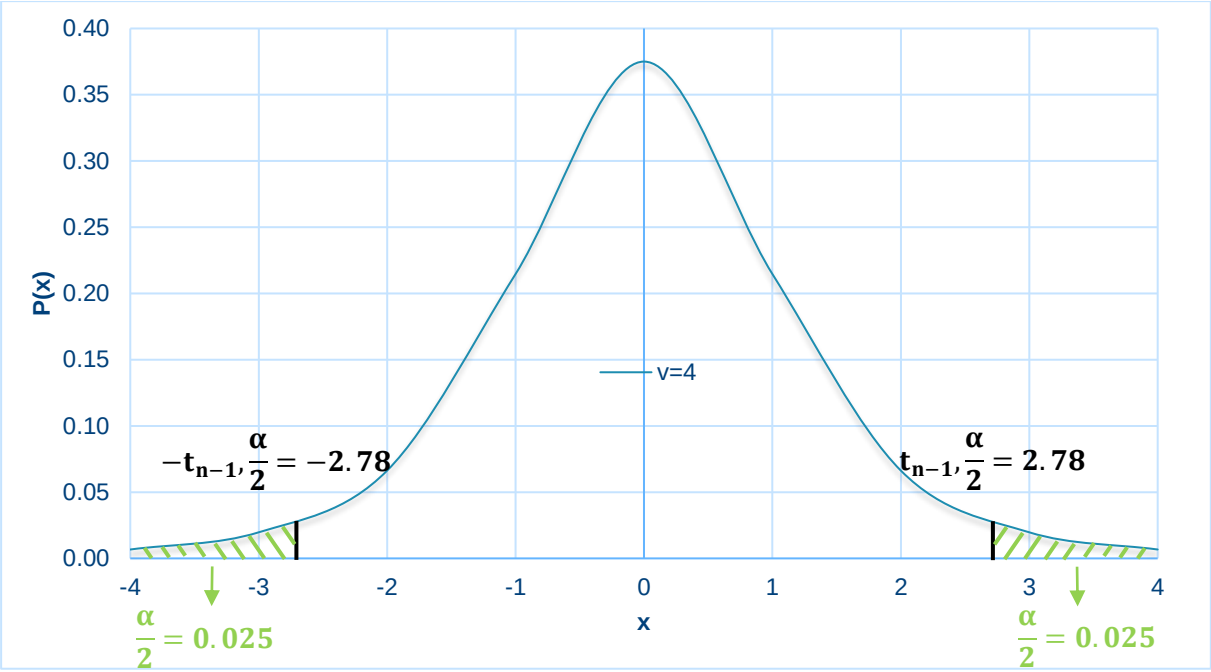

Figure 104: T-distribution for 4 degrees of freedom.

From the definition of a prediction interval,

$$\bar{x} - t_{\alpha/2} \times s \times \sqrt{1 + 1/n} < x_0 < \bar{x} + t_{\alpha/2} \times s \times \sqrt{1 + 1/n}$$

the upper and lower boundary of this interval can be calculated:

$$\text{Lower boundary} = \bar{x} - t_{\alpha/2} \times s \times \sqrt{1 + 1/n}$$

$$\text{Upper boundary} = \bar{x} + t_{\alpha/2} \times s \times \sqrt{1 + 1/n}$$

$$\bar{x} = \frac{(25.733 + 22.470 + 22.285 + 27.088 + 25.755)\ \text{MPa}}{5} = 24.67\ \text{MPa}$$

$$t_{\alpha/2} = 2.78$$

$$s = \text{STDEV(population)} = \sqrt{\frac{\sum_{i=1}^{n}(x_i - \bar{x})^2}{n}}$$

$$\sum_{i=1}^{n}(x_i - \bar{x})^2 = (25.73 - 24.66)^2 + (22.47 - 24.66)^2 + (22.29 - 24.66)^2 + (27.09 - 24.66)^2 + (25.76 - 24.66)^2 = 18.67$$

$$s = \sqrt{\frac{18.67}{5}} = 1.93$$

$$\text{Lower boundary} = 24.66 - 2.78 \times 1.93 \times \sqrt{1 + 1/5} = 18.79\ \text{MPa}$$

$$\text{Upper boundary} = 24.66 + 2.78 \times 1.93 \times \sqrt{1 + 1/5} = 30.54\ \text{MPa}$$

Finally, the **prediction interval** for this compression test can be written as:

$$18.79\ \mathrm{MPa} < x_0 < 30.54\ \mathrm{MPa}$$

Here x_0 is the value of the next compressive strength, which must be between the lower limit of $18.79\ \mathrm{MPa}$ and the upper limit of $30.54\ \mathrm{MPa}$ in order not to be cataloged as an outlier. Since $x_0 = 52.973\ \mathrm{MPa}$ in this case is greater than the upper limit of the prediction interval, this measurement value is considered an outlier. This observation lies at an abnormal distance from the other values in a random sample from the population. As a result, this value is not taken into account for further statistical analysis in the research data interpretation.

6.2 Effect of grinding and calcination on mean particle size

As already introduced in section 4.3.2.3, the effect of grinding of the MGS-1 into finer powder, and the effect of calcination of kaolinite into metakaolin on the mean particle size is determined by using the Keyence laser microscope. The analysis of the rough MGS-1 regolith with the laser microscope is shown in Figure 105.

All the aluminosilicate-rich materials that are used in this research were investigated, namely the rough MGS-1 regolith, the milled MGS-1, kaolinite and metakaolin. In each case a glass slide is used, where a suspension of the material to be tested in an alcohol solution was applied with the aid of a pipette. In this way, the most representative particle size distribution of the investigated material will be shown by using the Keyence laser microscope.

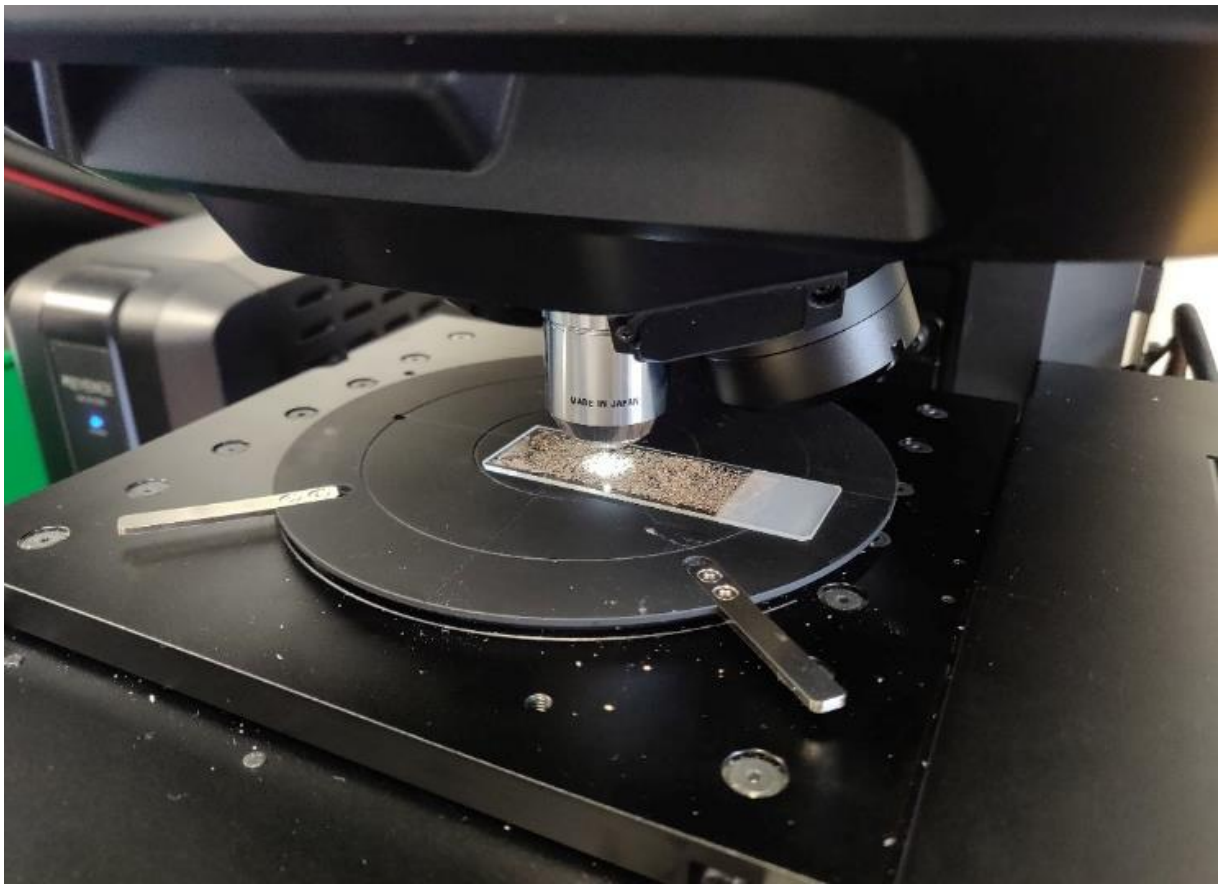

Figure 105: Keyence laser microscope with rough MGS-1 regolith on glass slide.

The purpose of this analysis is to determine the average grain distribution before and after the treatment. In this way, a scientifically supported estimate can be made of the effect of the treatment technique on the mean particle size of the investigated material.

6.2.1 Effect of grinding MGS-1

As already mentioned in section 3.2.3.3, the mean grain size of rough MGS-1 regolith is 122 μm (Cannon *et al.*, 2019). For the analysis with the Keyence laser microscope, the MGS-1 was studied at magnifications of 2.5x and 10x. These magnifications correspond to the scale of 300 μm and 100 μm, respectively, indicated on the figures below. Figures 106 and 107 visually show the grain distribution of MGS-1 at magnification of 2.5x, both before and after treatment.

Figure 106: MGS-1 before grinding – scale bar 300 μm.

Figure 107: MGS-1 after grinding for 6 hours by Bottle Roller – scale bar 300 μm.

By enlarging the magnification of the microscopic images to 10x, the materials are compared to a scale bar of 100 μm, as presented in Figures 108 and 109. Since the materials in certain fractions are smaller than the smallest sieve size of 63 μm, a sieve test analysis cannot give representative results. Figures 108 and 109 visually show the grain distribution of MGS-1 at magnification of 10x, both before and after treatment for 6 hours with the Bottle Roller.

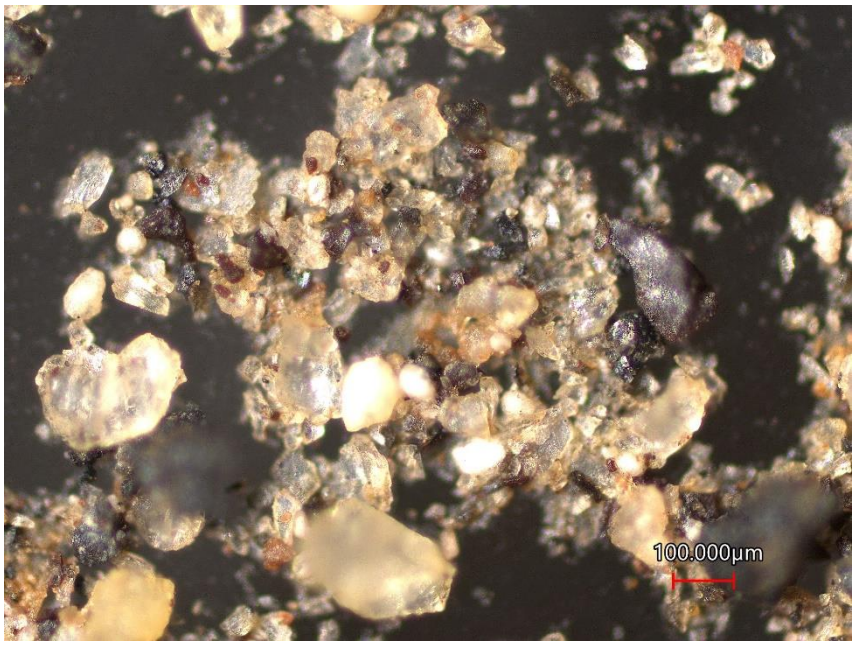

Figure 108: MGS-1 before grinding – scale bar 100 μm.

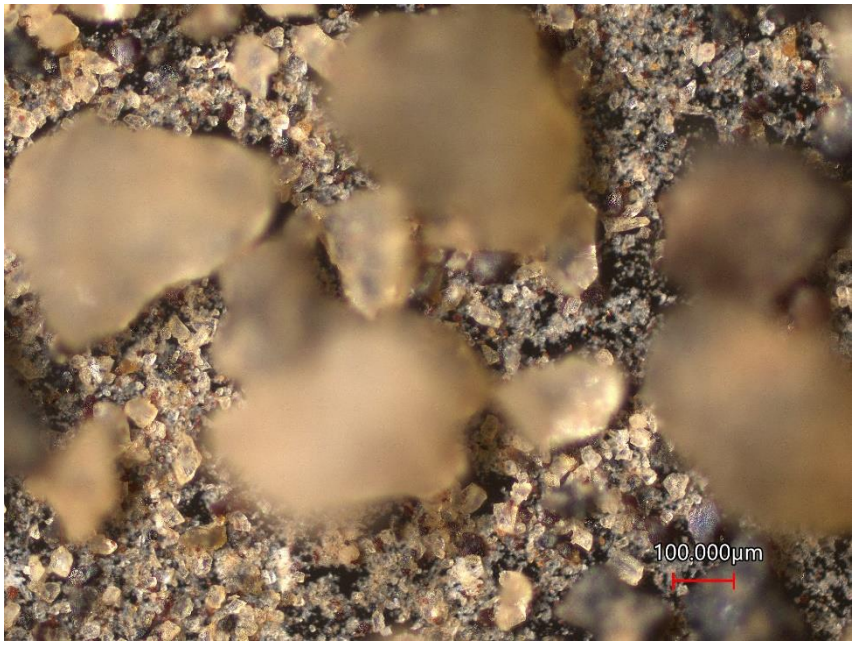

Figure 109: MGS-1 after grinding for 6 hours by Bottle Roller – scale bar 100 μm.

When examining the microscopic images of the MGS-1 before grinding, it is clearly visible that there is a large variation between the different sizes of the grains in the material. Almost 40 % of the grains have a grain size of approximately 200 μm. All other grains have a grain size close to 100 μm. After grinding the MGS-1 with the Bottle Roller for 6 hours, it is clearly visible from Figure 109 that some large fractions of 200-250 μm remain, and that the average fraction

has decreased to a grain size smaller than 63 μm. There are clearly much smaller grains present than was initially the case before grinding the MGS-1 regolith material.

6.2.2 Effect of calcination of kaolinite

The effect of the calcination on the grain size of the original kaolinite additive is determined based on three different magnifications with the Keyence laser microscope, whereby magnifications of 2.5x, 10x and 50x are used. The reason for conducting the analysis here on a smaller scale is the fact that kaolinite is a clay mineral, and therefore consists of finer powder than is the case for the MGS-1. Figures 110 and 111 visually show the grain distribution of kaolinite and metakaolin at magnification of 2.5x, both before and after calcination.

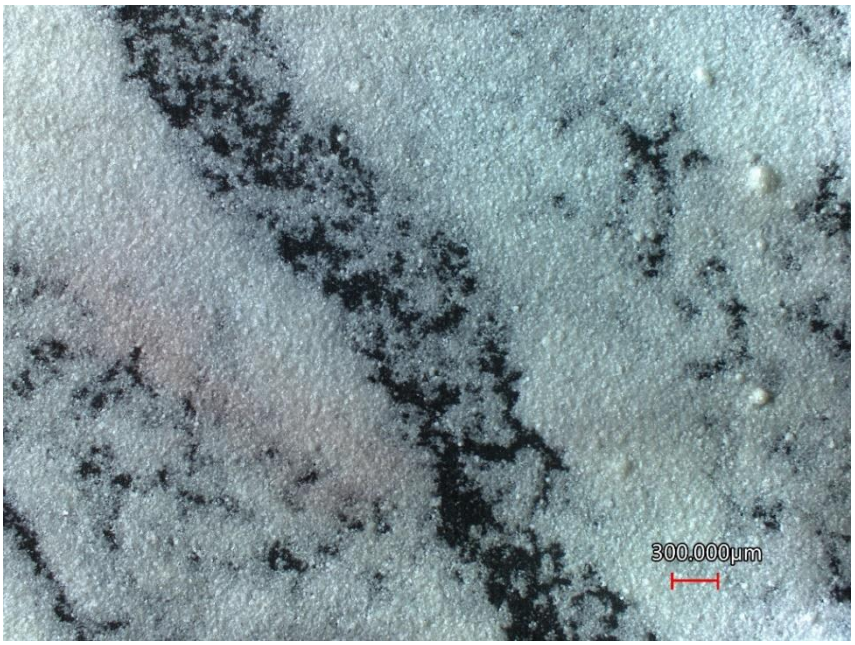

Figure 110: Kaolinite before calcination – scale bar 300 μm.

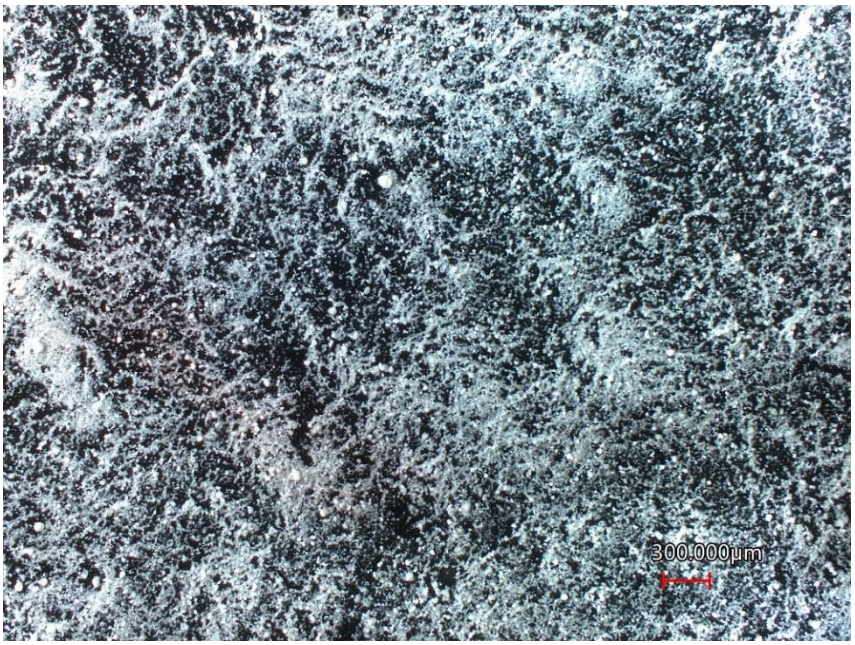

Figure 111: Metakaolin after calcination for 3 hours at 650 °C – scale bar 300 μm.

Figures 112 and 113 visually show the grain distribution of kaolinite and metakaolin compared to a scale bar of 100 µm, both before and after calcination. These microscopic images correspond to a magnification of 10x, while Figures 114 and 115 correspond to a magnification of 50x. There, the investigated materials are compared to a smaller scale bar of 20 µm.

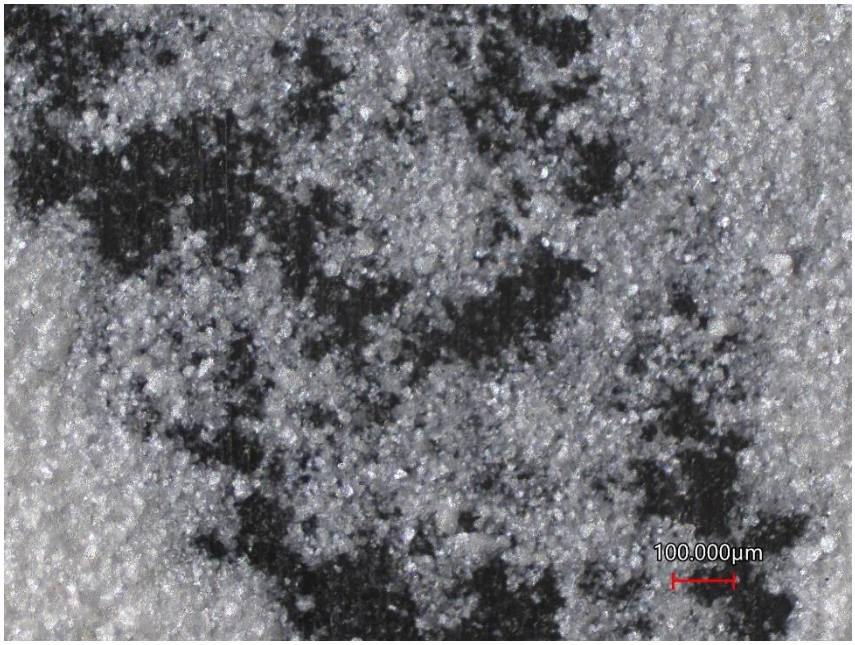

Figure 112: Kaolinite before calcination – scale bar 100 µm.

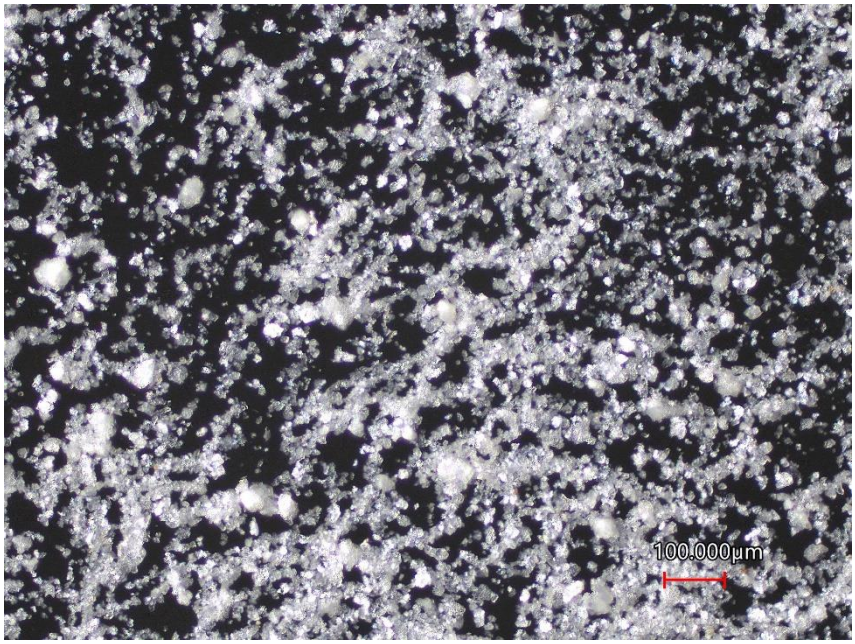

Figure 113: Metakaolin after calcination for 3 hours at 650 °C – scale bar 100 µm.

As already mentioned in section 4.1.4, during the conversion of kaolinite into metakaolin, an average mass reduction of 6 g takes place on a total weighed mass of 50 g of kaolinite. This mass reduction can be explained by the fact that a certain amount of water evaporates during the conversion of kaolinite into metakaolin. The reaction occurring during the calcination can be represented as follows:

$$Al_2O_3.2SiO_2.2H_2O \xrightarrow{\text{heating at 650 °C}} Al_2O_3.2SiO_2 + 2.H_2O \uparrow (\text{water evaporation})$$

From the observations at magnification of 10x it can be clearly seen that a less dense network of grains is observed after calcination, which can be an indication for the mass reduction.

To make a judgment about the change in mean grain size, it is necessary to study these powders on a smaller scale. For this, a magnification of 50x is applied, which also corresponds to a scale of 20 μm. Figures 114 and 115 visually show the grain distribution of kaolinite and metakaolin on a scale of 20 μm, both before and after calcination.

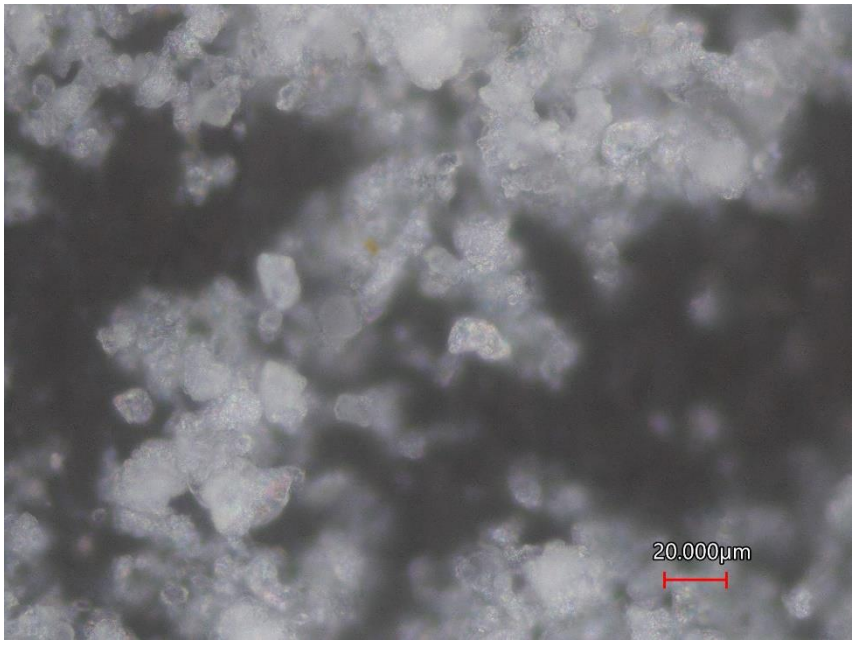

Figure 114: Kaolinite before calcination – scale bar 20 μm.

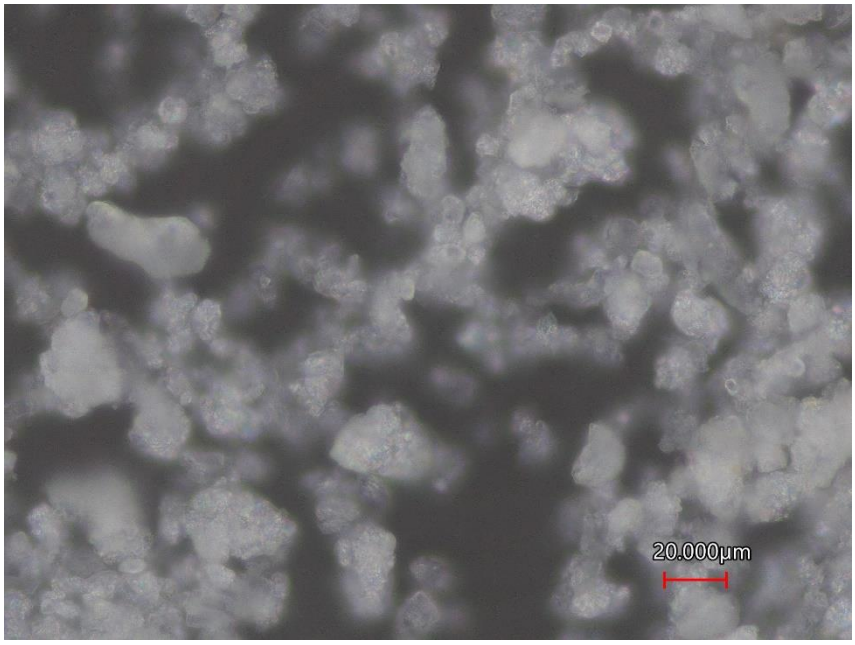

Figure 115: Metakaolin after calcination for 3 hours at 650 °C – scale bar 20 μm.

No significant change in mean grain size before and after calcination can be observed from the microscopic images obtained at 50x magnification. It should also be noted here that the surface area of the grains after calcination is smaller due to the evaporation of water. From this analysis it can be concluded that calcination has no effect on the average particle size.

6.3 Most optimal geopolymer mixture

6.3.1 $\mathbf{LiOH.H_2O + 7.5\ g\ NaOH}$-based geopolymers

In order to make a judgment about the most optimal geopolymer mixture, the focus is on the cylindrical geopolymers. This is because they give more reliable results due to the uniform compaction with the pellet press. Among all tested geopolymer mixtures, the $\mathrm{LiOH.H_2O} + 7.5\ \mathrm{g\ NaOH}$-based geopolymers show the best results in terms of compressive strength. The strength development of these cylindrical geopolymers after 1 day, 3 days and 7 days is presented in Table 17, and graphically shown in Figure 116.

Table 17: $\mathbf{LiOH.H_2O + 7.5\ g\ NaOH}$-based geopolymers (cylindrical samples).

sample	$f_{c,1d}\ [MPa]$	$f_{c,3d}\ [MPa]$	$f_{c,7d}\ [MPa]$
6M LiOH.H2O + 7.5g NaOH - 70°C oven cured	**11 ± 2**	**21 ± 2**	**27 ± 5**
8M LiOH.H2O + 7.5g NaOH - 70°C oven cured	**19.7 ± 0.2**	**29 ± 1**	**30 ± 2**

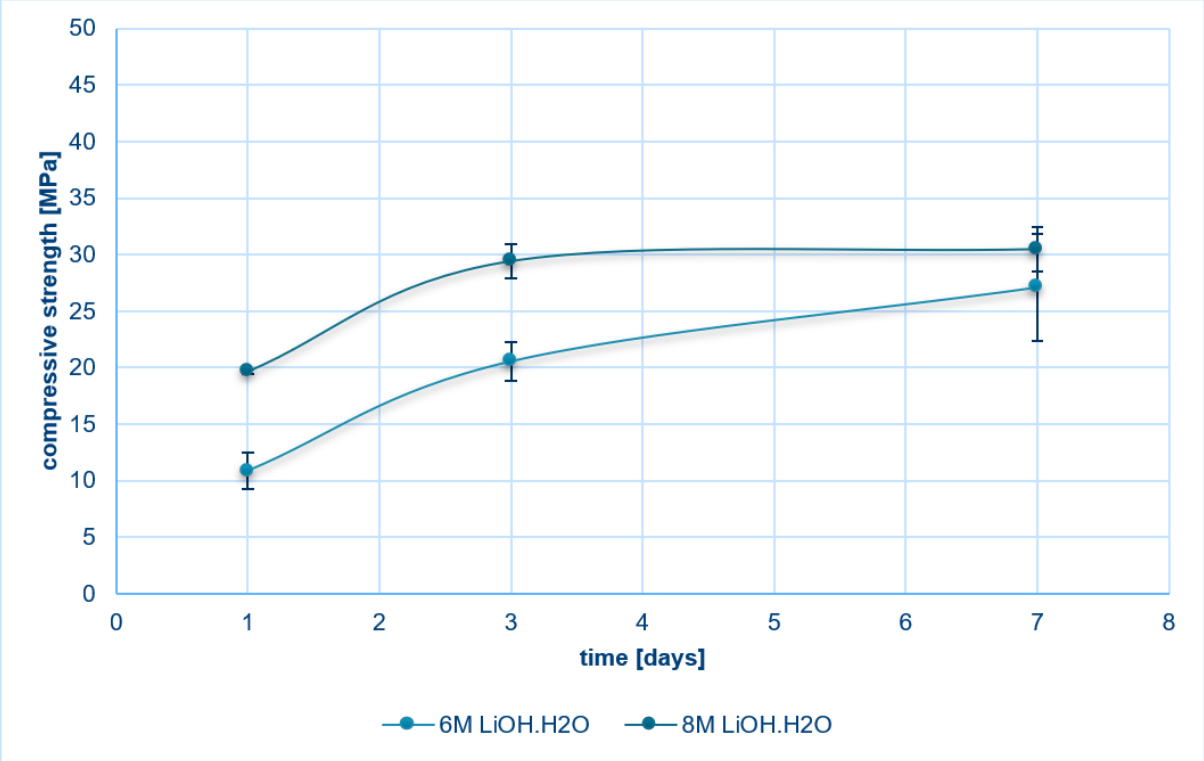

Figure 116: Most optimal geopolymer mixture; $\mathbf{LiOH.H_2O + 7.5\ g\ NaOH}$-based geopolymers (cylindrical samples).

This good performance in terms of compressive strength can be observed for both the cube and cylindrical geopolymer mixtures. A total of two different concentrations were made of this $\mathrm{LiOH.H_2O} + 7.5\ \mathrm{g\ NaOH}$ composition, both 6M and 8M. Both concentrations already give good early strength after 1 day, with compressive strengths of 11 MPa (6M $\mathrm{LiOH.H_2O} + 7.5\ \mathrm{g\ NaOH}$) and 20 MPa (8M $\mathrm{LiOH.H_2O} + 7.5\ \mathrm{g\ NaOH}$).

The increase in compressive strength is mainly perceived between 3 days and 7 days of curing at 70 °C. Finally, after 7 days, approximately the same strength is developed for both geopolymer mixtures, with a strength of 27 $\pm$ 5 MPa and 30 $\pm$ 2 MPa respectively for the 6M

and 8M $\mathrm{LiOH.H_2O} + 7.5\ \mathrm{g\ NaOH}$-based geopolymers. When a specific selection is made of the best global geopolymer composition, the 8M $\mathrm{LiOH.H_2O} + 7.5\ \mathrm{g\ NaOH}$ is declared as the winner. This geopolymer mixture develops an early strength, which means that it can be demoulded after a relatively short curing period. This early strength behaviour was already predicted from the FTIR analysis of the cube geopolymers, in section 5.3.3 of this Master's thesis. The $\mathrm{C-O}$ stretching vibrations from carbonate are present to a lesser extent with LiOH compared to NaOH. This implies that the $\mathrm{LiOH.H_2O}$-based geopolymers have a shorter setting time and higher porosity compared to the NaOH-based geopolymers (Wan-En et al., 2020). Due to the shorter setting time, a higher early strength is obtained, compared to the NaOH-based geopolymers. For use on Mars, this high early curing strength is an advantage, as structures can be built efficiently.

Besides the 8M $\mathrm{LiOH.H_2O} + 7.5\ \mathrm{g\ NaOH}$ being the most optimal geopolymer composition for the cylindrical geopolymers, the 10M $\mathrm{LiOH.H_2O} + 5\ \mathrm{g\ NaOH}$ geopolymer composition also achieves a high strength of 34 ± 7 MPa after curing for 7 days, and this for the cube geopolymers. Since the variability of this geopolymer composition shows a value of 7 MPa, this geopolymer composition is considered not representative. As a result, this geopolymer composition is not declared the most optimal, despite the fact that it develops a good strength over time.

It can be said with certainty that the results for compressive strength of the most optimal geopolymer composition, namely $\mathrm{LiOH.H_2O} + 7.5\ \mathrm{g\ NaOH}$-based geopolymers, are reliable and representative. The representativeness of the measurement results is scientifically supported for the following four reasons:

1. The upward trend in the development of compressive strength is observed in both cube and cylindrical mixtures. The final strength for the same geopolymer compositions of the cube mixtures is also 22-23 MPa, while for the cylindrical mixtures it is 27-30 MPa.
2. Between the results for both the cube and cylindrical geopolymers, no outliers were identified by the prediction interval analysis. This implies that these geopolymers show statistically acceptable values for the increase in the compressive strength.
3. The variability of the results is limited. The measurement results of compressive strength for the 6M $\mathrm{LiOH.H_2O} + 7.5\ \mathrm{g\ NaOH}$-based geopolymers show a maximum standard deviation of 5 MPa. For the 8M $\mathrm{LiOH.H_2O} + 7.5\ \mathrm{g\ NaOH}$-based geopolymers, only a maximum sample standard deviation of 2 MPa is determined.
4. Each time three different samples were tested, eliminating as much as possible the random errors that can occur during the measurements.

From the statistical analysis, the **most optimal geopolymer mixture** is found as **8M $\mathbf{LiOH.H_2O + 7.5\ g\ NaOH}$**.

6.3.2 Interpretation of the underlying mechanism for LiOH

The reason for the higher strength of the $\mathrm{LiOH.H_2O}$-based geopolymers is because of the less pronounced $\mathrm{C-O}$ stretching vibrations from carbonate compared to the NaOH-based geopolymers. In the FTIR spectrum of the $\mathrm{LiOH.H_2O}$-based geopolymers, a peak of 2924 $\mathrm{cm^{-1}}$ was observed in the cylindrical geopolymers, which can be attributed to $\mathrm{C-H}$ groups in the geopolymer matrix. This ensures that the mechanical strength of this geopolymer composition is better than the other geopolymers. In addition, lithium hydroxide is a strong base because it completely dissociates in an aqueous solution and produces a large number of $\mathrm{OH^-}$ ions.

6.3.3 Comparison to other studies on geopolymers

The mechanical strength properties of the $\mathrm{LiOH.H_2O} + 7.5\ \mathrm{g\ NaOH}$-based geopolymers are compared with four other studies. A number of studies have already been performed with lithium hydroxide as an alkali activator for geopolymers, but not yet in combination with the simulated Mars regolith material MGS-1. This combination of LiOH and MGS-1 makes this research so interesting and innovative.

Chen *et al*. (2012) investigated the production of geopolymer bricks based on sodium silicate, sodium hydroxide, potassium hydroxide and lithium hydroxide solutions. Here, simulated planetary materials were not used, but combustion ash was used as raw material. The geopolymers were cured at a temperature of 40 °C and a relative humidity of 100 %. After curing for 7 days, the best results were obtained for the geopolymers based on 10M KOH. A compressive strength of 18.8 MPa was measured here, while for the 10M LiOH-based geopolymers a compressive strength of 9.4 MPa was measured after curing for 7 days. Compared to the average compressive strength of 30 MPa for the 8M $\mathrm{LiOH.H_2O} + 7.5\ \mathrm{g\ NaOH}$-based geopolymers, a compressive strength is reached in this study that is 3.2 times greater than in the study on the geopolymer bricks.

Chakraborty (2019) used the MMS-1 Martian simulant as aluminosilicate material for the geopolymerisation. The best compressive strengths for the 10M geopolymers were achieved at $\mathrm{Na_2SiO_3/NaOH}$ ratio of 2.5. The geopolymers were cured at a temperature of 90 °C. After 1 day a compressive strength of 1.0 ± 0.1 MPa was determined, while after 3 days a compressive strength of 5.0 ± 0.3 MPa was determined. From these results it can be concluded that the most optimal geopolymers from this study exhibit a compressive strength that is 5.8 times greater than the case in the study of the geopolymerisation of MMS-1.

Alexiadis *et al*. (2017) used JSC MARS-1A simulant to perform the geopolymerisation. The geopolymers in this study were made based on 8M NaOH. The composition of the geopolymer mixture was fixed at 20 g of JSC MARS-1A simulant and 10 g of $\mathrm{K_2SiO_3}$. The oven curing of the geopolymer mixtures took place at a temperature of 80 °C over a period of 28 days. After curing the geopolymers for 28 days, a compressive strength of 2.5 ± 0.3 MPa was achieved. Also here it is immediately noticeable that this is a considerably lower compressive strength than that is achieved in this research with MGS-1.

A recent study by Mills *et al*. (2022) compared lunar and Martian regolith simulant-based geopolymer cements. In this study, the MGS-1C Martian simulant was used, which allows comparison with this Master's thesis research in a more representative way than the other three studies above. This MGS-1C was activated by a 37 wt% sodium silicate solution. The curing conditions for these geopolymers were ambient curing at a temperature of 20 °C for 7 days. After curing for 7 days, a compressive strength of 13.6 MPa was measured for these geopolymers. Compared to this research with MGS-1, about half of the strength is achieved after 7 days of curing. However, the comparison must take into account the different curing temperatures. Due to the higher curing temperature of 70 °C in this research, it makes sense that a greater compressive strength is achieved than in the study by Mills *et al*. (2022), where a lower curing temperature of 20 °C was used.

In general, it can be concluded that in this study a significantly higher compressive strength is achieved compared to the other four studies above. As already mentioned in the introduction, the goal of this research is to achieve a compressive strength of at least 10 MPa. With these results for the compressive strengths of the geopolymers, that goal has clearly been achieved.

6.4 Comparison of results from cube and cylindrical samples

To make the comparison between the results for the compressive strength between the cube and cylindrical geopolymers, the most optimal geopolymer mixtures 6M $\mathrm{LiOH.H_2O} + 7.5\ \mathrm{g\ NaOH}$ and 8M $\mathrm{LiOH.H_2O} + 7.5\ \mathrm{g\ NaOH}$ are investigated. Table 18 and Table 19 show the change in compressive strength over time.

Table 18: $\mathrm{LiOH.H_2O} + 7.5\ \mathrm{g\ NaOH}$-based geopolymers (cube samples).

sample	$f_{c,1d}\ [MPa]$	$f_{c,3d}\ [MPa]$	$f_{c,7d}\ [MPa]$
6M LiOH.H2O + 7.5g NaOH - 70°C oven cured	**20 ± 2**	**28 ± 2**	**22 ± 5**
8M LiOH.H2O + 7.5g NaOH - 70°C oven cured	**4 ± 1**	**6 ± 1**	**23 ± 3**

Table 19: $\mathrm{LiOH.H_2O} + 7.5\ \mathrm{g\ NaOH}$-based geopolymers (cylindrical samples).

sample	$f_{c,1d}\ [MPa]$	$f_{c,3d}\ [MPa]$	$f_{c,7d}\ [MPa]$
6M LiOH.H2O + 7.5g NaOH - 70°C oven cured	**11 ± 2**	**21 ± 2**	**27 ± 5**
8M LiOH.H2O + 7.5g NaOH - 70°C oven cured	**19.7 ± 0.2**	**29 ± 1**	**30 ± 2**

6.4.1 Conversion factor

The difference in compressive strength between the cube and cylindrical samples is expressed relative to each other as a percentage, and this after 1 day, 3 days and 7 days. In traditional concrete technology there exists a conversion factor of 0.65-0.90 between the strength of cubes and cylinders (Elwell, 1995):

$$\mathrm{f_{c,cyl}} = 0.65 - 0.90 \times \mathrm{f_{c,cub}}$$

The main difference between the testing of cylindrical and cube samples is capping. Cylinder ends are usually not parallel enough to mate properly with platens of compression testing devices. Therefore, cylindrical samples of considerable size must be capped by using neoprene or another suitable material for proper distribution of the applied load. Cubes, however, are not capped but cast in rigid moulds with sides that are plane and parallel. When performing the compression tests for cube samples, the cubes are flipped on their sides so that the machine platens mate properly with cube surfaces. For the Master's thesis research, the boundary conditions for the compression tests of the cube samples were the same as described above. The cylinder/cube strength ratio is affected by:

1. Casting, curing and testing procedure;
2. Sample geometry;
3. Level of strength;
4. Direction of loading and machine properties;
5. Aggregate grading.

Due to the fact that in this research very small samples are used (cubes 20x20x20 mm and cylinders Ø20x40 mm), which are only 13 % of the size of the traditional samples for concrete (cubes 150x150x150 mm and cylinders Ø150x300 mm), the traditional conversion factor of 0.80 will not be fully valid. This conversion factor of 0.80 is obtained from the Belgian standard NBN EN 12390-3, where:

$$\mathrm{f_{c,cyl,150x300}} = 0.80 \times \mathrm{f_{c,cub,150x150}}$$

In addition, the influence of the user-dependent errors during the compaction of the cube mixtures also has a large influence on the ultimate developed compressive strength. Larger samples, as is traditionally used in concrete research, will therefore obtain more representative measurement results, in terms of the obtained compressive strength.

6.4.2 Relative strength of cylindrical geopolymer samples

To determine the relative difference in strength between the cylindrical and cube geopolymer samples, the following ratio is used:

$$\Delta f_{c,x\ \mathrm{days}} = \frac{f_{c,\mathrm{cylindrical\ sample}}}{f_{c,\mathrm{cube\ sample}}}$$

❖ For 6M $LiOH.H_2O + 7.5\ g\ NaOH$:

- Compressive strength of cylindrical sample, relative to cube sample - after 1 day:

$$\Delta f_{c,1\ \mathrm{day}} = \frac{11\ \mathrm{MPa}}{20\ \mathrm{MPa}} = 0.55$$

- Compressive strength of cylindrical sample, relative to cube sample - after 3 days:

$$\Delta f_{c,3\ \mathrm{days}} = \frac{21\ \mathrm{MPa}}{28\ \mathrm{MPa}} = 0.75$$

- Compressive strength of cylindrical sample, relative to cube sample - after 7 days:

$$\Delta f_{c,7\ \mathrm{days}} = \frac{27\ \mathrm{MPa}}{22\ \mathrm{MPa}} = 1.23$$

❖ For 8M $LiOH.H_2O + 7.5\ g\ NaOH$:

- Compressive strength of cylindrical sample, relative to cube sample - after 1 day:

$$\Delta f_{c,1\ \mathrm{day}} = \frac{19.7\ \mathrm{MPa}}{4\ \mathrm{MPa}} = 4.93$$

- Compressive strength of cylindrical sample, relative to cube sample - after 3 days:

$$\Delta f_{c,3\ \mathrm{days}} = \frac{29\ \mathrm{MPa}}{6\ \mathrm{MPa}} = 4.88$$

- Compressive strength of cylindrical sample, relative to cube sample - after 7 days:

$$\Delta f_{c,7\ \mathrm{days}} = \frac{30\ \mathrm{MPa}}{23\ \mathrm{MPa}} = 1.30$$

From the above conversion factors it can be concluded that the cube samples for the 6M $LiOH.H_2O + 7.5\ g\ NaOH$ geopolymers show significantly better results than the cylindrical samples of the same geopolymer composition. In addition, the cube samples for the 8M $LiOH.H_2O + 7.5\ g\ NaOH$ geopolymers after curing for 1 day and 3 days at 70 °C show approximately five times smaller values in terms of compressive strength, compared to the

cylindrical samples. After curing for 7 days, almost the same compressive strength is achieved for both the cube and cylindrical geopolymer mixtures.

In general, it can be concluded that no unambiguous relationship can be found between the measurement results of the compressive strengths for the cubes and cylinders in this research. The biggest determining factor for this is the quality of compaction. In section 6.4.3 the values obtained for the compressive strengths of the cube and cylindrical samples are compared with values from literature.

6.4.3 Comparison of conversion factors to other studies

When the results of this research are compared with a study by Thampi *et al*. (2014), it appears that similar results are achieved for the compressive strength of geopolymers. Thampi *et al*. (2014) made fly ash-based geopolymers with a chemical composition of 46.2 w% SiO_2, 26.4 w% Al_2O_3 and 7.6 w% CaO. This composition shows that the used fly ash has a larger amount of Al_2O_3 and CaO than in the case of MGS-1. The addition of an additive such as matakaolin is unnecessary in that study.

The geopolymer mortar is prepared by a concentration of 16M $NaOH$. The $NaOH/Na_2SiO_3$ ratio is taken as 2.5. The fly ash is mixed with river sand for 3 minutes, then the liquid activators, sodium hydroxide and sodium silicate, are added to the mixture. Therefore, mixing continued for 4 extra minutes. The curing conditions were divided into 2 parts: 60 °C heat curing for 24 hours in laboratory oven, then left in ambient conditions for the rest of the curing time. The most important factor in this research is the size of the cube and cylindrical samples. Cubes of 50x50x50 mm and cylinders of ø50x100 mm were used in this study. This means that in the study for this Master's thesis samples were made 2.5 times smaller than in the study by Thampi *et al*. (2014).

The compressive strength tests on the cube and cylindrical geopolymer samples are performed at 7 days, 14 days and 28 days of curing. For the cube geopolymer samples a compressive strength of 30 MPa is reached after 7 days, while the cylindrical mixtures reach a compressive strength of 24 MPa.

$$\Delta f_{c,7\ \mathrm{days}} = \frac{24\ \mathrm{MPa}}{30\ \mathrm{MPa}} = 0.80$$

This means that the cylindrical geopolymer mixtures for this study achieve a strength of 80 % compared to the cube samples. As already mentioned in section 6.4.1, this value for the conversion factor is within the range of the expected conversion factors for the compressive strength of cubes and cylinders.

Ahmad *et al*. (2021) used the novel artificial intelligence technique ANFIS (adaptive neuro-fuzzy interference system) to predict the compressive strength of fly ash-based geopolymers. In that study, the influence of the alkaline to precursor ratio (0.3-0.5), the sodium silicate to sodium hydroxide ratio (2-3) and curing temperature were studied. The conclusions of the study showed that the highest compressive strength is obtained at an alkaline to precursor ratio of 0.4, whereby a compressive strength of 35 MPa was obtained.

Kumaravel & Girija (2014) studied the strength of high-strength geopolymer concrete. During that study, sodium hydroxide and sodium silicate were used as alkali activators. Fly ash and GGBS were used as geopolymer precursors, in a volume ratio of 50 % each. The geopolymer mixtures were performed in cubes of 100x100x100 mm and cylinders of ø150x300 mm. The

curing of the geopolymers took place through hot air curing at a temperature of 75°C. The results from this study were satisfactory. For the cube compressive strength a value of 58.5 MPa was obtained after curing for 7 days. The cylindrical samples achieved a compressive strength of 49.3 MPa after 7 days.

$$\Delta f_{c,7\ days} = \frac{49.3\ MPa}{58.5\ MPa} = 0.84$$

The conversion factor between the cube and cylindrical compressive strength is 0.84. This value is also within the expectations of the NBN EN 12390-3 standard. Since in the literature values for the conversion factors for the cube and cylindrical compressive strengths are also obtained in the range of 0.65-0.90, it can be concluded that the reliability of the results from this Master's thesis research for the cube geopolymer samples is remarkably lower.

As shown in the calculation of the conversion factors in section 6.4.2, the 6M $LiOH.H_2O + 7.5\ g\ NaOH$- based geopolymers achieve the most representative values for both the cube and cylindrical compressive strength. For the 8M $LiOH.H_2O + 7.5\ g\ NaOH$-based geopolymers, a greater variability is obtained between the cube and cylindrical compressive strength. As conclusion, these results are less representative for the cube samples. The reason for this can be found in the compaction of these geopolymers. For the cube geopolymers, this compaction was done using a less uniform and standardised method than for the cylindrical geopolymers.

6.5 Failure behaviour

An important part of this research is the analysis of the failure behaviour of the cube and cylindrical geopolymers. After each performed compression test, the value for the final compression strength was recorded. Each time, a picture of the failure pattern was also taken. Based on the failure pattern, it was already possible to estimate in advance whether or not the geopolymer will have a high compressive strength. Among the results, some very weak and very strong geopolymers were identified. In this section the main failure patterns are discussed, and also linked to the value for the achieved compressive strength.

In section 6.5.1 and section 6.5.2 a comparison is made between the relationship of the compressive strength and the failure patterns of the cube geopolymers. This is performed for the NaOH-based geopolymers as well as for the $LiOH.H_2O + 5\ g\ NaOH$-based geopolymers. The weakest geopolymer mixtures are shown in section 6.5.3. Finally, section 6.5.4 shows the most optimal geopolymer mixture, with the highest strength and best strength development.

6.5.1 NaOH-based geopolymers

Table 20: 8M NaOH-based cube geopolymers (3d).

17/02/2022	sample	$F_{max}\ [kN]$	$f_c\ [MPa]$	
	8M NaOH 3d 70°C - sample 1	7.811	19.528	
	8M NaOH 3d 70°C - sample 2	4.582	11.455	
	8M NaOH 3d 70°C - sample 3	6.396	15.990	
		$f_{c,mean}\ [MPa]$	**15.66**	16 ± 4
		σ	4.05	
		3σ	12.14	
		$f_{c,min}\ [MPa]$	11.61	
		$f_{c,max}\ [MPa]$	19.70	

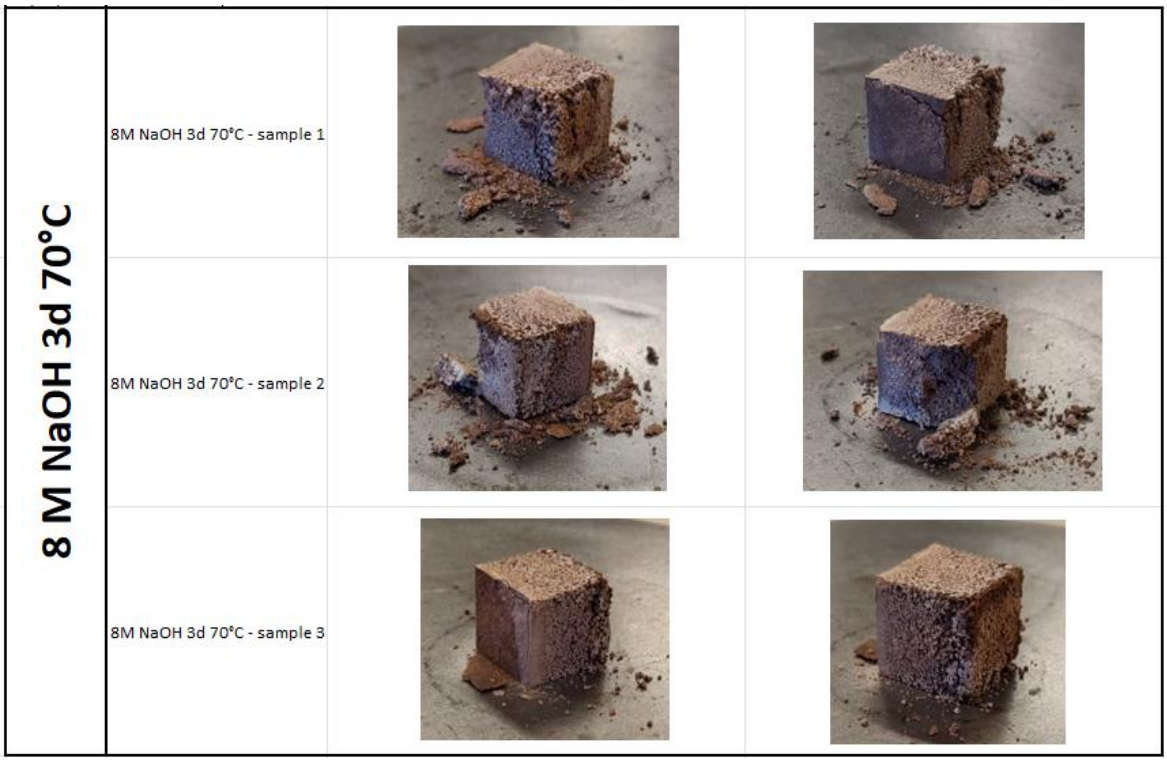

Figure 117: Failure profiles for NaOH-based cube geopolymers.

From the various failure patterns of all geopolymer samples, it can be predicted whether or not the mixture will exhibit a high compressive strength. It can be deduced from Figure 117 that the cube NaOH-based geopolymers show brittle fractures. In addition, the high porosity is also noticeable due to the poor compaction of the first geopolymer mixtures.

6.5.2 $\mathrm{LiOH.H_2O} + 5\ \mathrm{g\ NaOH}$-based geopolymers

Table 21: 8M $\mathrm{LiOH.H_2O} + 5\ \mathrm{g\ NaOH}$-based cube geopolymers (3d).

sample	$F_{max}\ [kN]$	$f_c\ [MPa]$	
8M LiOH.H2O + 5g NaOH 3d 70°C - sample 1	9.705	24.263	
8M LiOH.H2O + 5g NaOH 3d 70°C - sample 2	7.535	18.838	
8M LiOH.H2O + 5g NaOH 3d 70°C - sample 3	6.157	15.393	
	$f_{c,mean}\ [MPa]$	**19.50**	20 ± 4
	σ	4.47	
	3σ	13.42	
	$f_{c,min}\ [MPa]$	15.03	
	$f_{c,max}\ [MPa]$	23.97	

The $\mathrm{LiOH.H_2O} + 5\ \mathrm{g\ NaOH}$ -based geopolymers perform better than the NaOH -based geopolymers. The $\mathrm{LiOH.H_2O} + 5\ \mathrm{g\ NaOH}$-based geopolymers exhibit a more rigid unit and fracture along a longitudinal fracture plane, as shown in Figure 118.

Table 20 and Table 21 show that the $\mathrm{LiOH.H_2O} + 5\ \mathrm{g\ NaOH}$-based geopolymers achieve the greatest compressive strength on average. This can be immediately deduced from the better developed failure planes that arise. For example, with the $\mathrm{LiOH.H_2O} + 5\ \mathrm{g\ NaOH}$ -based geopolymers, it is clearly noticeable that the first geopolymer mixture shows a less pronounced crack pattern than the other two geopolymer mixtures. This is also noticeable in a significantly

higher compressive strength for the first sample, compared to both other geopolymer samples.

Figure 118: Failure profiles for $\mathbf{LiOH.H_2O + 5\ g\ NaOH}$-based cube geopolymers.

6.5.3 Weak geopolymer samples

Something remarkable was observed for the cylindrical geopolymers with the 8M NaOH-based geopolymers. During the production of these geopolymer samples, problems arose with the workability of the geopolymer mixture. When these geopolymers were subjected to the compression test, they broke immediately, as shown in Figure 119. Due to the fact that the two platens of the compression test continuously pressed against each other after the geopolymer has already broken quickly in a brittle manner, in some cases a non-representative value for the compressive strength was shown. A critical analysis of the measurement results is therefore of crucial importance. Therefore, both the compressive strength values and failure patterns were compared to each other.

Figure 119: 8M NaOH-based cylindrical geopolymers before (left) and after compression test (right).

6.5.4 Most optimal geopolymer samples

Table 22: 8M $\mathbf{LiOH.H_2O + 7.5\ g\ NaOH}$-based cube geopolymers (7d).

sample	F_{max} $[kN]$	f_c $[MPa]$	
8M LiOH.H2O + 7.5g NaOH 7d 70°C - sample 1	8.280	20.700	
8M LiOH.H2O + 7.5g NaOH 7d 70°C - sample 2	10.477	26.193	
8M LiOH.H2O + 7.5g NaOH 7d 70°C - sample 3	8.666	21.665	
	$f_{c,mean}$ $[MPa]$	**22.85**	23 ± 3
	σ	2.93	
	3σ	8.80	
	$f_{c,min}$ $[MPa]$	19.92	
	$f_{c,max}$ $[MPa]$	25.78	

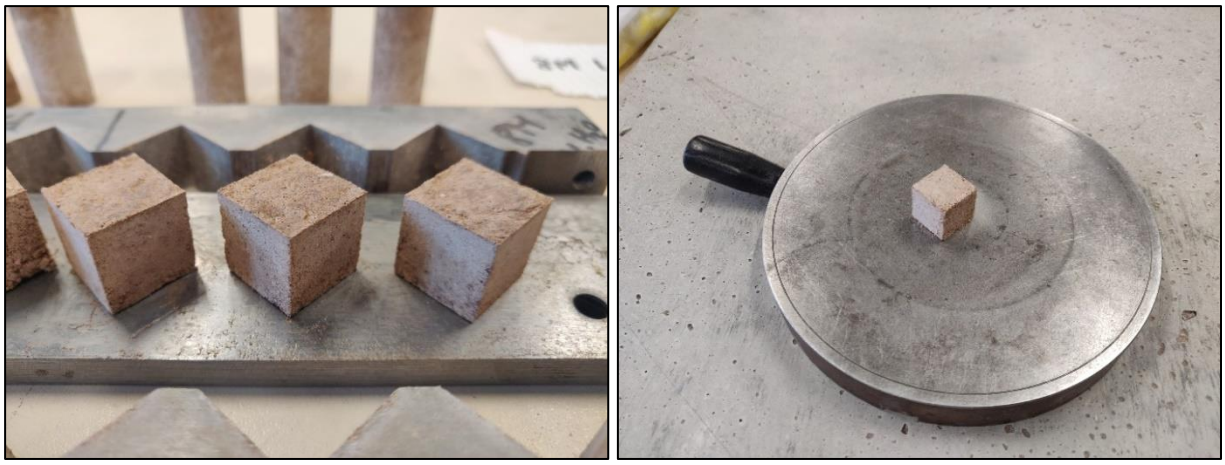

Figure 120: 8M $\mathbf{LiOH.H_2O + 7.5\ g\ NaOH}$-based cube geopolymers before (left) and after compression test (right).

From the left image of Figure 120, the produced 8M $\mathrm{LiOH.H_2O + 7.5\ g\ NaOH}$-based cube geopolymers are shown, where it can already be deduced that these geopolymers have a dense and coherent structure. Due to the good compaction and cooperation between the alkali activators sodium hydroxide, lithium hydroxide and sodium silicate, a good compressive strength is achieved for these cube geopolymer samples. The results after performing the compression test also showed that these cube geopolymers are difficult to crush with low compression pressures. This phenomenon confirms the high strength of the 8M $\mathrm{LiOH.H_2O + 7.5\ g\ NaOH}$-based cube geopolymers.

Table 23: 8M $\mathbf{LiOH.H_2O + 7.5\ g\ NaOH}$-based cylindrical geopolymers (7d).

sample	F_{max} $[kN]$	f_c $[MPa]$	
8M LiOH.H2O + 7.5g NaOH 7d 70°C - sample 1	10.192	32.442	
8M LiOH.H2O + 7.5g NaOH 7d 70°C - sample 2	9.558	30.424	
8M LiOH.H2O + 7.5g NaOH 7d 70°C - sample 3	8.979	28.581	
	$f_{c,mean}$ $[MPa]$	**30.48**	30 ± 2
	σ	1.93	
	3σ	5.79	
	$f_{c,min}$ $[MPa]$	28.55	
	$f_{c,max}$ $[MPa]$	32.41	

The cylindrical geopolymers of the same chemical composition achieve even better performance in terms of mechanical strength properties. Due to the uniform compaction of

these geopolymers with the pellet press, a higher strength is achieved than the cube geopolymers. A shear plane occurs with these cylindrical geopolymers when the maximum compressive strength is exceeded, as can be seen in the right image of Figure 121.

Due to the different geometry and larger height of the cylindrical geopolymers compared to the cube geopolymers, it is expected that a lower compressive strength is observed with the cylindrical geopolymers. These expectations are not fulfilled from the results of this optimal geopolymer composition. The cylindrical geopolymer samples has on average a 33 % higher compressive strength than the cube samples. From section 6.4.1, it is expected that the cylindrical geopolymers have a compressive strength of 65 to 90 % compared to the cube geopolymers. Here, because the compressive strength of the cylinders is higher than the cubes, this implies less representative cube geopolymers due to the non-uniform compaction.

Figure 121: 8M $\mathbf{LiOH.H_2O + 7.5\ g\ NaOH}$-based cylindrical geopolymers before (left) and after compression test (right).

6.6 Hiatus and limitations

6.6.1 Performing only one type of mechanical test

For the characterisation of the mechanical properties, only one type of test was performed, namely the compression test. For a better mechanical characterisation several types of tests have to be performed. Due to the large amount of different compositions to obtain the most optimal geopolymer composition, the focus was on only one type of test. This allows all other results to be easily analysed in relation to each other, and in a uniform manner.

Additional mechanical tests can be applied, such as the mechanical bending test. However, for this research, this test was not feasible as only samples were made in small quantities due to economic considerations. To perform the bending test, sufficiently large mixtures have to be made, which is a limitation in this study. The European Standard EN14651 Bend Testing is the test method for measuring the flexural tensile strength of concrete specimens. For this test, the dimensions of the test specimens are 150x150x550 mm.

Another possibility is to prepare a stress-strain diagram to obtain more specific information. Now only the strength was determined by means of a force-controlled compression test. Better interpretations of the measurement results can be made by means of a deformation-controlled compression test. In addition, by performing several tests for the determination of the

compressive strength of the geopolymers, durability tests can also be performed. With the freeze-thaw device, the extreme temperature variations from the planet Mars can be simulated to a minimum of -70 °C. Other tests to determine the behaviour of the geopolymers under the influence of radiation must also be performed. This is because the radiation amounts and intensity on Mars assume high values.

6.6.2 Geopolymer samples made on small scale

Because of the limited amount of MGS-1 regolith material due to the high research costs, it was only suitable, from an economic point of view, to make small samples. A maximum amount of 20 kg of MGS-1 was available for this study. For the cube geopolymers, cube molds of 20x20x20 mm are used. A cylindrical mould of ∅20x40 mm was used for the cylindrical geopolymers. By using these small samples, the question has to be asked whether the compressive strength will assume a different value than in the case of large samples. Compressive strength is expressed as a force per unit area. By definition, the change in area does not affect the value of the compressive strength, since a smaller surface must be able to withstand a lower compressive force in order to obtain the same compressive strength as that of a large surface.

In reality, a deviation in the value for the compressive strength is observed if small samples are used. For example, the compaction of the material will be a critical parameter for small samples. A small inaccuracy in the compaction will therefore be reflected in a greater impact on the end result than if larger samples are used. Overall, it can be concluded that samples on a larger scale give more representative results for the compressive strength.

6.6.3 Addition of sodium hydroxide due to poor solubility

Due to the poor solubility of the lithium hydroxide in the sodium silicate solution, sodium hydroxide pellets were used to catalyse the reaction. Choosing to generate an exothermic reaction by adding sodium hydroxide is not the most efficient way to increase the solubility. To increase the solubility, the sodium silicate solution could already be preheated. In the phase of the laboratory work during the research, this was not extensively considered. No other ways were investigated to increase the solubility of the lithium hydroxide.

In retrospect, there are several influencing factors that determine the solubility of a substance. For example, factors such as temperature, pressure and polarity are the most important to determine whether a substance is well soluble. As already applied in this case of poor solubility of lithium hydroxide in the sodium silicate solution, the increase in temperature has a positive influence on the solubility of a substance.

In addition, the pressure mainly ensures that gases dissolve more easily. The pressure is therefore of less importance when it comes to alkali liquids. This is an important advantage for producing geopolymers on Mars, as the pressure on Mars is almost negligible. As a last important influencing factor, the polarity plays a major role in determining the degree of solubility. Polar substances dissolve more easily in a polar solvent, while apolar substances dissolve more easily in apolar solvents.

From this experiential knowledge, it can mainly be concluded that the preparation of the laboratory work is a crucial point. If problems arise during the performance of the laboratory work, this must also be considered critically.

7 CONCLUSIONS

This Master's thesis with the aim of developing a suitable geopolymer binder from in situ raw materials to build on Mars was a challenge for me. The research question is critically investigated by performing a combination of literature review and laboratory work:

"How can we develop a series of geopolymers from in situ Martian materials to build on Mars?"

A systematic approach by dividing this research question into five different work packages led to the success of this Master's thesis. Initially, it can be concluded that there are several challenges to make building and populating of the planet Mars possible. The extreme temperature variations, strong galactic cosmic rays and low pressure on Mars were examined. The materials for building on Mars must be able to withstand these extreme conditions. Geopolymers are used during this research because they require less water and energy than for the production of traditional Portland cement, and water is a scarce resource on Mars.

An innovative part of the research is that lithium hydroxide was used as activator for the geopolymerisation. Jones *et al*. (2020) showed that lithium hydroxide can provide good resistance to radiation. To withstand the intense radiation on Mars, lithium hydroxide was used as alkali activator. For the investigation of simulated Martian raw regolith, lithium hydroxide has not previously been used to activate the geopolymerisation mechanism. Chen *et al*. (2012) conducted a study on the production of geopolymer bricks with 10M LiOH-based geopolymers. A compressive strength of 9.4 MPa was measured after curing for 7 days at a temperature of 40 °C. Compared to the average compressive strength of 30 MPa for the 8M $\mathrm{LiOH.H_2O} + 7.5\ \mathrm{g\ NaOH}$ -based geopolymers and 34 MPa for the 10M $\mathrm{LiOH.H_2O} + 5\ \mathrm{g\ NaOH}$ -based geopolymers, the compressive strengths reached in this Master's thesis research are 3 to 4 times higher than in the study Chen *et al*. (2012). Furthermore, hardly any studies were performed for the geopolymerisation with lithium hydroxide as alkali activator.

Through a detailed literature review, various mix designs were drawn up in which the concentration of alkali activator was set as a variable. In total, 11 and 7 different geopolymer mixtures were used for cube and cylindrical geopolymer samples, respectively. From the results of the mechanical and chemical characterisation the most optimal geopolymer mixture could be determined.

The results showed that the cube geopolymer samples are less reliable and representative in the results for the compressive strength. This is because a difficult uniform compaction could be performed for these geopolymer mixtures. The cylindrical geopolymer samples were compacted with the pellet press in four different layers, making the compressive strength results for these geopolymers more reliable than those of the cube geopolymer samples. The final conclusion from the laboratory tests is that the $\mathrm{LiOH.H_2O} + 7.5\ \mathrm{g\ NaOH}$ -based geopolymers give the best results for compressive strength. Since lithium hydroxide achieved better results for compressive strength than sodium hydroxide, this is a positive and encouraging message to conduct further research with lithium hydroxide as activator.

The results of the laboratory work are satisfactory. When both the results of the cube and cylinder geopolymer samples are analysed, the same trends in final strength and strength development are found for the geopolymers based on 8M $\mathrm{LiOH.H_2O} + 5\ \mathrm{g\ NaOH}$, 6M

$\mathrm{LiOH.H_2O}$ + 7,5 g NaOH and 8M $\mathrm{LiOH.H_2O}$ + 7,5 g NaOH. Since these representative results for the compressive strengths of both the cube and cylindrical geopolymer samples occur with the LiOH-based geopolymers, a strong geopolymer matrix is obtained.

The results for the compressive strengths of both the cube and cylindrical geopolymer samples, with oven curing for 7 days at a temperature of 70 °C, are as follows:

8M $\mathbf{LiOH.H_2O}$ + 5 g NaOH	cube: 20 $\pm$ 8 MPa	cylinder: 21 $\pm$ 4 MPa
6M $\mathbf{LiOH.H_2O}$ + 7,5 g NaOH	cube: 22 $\pm$ 5 MPa	cylinder: 27 $\pm$ 5 MPa
8M $\mathbf{LiOH.H_2O}$ + 7,5 g NaOH	cube: 23 $\pm$ 3 MPa	cylinder: 30 $\pm$ 2 MPa

The most optimal geopolymer mixture during this research is defined at **8M $\mathbf{LiOH.H_2O}$ + 7,5 g NaOH**. A combination of alkali activators lithium hydroxide and sodium hydroxide was added to a sodium silicate solution with chemical composition of 7.9 % $\mathrm{Na_2O}$ and 25.9 % $\mathrm{SiO_2}$. Metakaolin was used as an additive for the simulated Mars raw regolith MGS-1 material. The volume ratio for the liquid activator/aluminosilicate material was set at 0.3. In addition, the volume ratio for the metakaolin/MGS-1 was fixed at 0.2.

The FTIR analysis for the highest compressive strength geopolymers show three distinct peaks according to the wavelength spectrum. The first two peaks at wavelengths of 3350 $\mathrm{cm^{-1}}$ and 1630 $\mathrm{cm^{-1}}$ are respectively related to the stretching vibrations of $-\mathrm{OH}$ groups and water molecules. The peak observed at wavelength of 967 $\mathrm{cm^{-1}}$ represents the $\mathrm{Si-O-Si}$ asymmetric stretching vibrations in the geopolymer mixture.

The use of lithium hydroxide as an alkali activator can certainly be further investigated. In this research, an impetus was already given to further research, in which better results are obtained for lithium hydroxide than for sodium hydroxide when added to sodium silicate. This gives an innovative quality to this Master's thesis, making a contribution to contemporary industrial developments and changes in society.

Thanks to a critical research attitude and an efficient division of the laboratory work, I was able to successfully complete this Master's thesis. As a result, it can finally be concluded that the aim of the research was achieved by offering added value and social relevance.

8 FUTURE RESEARCH

This research can be seen as an exploration through the extensive field of interest in the world of geopolymers. A rough mix design was set up to vary as many different parameters as possible. It was important to discover the influence of the different parameters. The good results that were found in this research project may serve as an impetus for further research.

8.1 Standards and regulations

In the future, the focus should also be on setting standards and guidelines to enable building on the planet Mars. Such standards must state clear minimum requirements that the design and production of geopolymers must meet. This standards contain information at which a good geopolymer mixture must meet in order to be suitable for building on Mars. For example, a critical mix design can be identified, which must be respected to keep building on Mars possible and, above all, safe.

To draw up such standards and regulations, it is necessary to have a good knowledge of all foreseeable forces and engaging actions. For example, further in-depth research will have to be done on the different types of radiation, the extreme atmospheric conditions, and their interaction with different materials.

8.2 Smart and efficient building technologies

In addition to search an optimal geopolymer and draw up standards, consideration must also be given to the practical implementation of building on Mars. For example, in first instance a business plan must be drawn up for the transport of humans and machines to the planet. The aim is to achieve the highest possible degree of automation. For example, techniques such as 3D printing of architectural structures can offer added value to build efficiently on Mars. Particular attention should be paid to the processability of the structural elements to be printed.

A study by Kading & Straub (2015) has already examined the possibility of 3D printing on Mars. It is the intention that robot constructions form a functional basis for human habitation on the Red Planet. The emphasis is mainly on the advancement of technological aspects.

Another study by Yashar *et al*. (2019) mainly focuses on the architectural principles that must be respected to enable the 3D printing of structures on Mars. Before the 3D printing technology of geopolymer concrete is possible, the preconditions must be met. By this we mean a suitable viscosity and temperature of the geopolymer mixture to enable 3D printing. For this, controlled atmosphere conditions must be possible in order to keep the efficiency of the construction process as high as possible.

The principles for processing an ISRU based concrete material are discussed. In addition, the physiological and psychological well-being of astronauts is also taken into account, in order to protect them against all kinds of harmful radiation patterns and to provide the necessary amount of light in the structure. However, it is not the intention to build one massive structure, but a smart structure with many facilities to make life easier.

8.3 Development of innovative concrete types

8.3.1 Sulfur concrete

A research from 2016 by a group of scientists at University's McCormick of Engineering resulted in a 3D printable concrete made entirely from local materials on Mars. In situ resources were also used in this research. Molten sulfur was used for the production of the innovative concrete type. The advantage of using sulfur as a raw material for concrete is that it is abundant on the Red Planet.

This type of concrete hardens in just two to three hours, making it potential for 3D printing purposes. Besides the advantage that sulfur fractions are present in excess on Mars, this also has the positive property that it is resistant to corrosion. The sulfur concrete does not only act as a binding agent for the various components, it also reacts with the minerals in the Mars' soil. This creates a compact structure that is well anchored to the Martian surface. This is due to the good cooperation between the sulfur and the Mars regolith material.

A recent study was conducted by Li *et al*. (2021) on the reaction mechanism during the production of sulfur concrete. Figure 122 shows visually how the sulphate particles react with the ferrous particles (a) under the influence of increased temperature, to obtain molten sulfur (b). Finally, after hardening, a rigid concrete structure has been formed (c).

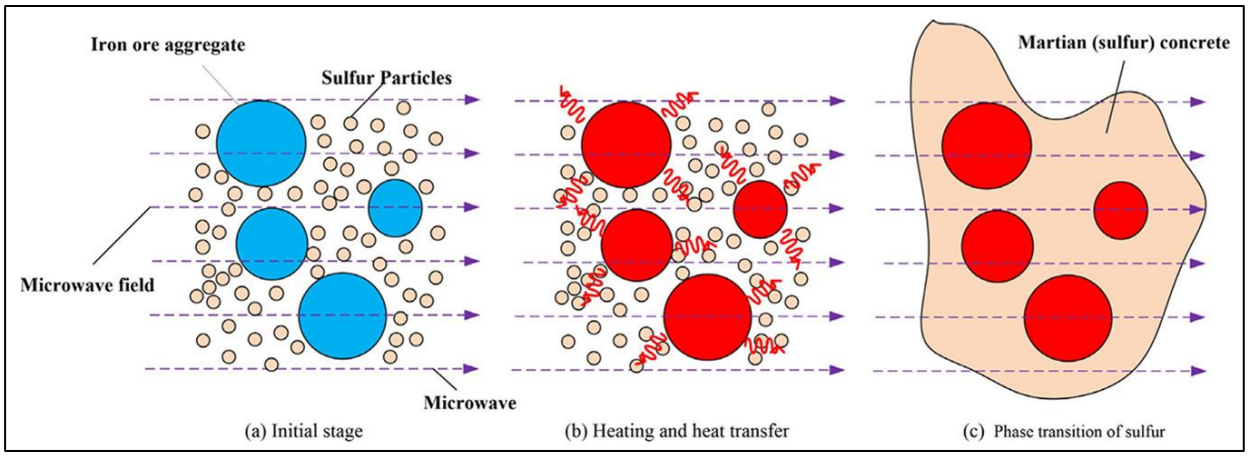

Figure 122: Formation of Martian sulfur concrete. (Li *et al*., 2021)

8.3.2 Natural 'living' concrete

In addition to the research on 3D printing of sulfur concrete, a study was conducted in 2020 on natural 'living' concrete. This research was conducted by scientists from the University of Colorado Boulder. The secret behind the production of this 'living' concrete is in fact the use of gelatin. In addition to gelatin, the cyanobacterium is also used, which is better known as blue-green algae. The advantage of such 'living' concrete is that it is quick and easy to make, as the growth of the bacteria increases exponentially with the exposure to photosynthesis. In addition, the concrete structure has a self-healing property due to the bacterial compositions. In addition to the presence of light, bacteria also need a suitable temperature in order to survive. The widely varying temperature on the planet Mars is therefore a critical point in the design of this type of concrete. Hence, further research needs to be carried out on the

behaviour of the strength development of the concrete after exposure to strongly fluctuating temperatures.

A disadvantage of this natural concrete is that it is less strong than the traditional concrete used on Earth, which is made of traditional cement as binder. But this natural concrete has no problem supporting a 75 kg person after ambient curing for 28 days. In the tests for determining the compressive strength of the concrete, cube shaped test samples of 10x10 mm² were made. In this way, this 'living' concrete still achieves a compressive strength of around $7.36\ \mathrm{MPa}$, which is an acceptable strength for infrastructure purposes.

$$\sigma = \frac{\mathrm{F}}{\mathrm{A_{beam}}} = \frac{75\ \mathrm{kg} \times 9.81\ \mathrm{m/s^2}}{0.010\ \mathrm{m} \times\ 0.010\ \mathrm{m}} = 7.36 \times 10^6\ \mathrm{N/m^2} = 7.36\ \mathrm{MPa}$$

However, when this compressive strength is compared to that of geopolymers, the most optimal geopolymer mixtures achieve a strength that is more than twice as high, as compressive strengths of up to $30\ \mathrm{MPa}$ have been achieved with geopolymers in this research.

This type of natural concrete has a certain potential to be used as concrete on Mars, as it is a light material and, above all, easy to produce by the use of local natural resources. This building material has beneficial ecological and logistic properties for potential use on Mars. However, the research in this Master's thesis shows that the use of geopolymers in terms of strength is more suitable than the use of natural 'living' concrete.

8.4 Body fluids as raw materials

In 2021, researchers at the University of Manchester have developed a range of creative building materials based on astronaut body fluids and Mars regolith material. Through blood, urine and sweat, a mixture is made that develops the strength of a traditional low-strength concrete on Earth. The use of blood is applied for the production to make the grout more fluid, which generally results in better properties. The proteins are mainly used from this blood, which are then clotted in order to act as a binder.

Water is filtered from urine, which must be added to the solid substance. The use of water for the production of building materials is a critical point here, due to the small presence on Mars. The astronauts would rather drink this precious water themselves, rather than use it as a raw material for the production of building materials. The optimum amount of water to be added to the mixture must be well described in advance. An excessive amount of water will result in a lower strength because there will be more voids in the concrete. However, if too little water is added, a strong mixture will be obtained, but then you compromise on workability.

By using these natural human body fluids, lower strength is obtained than the concrete used on Earth. An advantage of the planet Mars is that its gravity is only 38 % of that on Earth. This means that the structures on Mars must be made less strong than on Earth, although it must be ensured that the structures can offer sufficient resistance against possible meteorite impacts or against fierce dust storms. These dust storms have been characterised as the most determining load in the design of structures on Mars. While gravity creates vertical loads, these dust storms will generate horizontal loads on the local structures. As mentioned in section 3.1.4.2, these dust storms can reach wind speeds of up to 40 m/s. Compared to the average wind speed in Belgium of 20.6 m/s, this is an extremely high value. The maximum measured wind speed in Belgium dates from 1990, with a value of 46.7 m/s. As a result, local pressure differences and sediment transported by the wind generate additional forces on the structures.

8.5 Mars exploration: scientific problems

8.5.1 Mining of raw building materials

Further research must certainly be carried out into possibilities for efficient mining of the raw materials. For example, the clay minerals in the form of kaolinite and the alkali activators are considered. Extensive research is needed into the presence of ores and various raw materials on the surface and in the soil of Mars. The locations on Mars where these resources are present must be clearly indicated for the first Mars missions. In addition, a feasibility study must also be made, which clearly highlights all possible risks of the extraction and mining purposes.

From a study by Reches (2019) into the different possible concrete types on Mars, an overview is given of the different identified raw materials on the planet. Currently, rovers are further investigating the various rocks and soil types on Mars. Figure 123 shows an overview of several raw materials already registered on Mars, and it also shows a map of the amount of water available on the surface of the planet Mars.

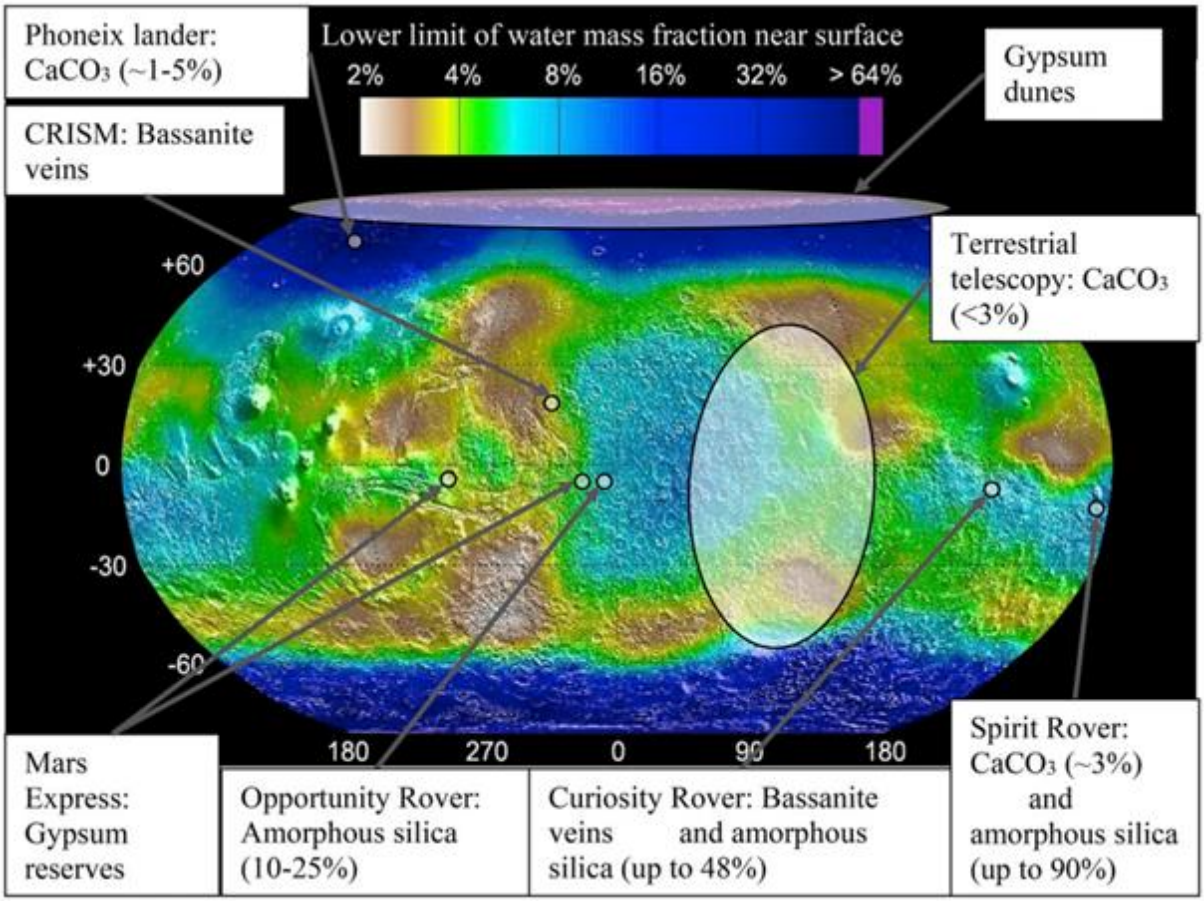

Figure 123: Possible resources on Mars for binder production. (Reches, 2019)

From this graphical representation, it can be concluded that a large amount of amorphous silica is mainly present on Mars, and this raw material was identified at three different locations by three different rovers. The large presence of amorphous silica has a positive effect on the possibility to use the aluminosilicate-rich soil of Mars as a geopolymer precursor.

Possible additives such as gypsum and calcium carbonate are established on the planet to a lesser extent. Further research should reveal where other potentially interesting ores are

available on the planet Mars. New building materials, such as more advanced geopolymer binders, can then be developed from these new raw materials. The research into possible raw materials for building purposes on Mars, is certainly not over yet.

8.5.2 Production of geopolymers on Mars

The production of the geopolymers must be possible under controlled conditions. The natural environment of Mars is not suitable for this because of the extremely low pressure and rapidly varying temperatures. The temperature and pressure must be kept constant so that the alkali liquids can be made to activate the geopolymer precursors. In the broad context, a design has to be made of a spaceship with a closed shell. From this closed whole it must be made possible to erect structures. This means that new ideas about smart construction methods need to be developed that make building possible from the inside out.

8.5.3 Water entrapped in rocks and sand

The presence of water on Mars has been investigated several times by NASA. Beginning in the 1970s, the first traces of water had been detected on the Red Planet by space probes Mariner 9 and Viking. One of the most recent indications of the presence of water on Mars comes from a group of researchers at the National Institute of Astrophysics in Italy. This 2018 study published that a lake about 20 kilometers across had been found, located a mile below the Martian surface.

Also in the same year, several scientists at the US Geological Survey claimed that eight regions had been found where erosion has uncovered large ice deposits between one and a hundred meters below the surface of the planet Mars. It soon becomes clear that there is still uncertainty about the presence of water on the surface of the planet. Hence, further research needs to be carried out to create more scientific certainty about this.

8.5.4 Thin Martian atmosphere

A suitable atmosphere is one of the most important characteristics a planet needs to support human life. For the planet Mars, this atmosphere consists of a very thin layer, and it contains the wrong harmful gases, such as the excessive amount of CO_2. Hence, methods have to be studied that make it possible to convert the carbon dioxide from the air into oxygen, as was already discussed with the MOXIE experiment in the introduction.

8.5.5 High levels of radiation

Further research needs to be carried out into the influence of the radiation on Mars on the human body. Harmful radiation easily penetrates the thin atmosphere of the planet Mars. The sun and all the stars can be thought of as fusion reactors that emit large amounts of electromagnetic radiation, including large fractions of X-ray and ultraviolet radiation. The centers of galaxies also emit high-energy protons. This can cause radiation sickness. In addition, radiation can strongly adversely affect the central nervous system of people. Furthermore, the presence of radiation significantly increases the risk of diseases such as cancer and other degenerative diseases.

References

Adachi, H., Uchida, K. I., Saitoh, E., & Maekawa, S. (2013). Theory of the spin Seebeck effect. *Reports on Progress in Physics*, *76*(3), 036501.

Albert, M. J. (2020). The dangers of decoupling: earth system crisis and the 'Fourth Industrial Revolution'. *Global Policy*, *11*(2), 245-254.

Aleem, M. A., & Arumairaj, P. D. (2012). Geopolymer concrete–a review. *International journal of engineering sciences & emerging technologies*, *1*(2), 118-122.

Alexiadis, A., Alberini, F., & Meyer, M. E. (2017). Geopolymers from lunar and Martian soil simulants. *Advances in Space Research*, *59*(1), 490-495.

Almutairi, A. L., Tayeh, B. A., Adesina, A., Isleem, H. F., & Zeyad, A. M. (2021). Potential applications of geopolymer concrete in construction: A review. *Case Studies in Construction Materials*, *15*, e00733.

Arioz, E., Arioz, Ö., & Koçkar, Ö. M. (2013). The effect of curing conditions on the properties of geopolymer samples. *International Journal of Chemical Engineering and Applications*, *4*(6), 423.

Aryal, N., Chen, J., Bhattarai, K., Hennrich, O., Handayani, I., Kramer, M., ... & Gross, H. (2022). High Plasticity of the Amicetin Biosynthetic Pathway in Streptomyces sp. SHP 22-7 Led to the Discovery of Streptcytosine P and Cytosaminomycins F and G and Facilitated the Production of 12F-Plicacetin. *Journal of Natural Products*, *85*(3), 530-539.

Ashbrook, J. (1953). A new determination of the rotation period of the planet Mars. *The Astronomical Journal*, *58*, 145.

Atiş, C. D., Görür, E. B., Karahan, O. K. A. N., Bilim, C., İlkentapar, S. E. R. H. A. N., & Luga, E. (2015). Very high strength (120 MPa) class F fly ash geopolymer mortar activated at different NaOH amount, heat curing temperature and heat curing duration. *Construction and building materials*, *96*, 673-678.

Atkin, B., & Skitmore, M. (2008). Stakeholder management in construction. *Construction management and economics*, *26*(6), 549-552.

Aupoil, J., Champenois, J. B., de Lacaillerie, J. B. D. E., & Poulesquen, A. (2019). Interplay between silicate and hydroxide ions during geopolymerization. *Cement and Concrete Research*, *115*, 426-432.

Baker, C. L., Jue, L. R., & Wills, J. H. (1950). The system Na2O-SiO2-H2O at 50, 70 and 90°. *Journal of the American Chemical Society*, *72*(12), 5369-5382.

Bakharev, T. (2005). Resistance of geopolymer materials to acid attack. *Cement and concrete research*, *35*(4), 658-670.

Barrer, R. M. (1982). *Hydrothermal chemistry of zeolites*. Academic press.

Bassil, N. M., Bewsher, A. D., Thompson, O. R., & Lloyd, J. R. (2015). Microbial degradation of cellulosic material under intermediate-level waste simulated conditions. *Mineralogical Magazine*, *79*(6), 1433-1441.

Bell, J. L., Sarin, P., Provis, J. L., Haggerty, R. P., Driemeyer, P. E., Chupas, P. J., van Deventer, J. S. J., Kriven, W. M. (2008) Atomic structure of a cesium aluminosilicate geopolymer : A pair distribution function study, *Chemistry of Materials,* 20(14), 4768-4776. doi:10.1021/cm703369s.

Bernal, S. A., Provis, J. L., Mejía de Gutiérrez, R., & van Deventer, J. S. (2015). Accelerated carbonation testing of alkali-activated slag/metakaolin blended concretes: effect of exposure conditions. *Materials and Structures*, *48*(3), 653-669.

Bernal, S. A., van Deventer, J. S., & Provis, J. L. (2015). What happens to 5 year old metakaolin geopolymers' the effect of alkali cation. In *Calcined Clays for Sustainable Concrete* (pp. 315-321). Springer, Dordrecht.

Bish, D. L., Blake, D. F., Vaniman, D. T., Chipera, S. J., Morris, R. V., Ming, D. W., ... & Gaboriaud, A. (2013). X-ray diffraction results from Mars Science Laboratory: Mineralogy of Rocknest at Gale crater. *science*, *341*(6153), 1238932.

Boeder, P. A., & Soares, C. E. (2020, August). Mars 2020: mission, science objectives and build. In *Systems Contamination: Prediction, Control, and Performance 2020* (Vol. 11489, p. 1148903). SPIE.

Cannon, K. M., Britt, D. T., Smith, T. M., Fritsche, R. F., & Batcheldor, D. (2019). Mars global simulant MGS-1: A Rocknest-based open standard for basaltic martian regolith simulants. *Icarus*, *317*, 470-478.

Carlile, M. J., Watkinson, S. C., & Gooday, G. W. (2001). *The fungi*. Gulf Professional Publishing.

Certini, G., Karunatillake, S., Zhao, Y. Y. S., Meslin, P. Y., Cousin, A., Hood, D. R., & Scalenghe, R. (2020). Disambiguating the soils of mars. *Planetary and Space Science*, *186*, 104922.

Chakraborty, S. (2019). *Geopolymerization of Simulated Martian Soil* (Doctoral dissertation, Tennessee Technological University).

Chen, C., Li, Q., Shen, L., & Zhai, J. (2012). Feasibility of manufacturing geopolymer bricks using circulating fluidized bed combustion bottom ash. *Environmental technology*, *33*(11), 1313-1321.

Chen, K., Wu, D., Xia, L., Cai, Q., & Zhang, Z. (2021). Geopolymer concrete durability subjected to aggressive environments–a review of influence factors and comparison with ordinary Portland cement. *Construction and Building Materials*, *279*, 122496.

Chinyio, E., Singh, S., & Suresh, S. (2022). A review of stakeholder management in construction. *Research Companion to Construction Economics*, 422-444.

Christensen, T. H. (2011). Introduction to waste management. In *Solid Waste Technology and Management* (pp. 3-16). Wiley.

Cleland, D. I. (1995). Leadership and the project-management body of knowledge. *International Journal of Project Management*, *13*(2), 83-88.

Cohen-Adad, R., Tranquard, A., Peronne, R., Negri, P., & Rollet, A. P. (1960). Le systeme eau-hydroxyde de sodium. *Comptes Rendus Hebdomadaires Des Seances De L Academie Des Sciences*, *251*(19), 2035-2037.

Cortesão, M., Schütze, T., Marx, R., Moeller, R., & Meyer, V. (2020). Fungal biotechnology in space: why and how?. In *Grand Challenges in Fungal Biotechnology* (pp. 501-535). Springer, Cham.

Criado, M., Palomo, A., & Fernández-Jiménez, A. (2005). Alkali activation of fly ashes. Part 1: Effect of curing conditions on the carbonation of the reaction products. *Fuel*, *84*(16), 2048-2054.

D'Elia, A., Pinto, D., Eramo, G., Laviano, R., Palomo, A., & Fernández-Jiménez, A. (2020). Effect of alkali concentration on the activation of carbonate-high illite clay. *Applied Sciences*, *10*(7), 2203.

Dadachova, E., Bryan, R. A., Huang, X., Moadel, T., Schweitzer, A. D., Aisen, P., ... & Casadevall, A. (2007). Ionizing radiation changes the electronic properties of melanin and enhances the growth of melanized fungi. *PloS one*, *2*(5), e457.

Dass, R. S. (2017). The high probability of life on mars: a brief review of the evidence. *Cosmology*, *27*, 62-73.

Davidovits, J. (1928a) The need to creat a new technical language for the transfer of basic scientific information. *Transfer and Exploitation of Scientific and Technical Information, EUR7716.* Luxembourg, Commission of the European Communities.

Davidovits, J. (1928b) Mineral polymers and methods of making them, U.S. Patent 4,349,386.

Davidovits, J. (1984) Synthetic mineral polymer compound of the silicoaluminates family and preparation process, U.S. Patent 4,472,199.

Davidovits, J. (1994, October). Properties of geopolymer cements. In *First international conference on alkaline cements and concretes* (Vol. 1, pp. 131-149). Kiev, Ukraine: Kiev State Technical University.

Davis, J. M., Balme, M., Grindrod, P. M., Williams, R. M. E., & Gupta, S. (2016). Extensive Noachian fluvial systems in Arabia Terra: Implications for early Martian climate. *Geology*, *44*(10), 847-850.

Diamond, S. (1986). Particle morphologies in fly ash. *Cement and Concrete Research*, *16*(4), 569-579.

Dobrijevic, M., & Bertrix, I. (2022). Les satellites de Jupiter et la troisième loi de Kepler.

Dundas, C. M., Bramson, A. M., Ojha, L., Wray, J. J., Mellon, M. T., Byrne, S., ... & Sutton, S. (2017, December). Ice exposures and landscape evolution in the Martian mid-latitudes. In *AGU Fall Meeting Abstracts* (Vol. 2017, pp. P52C-05).

Dupuis, R., Pellenq, R., Champenois, J. B., & Poulesquen, A. (2020). Dissociation mechanisms of dissolved alkali silicates in sodium hydroxide. *The Journal of Physical Chemistry C*, *124*(15), 8288-8294.

Duxson P., Lukey, G. C., Separovic, F., Kriven W. M. and van Deventer J. S. J. (2005a) Modeling speciation in highly concentrated alkaline silicate solution. *Industrial and Engineering Chemistry Research,* 44, 8899-8908. doi:10.1021/ie050700i.

Duxson, P., and Provis, J. L. (2008) Designing precursors for geopolymers cements. *Journal of the American Ceramic Society,* 91, 3864-3869. doi :10.1111/j.1551-2916.2008.02787.x

Duxson, P., Fernandez-Jiménez, A., Provis, J. L., Lukey, G. C., Palomo A. and van Deventer J. S. J. (2007). 'Geopolymer technology : the current state of the art.' *Journal of Materials Science,* 42: 2917-2933.

Duxson, P., Lukey, G. C., Separovic, F. and van Deventer, J. S. J. (2005) The effect of alkali cations on aluminum incorporation in geopolymeric gels. *Industrial and Engineering Chemistery Research,* 44, 832-839. doi :10.1021/ie0494216.

Duxson, P., Mallicoat, S. W., Lukey, G. C., Kriven W.M. and van Deventer J. S. J. (2005). 'Understanding the relationship between geopolymer composition, microstructure and mechanical properties.' *Colliods and Surfaces A: Physiochemical and Engineering Aspect,* 269: 47-58.

Duxson, P., Mallicoatn S. W., Lukey, G. C., Kriven W. M. and van Deventer J. S. J. (2007) The effect of alkali and Si/Al ratio on the development of mechanical properties of metakaolin-based geopolymers. *Colliods and Surfaces A – Physicochemical and Engineering Aspects,* 292, 8-20. doi:10.1016/j.colsurfa.2006.05.044.

Elwell, D. J., & Fu, G. (1995). *Compression testing of concrete: cylinders vs. cubes* (No. FHWA/NY/SR-95/119).

Fairén, A. G., Davila, A. F., Gago-Duport, L., Amils, R., & McKay, C. P. (2009). Stability against freezing of aqueous solutions on early Mars. *Nature*, *459*(7245), 401-404.

Favier, A., Hot, J., Habert, G., de Lacaillerie, J. B. D. E., & Roussel, N. (2013, September). Rheology of geopolymer: comparative study between Portland cement and metakaolin based geopolymer. In *1st RILEM International Conference on Rheology and Processing of Construction Materials., RILEM Publications sarl, Paris: France* (pp. 49-56).

Favier, A., Hot, J., Habert, G., Roussel, N., & de Lacaillerie, J. B. D. E. (2014). Flow properties of MK-based geopolymer pastes. A comparative study with standard Portland cement pastes. *Soft Matter*, *10*(8), 1134-1141.

Feng, L., & Chen, Z. L. (2008). Research progress on dissolution and functional modification of cellulose in ionic liquids. *Journal of Molecular Liquids*, *142*(1-3), 1-5.

Fernandez-Jiménez, A. and Palomo, A. (2003) Characterisation of fly ashes. Potential reactivity as alkaline cements. *Fuel,* 82,2259-2265. doi:10.1016/S0016-2361(03)00194-7.

Fernández-Jiménez, A., Palomo, A., Sobrados, I., & Sanz, J. (2006). The role played by the reactive alumina content in the alkaline activation of fly ashes. *Microporous and Mesoporous materials*, *91*(1-3), 111-119.

Gaboriaud, F., Nonat, A., Chaumont, D., & Craievich, A. (1999). Aggregation and gel formation in basic silico− calco− alkaline solutions studied: a SAXS, SANS, and ELS study. *The Journal of Physical Chemistry B*, *103*(28), 5775-5781.

Gavezzotti, A. (2021). Organic crystal nucleation and growth: Little knowledge, much mystery. In *Theoretical and Computational Chemistry* (Vol. 20, pp. 201-229). Elsevier.

Gavezzotti, A. (2021). *The Crystalline States of Organic Compounds* (Vol. 20). Elsevier.

Golitsyn, G. S. (1971). Estimates of boundary layer parameters in the atmospheres of the terrestrial planets. In *Symposium-International Astronomical Union* (Vol. 40, pp. 297-303). Cambridge University Press.

Golitsyn, G. S. (1973). On the Martian dust storms. *Icarus*, *18*(1), 113-119.

Golombek, M., Warner, N. H., Grant, J. A., Hauber, E., Ansan, V., Weitz, C. M., ... & Banerdt, W. B. (2020). Geology of the InSight landing site on Mars. *Nature communications*, *11*(1), 1-11.

Gurvich, L. V., Bergman, G. A., Gorokhov, L. N., Iorish V. S;, Leonidov, V. Y. and Yungman, V. S. (1997) Thermodynamic properties of alkali metal hdroxides. Part 2. Potassium, rubidium, and cesium hydroxides. *Journal of Physical and Chemical Reference Data,* 26, 1031-1110.

Gurvich, L. V., Bergman, G. A., Gorokhov, L. N., Iorish, V. S., Leonidov, V. Y., & Yungman, V. S. (1996). Thermodynamic properties of alkali metal hydroxides. Part 1. Lithium and sodium hydroxides. *Journal of Physical and Chemical Reference Data*, *25*(4), 1211-1276.

Haberle, R. M., Clancy, R. T., Forget, F., Smith, M. D., & Zurek, R. W. (Eds.). (2017). *The atmosphere and climate of Mars*. Cambridge University Press.

He, Y. T., Wan, J., & Tokunaga, T. (2008). Kinetic stability of hematite nanoparticles: the effect of particle sizes. *Journal of nanoparticle research*, *10*(2), 321-332.

Hecht, M., Hoffman, J., Rapp, D., McClean, J., SooHoo, J., Schaefer, R., ... & Ponce, A. (2021). Mars oxygen ISRU experiment (MOXIE). *Space Science Reviews*, *217*(1), 1-76.

Hos, J. P., McCormick, P. G., & Byrne, L. T. (2002). Investigation of a synthetic aluminosilicate inorganic polymer. *Journal of Materials Science*, *37*(11), 2311-2316.

Howell (2022), E. Mars missions: A brief history.

Huang, Y., Gong, L., Pan, Y., Li, C., Zhou, T., & Cheng, X. (2018). Facile construction of the aerogel/geopolymer composite with ultra-low thermal conductivity and high mechanical performance. *RSC advances*, *8*(5), 2350-2356.

Iler, R. K., (1979). *The Chemistry of Silica,* John Wiley and Sons Inc., 835pp.

Ilić, B., Radonjanin, V., Malešev, M., Zdujić, M., & Mitrović, A. (2016). Effects of mechanical and thermal activation on pozzolanic activity of kaolin containing mica. *Applied Clay Science*, *123*, 173-181.

Jakosky, B.M., Haberle, R.M. (1992). "The Seasonal Behavior of Water on Mars". In Kieffer, H.H.; et al. (eds.). *Mars*. Tucson, AZ: University of Arizona Press. pp. 969–1016.

Johnson, F. S. (1965). Atmosphere of mars. *Science*, *150*(3702), 1445-1448.

Johnson, T. E., Morrissey, L. J., Nemchin, A. A., Gardiner, N. J., & Snape, J. F. (2021). The phases of the Moon: Modelling crystallisation of the lunar magma ocean through equilibrium thermodynamics. *Earth and Planetary Science Letters*, *556*, 116721.

Jones, J. M., Mason, P. E., & Williams, A. (2019). A compilation of data on the radiant emissivity of some materials at high temperatures. *Journal of the Energy Institute*, *92*(3), 523-534.

Jones, J. P., Jones, S. C., Billings, K. J., Pasalic, J., Bugga, R. V., Krause, F. C., ... & Brandon, E. J. (2020). Radiation effects on lithium CFx batteries for future spacecraft and landers. *Journal of Power Sources*, *471*, 228464.

Kading, B., & Straub, J. (2015). Utilising in-situ resources and 3D printing structures for a manned Mars mission. *Acta Astronautica*, *107*, 317-326.

Kamps, O. M., Hewson, R. D., van Ruitenbeek, F. J. A., & van der Meer, F. D. (2020). Defining surface types of Mars using global CRISM summary product maps. *Journal of Geophysical Research: Planets*, *125*(8), e2019JE006337.

Kaneco, S., Iiba, K., Hiei, N. H., Ohta, K., Mizuno, T., & Suzuki, T. (1999). Electrochemical reduction of carbon dioxide to ethylene with high Faradaic efficiency at a Cu electrode in CsOH/methanol. *Electrochimica Acta*, *44*(26), 4701-4706.

Karlsen, J. T. (2002). Project stakeholder management. *Engineering Management Journal*, *14*(4), 19-24.

Karym, H., Chbihi, M. E. M., Benmokhtar, S., Belaaouad, S., & Moutaabbid, M. (2015). Caracterisation of the Kaolinite Clay Minerals (Nador-North Morocco) Using Infrared Spectroscopy and Calorimetry of Dissolution. *International Journal of Recent Scientific Research*, *6*, 4444-4448.

Kass, D. M., Schofield, J. T., Kleinböhl, A., McCleese, D. J., Heavens, N. G., Shirley, J. H., & Steele, L. J. (2020). Mars Climate Sounder observation of Mars' 2018 global dust storm. *Geophysical Research Letters*, *47*(23), e2019GL083931.

Kerr, R. A. (2013). "Radiation Will Make Astronauts' Trip to Mars Even Riskier". *Science*. 340 (6136): 1031.

Khalifa AZ, Cizer O, Pontikes Y et al. (2020) Advances in alkali-activation of clay minerals. *Cement and Concrete Research* 132: 106050

Kirchherr, J., Reike, D., & Hekkert, M. (2017). Conceptualizing the circular economy: An analysis of 114 definitions. *Resources, conservation and recycling*, *127*, 221-232.

Kriven, W. M., Bell, J. L., Mallicoat, S. W., & Gordon, M. (2007). Intrinsic microstructure and properties of metakaolin-based geopolymers. In *International Workshop on Geopolymer Binders-Interdependence of Composition, Structure and Properties* (p. 71).

Kumaravel, S., & Girija, K. (2014). Development of high-strength Geopolymer concrete. *Journal of Construction Engineering, Technology and Management*, *4*(1).

Lahoti, M., Tan, K. H., & Yang, E. H. (2019). A critical review of geopolymer properties for structural fire-resistance applications. *Construction and Building Materials*, *221*, 514-526.

Laliberte, M. (2007). Model for calculating the viscosity of aqueous solutions. *Journal of Chemical & Engineering Data*, *52*(2), 321-335.

Lam, L., Wong, Y. L., & Poon, C. S. (1998). Effect of fly ash and silica fume on compressive and fracture behaviors of concrete. *Cement and Concrete research*, *28*(2), 271-283.

Lambertin, D., Boher, C., Dannoux-Papin, A., Galliez, K., Rooses, A., & Frizon, F. (2013). Influence of gamma ray irradiation on metakaolin based sodium geopolymer. *Journal of nuclear materials*, *443*(1-3), 311-315.

Larsen, S. E., Jørgensen, H. E., Landberg, L., & Tillman, J. E. (2002). Aspects of the atmospheric surface layers on Mars and Earth. *Boundary-Layer Meteorology*, *105*(3), 451-470.

Lee, S., Kim, Y. J., & Moon, H. S. (2003). Energy-Filtering Transmission Electron Microscopy (EF-TEM) Study of a Modulated Structure in Metakaolinite, Represented by a 14 Å Modulation. *Journal of the American Ceramic Society*, *86*(1), 174-176.

Lee, W. K. W., & Van Deventer, J. S. J. (2003). Use of infrared spectroscopy to study geopolymerization of heterogeneous amorphous aluminosilicates. *Langmuir*, *19*(21), 8726-8734.

Leovy, C. (2001). Weather and climate on Mars. *Nature*, *412*(6843), 245-249.

Li, H., Meng, H., Lan, M., Zhou, J., Xu, M., Zhao, X., & Xiang, B. (2021). Development of a novel material and casting method for in situ construction on Mars. *Powder Technology*, *390*, 219-229.

Li, Q., Creaser, D., & Sterte, J. (2002). An investigation of the nucleation/crystallization kinetics of nanosized colloidal faujasite zeolites. *Chemistry of materials*, *14*(3), 1319-1324.

Li, X., & Gress, D. L. (2006). Mitigating Alkali–Silica Reaction in Concrete Containing Recycled Concrete Aggregate. *Transportation Research Record*, *1979*(1), 30-35.

Li, Z. and Liu, S. (2007) Influence of slag as additive on compressive strenght of fly ash-based geopolymer. *Journal of Materials in Civil Engineering,* 19, 470-474. doi:10.1061/(ASCE)0899-1561(2007)19:6(470)

Lin, K. L., Lo, K. W., Cheng, T. W., Lin, W. T., & Lin, Y. W. (2020). Influence of SiC sludge on the microstructure of geopolymers. *Materials*, *13*(9), 2203.

Lin, K. L., Lo, K. W., Cheng, T. W., Lin, W. T., & Lin, Y. W. (2020). Influence of SiC sludge on the microstructure of geopolymers. *Materials*, *13*(9), 2203.

Lingyu, T., Dongpo, H., Jianing, Z. & Hongguang, W. (2021). Durability of geopolymers and geopolymer concretes: A review. *REVIEWS ON ADVANCED MATERIALS SCIENCE*, 60(1), 1-14.

Liu, J., Li, H., Sun, L., Guo, Z., Harvey, J., Tang, Q., ... & Jia, M. (2021). In-situ resources for infrastructure construction on Mars: A review. *International Journal of Transportation Science and Technology*.

Liu, J., Michalski, J. R., & Zhou, M. F. (2021). Intense subaerial weathering of eolian sediments in Gale crater, Mars. *Science Advances*, *7*(32), eabh2687.

Livi, C. N., & Repette, W. L. (2017). Effect of NaOH concentration and curing regime on geopolymer. *Revista IBRACON de Estruturas e Materiais*, *10*, 1174-1181.

Livi, C. N., & Repette, W. L. (2017). Effect of NaOH concentration and curing regime on geopolymer. *Revista IBRACON de Estruturas e Materiais*, *10*, 1174-1181.

Lumley, J. S. (1993). The ASR expansion of concrete prisms made from cements partially replaced by ground granulated blast furnace slag. *Construction and Building Materials*, *7*(2), 95-99.

MacKenzie, K. J. D., Brown, I. W. M., Meinhold, R. H., & Bowden, M. E. (1985). Outstanding problems in the kaolinite-mullite reaction sequence investigated by 29Si and 27Al solid-state nuclear magnetic resonance: I, metakaolinite. *Journal of the American Ceramic Society*, *68*(6), 293-297.

MacKenzie, K. J., Brew, D. R., Fletcher, R. A., & Vagana, R. (2007). Formation of aluminosilicate geopolymers from 1: 1 layer-lattice minerals pre-treated by various methods: a comparative study. *Journal of materials science*, *42*(12), 4667-4674.

Madavarapu, S. B. (2014). *FTIR analysis of alkali activated slag and fly ash using deconvolution techniques*. Arizona State University.

Majidi, B. (2009). Geopolymer technology, from fundamentals to advanced applications: a review. *Materials Technology*, *24*(2), 79-87.

Masoumifard, N., Guillet-Nicolas, R., & Kleitz, F. (2018). Synthesis of engineered zeolitic materials: from classical zeolites to hierarchical core–shell materials. *Advanced Materials*, *30*(16), 1704439.

Massachusetts Institute of Technology. (2007, December 27). How Mars Could Have Been Warm And Wet But Limestone Free. *ScienceDaily*. Retrieved May 9, 2022 from www.sciencedaily.com

Mesalam, R., Williams, H. R., Ambrosi, R. M., Kramer, D. P., Barklay, C. D., García-Cañadas, J., ... & Weston, D. P. (2019). Impedance spectroscopy characterization of neutron irradiated thermoelectric modules for space nuclear power. *AIP Advances*, *9*(5), 055006.

Mills, J. N., Katzarova, M., & Wagner, N. J. (2022). Comparison of lunar and Martian regolith simulant-based geopolymer cements formed by alkali-activation for in-situ resource utilization. *Advances in Space Research*, *69*(1), 761-777.

Mittal, I., & Gupta, R. K. (2015). Natural resources depletion and economic growth in present era. *SOCH-Mastnath Journal of Science & Technology (BMU, Rohtak)(ISSN: 0976-7312)*, *10*(3).

Mo, B. H., Zhu, H., Cui, X. M., He, Y., & Gong, S. Y. (2014). Effect of curing temperature on geopolymerization of metakaolin-based geopolymers. *Applied clay science*, *99*, 144-148.

Mo, B. H., Zhu, H., Cui, X. M., He, Y., & Gong, S. Y. (2014). Effect of curing temperature on geopolymerization of metakaolin-based geopolymers. *Applied clay science*, *99*, 144-148.

Monnin, C., & Dubois, M. (2005). Thermodynamics of the LiOH+ H2O system. *Journal of Chemical & Engineering Data*, *50*(4), 1109-1113.

Montes, C., Broussard, K., Gongre, M., Simicevic, N., Mejia, J., Tham, J., ... & Davis, G. (2015). Evaluation of lunar regolith geopolymer binder as a radioactive shielding material for space exploration applications. *Advances in Space Research*, *56*(6), 1212-1221.

Nahm, Steven. (2015). Re: What's the significance of % transmittance in FTIR?. Retrieved from:https://www.researchgate.net/post/Whats-the-significance-of-transmittance-in-FTIR/

NASA, 2012. "Sodium hydroxide, NaOH, reacts the same as Lithium hydroxide and is much cheaper. Why NASA uses LiOH instead of NaOH on its space missions ?" *eNotes Editorial*

Naser, M. Z. (2019). Extraterrestrial construction materials. *Progress in materials science*, *105*, 100577.

Naser, M. Z., & Chehab, A. I. (2018). Materials and design concepts for space-resilient structures. *Progress in Aerospace Sciences*, *98*, 74-90.

Nath, S. K., Mukherjee, S., Maitra, S., & Kumar, S. (2017). Kinetics study of geopolymerization of fly ash using isothermal conduction calorimetry. *Journal of Thermal Analysis and Calorimetry*, *127*(3), 1953-1961.

Nazari-Sharabian, M., Aghababaei, M., Karakouzian, M., & Karami, M. (2020). Water on Mars—a literature review. *Galaxies*, *8*(2), 40.

Ng, L. M., & Simmons, R. (1999). Infrared spectroscopy. *Analytical chemistry*, *71*(12), 343-350.

Nordberg, M. E., Mochel, E. L., Garfinkel, H. M., & Olcott, J. S. (1964). Strengthening by ion exchange. *Journal of the American Ceramic Society*, *47*(5), 215-219.

Novais, R. M., Pullar, R. C., & Labrincha, J. A. (2020). Geopolymer foams: An overview of recent advancements. *Progress in Materials Science*, *109*, 100621.

Novikova, N. D., Pierson, D. L., Poddubko, S. V., Deshevaya, Y. A., Ott, C. M., Castro, V. A., & Bruce, R. J. (2009). Microbiology of the international space station. *US and Russian Cooperation in Space Biology and Medicine*, *5*, 263-278.

Paiva, H., Velosa, A., Cachim, P., & Ferreira, V. M. (2016). Effect of pozzolans with different physical and chemical characteristics on concrete properties. *Materiales de Construcción*, *66*(322), e083-e083.

Pan, J. W., Feng, Y. T., Wang, J. T., Sun, Q. C., Zhang, C. H., & Owen, D. R. J. (2012). Modeling of alkali-silica reaction in concrete: a review. *Frontiers of Structural and Civil Engineering*, *6*(1), 1-18.

Panda, B., Unluer, C., & Tan, M. J. (2018). Investigation of the rheology and strength of geopolymer mixtures for extrusion-based 3D printing. *Cement and Concrete Composites*, *94*, 307-314.

Papajohn, D., Brinker, C., & El Asmar, M. (2017). MARS: Metaframework for assessing ratings of sustainability for buildings and infrastructure. *Journal of Management in Engineering*, *33*(1), 04016026.

Paris, J. M., Roessler, J. G., Ferraro, C. C., DeFord, H. D., & Townsend, T. G. (2016). A review of waste products utilized as supplements to Portland cement in concrete. *Journal of Cleaner Production*, *121*, 1-18.

Pask, J. A. (1998). The Al 2 O 3-Sio 2 System: Logical Analysis of Phenomenological Experimental Data. In *Ceramic Microstructures* (pp. 255-262). Springer, Boston, MA.

Petrescu, R. V., Aversa, R., Apicella, A., Kozaitis, S., Abu-Lebdeh, T., & Petrescu, F. I. (2018). There is Life on Mars?. *American Journal of Engineering and Applied Sciences*, *11*(1), 78-91.

Pickering, S. U. (1893). LXI.—The hydrates of sodium, potassium, and lithium hydroxides. *Journal of the Chemical Society, Transactions*, *63*, 890-909.

Pla-García, J., Rafkin, S. C., Martinez, G. M., Vicente-Retortillo, Á., Newman, C. E., Savijärvi, H., ... & Harri, A. M. (2020). Meteorological predictions for Mars 2020 Perseverance Rover landing site at Jezero crater. *Space science reviews*, *216*(8), 1-21.

Provis, J. L. (2009). Activating solution chemistry for geopolymers. In *Geopolymers* (pp. 50-71). Woodhead Publishing.

Provis, J. L. and Vlachos, D. G. (2006) Silica nanoparticle formation in the TPAOH-TEOS-H2O system : A population balance model. *Journal of Physical Chemistry B,* 110,3098-3108. doi:10.1021/jp056658m.

Provis, J. L., & Rees, C. A. (2009). Geopolymer synthesis kinetics. In *Geopolymers* (pp. 118-136). Woodhead Publishing.

Provis, J. L., (2006), Ph.D. Thesis, Department of Chemical and Biomolecular Engineering, University of Melbourne.

Provis, J. L., Duxson, P., Lukey, G. C., Separovic, F., Kriven, W. M., & Van Deventer, J. S. (2005). Modeling speciation in highly concentrated alkaline silicate solutions. *Industrial & engineering chemistry research*, *44*(23), 8899-8908.

Provis, J. L., Lukey, G. C. and van Deventer, J. S. J. (2005b) Do geopolymers actually contain nanocrystalline zeolites? – A reexamination of existing results. *Chemistry of Materials,* 17, 3075-3085. doi:10.1021/cm050230i.

Provis, J. L., Muntingh, Y., Lloyd, R. R., Xu, H., Keyte, L. M., Lorenzen, L., ... & van Deventer, J. S. (2007, October). Will geopolymers stand the test of time?. In *Ceramic Engineering and Science Proceedings* (Vol. 28, No. 9, pp. 235-248).

Puligilla, S., & Mondal, P. (2015). Co-existence of aluminosilicate and calcium silicate gel characterized through selective dissolution and FTIR spectral subtraction. *Cement and Concrete Research*, *70*, 39-49.

Radnai, T., May, P. M., Hefter, G. T., & Sipos, P. (1998). Structure of aqueous sodium aluminate solutions: A solution X-ray diffraction study. *The Journal of Physical Chemistry A*, *102*(40), 7841-7850.

Rampe, E. B., Ming, D. W., Blake, D. F., Bristow, T. F., Chipera, S. J., Grotzinger, J. P., ... & Thompson, L. M. (2017). Mineralogy of an ancient lacustrine mudstone succession from the Murray formation, Gale crater, Mars. *Earth and Planetary Science Letters*, *471*, 172-185.

Reches, Y. (2019). Concrete on Mars: Options, challenges, and solutions for binder-based construction on the Red Planet. *Cement and Concrete Composites*, *104*, 103349.

Rees, C. A. (2007), PhD Thesis, Department of Chemical and Biomolecular Engineering, University of Melbourne.

Rees, C. A. (2007). *Mechanisms and kinetics of gel formation in geopolymers* (Doctoral dissertation).

Reyngold, M., Wu, A. J., McLane, A., Zhang, Z., Hsu, M., Stein, N. F., ... & Rimner, A. (2013). Toxicity and outcomes of thoracic re-irradiation using stereotactic body radiation therapy (SBRT). *Radiation oncology*, *8*(1), 1-7.

Rickard, W. D., Kealley, C. S., & Van Riessen, A. (2015). Thermally induced microstructural changes in fly ash geopolymers: Experimental results and proposed model. *Journal of the American Ceramic Society*, *98*(3), 929-939.

Rocha, J., & Klinowski, J. (1990). 29Si and 27Al magic-angle-spinning NMR studies of the thermal transformation of kaolinite. *Physics and Chemistry of Minerals*, *17*(2), 179-186.

Romagnoli, M., Leonelli, C., Kamse, E., & Gualtieri, M. L. (2012). Rheology of geopolymer by DOE approach. *Construction and Building Materials*, *36*, 251-258.

Roser, M., Ritchie, H., & Ortiz-Ospina, E. (2013). World population growth. *Our world in data*.

Rovnaník, P. (2010). Effect of curing temperature on the development of hard structure of metakaolin-based geopolymer. *Construction and building materials*, *24*(7), 1176-1183.

Sabir, B. B., Wild, S., & Bai, J. (2001). Metakaolin and calcined clays as pozzolans for concrete: a review. *Cement and concrete composites*, *23*(6), 441-454.

Saganti, P. B., Cucinotta, F. A., Wilson, J. W., Simonsen, L. C., & Zeitlin, C. (2004). Radiation climate map for analyzing risks to astronauts on the Mars surface from galactic cosmic rays. *2001 Mars Odyssey*, 143-156.

Sagoe-Crentsil, K., & Weng, L. (2007). Dissolution processes, hydrolysis and condensation reactions during geopolymer synthesis: Part II. High Si/Al ratio systems. *Journal of materials science*, *42*(9), 3007-3014.

Saleh, H. M., & Eskander, S. B. (2020). Innovative cement-based materials for environmental protection and restoration. In *New Materials in Civil Engineering* (pp. 613-641). Butterworth-Heinemann.

Sarraf-mamoory, R., Demopoulos, G.P. & Drew, R.A.L. Preparation of fine copper powders from organic media by reaction with hydrogen under pressure: Part II. The kinetics of particle

nucleation, growth, and dispersion. *Metall Mater Trans B* 27, 585–594 (1996). https://doi.org/10.1007/BF02915656

Shelby, J. E. (2005). Immiscibility/phase separation. In *Introduction to Glass Science and Technology* (pp. 51-71).

Sibly, R. M., & Hone, J. (2002). Population growth rate and its determinants: an overview. *Philosophical Transactions of the Royal Society of London. Series B: Biological Sciences*, *357*(1425), 1153-1170.

Simonson, J. M., Mesmer, R. E., & Rogers, P. S. Z. (1989). The enthalpy of dilution and apparent molar heat capacity of NaOH (aq) to 523 K and 40 MPa. *The Journal of Chemical Thermodynamics*, *21*(6), 561-584.

Singh, B., Ishwarya, G., Gupta, M., & Bhattacharyya, S. K. (2015). Geopolymer concrete: A review of some recent developments. *Construction and building materials*, *85*, 78-90.

Sipos, P. M., Hefter, G., & May, P. M. (2000). Viscosities and densities of highly concentrated aqueous MOH solutions (M+= Na+, K+, Li+, Cs+,(CH3) 4N+) at 25.0° C. *Journal of Chemical & Engineering Data*, *45*(4), 613-617.

Škvára, F., Kopecký, L., Nemecek, J., & Bittnar, Z. D. E. N. Ì. K. (2006). Microstructure of geopolymer materials based on fly ash. *Ceramics-Silikaty*, *50*(4), 208-215.

Smith, P. H., Bell III, J. F., Bridges, N. T., Britt, D. T., Gaddis, L., Greeley, R., ... & Wegryn, E. (1997). Results from the Mars Pathfinder camera. *Science*, *278*(5344), 1758-1765.

Snell, C., Tempest, B., & Gentry, T. (2017). Comparison of the thermal characteristics of portland cement and geopolymer cement concrete mixes. *Journal of Architectural Engineering*, *23*(2), 04017002.

Stella, P. M., & Herman, J. A. (2018). Mars Optimized Solar Cells.

Talling, B. (2002). Geopolymers give fire safety to cruise ships. *Geopolymers*.

Taylor, A. J., McDowell, J. C., & Elvis, M. (2022). Phobos and Mars orbit as a base for asteroid exploration and mining. *Planetary and Space Science*, *214*, 105450.

Thampi, T., Sreevidya, V., & Venkatasubramani, R. (2014). Strength studies on geopolymer mortar for ferro geopolymer water tank. *International Journal of Advanced Structures and Geotechnical Engineering*, *3*(2), 102-105.

Thomas, N. H., Ehlmann, B. L., Meslin, P. Y., Rapin, W., Anderson, D. E., Rivera-Hernández, F. & Wiens, R. C. (2019). Mars Science Laboratory observations of chloride salts in Gale crater, Mars. *Geophysical Research Letters*, *46*(19), 10754-10763.

Timoumi, R., François, P., Le Postollec, A., Dobrijevic, M., Grégoire, B., Poinot, P., & Geffroy-Rodier, C. (2022). Focused ultrasound extraction versus microwave-assisted extraction for extraterrestrial objects analysis. *Analytical and Bioanalytical Chemistry*, *414*(12), 3643-3651.

Tuyan, M., Andiç-Çakir, Ö., & Ramyar, K. (2018). Effect of alkali activator concentration and curing condition on strength and microstructure of waste clay brick powder-based geopolymer. *Composites Part B: Engineering*, *135*, 242-252.

Vail, J. G. (1952) *Soluble Silicates: Their Properties and Uses,* New York, Reinhold.

Van Chanh, N., Trung, B. D., & Van Tuan, D. (2008, November). Recent research geopolymer concrete. In *The 3rd ACF International Conference-ACF/VCA, Vietnam* (Vol. 18, pp. 235-241).

Van Deventer, J. S. J., Provis, J. L., Duxson, P., & Lukey, G. C. (2007). Reaction mechanisms in the geopolymeric conversion of inorganic waste to useful products. *Journal of hazardous materials*, *139*(3), 506-513.

Viviano-Beck, C. E., Murchie, S. L., Beck, A. W., & Dohm, J. M. (2017). Compositional and structural constraints on the geologic history of eastern Tharsis Rise, Mars. *Icarus*, *284*, 43-58.

Walpole, R. E., Myers, R. H., Myers, S. L., & Keying, E. Y. (2013). *Probability and Statistics for Engineers and Scientists: Pearson New International Edition*. Pearson Higher Ed.

Wan-En, O., Yun-Ming, L., Li-Ngee, H., Abdullah, M. M. A. B., & Shee-Ween, O. (2020, June). The Effect of Sodium Carbonate on the Fresh and Hardened Properties of Fly Ash-Based One-Part Geopolymer. In *IOP Conference Series: Materials Science and Engineering* (Vol. 864, No. 1, p. 012197). IOP Publishing.

Wang, G., Zhao, D., Sorte, E., Holmes, S., Conradi, M. S., & Majzoub, E. H. (2015). First-principles investigation of the solubility of the hydroxides and hydrides of alkali metals.

Wang, H., Li, H., & Yan, F. (2005). Synthesis and mechanical properties of metakaolinite-based geopolymer. *Colloids and Surfaces A: Physicochemical and Engineering Aspects*, *268*(1-3), 1-6.

Webster, C. R., Mahaffy, P. R., Atreya, S. K., Flesch, G. J., Farley, K. A., MSL Science Team, ... & Pinet, P. (2013). Low upper limit to methane abundance on Mars. *Science*, *342*(6156), 355-357.

Weldes, H. H., & Lange, K. R. (1969). Properties of soluble silicates. *Industrial & Engineering Chemistry*, *61*(4), 29-44.

Weng, L., & Sagoe-Crentsil, K. (2007). Dissolution processes, hydrolysis and condensation reactions during geopolymer synthesis: Part I—Low Si/Al ratio systems. *Journal of materials science*, *42*(9), 2997-3006.

Xu, H., & Van Deventer, J. S. J. (2000). The geopolymerisation of alumino-silicate minerals. *International journal of mineral processing*, *59*(3), 247-266.

Xu, H., & Van Deventer, J. S. J. (2000). The geopolymerisation of alumino-silicate minerals. *International journal of mineral processing*, *59*(3), 247-266.

Xu, H., Lukey, G. C. and van Deventer, J. S. J. (2004) The activation of Class C-, Class F-fly ash and blast furnace slag using geopolymerisation. *Proceeding of 8th CANMET/ ACI International Conference on Fly Ash, Silica Fume, Slag and Natural Pozzolans in Concrete,* Las Vegas, NV, Malhotra, V. M. (Ed.), 797-819.

Xue, Y., & Jin, S. (2013, December). Martian minerals components at Gale crater detected by MRO CRISM hyperspectral images. In *2013 2nd International Symposium on Instrumentation and Measurement, Sensor Network and Automation (IMSNA)* (pp. 1067-1070). IEEE.

Yang, X., Zhu, W., & Yang, Q. (2008). The viscosity properties of sodium silicate solutions. *Journal of Solution Chemistry*, *37*(1), 73-83.

Yaseen, S. A., Yiseen, G. A., & Li, Z. (2019). Elucidation of calcite structure of calcium carbonate formation based on hydrated cement mixed with graphene oxide and reduced graphene oxide. *ACS omega*, *4*(6), 10160-10170.

Yashar, M., Ciardullo, C., Morris, M., Pailes-Friedman, R., Moses, R., & Case, D. (2019, July). Mars x-house: Design principles for an autonomously 3D-printed ISRU surface habitat. 49th International Conference on Environmental Systems.

Zeitlin, C., Cleghorn, T., Cucinotta, F., Saganti, P., Andersen, V., Lee, K., ... & Badhwar, G. (2004). Overview of the Martian radiation environment experiment. *Advances in Space Research*, *33*(12), 2204-2210.

Zeri, M., S Alvalá, R. C., Carneiro, R., Cunha-Zeri, G., Costa, J. M., Rossato Spatafora, L., ... & Marengo, J. (2018). Tools for communicating agricultural drought over the Brazilian Semiarid using the soil moisture index. *Water*, *10*(10), 1421.

Zhan, Y., Song, K., Shi, Z., Wan, C., Pan, J., Li, D., ... & Jiang, L. (2020). Influence of reduction temperature on Ni particle size and catalytic performance of Ni/Mg (Al) O catalyst for CO2 reforming of CH4. *International Journal of Hydrogen Energy*, *45*(4), 2794-2807.

Zhang, Z., Wang, H., Provis, J. L., & Reid, A. (2013). Efflorescence: a critical challenge for geopolymer applications?. In *Concrete Institute of Australia's Biennial National Conference 2013* (pp. 1-10). Concrete Institute of Australia.

Ziyuan, O., & Fugen, X. (2011). Major scientific issues involved in Mars exploration. *Spacecraft Environment Engineering*, *28*(3), 205-217.

Annexes

Annex A	Geopolymer mix design calculations
Annex B	Planning schedule for laboratory work
Annex C	Compression test results - cube samples
Annex D	Compression test results - cylindrical samples
Annex E	FTIR results - cube samples
Annex F	FTIR results - cylindrical samples

Accompanying explanation with annexes

1. In the measurement results that represent the compressive strengths, certain results are marked with a red colour. These red values indicate that they do not pass the statistical test regarding the prediction interval, based on the other results for that geopolymer composition. Therefore, the red coloured values mean that they are less reliable than the others.

2. Four wavelengths are given in the tables for the representation of the FTIR results. These are the wavelengths at which the peaks of transmission occur in the wavelength spectrum. Four peaks were generally noticed for the investigated geopolymers, as illustrated in Figure 124. If no value is entered for the relevant wavelength, this means that no clear peak was perceptible. The mean value of the wavelengths at which the peak occurs is shown in bold below the tables.

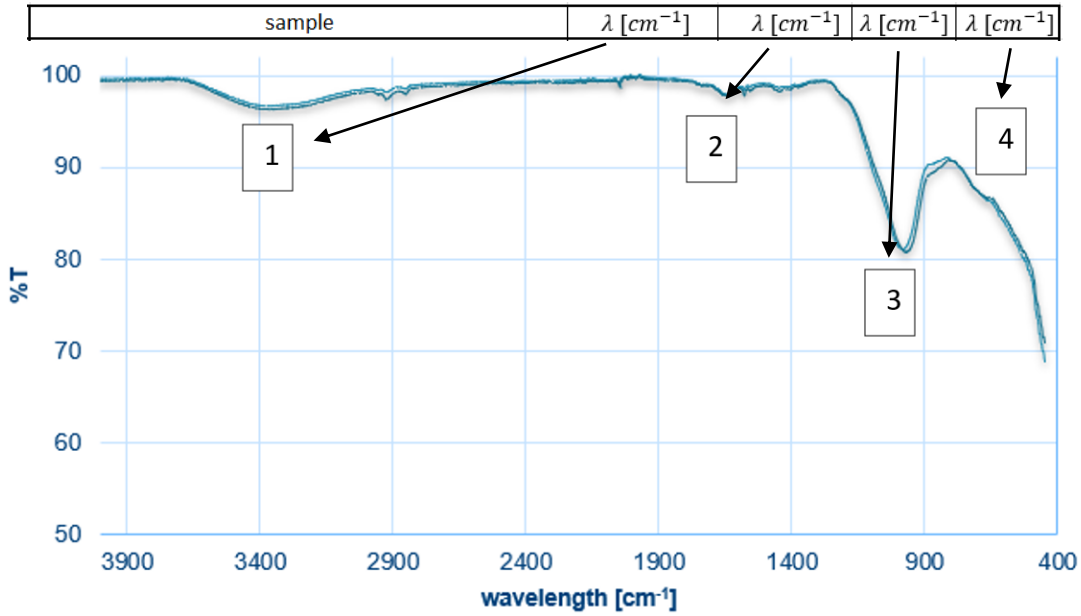

Figure 124: Illustration of four common peaks for FTIR results.

Bijlage A GEOPOLYMER MIX DESIGN CALCULATIONS

boundary conditions for chemical products

liquid activator to solid aluminosilicate ratio			0.3				
kaolinite to MGS-1 ratio			0.2				
ρ_{MGS-1}	1.29 g/cm³	M_{NaOH}	39.997 g/mol	11.61% wt%	Na_2SiO_3		
ρ_{NaOH}	2.13 g/cm³	M_{LiOH}	23.95 g/mol	0.1161			
ρ_{LiOH}	1.46 g/cm³	$M_{Na_2SiO_3}$	122.06 g/mol	1.2746 mol	Na_2SiO_3	per l solution	
$\rho_{Na_2SiO_3\ solution}$	1.34 g/cm³	$M_{LiOH.H_2O}$	41.96 g/mol				
$\rho_{LiOH.H_2O}$	1.51 g/cm³	$M_{kaolinite}$	258.16 g/mol	11.6 g	Na_2SiO_3	100 g	
$\rho_{kaolinite}$	2.62 g/cm³			8.66 ml	Na_2SiO_3	100 ml	

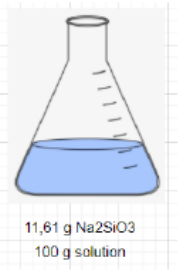

Requirements for geopolymers (mass ratios)

Na_2O / binder	0,04 -> 0,09
H_2O / binder	0,05 -> 0,3
Na_2O / SiO_2	1 -> 2

boundary conditions for chemical products

For 100 ml

6 M		8 M		10 M		12 M	
m_{NaOH}	23.998 g	m_{NaOH}	31.998 g	m_{NaOH}	39.997 g	m_{NaOH}	47.996 g
$m_{LiOH.H_2O}$	25.176 g	$m_{LiOH.H_2O}$	33.568 g	$m_{LiOH.H_2O}$	41.960 g	$m_{LiOH.H_2O}$	50.352 g

mix design of NaOH-based geopolymers

For 100 ml

	8 M NaOH	10 M NaOH	12 M NaOH
$V_{alumino}$	70.00 ml	70.00 ml	70.00 ml
m_{MGS-1}	72.24 g	72.24 g	72.24 g
m_{kaolin}	36.68 g	36.68 g	36.68 g
$V_{activator}$	30.00 ml	30.00 ml	30.00 ml
V_{NaOH}	4.51 ml	5.63 ml	6.76 ml
$V_{Na_2SiO_3}$	25.49 ml	24.37 ml	23.24 ml

Figure 125: Mix design of geopolymers – part 1.

m_{NaOH}	9.60 g	12.00 g	14.40 g	
$m_{Na_2SiO_3}$	34.16 g	32.65 g	31.14 g	

mix design of LiOH.H2O-based geopolymers

For 100 ml

	6 M $LiOH.H_2O$	8 M $LiOH.H_2O$	10 M $LiOH.H_2O$	12 M $LiOH.H_2O$
$V_{alumino}$	70.00 ml	70.00 ml	70.00 ml	70.00 ml
m_{MGS-1}	72.24 g	72.24 g	72.24 g	72.24 g
m_{kaolin}	36.68 g	36.68 g	36.68 g	36.68 g
$V_{activator}$	30.00 ml	30.00 ml	30.00 ml	30.00 ml
$V_{LiOH.H_2O}$	5.00 ml	6.67 ml	8.34 ml	10.00 ml
$V_{Na_2SiO_3}$	25.00 ml	23.33 ml	21.66 ml	20.00 ml
$m_{LiOH.H_2O}$	7.55 g	10.07 g	12.59 g	15.11 g
$m_{Na_2SiO_3}$	33.50 g	31.26 g	29.03 g	26.80 g

pellet press - mass per compacted layer

pellet press (cylindrical samples of 20x40 mm)

1 cylinder 12566 mm^3

calculation of compaction supply: 1.26E-05 m^3

0.0126 l

6 cylinders of 8M NaOH 12.6 ml

6 cylinders of 8M LiOH.H2O 12.6 cm^3

8 M NaOH	8 M $LiOH.H_2O$	6 M $LiOH.H_2O$
19.19 g geopolymer mixture	18.88 g geopolymer mixture	18.85 g geopolymer mixture
4.80 g/layer (compaction in 4 layers)	4.72 g/layer (compaction in 4 layers)	4.71 g/layer (compaction in 4 layers)
6.40 g/layer (compaction in 4 layers)	6.29 g/layer (compaction in 4 layers)	6.28 g/layer (compaction in 4 layers)

Figure 126: Mix design of geopolymers - part 2.

Bijlage B PLANNING SCHEDULE FOR LABORATORY WORK

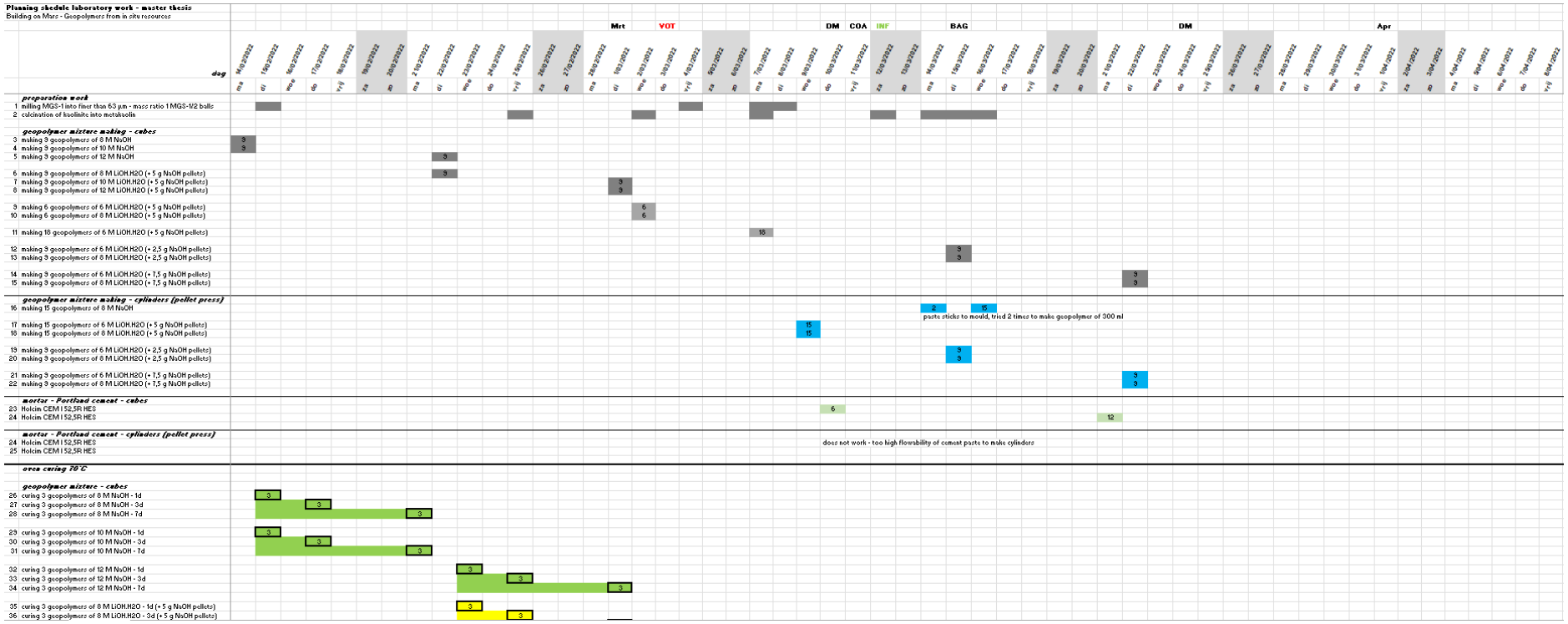

Figure 127: Planning schedule for laboratory work - part 1.

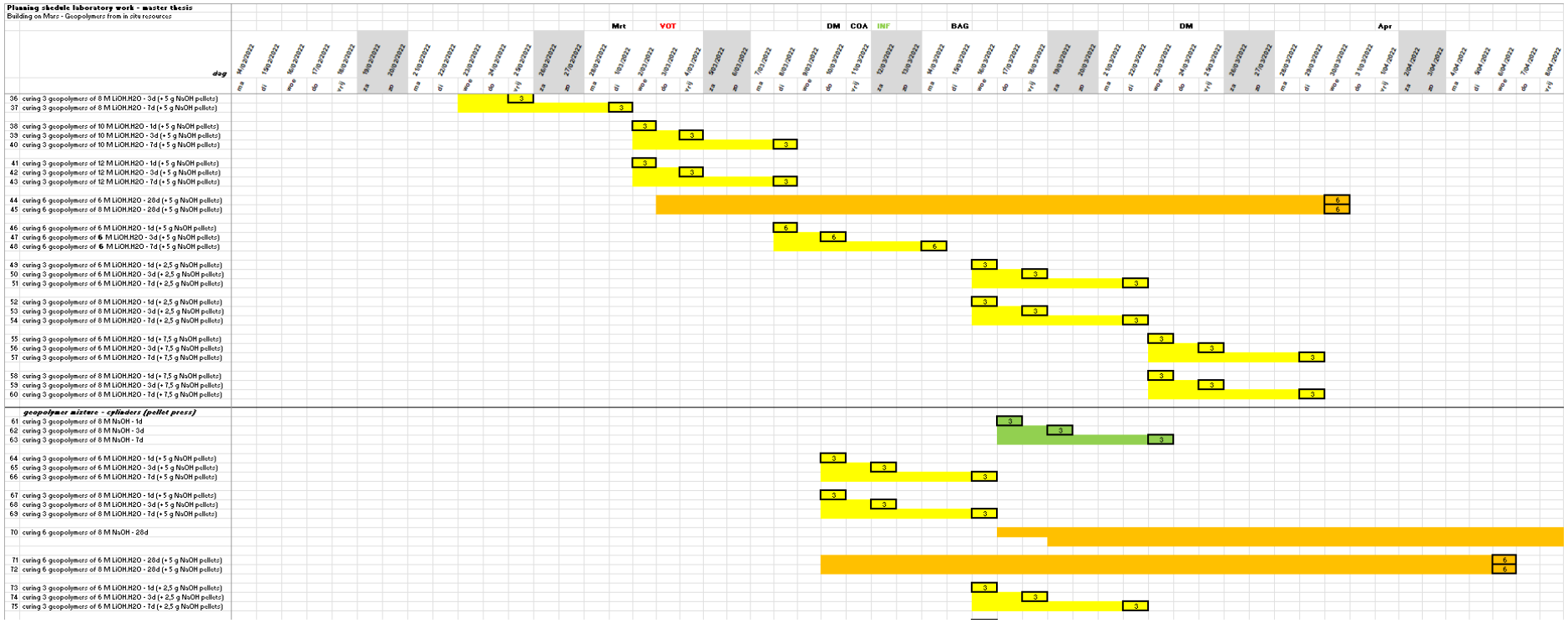

Figure 128: Planning schedule for laboratory work - part 2.

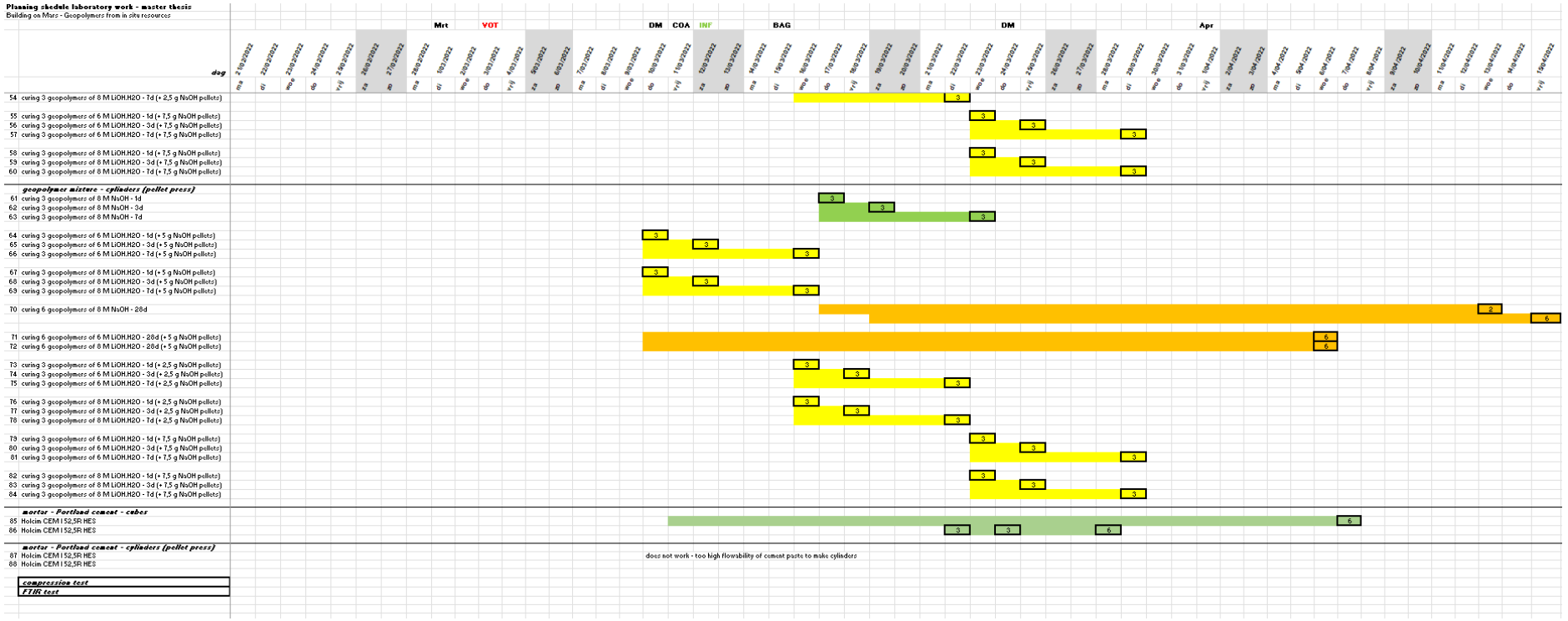

Figure 129: Planning schedule for laboratory work - part 3.

Bijlage C COMPRESSION TEST RESULTS - CUBE SAMPLES

Table 24: 8M NaOH-based geopolymers (1d).

15/02/2022	sample	F_{max} $[kN]$	f_c $[MPa]$	
	8M NaOH 1d 70°C - sample 1	2.305	5.763	
	8M NaOH 1d 70°C - sample 2	3.234	8.085	
	8M NaOH 1d 70°C - sample 3	3.504	8.760	
		$f_{c,mean}$ $[MPa]$	**7.54**	8 ± 2
		σ	1.57	
		3σ	4.72	
		$f_{c,min}$ $[MPa]$	5.96	
		$f_{c,max}$ $[MPa]$	9.11	

Table 25: 10M NaOH-based geopolymers (1d).

	sample	F_{max} $[kN]$	f_c $[MPa]$	
	10M NaOH 1d 70°C - sample 1	2.435	6.088	
	10M NaOH 1d 70°C - sample 2	1.664	4.160	
	10M NaOH 1d 70°C - sample 3	1.533	3.833	
		$f_{c,mean}$ $[MPa]$	**4.69**	5 ± 1
		σ	1.22	
		3σ	3.66	
		$f_{c,min}$ $[MPa]$	3.47	
		$f_{c,max}$ $[MPa]$	5.91	

Table 26: 12M NaOH-based geopolymers (1d).

23/02/2022	sample	F_{max} $[kN]$	f_c $[MPa]$	
	12M NaOH 1d 70°C - sample 1	2.760	6.900	
	12M NaOH 1d 70°C - sample 2	2.844	7.110	
	12M NaOH 1d 70°C - sample 3	3.243	8.108	
		$f_{c,mean}$ $[MPa]$	**7.37**	7.4 ± 0.7
		σ	0.65	
		3σ	1.94	
		$f_{c,min}$ $[MPa]$	6.73	
		$f_{c,max}$ $[MPa]$	8.02	

Table 27: 8M $LiOH.H_2O$ + 5 g NaOH-based geopolymers (1d).

	sample	F_{max} $[kN]$	f_c $[MPa]$	
	8M LiOH.H2O + 5g NaOH 1d 70°C - sample 1	9.824	24.560	
	8M LiOH.H2O + 5g NaOH 1d 70°C - sample 2	10.467	26.168	
	8M LiOH.H2O + 5g NaOH 1d 70°C - sample 3	11.267	28.168	
		$f_{c,mean}$ $[MPa]$	**26.30**	26 ± 2
		σ	1.81	
		3σ	5.42	
		$f_{c,min}$ $[MPa]$	24.49	
		$f_{c,max}$ $[MPa]$	28.11	

Table 28: 10M $LiOH.H_2O + 5$ g NaOH-based geopolymers (1d).

2/03/2022	sample	F_{max} [kN]	f_c [MPa]	
	10M LiOH.H2O + 5g NaOH 1d 70°C - sample 1	8.013	20.033	
	10M LiOH.H2O + 5g NaOH 1d 70°C - sample 2	6.589	16.473	
	10M LiOH.H2O + 5g NaOH 1d 70°C - sample 3	6.175	15.438	
		$f_{c,mean}$ [MPa]	**17.31**	17 ± 2
		σ	2.41	
		3σ	7.23	
		$f_{c,min}$ [MPa]	14.90	
		$f_{c,max}$ [MPa]	19.72	

Table 29: 12M $LiOH.H_2O + 5$ g NaOH-based geopolymers (1d).

sample	F_{max} [kN]	f_c [MPa]	
12M LiOH.H2O + 5g NaOH 1d 70°C - sample 1	3.132	7.830	
12M LiOH.H2O + 5g NaOH 1d 70°C - sample 2	2.732	6.830	
12M LiOH.H2O + 5g NaOH 1d 70°C - sample 3	2.249	5.623	
	$f_{c,mean}$ [MPa]	**6.76**	7 ± 1
	σ	1.11	
	3σ	3.32	
	$f_{c,min}$ [MPa]	5.66	
	$f_{c,max}$ [MPa]	7.87	

Table 30: 6M $LiOH.H_2O + 5$ g NaOH-based geopolymers (1d).

8/03/2022	sample	F_{max} [kN]	f_c [MPa]	
	6M LiOH.H2O + 5g NaOH 1d 70°C - sample 1	3.364	8.410	
	6M LiOH.H2O + 5g NaOH 1d 70°C - sample 2	3.615	9.038	
	6M LiOH.H2O + 5g NaOH 1d 70°C - sample 3	2.677	6.693	
	6M LiOH.H2O + 5g NaOH 1d 70°C - sample 4	3.857	9.643	
	6M LiOH.H2O + 5g NaOH 1d 70°C - sample 5	4.582	11.455	
	6M LiOH.H2O + 5g NaOH 1d 70°C - sample 6	3.727	9.318	
		$f_{c,mean}$ [MPa]	**9.09**	9 ± 2
		σ	1.56	
		3σ	4.68	
		$f_{c,min}$ [MPa]	7.53	
		$f_{c,max}$ [MPa]	10.65	

Table 31: 6M $LiOH.H_2O + 2.5$ g NaOH-based geopolymers (1d).

16/03/2022	sample	F_{max} [kN]	f_c [MPa]	
	6M LiOH.H2O + 2.5g NaOH 1d 70°C - sample 1	1.162	2.905	
	6M LiOH.H2O + 2.5g NaOH 1d 70°C - sample 2	33.785	84.463	
	6M LiOH.H2O + 2.5g NaOH 1d 70°C - sample 3	1.171	2.928	
		$f_{c,mean}$ [MPa]	**2.92**	2.92 ± 0.02
		σ	0.02	
		3σ	0.05	
		$f_{c,min}$ [MPa]	2.90	
		$f_{c,max}$ [MPa]	2.93	

Table 32: 8M $LiOH.H_2O + 2.5$ g NaOH-based geopolymers (1d).

	sample	F_{max} [kN]	f_c [MPa]	
	8M LiOH.H2O + 2.5g NaOH 1d 70°C - sample 1	3.058	7.645	
	8M LiOH.H2O + 2.5g NaOH 1d 70°C - sample 2	2.147	5.368	
	8M LiOH.H2O + 2.5g NaOH 1d 70°C - sample 3	2.686	6.715	
		$f_{c,mean}$ [MPa]	**6.58**	7 ± 1
		σ	1.15	
		3σ	3.44	
		$f_{c,min}$ [MPa]	5.43	
		$f_{c,max}$ [MPa]	7.72	

Table 33: CEM I 52.5R HES (1d).

22/03/2022	sample	F_{max} [kN]	f_c [MPa]	
	Holcim CEM I 52.5R HES 1d 70°C - sample 1	29.824	74.560	
	Holcim CEM I 52.5R HES 1d 70°C - sample 2	31.434	78.585	
	Holcim CEM I 52.5R HES 1d 70°C - sample 3	32.751	81.878	
		$f_{c,mean}$ [MPa]	**78.34**	78 ± 4
		σ	3.66	
		3σ	10.99	
		$f_{c,min}$ [MPa]	74.68	
		$f_{c,max}$ [MPa]	82.01	

Table 34: 6M $LiOH.H_2O + 7.5$ g NaOH-based geopolymers (1d).

23/03/2022	sample	F_{max} [kN]	f_c [MPa]	
	6M LiOH.H2O + 7.5g NaOH 1d 70°C - sample 1	8.785	21.963	
	6M LiOH.H2O + 7.5g NaOH 1d 70°C - sample 2	7.453	18.633	
	6M LiOH.H2O + 7.5g NaOH 1d 70°C - sample 3	7.802	19.505	
		$f_{c,mean}$ [MPa]	**20.03**	20 ± 2
		σ	1.73	
		3σ	5.18	
		$f_{c,min}$ [MPa]	18.31	
		$f_{c,max}$ [MPa]	21.76	

Table 35: 8M $LiOH.H_2O + 7.5$ g NaOH-based geopolymers (1d).

	sample	F_{max} [kN]	f_c [MPa]	
	8M LiOH.H2O + 7.5g NaOH 1d 70°C - sample 1	1.682	4.205	
	8M LiOH.H2O + 7.5g NaOH 1d 70°C - sample 2	2.165	5.413	
	8M LiOH.H2O + 7.5g NaOH 1d 70°C - sample 3	1.403	3.508	
		$f_{c,mean}$ [MPa]	**4.38**	4 ± 1
		σ	0.96	
		3σ	2.89	
		$f_{c,min}$ [MPa]	3.41	
		$f_{c,max}$ [MPa]	5.34	

Table 36: 8M NaOH-based geopolymers (3d).

17/02/2022	sample	F_{max} [kN]	f_c [MPa]	
	8M NaOH 3d 70°C - sample 1	7.811	19.528	
	8M NaOH 3d 70°C - sample 2	4.582	11.455	
	8M NaOH 3d 70°C - sample 3	6.396	15.990	
		$f_{c,mean}$ [MPa]	**15.66**	16 ± 4
		σ	4.05	
		3σ	12.14	
		$f_{c,min}$ [MPa]	11.61	
		$f_{c,max}$ [MPa]	19.70	

Table 37: 10M NaOH-based geopolymers (3d).

	sample	F_{max} [kN]	f_c [MPa]	
	10M NaOH 3d 70°C - sample 1	1.580	3.950	
	10M NaOH 3d 70°C - sample 2	2.435	6.088	
	10M NaOH 3d 70°C - sample 3	3.030	7.575	
		$f_{c,mean}$ [MPa]	**5.87**	6 ± 2
		σ	1.82	
		3σ	5.47	
		$f_{c,min}$ [MPa]	4.05	
		$f_{c,max}$ [MPa]	7.69	

Table 38: 12M NaOH-based geopolymers (3d).

25/02/2022	sample	F_{max} [kN]	f_c [MPa]	
	12M NaOH 3d 70°C - sample 1	2.156	5.390	
	12M NaOH 3d 70°C - sample 2	2.704	6.760	
	12M NaOH 3d 70°C - sample 3	3.773	9.433	
		$f_{c,mean}$ [MPa]	**7.19**	7 ± 2
		σ	2.06	
		3σ	6.17	
		$f_{c,min}$ [MPa]	5.14	
		$f_{c,max}$ [MPa]	9.25	

Table 39: 8M $LiOH.H_2O$ + 5 g NaOH-based geopolymers (3d).

	sample	F_{max} [kN]	f_c [MPa]	
	8M LiOH.H2O + 5g NaOH 3d 70°C - sample 1	9.705	24.263	
	8M LiOH.H2O + 5g NaOH 3d 70°C - sample 2	7.535	18.838	
	8M LiOH.H2O + 5g NaOH 3d 70°C - sample 3	6.157	15.393	
		$f_{c,mean}$ [MPa]	**19.50**	20 ± 4
		σ	4.47	
		3σ	13.42	
		$f_{c,min}$ [MPa]	15.03	
		$f_{c,max}$ [MPa]	23.97	

Table 40: 10M $LiOH.H_2O + 5$ g NaOH-based geopolymers (3d).

4/03/2022	sample	F_{max} [kN]	f_c [MPa]	
	10M LiOH.H2O + 5g NaOH 3d 70°C - sample 1	11.065	27.663	
	10M LiOH.H2O + 5g NaOH 3d 70°C - sample 2	8.574	21.435	
	10M LiOH.H2O + 5g NaOH 3d 70°C - sample 3	7.682	19.205	
		$f_{c,mean}$ [MPa]	**22.77**	23 ± 4
		σ	4.38	
		3σ	13.15	
		$f_{c,min}$ [MPa]	18.38	
		$f_{c,max}$ [MPa]	27.15	

Table 41: 12M $LiOH.H_2O + 5$ g NaOH-based geopolymers (3d).

	sample	F_{max} [kN]	f_c [MPa]	
	12M LiOH.H2O + 5g NaOH 3d 70°C - sample 1	4.582	11.455	
	12M LiOH.H2O + 5g NaOH 3d 70°C - sample 2	4.925	12.313	
	12M LiOH.H2O + 5g NaOH 3d 70°C - sample 3	4.582	11.455	
		$f_{c,mean}$ [MPa]	**11.74**	11.7 ± 0.5
		σ	0.50	
		3σ	1.49	
		$f_{c,min}$ [MPa]	11.25	
		$f_{c,max}$ [MPa]	12.24	

Table 42: 6M $LiOH.H_2O + 5$ g NaOH-based geopolymers (3d).

10/03/2022	sample	F_{max} [kN]	f_c [MPa]	
	6M LiOH.H2O + 5g NaOH 3d 70°C - sample 1	4.768	11.920	
	6M LiOH.H2O + 5g NaOH 3d 70°C - sample 2	4.387	10.968	
	6M LiOH.H2O + 5g NaOH 3d 70°C - sample 3	2.388	5.970	
	6M LiOH.H2O + 5g NaOH 3d 70°C - sample 4	5.100	12.750	
	6M LiOH.H2O + 5g NaOH 3d 70°C - sample 5	3.922	9.805	
	6M LiOH.H2O + 5g NaOH 3d 70°C - sample 6	2.370	5.925	
		$f_{c,mean}$ [MPa]	**9.56**	10 ± 3
		σ	2.96	
		3σ	8.89	
		$f_{c,min}$ [MPa]	6.59	
		$f_{c,max}$ [MPa]	12.52	

Table 43: 6M $LiOH.H_2O + 2.5$ g NaOH-based geopolymers (3d).

18/03/2022	sample	F_{max} [kN]	f_c [MPa]	
	6M LiOH.H2O + 2.5g NaOH 3d 70°C - sample 1	29.514	73.785	
	6M LiOH.H2O + 2.5g NaOH 3d 70°C - sample 2	1.032	2.580	
	6M LiOH.H2O + 2.5g NaOH 3d 70°C - sample 3	1.190	2.975	
		$f_{c,mean}$ [MPa]	**2.78**	2.8 ± 0.3
		σ	0.28	
		3σ	0.84	
		$f_{c,min}$ [MPa]	2.50	
		$f_{c,max}$ [MPa]	3.06	

Table 44: 8M $LiOH.H_2O + 2.5$ g NaOH-based geopolymers (3d).

sample	F_{max} [kN]	f_c [MPa]	
8M LiOH.H2O + 2.5g NaOH 3d 70°C - sample 1	3.717	9.293	
8M LiOH.H2O + 2.5g NaOH 3d 70°C - sample 2	4.136	10.340	
8M LiOH.H2O + 2.5g NaOH 3d 70°C - sample 3	4.675	11.688	
	$f_{c,mean}$ [MPa]	**10.44**	10 ± 1
	σ	1.20	
	3σ	3.60	
	$f_{c,min}$ [MPa]	9.24	
	$f_{c,max}$ [MPa]	11.64	

Table 45: CEM I 52.5R HES (3d).

24/03/2022	sample	F_{max} [kN]	f_c [MPa]	
	Holcim CEM I 52.5R HES 3d 70°C - sample 1	32.157	80.393	
	Holcim CEM I 52.5R HES 3d 70°C - sample 2	25.703	64.258	
	Holcim CEM I 52.5R HES 3d 70°C - sample 3	6.148	15.370	
		$f_{c,mean}$ [MPa]	**72.33**	72 ± 11
		σ	11.41	
		3σ	34.23	
		$f_{c,min}$ [MPa]	60.92	
		$f_{c,max}$ [MPa]	83.73	

Table 46: 6M $LiOH.H_2O + 7.5$ g NaOH-based geopolymers (3d).

25/03/2022	sample	F_{max} [kN]	f_c [MPa]	
	6M LiOH.H2O + 7.5g NaOH 3d 70°C - sample 1	11.763	29.408	
	6M LiOH.H2O + 7.5g NaOH 3d 70°C - sample 2	10.173	25.433	
	6M LiOH.H2O + 7.5g NaOH 3d 70°C - sample 3	11.653	29.133	
		$f_{c,mean}$ [MPa]	**27.99**	28 ± 2
		σ	2.22	
		3σ	6.66	
		$f_{c,min}$ [MPa]	25.77	
		$f_{c,max}$ [MPa]	30.21	

Table 47: 8M $LiOH.H_2O + 7.5$ g NaOH-based geopolymers (3d).

sample	F_{max} [kN]	f_c [MPa]	
8M LiOH.H2O + 7.5g NaOH 3d 70°C - sample 1	2.723	6.808	
8M LiOH.H2O + 7.5g NaOH 3d 70°C - sample 2	1.896	4.740	
8M LiOH.H2O + 7.5g NaOH 3d 70°C - sample 3	2.639	6.598	
	$f_{c,mean}$ [MPa]	**6.05**	6 ± 1
	σ	1.14	
	3σ	3.41	
	$f_{c,min}$ [MPa]	4.91	
	$f_{c,max}$ [MPa]	7.19	

Table 48: 8M NaOH-based geopolymers (7d).

21/02/2022	sample	F_{max} [kN]	f_c [MPa]	
	8M NaOH 7d 70°C - sample 1	4.971	12.428	
	8M NaOH 7d 70°C - sample 2	3.764	9.410	
	8M NaOH 7d 70°C - sample 3	3.764	9.410	
		$f_{c,mean}$ [MPa]	**10.42**	11 ± 2
		σ	1.74	
		3σ	5.23	
		$f_{c,min}$ [MPa]	8.67	
		$f_{c,max}$ [MPa]	12.16	

Table 49: 10M NaOH-based geopolymers (7d).

	sample	F_{max} [kN]	f_c [MPa]	
	10M NaOH 7d 70°C - sample 1	3.234	8.085	
	10M NaOH 7d 70°C - sample 2	3.197	7.993	
	10M NaOH 7d 70°C - sample 3	1.747	4.368	
		$f_{c,mean}$ [MPa]	**6.82**	7 ± 2
		σ	2.12	
		3σ	6.36	
		$f_{c,min}$ [MPa]	4.69	
		$f_{c,max}$ [MPa]	8.94	

Table 50: 12M NaOH-based geopolymers (7d).

1/03/2022	sample	F_{max} [kN]	f_c [MPa]	
	12M NaOH 7d 70°C - sample 1	3.439	8.598	
	12M NaOH 7d 70°C - sample 2	2.630	6.575	
	12M NaOH 7d 70°C - sample 3	3.671	9.178	
		$f_{c,mean}$ [MPa]	**8.12**	8 ± 1
		σ	1.37	
		3σ	4.10	
		$f_{c,min}$ [MPa]	6.75	
		$f_{c,max}$ [MPa]	9.48	

Table 51: 6M $LiOH.H_2O$ + 5 g NaOH-based geopolymers (7d).

14/03/2022	sample	F_{max} [kN]	f_c [MPa]	
	6M LiOH.H2O + 5g NaOH 7d 70°C - sample 1	4.182	10.455	
	6M LiOH.H2O + 5g NaOH 7d 70°C - sample 2	5.054	12.635	
	6M LiOH.H2O + 5g NaOH 7d 70°C - sample 3	3.764	9.410	
	6M LiOH.H2O + 5g NaOH 7d 70°C - sample 4	3.699	9.248	
	6M LiOH.H2O + 5g NaOH 7d 70°C - sample 5	3.690	9.225	
	6M LiOH.H2O + 5g NaOH 7d 70°C - sample 6	2.872	7.180	
		$f_{c,mean}$ [MPa]	**9.69**	10 ± 2
		σ	1.79	
		3σ	5.37	
		$f_{c,min}$ [MPa]	7.90	
		$f_{c,max}$ [MPa]	11.48	

Table 52: 8M $LiOH.H_2O + 5$ g NaOH-based geopolymers (7d).

1/03/2022	sample	F_{max} [kN]	f_c [MPa]	
	8M LiOH.H2O + 5g NaOH 7d 70°C - sample 1	11.166	27.915	
	8M LiOH.H2O + 5g NaOH 7d 70°C - sample 2	5.320	13.300	
	8M LiOH.H2O + 5g NaOH 7d 70°C - sample 3	6.965	17.413	
		$f_{c,mean}$ [MPa]	**19.54**	20 ± 8
		σ	7.54	
		3σ	22.61	
		$f_{c,min}$ [MPa]	12.01	
		$f_{c,max}$ [MPa]	27.08	

Table 53: 10M $LiOH.H_2O + 5$ g NaOH-based geopolymers (7d).

8/03/2022	sample	F_{max} [kN]	f_c [MPa]	
	10M LiOH.H2O + 5g NaOH 7d 70°C - sample 1	10.486	26.215	
	10M LiOH.H2O + 5g NaOH 7d 70°C - sample 2	14.025	35.063	
	10M LiOH.H2O + 5g NaOH 7d 70°C - sample 3	15.846	39.615	
		$f_{c,mean}$ [MPa]	**33.63**	34 ± 7
		σ	6.81	
		3σ	20.44	
		$f_{c,min}$ [MPa]	26.82	
		$f_{c,max}$ [MPa]	40.44	

Table 54: 12M $LiOH.H_2O + 5$ g NaOH-based geopolymers (7d).

	sample	F_{max} [kN]	f_c [MPa]	
	12M LiOH.H2O + 5g NaOH 7d 70°C - sample 1	6.690	16.725	
	12M LiOH.H2O + 5g NaOH 7d 70°C - sample 2	6.331	15.828	
	12M LiOH.H2O + 5g NaOH 7d 70°C - sample 3	5.909	14.773	
		$f_{c,mean}$ [MPa]	**15.78**	16 ± 1
		σ	0.98	
		3σ	2.93	
		$f_{c,min}$ [MPa]	14.80	
		$f_{c,max}$ [MPa]	16.75	

Table 55: 6M $LiOH.H_2O + 2.5$ g NaOH-based geopolymers (7d).

22/03/2022	sample	F_{max} [kN]	f_c [MPa]	
	6M LiOH.H2O + 2.5g NaOH 7d 70°C - sample 1	1.468	3.670	
	6M LiOH.H2O + 2.5g NaOH 7d 70°C - sample 2	1.645	4.113	
	6M LiOH.H2O + 2.5g NaOH 7d 70°C - sample 3	1.654	4.135	
		$f_{c,mean}$ [MPa]	**3.97**	4.0 ± 0.3
		σ	0.26	
		3σ	0.79	
		$f_{c,min}$ [MPa]	3.71	
		$f_{c,max}$ [MPa]	4.23	

Table 56: 8M $LiOH.H_2O + 2.5$ g NaOH-based geopolymers (7d).

sample	F_{max} [kN]	f_c [MPa]	
8M LiOH.H2O + 2.5g NaOH 7d 70°C - sample 1	2.714	6.785	
8M LiOH.H2O + 2.5g NaOH 7d 70°C - sample 2	5.403	13.508	
8M LiOH.H2O + 2.5g NaOH 7d 70°C - sample 3	4.257	10.643	
	$f_{c,mean}$ [MPa]	**10.31**	10 ± 3
	σ	3.37	
	3σ	10.12	
	$f_{c,min}$ [MPa]	6.94	
	$f_{c,max}$ [MPa]	13.69	

Table 57: CEM I 52.5R HES (7d).

28/03/2022	sample	F_{max} [kN]	f_c [MPa]	
	Holcim CEM I 52.5R HES 7d 70°C - sample 1	29.597	73.993	
	Holcim CEM I 52.5R HES 7d 70°C - sample 2	28.648	71.620	
	Holcim CEM I 52.5R HES 7d 70°C - sample 3	27.235	68.088	
	Holcim CEM I 52.5R HES 7d 70°C - sample 4	13.776	34.440	
	Holcim CEM I 52.5R HES 7d 70°C - sample 5	21.782	54.455	
	Holcim CEM I 52.5R HES 7d 70°C - sample 6	28.503	71.258	
		$f_{c,mean}$ [MPa]	**71.24**	71 ± 2
		σ	2.43	
		3σ	7.28	
		$f_{c,min}$ [MPa]	68.81	
		$f_{c,max}$ [MPa]	73.67	

Table 58: 6M $LiOH.H_2O + 7.5$ g NaOH-based geopolymers (7d).

29/03/2022	sample	F_{max} [kN]	f_c [MPa]	
	6M LiOH.H2O + 7.5g NaOH 7d 70°C - sample 1	8.069	20.173	
	6M LiOH.H2O + 7.5g NaOH 7d 70°C - sample 2	11.093	27.733	
	6M LiOH.H2O + 7.5g NaOH 7d 70°C - sample 3	7.434	18.585	
		$f_{c,mean}$ [MPa]	**22.16**	22 ± 5
		σ	4.89	
		3σ	14.66	
		$f_{c,min}$ [MPa]	17.28	
		$f_{c,max}$ [MPa]	27.05	

Table 59: 8M $LiOH.H_2O + 7.5$ g NaOH-based geopolymers (7d).

sample	F_{max} [kN]	f_c [MPa]	
8M LiOH.H2O + 7.5g NaOH 7d 70°C - sample 1	8.280	20.700	
8M LiOH.H2O + 7.5g NaOH 7d 70°C - sample 2	10.477	26.193	
8M LiOH.H2O + 7.5g NaOH 7d 70°C - sample 3	8.666	21.665	
	$f_{c,mean}$ [MPa]	**22.85**	23 ± 3
	σ	2.93	
	3σ	8.80	
	$f_{c,min}$ [MPa]	19.92	
	$f_{c,max}$ [MPa]	25.78	

Table 60: 6M $LiOH.H_2O + 5$ g $NaOH$-based geopolymers (28d).

30/03/2022	sample	F_{max} $[kN]$	f_c $[MPa]$	
	6M LiOH.H2O + 5g NaOH 28d 70°C - sample 1	21.189	52.973	
	6M LiOH.H2O + 5g NaOH 28d 70°C - sample 2	10.293	25.733	
	6M LiOH.H2O + 5g NaOH 28d 70°C - sample 3	8.988	22.470	
	6M LiOH.H2O + 5g NaOH 28d 70°C - sample 4	8.914	22.285	
	6M LiOH.H2O + 5g NaOH 28d 70°C - sample 5	10.835	27.088	
	6M LiOH.H2O + 5g NaOH 28d 70°C - sample 6	10.302	25.755	
		$f_{c,mean}$ $[MPa]$	**24.67**	25 ± 2
		σ	2.16	
		3σ	6.48	
		$f_{c,min}$ $[MPa]$	22.51	
		$f_{c,max}$ $[MPa]$	26.83	

Table 61: 8M $LiOH.H_2O + 5$ g $NaOH$-based geopolymers (28d).

30/03/2022	sample	F_{max} $[kN]$	f_c $[MPa]$	
	8M LiOH.H2O + 5g NaOH 28d 70°C - sample 1	8.243	20.608	
	8M LiOH.H2O + 5g NaOH 28d 70°C - sample 2	10.247	25.618	
	8M LiOH.H2O + 5g NaOH 28d 70°C - sample 3	9.833	24.583	
	8M LiOH.H2O + 5g NaOH 28d 70°C - sample 4	8.850	22.125	
	8M LiOH.H2O + 5g NaOH 28d 70°C - sample 5	7.995	19.988	
	8M LiOH.H2O + 5g NaOH 28d 70°C - sample 6	7.453	18.633	
		$f_{c,mean}$ $[MPa]$	**21.93**	22 ± 3
		σ	2.72	
		3σ	8.17	
		$f_{c,min}$ $[MPa]$	19.20	
		$f_{c,max}$ $[MPa]$	24.65	

Table 62: CEM I 52.5R HES (28d).

6/04/2022	sample	F_{max} $[kN]$	f_c $[MPa]$	
	Holcim CEM I 52,5R HES 28d 70°C - sample 1	41.760	104.400	
	Holcim CEM I 52,5R HES 28d 70°C - sample 2	5.008	12.520	
	Holcim CEM I 52,5R HES 28d 70°C - sample 3	33.080	82.700	
	Holcim CEM I 52,5R HES 28d 70°C - sample 4	35.321	88.303	
	Holcim CEM I 52,5R HES 28d 70°C - sample 5	38.175	95.438	
	Holcim CEM I 52,5R HES 28d 70°C - sample 6	36.263	90.658	
		$f_{c,mean}$ $[MPa]$	**92.30**	92 ± 8
		σ	8.17	
		3σ	24.51	
		$f_{c,min}$ $[MPa]$	84.13	
		$f_{c,max}$ $[MPa]$	100.47	

Bijlage D COMPRESSION TEST RESULTS - CYLINDRICAL SAMPLES

Table 63: 6M $LiOH.H_2O$ + 5 g NaOH-based geopolymers (1d).

10/03/2022	sample	F_{max} [kN]	f_c [MPa]	
	6M LiOH.H2O + 5g NaOH 1d 70°C - sample 1	5.789	18.427	
	6M LiOH.H2O + 5g NaOH 1d 70°C - sample 2	5.238	16.673	
	6M LiOH.H2O + 5g NaOH 1d 70°C - sample 3	10.523	33.496	
		$f_{c,mean}$ [MPa]	**17.55**	18 ± 1
		σ	1.24	
		3σ	3.72	
		$f_{c,min}$ [MPa]	16.31	
		$f_{c,max}$ [MPa]	18.79	

Table 64: 8M $LiOH.H_2O$ + 5 g NaOH-based geopolymers (1d).

sample	F_{max} [kN]	f_c [MPa]	
8M LiOH.H2O + 5g NaOH 1d 70°C - sample 1	5.421	17.256	
8M LiOH.H2O + 5g NaOH 1d 70°C - sample 2	5.247	16.702	
8M LiOH.H2O + 5g NaOH 1d 70°C - sample 3	5.909	18.809	
	$f_{c,mean}$ [MPa]	**17.59**	18 ± 1
	σ	1.09	
	3σ	3.28	
	$f_{c,min}$ [MPa]	16.50	
	$f_{c,max}$ [MPa]	18.68	

Table 65: 6M $LiOH.H_2O$ + 2.5 g NaOH-based geopolymers (1d).

16/03/2022	sample	F_{max} [kN]	f_c [MPa]	
	6M LiOH.H2O + 2.5g NaOH 1d 70°C - sample 1	36.876	117.380	
	6M LiOH.H2O + 2.5g NaOH 1d 70°C - sample 2	1.180	3.756	
	6M LiOH.H2O + 2.5g NaOH 1d 70°C - sample 3	1.450	4.615	
		$f_{c,mean}$ [MPa]	**4.19**	4.2 ± 0.6
		σ	0.61	
		3σ	1.82	
		$f_{c,min}$ [MPa]	3.58	
		$f_{c,max}$ [MPa]	4.79	

Table 66: 8M $LiOH.H_2O$ + 2.5 g NaOH-based geopolymers (1d).

sample	F_{max} [kN]	f_c [MPa]	
8M LiOH.H2O + 2.5g NaOH 1d 70°C - sample 1	5.091	16.205	
8M LiOH.H2O + 2.5g NaOH 1d 70°C - sample 2	4.786	15.234	
8M LiOH.H2O + 2.5g NaOH 1d 70°C - sample 3	6.653	21.177	
	$f_{c,mean}$ [MPa]	**17.54**	18 ± 3
	σ	3.19	
	3σ	9.56	
	$f_{c,min}$ [MPa]	14.35	
	$f_{c,max}$ [MPa]	20.73	

Table 67: 8M NaOH-based geopolymers (1d).

17/03/2022	sample	F_{max} [kN]	f_c [MPa]	
	8M NaOH 1d 70°C - sample 1	1.152	3.667	
	8M NaOH 1d 70°C - sample 2	14.319	45.579	
	8M NaOH 1d 70°C - sample 3	5.081	16.173	
		$f_{c,mean}$ [MPa]	**3.67**	4
		σ	0.00	
		3σ	0.00	
		$f_{c,min}$ [MPa]	3.67	
		$f_{c,max}$ [MPa]	3.67	

Table 68: 6M $LiOH.H_2O + 7.5$ g NaOH-based geopolymers (1d).

23/03/2022	sample	F_{max} [kN]	f_c [MPa]	
	6M LiOH.H2O + 7.5g NaOH 1d 70°C - sample 1	3.931	12.513	
	6M LiOH.H2O + 7.5g NaOH 1d 70°C - sample 2	2.937	9.349	
	6M LiOH.H2O + 7.5g NaOH 1d 70°C - sample 3	3.401	10.826	
		$f_{c,mean}$ [MPa]	**10.90**	11 ± 2
		σ	1.58	
		3σ	4.75	
		$f_{c,min}$ [MPa]	9.31	
		$f_{c,max}$ [MPa]	12.48	

Table 69: 8M $LiOH.H_2O + 7.5$ g NaOH-based geopolymers (1d).

	sample	F_{max} [kN]	f_c [MPa]	
	8M LiOH.H2O + 7.5g NaOH 1d 70°C - sample 1	6.175	19.656	
	8M LiOH.H2O + 7.5g NaOH 1d 70°C - sample 2	6.240	19.863	
	8M LiOH.H2O + 7.5g NaOH 1d 70°C - sample 3	6.102	19.423	
		$f_{c,mean}$ [MPa]	**19.65**	19.7 ± 0.2
		σ	0.22	
		3σ	0.66	
		$f_{c,min}$ [MPa]	19.43	
		$f_{c,max}$ [MPa]	19.87	

Table 70: 6M $LiOH.H_2O + 5$ g NaOH-based geopolymers (3d).

12/03/2022	sample	F_{max} [kN]	f_c [MPa]	
	6M LiOH.H2O + 5g NaOH 3d 70°C - sample 1	7.343	23.373	
	6M LiOH.H2O + 5g NaOH 3d 70°C - sample 2	9.971	31.739	
	6M LiOH.H2O + 5g NaOH 3d 70°C - sample 3	10.109	32.178	
		$f_{c,mean}$ [MPa]	**31.96**	32.0 ± 0.3
		σ	0.31	
		3σ	0.93	
		$f_{c,min}$ [MPa]	31.65	
		$f_{c,max}$ [MPa]	32.27	

Table 71: 8M $LiOH.H_2O + 5$ g NaOH-based geopolymers (3d).

sample	F_{max} [kN]	f_c [MPa]	
8M LiOH.H2O + 5g NaOH 3d 70°C - sample 1	5.651	17.988	
8M LiOH.H2O + 5g NaOH 3d 70°C - sample 2	8.730	27.788	
8M LiOH.H2O + 5g NaOH 3d 70°C - sample 3	7.618	24.249	
	$f_{c,mean}$ [MPa]	**23.34**	23 ± 5
	σ	4.96	
	3σ	14.89	
	$f_{c,min}$ [MPa]	18.38	
	$f_{c,max}$ [MPa]	28.30	

Table 72: 6M $LiOH.H_2O + 2.5$ g NaOH-based geopolymers (3d).

18/03/2022	sample	F_{max} [kN]	f_c [MPa]	
	6M LiOH.H2O + 2.5g NaOH 3d 70°C - sample 1	1.942	6.182	
	6M LiOH.H2O + 2.5g NaOH 3d 70°C - sample 2	2.593	8.254	
	6M LiOH.H2O + 2.5g NaOH 3d 70°C - sample 3	2.249	7.159	
		$f_{c,mean}$ [MPa]	**7.20**	7 ± 1
		σ	1.04	
		3σ	3.11	
		$f_{c,min}$ [MPa]	6.16	
		$f_{c,max}$ [MPa]	8.23	

Table 73: 8M $LiOH.H_2O + 2.5$ g NaOH-based geopolymers (3d).

sample	F_{max} [kN]	f_c [MPa]	
8M LiOH.H2O + 2.5g NaOH 3d 70°C - sample 1	9.631	30.656	
8M LiOH.H2O + 2.5g NaOH 3d 70°C - sample 2	9.649	30.714	
8M LiOH.H2O + 2.5g NaOH 3d 70°C - sample 3	7.315	23.284	
	$f_{c,mean}$ [MPa]	**28.22**	28 ± 4
	σ	4.27	
	3σ	12.82	
	$f_{c,min}$ [MPa]	23.95	
	$f_{c,max}$ [MPa]	32.49	

Table 74: 8M NaOH-based geopolymers (3d).

19/03/2022	sample	F_{max} [kN]	f_c [MPa]	
	8M NaOH 3d 70°C - sample 1	1.134	3.610	
	8M NaOH 3d 70°C - sample 2	9.447	30.071	
	8M NaOH 3d 70°C - sample 3	1.138	3.622	
		$f_{c,mean}$ [MPa]	**3.62**	3.62 ± 0.01
		σ	0.01	
		3σ	0.03	
		$f_{c,min}$ [MPa]	3.61	
		$f_{c,max}$ [MPa]	3.63	

Table 75: 6M $LiOH.H_2O + 7.5$ g NaOH-based geopolymers (3d).

25/03/2022	sample	F_{max} [kN]	f_c [MPa]	
	6M LiOH.H2O + 7.5g NaOH 3d 70°C - sample 1	6.644	21.149	
	6M LiOH.H2O + 7.5g NaOH 3d 70°C - sample 2	6.883	21.909	
	6M LiOH.H2O + 7.5g NaOH 3d 70°C - sample 3	5.863	18.663	
		$f_{c,mean}$ [MPa]	**20.57**	21 ± 2
		σ	1.70	
		3σ	5.09	
		$f_{c,min}$ [MPa]	18.88	
		$f_{c,max}$ [MPa]	22.27	

Table 76: 8M $LiOH.H_2O + 7.5$ g NaOH-based geopolymers (3d).

sample	F_{max} [kN]	f_c [MPa]	
8M LiOH.H2O + 7.5g NaOH 3d 70°C - sample 1	9.631	30.656	
8M LiOH.H2O + 7.5g NaOH 3d 70°C - sample 2	9.374	29.838	
8M LiOH.H2O + 7.5g NaOH 3d 70°C - sample 3	8.721	27.760	
	$f_{c,mean}$ [MPa]	**29.42**	29 ± 1
	σ	1.49	
	3σ	4.48	
	$f_{c,min}$ [MPa]	27.92	
	$f_{c,max}$ [MPa]	30.91	

Table 77: 6M $LiOH.H_2O + 5$ g NaOH-based geopolymers (7d).

16/03/2022	sample	F_{max} [kN]	f_c [MPa]	
	6M LiOH.H2O + 5g NaOH 7d 70°C - sample 1	9.420	29.985	
	6M LiOH.H2O + 5g NaOH 7d 70°C - sample 2	10.513	33.464	
	6M LiOH.H2O + 5g NaOH 7d 70°C - sample 3	10.890	34.664	
		$f_{c,mean}$ [MPa]	**32.70**	33 ± 2
		σ	2.43	
		3σ	7.29	
		$f_{c,min}$ [MPa]	30.27	
		$f_{c,max}$ [MPa]	35.13	

Table 78: 8M $LiOH.H_2O + 5$ g NaOH-based geopolymers (7d).

sample	F_{max} [kN]	f_c [MPa]	
8M LiOH.H2O + 5g NaOH 7d 70°C - sample 1	7.269	23.138	
8M LiOH.H2O + 5g NaOH 7d 70°C - sample 2	9.254	29.456	
8M LiOH.H2O + 5g NaOH 7d 70°C - sample 3	7.425	23.635	
	$f_{c,mean}$ [MPa]	**25.41**	25 ± 4
	σ	3.51	
	3σ	10.54	
	$f_{c,min}$ [MPa]	21.90	
	$f_{c,max}$ [MPa]	28.92	

Table 79: 6M $LiOH.H_2O + 2.5$ g NaOH-based geopolymers (7d).

22/03/2022	sample	F_{max} [kN]	f_c [MPa]	
	6M LiOH.H2O + 2.5g NaOH 7d 70°C - sample 1	3.113	9.909	
	6M LiOH.H2O + 2.5g NaOH 7d 70°C - sample 2	3.708	11.803	
	6M LiOH.H2O + 2.5g NaOH 7d 70°C - sample 3	3.299	10.501	
		$f_{c,mean}$ [MPa]	**10.74**	11 ± 1
		σ	0.97	
		3σ	2.91	
		$f_{c,min}$ [MPa]	9.77	
		$f_{c,max}$ [MPa]	11.71	

Table 80: 8M $LiOH.H_2O + 2.5$ g NaOH-based geopolymers (7d).

	sample	F_{max} [kN]	f_c [MPa]	
	8M LiOH.H2O + 2.5g NaOH 7d 70°C - sample 1	7.269	23.138	
	8M LiOH.H2O + 2.5g NaOH 7d 70°C - sample 2	8.262	26.299	
	8M LiOH.H2O + 2.5g NaOH 7d 70°C - sample 3	7.407	23.577	
		$f_{c,mean}$ [MPa]	**24.34**	24 ± 2
		σ	1.71	
		3σ	5.14	
		$f_{c,min}$ [MPa]	22.63	
		$f_{c,max}$ [MPa]	26.05	

Table 81: 8M NaOH-based geopolymers (7d).

23/03/2022	sample	F_{max} [kN]	f_c [MPa]	
	8M NaOH 7d 70°C - sample 1	1.097	3.492	
	8M NaOH 7d 70°C - sample 2	1.338	4.259	
	8M NaOH 7d 70°C - sample 3	1.332	4.240	
		$f_{c,mean}$ [MPa]	**4.00**	4.0 ± 0.4
		σ	0.44	
		3σ	1.31	
		$f_{c,min}$ [MPa]	3.56	
		$f_{c,max}$ [MPa]	4.43	

Table 82: 6M $LiOH.H_2O + 7.5$ g NaOH-based geopolymers (7d).

29/03/2022	sample	F_{max} [kN]	f_c [MPa]	
	6M LiOH.H2O + 7.5g NaOH 7d 70°C - sample 1	7.793	24.806	
	6M LiOH.H2O + 7.5g NaOH 7d 70°C - sample 2	10.219	32.528	
	6M LiOH.H2O + 7.5g NaOH 7d 70°C - sample 3	7.545	24.016	
		$f_{c,mean}$ [MPa]	**27.12**	27 ± 5
		σ	4.70	
		3σ	14.11	
		$f_{c,min}$ [MPa]	22.41	
		$f_{c,max}$ [MPa]	31.82	

Table 83: 8M $LiOH.H_2O + 7.5$ g NaOH-based geopolymers (7d).

	sample	F_{max} [kN]	f_c [MPa]	
	8M LiOH.H2O + 7.5g NaOH 7d 70°C - sample 1	10.192	32.442	
	8M LiOH.H2O + 7.5g NaOH 7d 70°C - sample 2	9.558	30.424	
	8M LiOH.H2O + 7.5g NaOH 7d 70°C - sample 3	8.979	28.581	
		$f_{c,mean}$ [MPa]	**30.48**	30 ± 2
		σ	1.93	
		3σ	5.79	
		$f_{c,min}$ [MPa]	28.55	
		$f_{c,max}$ [MPa]	32.41	

Table 84: 6M $LiOH.H_2O + 5$ g NaOH-based geopolymers (28d).

6/04/2022	sample	F_{max} [kN]	f_c [MPa]	
	6M LiOH.H2O + 5g NaOH 28d 70°C - sample 1	14.741	46.922	
	6M LiOH.H2O + 5g NaOH 28d 70°C - sample 2	6.864	21.849	
	6M LiOH.H2O + 5g NaOH 28d 70°C - sample 3	9.576	30.481	
	6M LiOH.H2O + 5g NaOH 28d 70°C - sample 4	5.734	18.252	
	6M LiOH.H2O + 5g NaOH 28d 70°C - sample 5	10.468	33.321	
	6M LiOH.H2O + 5g NaOH 28d 70°C - sample 6	6.644	21.149	
		$f_{c,mean}$ [MPa]	**25.01**	25 ± 7
		σ	6.51	
		3σ	19.53	
		$f_{c,min}$ [MPa]	18.50	
		$f_{c,max}$ [MPa]	31.52	

Table 85: 8M $LiOH.H_2O + 5$ g NaOH-based geopolymers (28d).

6/04/2022	sample	F_{max} [kN]	f_c [MPa]	
	8M LiOH.H2O + 5g NaOH 28d 70°C - sample 1	7.977	25.392	
	8M LiOH.H2O + 5g NaOH 28d 70°C - sample 2	6.791	21.616	
	8M LiOH.H2O + 5g NaOH 28d 70°C - sample 3	7.967	25.360	
	8M LiOH.H2O + 5g NaOH 28d 70°C - sample 4	6.138	19.538	
	8M LiOH.H2O + 5g NaOH 28d 70°C - sample 5	5.945	18.924	
	8M LiOH.H2O + 5g NaOH 28d 70°C - sample 6	4.962	15.795	
		$f_{c,mean}$ [MPa]	**21.10**	21 ± 4
		σ	3.80	
		3σ	11.40	
		$f_{c,min}$ [MPa]	17.31	
		$f_{c,max}$ [MPa]	24.90	

Table 86: 8M NaOH-based geopolymers (28d).

15/04/2022	sample	F_{max} $[kN]$	f_c $[MPa]$	
	8M NaOH 28d 70°C - sample 1	1.273	4.052	
	8M NaOH 28d 70°C - sample 2	2.230	7.098	
	8M NaOH 28d 70°C - sample 3	1.329	4.230	
	8M NaOH 28d 70°C - sample 4	1.059	3.371	
	8M NaOH 28d 70°C - sample 5	1.162	3.699	
	8M NaOH 28d 70°C - sample 6	1.403	4.466	
	8M NaOH 28d 70°C - sample 7	2.677	8.521	
	8M NaOH 28d 70°C - sample 8	3.550	11.300	
		$f_{c,mean}$ $[MPa]$	**5.84**	6 ± 3
		σ	2.85	
		3σ	8.56	
		$f_{c,min}$ $[MPa]$	2.99	
		$f_{c,max}$ $[MPa]$	8.69	

Bijlage E FTIR RESULTS - CUBE SAMPLES

Table 87: 8M NaOH-based geopolymers (1d).

15/02/2022	sample	$\lambda\ [cm^{-1}]$	$\lambda\ [cm^{-1}]$	$\lambda\ [cm^{-1}]$	$\lambda\ [cm^{-1}]$
	8M NaOH 1d 70°C - sample 1	3328.89	1648.72	981.93	
	8M NaOH 1d 70°C - sample 2	3326.25		984.59	
	8M NaOH 1d 70°C - sample 3	3330.70	1433.10	986.44	
		3328.61	**1540.91**	**984.32**	

Table 88: 10M NaOH-based geopolymers (1d).

	sample	$\lambda\ [cm^{-1}]$	$\lambda\ [cm^{-1}]$	$\lambda\ [cm^{-1}]$	$\lambda\ [cm^{-1}]$
	10M NaOH 1d 70°C - sample 1	3309.27	1440.07	977.93	
	10M NaOH 1d 70°C - sample 2	3301.84	1430.56	972.64	
	10M NaOH 1d 70°C - sample 3	3301.08	1649.55	971.76	
		3304.06	**1506.73**	**974.11**	

Table 89: 12M NaOH-based geopolymers (1d).

23/02/2022	sample	$\lambda\ [cm^{-1}]$	$\lambda\ [cm^{-1}]$	$\lambda\ [cm^{-1}]$	$\lambda\ [cm^{-1}]$
	12M NaOH 1d 70°C - sample 1			968.07	
	12M NaOH 1d 70°C - sample 2	3349.96		966.93	
	12M NaOH 1d 70°C - sample 3			971.05	
		3349.96		**968.68**	

Table 90: 6M $LiOH.H_2O$ + 5 g NaOH-based geopolymers (1d).

8/03/2022	sample	$\lambda\ [cm^{-1}]$	$\lambda\ [cm^{-1}]$	$\lambda\ [cm^{-1}]$	$\lambda\ [cm^{-1}]$
	6M LiOH.H2O + 5g NaOH 1d 70°C - sample 1	3377.09		978.82	
	6M LiOH.H2O + 5g NaOH 1d 70°C - sample 2	3376.26	1646.40	977.75	
	6M LiOH.H2O + 5g NaOH 1d 70°C - sample 3	3361.25	1647.81	970.90	
	6M LiOH.H2O + 5g NaOH 1d 70°C - sample 4	3401.74		987.38	
	6M LiOH.H2O + 5g NaOH 1d 70°C - sample 5	3382.52		972.32	
	6M LiOH.H2O + 5g NaOH 1d 70°C - sample 6	3377.52	1647.96	974.96	
		3379.40	**1647.39**	**977.02**	

Table 91: 8M $LiOH.H_2O$ + 5 g NaOH-based geopolymers (1d).

23/02/2022	sample	$\lambda\ [cm^{-1}]$	$\lambda\ [cm^{-1}]$	$\lambda\ [cm^{-1}]$	$\lambda\ [cm^{-1}]$
	8M LiOH.H2O + 5g NaOH 1d 70°C - sample 1	3364.95	1642.95	970.30	
	8M LiOH.H2O + 5g NaOH 1d 70°C - sample 2	3365.80	1644.81	969.43	
	8M LiOH.H2O + 5g NaOH 1d 70°C - sample 3			975.44	
		3365.38	**1643.88**	**971.72**	

Table 92: 10M $LiOH.H_2O$ + 5 g NaOH-based geopolymers (1d).

2/03/2022	sample	$\lambda\ [cm^{-1}]$	$\lambda\ [cm^{-1}]$	$\lambda\ [cm^{-1}]$	$\lambda\ [cm^{-1}]$
	10M LiOH.H2O + 5g NaOH 1d 70°C - sample 1	3358.65	1646.69	959.96	
	10M LiOH.H2O + 5g NaOH 1d 70°C - sample 2	3371.55	1641.58	958.18	
	10M LiOH.H2O + 5g NaOH 1d 70°C - sample 3	3356.99	1638.95	954.07	691.00
		3362.40	**1642.41**	**957.40**	**691.00**

Table 93: 12M $LiOH.H_2O$ + 5 g NaOH-based geopolymers (1d).

	sample	$\lambda\ [cm^{-1}]$	$\lambda\ [cm^{-1}]$	$\lambda\ [cm^{-1}]$	$\lambda\ [cm^{-1}]$
	12M LiOH.H2O + 5g NaOH 1d 70°C - sample 1	3376.79	1635.07	951.85	693.88
	12M LiOH.H2O + 5g NaOH 1d 70°C - sample 2	3361.63	1637.82	951.57	691.28
	12M LiOH.H2O + 5g NaOH 1d 70°C - sample 3	3377.21		955.32	690.55
		3371.88	**1636.45**	**952.91**	**691.90**

Table 94: 6M $LiOH.H_2O + 2.5$ g NaOH-based geopolymers (1d).

16/03/2022	sample	$\lambda\ [cm^{-1}]$	$\lambda\ [cm^{-1}]$	$\lambda\ [cm^{-1}]$	$\lambda\ [cm^{-1}]$
	6M LiOH.H2O + 2.5g NaOH 1d 70°C - sample 1	3365.59	1643.86	1008.39	
	6M LiOH.H2O + 2.5g NaOH 1d 70°C - sample 2	3351.12	1641.77	1008.47	
	6M LiOH.H2O + 2.5g NaOH 1d 70°C - sample 3	3368.10	1641.66	1012.09	
		3361.60	**1642.43**	**1009.65**	

Table 95: 8M $LiOH.H_2O + 2.5$ g NaOH-based geopolymers (1d).

	sample	$\lambda\ [cm^{-1}]$	$\lambda\ [cm^{-1}]$	$\lambda\ [cm^{-1}]$	$\lambda\ [cm^{-1}]$
	8M LiOH.H2O + 2.5g NaOH 1d 70°C - sample 1	3366.15		979.08	
	8M LiOH.H2O + 2.5g NaOH 1d 70°C - sample 2	3370.50	1643.86	973.27	
	8M LiOH.H2O + 2.5g NaOH 1d 70°C - sample 3	3400.62	1642.21	975.04	
		3379.09	**1643.04**	**975.80**	

Table 96: CEM I 52.5R HES (1d).

22/03/2022	sample	$\lambda\ [cm^{-1}]$	$\lambda\ [cm^{-1}]$	$\lambda\ [cm^{-1}]$	$\lambda\ [cm^{-1}]$
	Holcim CEM I 52.5R HES 1d 70°C - sample 1			958.42	
	Holcim CEM I 52.5R HES 1d 70°C - sample 2			958.77	
	Holcim CEM I 52.5R HES 1d 70°C - sample 3			954.30	
				957.16	

Table 97: 6M $LiOH.H_2O + 7.5$ g NaOH-based geopolymers (1d).

23/03/2022	sample	$\lambda\ [cm^{-1}]$	$\lambda\ [cm^{-1}]$	$\lambda\ [cm^{-1}]$	$\lambda\ [cm^{-1}]$
	6M LiOH.H2O + 7.5g NaOH 1d 70°C - sample 1	3368.06	1643.02	979.67	
	6M LiOH.H2O + 7.5g NaOH 1d 70°C - sample 2	3355.53	1643.13	981.00	
	6M LiOH.H2O + 7.5g NaOH 1d 70°C - sample 3	3369.15	1643.37	983.26	
		3364.25	**1643.17**	**981.31**	

Table 98: 8M $LiOH.H_2O + 7.5$ g NaOH-based geopolymers (1d).

	sample	$\lambda\ [cm^{-1}]$	$\lambda\ [cm^{-1}]$	$\lambda\ [cm^{-1}]$	$\lambda\ [cm^{-1}]$
	8M LiOH.H2O + 7.5g NaOH 1d 70°C - sample 1	3364.19	1643.00	971.08	
	8M LiOH.H2O + 7.5g NaOH 1d 70°C - sample 2	3366.68	1642.22	959.07	
	8M LiOH.H2O + 7.5g NaOH 1d 70°C - sample 3	3355.93	1642.48	968.09	
		3362.27	**1642.57**	**966.08**	

Table 99: 8M NaOH-based geopolymers (3d).

17/02/2022	sample	$\lambda\ [cm^{-1}]$	$\lambda\ [cm^{-1}]$	$\lambda\ [cm^{-1}]$	$\lambda\ [cm^{-1}]$
	8M NaOH 3d 70°C - sample 1			984.12	
	8M NaOH 3d 70°C - sample 2	2923.28		979.02	
	8M NaOH 3d 70°C - sample 3			981.70	
		2923.28		**981.61**	

Table 100: 10M NaOH-based geopolymers (3d).

	sample	$\lambda\ [cm^{-1}]$	$\lambda\ [cm^{-1}]$	$\lambda\ [cm^{-1}]$	$\lambda\ [cm^{-1}]$
	10M NaOH 3d 70°C - sample 1			978.71	
	10M NaOH 3d 70°C - sample 2		1444.94	972.67	
	10M NaOH 3d 70°C - sample 3			976.02	
			1444.94	**975.80**	

Table 101: 12M NaOH-based geopolymers (3d).

25/02/2022	sample	$\lambda\ [cm^{-1}]$	$\lambda\ [cm^{-1}]$	$\lambda\ [cm^{-1}]$	$\lambda\ [cm^{-1}]$
	12M NaOH 3d 70°C - sample 1			969.07	
	12M NaOH 3d 70°C - sample 2			968.22	
	12M NaOH 3d 70°C - sample 3			968.60	
				968.63	

Table 102: 6M $LiOH.H_2O + 5$ g NaOH-based geopolymers (3d).

10/03/2022	sample	$\lambda\ [cm^{-1}]$	$\lambda\ [cm^{-1}]$	$\lambda\ [cm^{-1}]$	$\lambda\ [cm^{-1}]$
	6M LiOH.H2O + 5g NaOH 3d 70°C - sample 1			994.94	
	6M LiOH.H2O + 5g NaOH 3d 70°C - sample 2			991.00	
	6M LiOH.H2O + 5g NaOH 3d 70°C - sample 3			987.14	
	6M LiOH.H2O + 5g NaOH 3d 70°C - sample 4			994.37	
	6M LiOH.H2O + 5g NaOH 3d 70°C - sample 5			995.37	
	6M LiOH.H2O + 5g NaOH 3d 70°C - sample 6			999.17	
				993.67	

Table 103: 8M $LiOH.H_2O + 5$ g NaOH-based geopolymers (3d).

25/02/2022	sample	$\lambda\ [cm^{-1}]$	$\lambda\ [cm^{-1}]$	$\lambda\ [cm^{-1}]$	$\lambda\ [cm^{-1}]$
	8M LiOH.H2O + 5g NaOH 3d 70°C - sample 1	3386.19		966.01	
	8M LiOH.H2O + 5g NaOH 3d 70°C - sample 2	3360.00		974.75	
	8M LiOH.H2O + 5g NaOH 3d 70°C - sample 3	3367.81		971.72	
		3371.33		**970.83**	

Table 104: 10M $LiOH.H_2O + 5$ g NaOH-based geopolymers (3d).

4/03/2022	sample	$\lambda\ [cm^{-1}]$	$\lambda\ [cm^{-1}]$	$\lambda\ [cm^{-1}]$	$\lambda\ [cm^{-1}]$
	10M LiOH.H2O + 5g NaOH 3d 70°C - sample 1			967.15	694.92
	10M LiOH.H2O + 5g NaOH 3d 70°C - sample 2			959.83	693.41
	10M LiOH.H2O + 5g NaOH 3d 70°C - sample 3			962.94	
				963.31	**694.17**

Table 105: 12M $LiOH.H_2O + 5$ g NaOH-based geopolymers (3d).

	sample	$\lambda\ [cm^{-1}]$	$\lambda\ [cm^{-1}]$	$\lambda\ [cm^{-1}]$	$\lambda\ [cm^{-1}]$
	12M LiOH.H2O + 5g NaOH 3d 70°C - sample 1			955.62	694.49
	12M LiOH.H2O + 5g NaOH 3d 70°C - sample 2			955.03	693.27
	12M LiOH.H2O + 5g NaOH 3d 70°C - sample 3			956.35	692.35
				955.67	**693.37**

Table 106: 6M $LiOH.H_2O + 2.5$ g NaOH-based geopolymers (3d).

18/03/2022	sample	$\lambda\ [cm^{-1}]$	$\lambda\ [cm^{-1}]$	$\lambda\ [cm^{-1}]$	$\lambda\ [cm^{-1}]$
	6M LiOH.H2O + 2.5g NaOH 3d 70°C - sample 1			1008.51	
	6M LiOH.H2O + 2.5g NaOH 3d 70°C - sample 2			1006.98	
	6M LiOH.H2O + 2.5g NaOH 3d 70°C - sample 3			1010.95	
				1008.81	

Table 107: 8M $LiOH.H_2O + 2.5$ g NaOH-based geopolymers (3d).

	sample	$\lambda\ [cm^{-1}]$	$\lambda\ [cm^{-1}]$	$\lambda\ [cm^{-1}]$	$\lambda\ [cm^{-1}]$
	8M LiOH.H2O + 2.5g NaOH 3d 70°C - sample 1			976.24	
	8M LiOH.H2O + 2.5g NaOH 3d 70°C - sample 2			977.66	
	8M LiOH.H2O + 2.5g NaOH 3d 70°C - sample 3			971.03	
				974.98	

Table 108: CEM I 52.5R HES (3d).

24/03/2022	sample	$\lambda\ [cm^{-1}]$	$\lambda\ [cm^{-1}]$	$\lambda\ [cm^{-1}]$	$\lambda\ [cm^{-1}]$
	Holcim CEM I 52.5R HES 3d 70°C - sample 1			960.86	
	Holcim CEM I 52.5R HES 3d 70°C - sample 2			956.83	
	Holcim CEM I 52.5R HES 3d 70°C - sample 3			952.12	
				956.60	

Table 109: 6M $LiOH.H_2O + 7.5$ g NaOH-based geopolymers (3d).

25/03/2022	sample	$\lambda\ [cm^{-1}]$	$\lambda\ [cm^{-1}]$	$\lambda\ [cm^{-1}]$	$\lambda\ [cm^{-1}]$
	6M LiOH.H2O + 7.5g NaOH 3d 70°C - sample 1			984.41	
	6M LiOH.H2O + 7.5g NaOH 3d 70°C - sample 2	3386.06		980.34	
	6M LiOH.H2O + 7.5g NaOH 3d 70°C - sample 3	3387.76		984.42	
		3386.91		**983.06**	

Table 110: 8M $LiOH.H_2O + 7.5$ g NaOH-based geopolymers (3d).

	sample	$\lambda\ [cm^{-1}]$	$\lambda\ [cm^{-1}]$	$\lambda\ [cm^{-1}]$	$\lambda\ [cm^{-1}]$
	8M LiOH.H2O + 7.5g NaOH 3d 70°C - sample 1			967.41	
	8M LiOH.H2O + 7.5g NaOH 3d 70°C - sample 2			970.85	
	8M LiOH.H2O + 7.5g NaOH 3d 70°C - sample 3			969.03	
				969.10	

Table 111: 8M NaOH-based geopolymers (7d).

21/02/2022	sample	$\lambda\ [cm^{-1}]$	$\lambda\ [cm^{-1}]$	$\lambda\ [cm^{-1}]$	$\lambda\ [cm^{-1}]$
	8M NaOH 7d 70°C - sample 1			979.45	
	8M NaOH 7d 70°C - sample 2			980.55	
	8M NaOH 7d 70°C - sample 3			987.75	
				982.58	

Table 112: 10M NaOH-based geopolymers (7d).

		$\lambda\ [cm^{-1}]$	$\lambda\ [cm^{-1}]$	$\lambda\ [cm^{-1}]$	$\lambda\ [cm^{-1}]$
	10M NaOH 7d 70°C - sample 1		1446.93	975.66	
	10M NaOH 7d 70°C - sample 2			972.32	
	10M NaOH 7d 70°C - sample 3			975.82	
			1446.93	**974.60**	

Table 113: 12M NaOH-based geopolymers (7d).

1/03/2022		$\lambda\ [cm^{-1}]$	$\lambda\ [cm^{-1}]$	$\lambda\ [cm^{-1}]$	$\lambda\ [cm^{-1}]$
	12M NaOH 7d 70°C - sample 1			975.00	
	12M NaOH 7d 70°C - sample 2			968.48	
	12M NaOH 7d 70°C - sample 3			975.52	
				973.00	

Table 114: 6M $LiOH.H_2O + 5$ g NaOH-based geopolymers (7d).

14/03/2022	sample	$\lambda\ [cm^{-1}]$	$\lambda\ [cm^{-1}]$	$\lambda\ [cm^{-1}]$	$\lambda\ [cm^{-1}]$
	6M LiOH.H2O + 5g NaOH 7d 70°C - sample 1			994.93	
	6M LiOH.H2O + 5g NaOH 7d 70°C - sample 2			975.57	
	6M LiOH.H2O + 5g NaOH 7d 70°C - sample 3			987.72	
	6M LiOH.H2O + 5g NaOH 7d 70°C - sample 4			991.11	
	6M LiOH.H2O + 5g NaOH 7d 70°C - sample 5			995.25	
	6M LiOH.H2O + 5g NaOH 7d 70°C - sample 6			986.52	
				988.52	

Table 115: 8M $LiOH.H_2O + 5$ g NaOH-based geopolymers (7d).

1/03/2022		$\lambda\ [cm^{-1}]$	$\lambda\ [cm^{-1}]$	$\lambda\ [cm^{-1}]$	$\lambda\ [cm^{-1}]$
	8M LiOH.H2O + 5g NaOH 7d 70°C - sample 1			975.29	
	8M LiOH.H2O + 5g NaOH 7d 70°C - sample 2			975.32	
	8M LiOH.H2O + 5g NaOH 7d 70°C - sample 3			977.86	
				976.16	

Table 116: 10M $LiOH.H_2O + 5$ g NaOH-based geopolymers (7d).

8/03/2022		$\lambda\ [cm^{-1}]$	$\lambda\ [cm^{-1}]$	$\lambda\ [cm^{-1}]$	$\lambda\ [cm^{-1}]$
	10M LiOH.H2O + 5g NaOH 7d 70°C - sample 1			965.79	
	10M LiOH.H2O + 5g NaOH 7d 70°C - sample 2			962.10	
	10M LiOH.H2O + 5g NaOH 7d 70°C - sample 3			961.59	
				963.16	

Table 117: 12M $LiOH.H_2O + 5$ g NaOH-based geopolymers (7d).

		$\lambda\ [cm^{-1}]$	$\lambda\ [cm^{-1}]$	$\lambda\ [cm^{-1}]$	$\lambda\ [cm^{-1}]$
	12M LiOH.H2O + 5g NaOH 7d 70°C - sample 1			960.47	695.34
	12M LiOH.H2O + 5g NaOH 7d 70°C - sample 2			955.57	694.01
	12M LiOH.H2O + 5g NaOH 7d 70°C - sample 3			954.63	693.05
				956.89	**694.13**

Table 118: 6M $LiOH.H_2O + 2.5$ g NaOH-based geopolymers (7d).

22/03/2022	sample	$\lambda\ [cm^{-1}]$	$\lambda\ [cm^{-1}]$	$\lambda\ [cm^{-1}]$	$\lambda\ [cm^{-1}]$
	6M LiOH.H2O + 2.5g NaOH 7d 70°C - sample 1			1009.98	
	6M LiOH.H2O + 2.5g NaOH 7d 70°C - sample 2			1011.58	
	6M LiOH.H2O + 2.5g NaOH 7d 70°C - sample 3			1011.71	
				1011.09	

Table 119: 8M $LiOH.H_2O + 2.5$ g NaOH-based geopolymers (7d).

	sample	$\lambda\ [cm^{-1}]$	$\lambda\ [cm^{-1}]$	$\lambda\ [cm^{-1}]$	$\lambda\ [cm^{-1}]$
	8M LiOH.H2O + 2.5g NaOH 7d 70°C - sample 1			975.51	
	8M LiOH.H2O + 2.5g NaOH 7d 70°C - sample 2			979.51	
	8M LiOH.H2O + 2.5g NaOH 7d 70°C - sample 3			978.90	
				977.97	

Table 120: CEM I 52.5R HES (7d).

28/03/2022	sample	$\lambda\ [cm^{-1}]$	$\lambda\ [cm^{-1}]$	$\lambda\ [cm^{-1}]$	$\lambda\ [cm^{-1}]$
	Holcim CEM I 52.5R HES 7d 70°C - sample 1			959.53	
	Holcim CEM I 52.5R HES 7d 70°C - sample 2			958.72	
	Holcim CEM I 52.5R HES 7d 70°C - sample 3			958.69	
	Holcim CEM I 52.5R HES 7d 70°C - sample 4		1737.87	955.97	
	Holcim CEM I 52.5R HES 7d 70°C - sample 5		1738.55	956.03	
	Holcim CEM I 52.5R HES 7d 70°C - sample 6	3643.08	1738.50	956.07	
		3643.08	**1738.31**	**957.50**	

Table 121: 6M $LiOH.H_2O + 7.5$ g NaOH-based geopolymers (7d).

29/03/2022	sample	$\lambda\ [cm^{-1}]$	$\lambda\ [cm^{-1}]$	$\lambda\ [cm^{-1}]$	$\lambda\ [cm^{-1}]$
	6M LiOH.H2O + 7.5g NaOH 7d 70°C - sample 1			993.12	
	6M LiOH.H2O + 7.5g NaOH 7d 70°C - sample 2			989.22	
	6M LiOH.H2O + 7.5g NaOH 7d 70°C - sample 3			988.83	
				990.39	

Table 122: 8M $LiOH.H_2O + 7.5$ g NaOH-based geopolymers (7d).

		$\lambda\ [cm^{-1}]$	$\lambda\ [cm^{-1}]$	$\lambda\ [cm^{-1}]$	$\lambda\ [cm^{-1}]$
	8M LiOH.H2O + 7.5g NaOH 7d 70°C - sample 1			984.38	
	8M LiOH.H2O + 7.5g NaOH 7d 70°C - sample 2			985.42	
	8M LiOH.H2O + 7.5g NaOH 7d 70°C - sample 3			982.82	
				984.21	

Table 123: 6M $LiOH.H_2O + 5$ g NaOH-based geopolymers (28d).

30/03/2022	sample	$\lambda\ [cm^{-1}]$	$\lambda\ [cm^{-1}]$	$\lambda\ [cm^{-1}]$	$\lambda\ [cm^{-1}]$
	6M LiOH.H2O + 5g NaOH 28d 70°C - sample 1			986.53	
	6M LiOH.H2O + 5g NaOH 28d 70°C - sample 2			990.59	
	6M LiOH.H2O + 5g NaOH 28d 70°C - sample 3			991.59	
	6M LiOH.H2O + 5g NaOH 28d 70°C - sample 4			992.48	
	6M LiOH.H2O + 5g NaOH 28d 70°C - sample 5			989.24	
	6M LiOH.H2O + 5g NaOH 28d 70°C - sample 6			991.78	
				990.37	

Table 124: 8M $LiOH.H_2O + 5$ g NaOH-based geopolymers (28d).

30/03/2022	sample	$\lambda\ [cm^{-1}]$	$\lambda\ [cm^{-1}]$	$\lambda\ [cm^{-1}]$	$\lambda\ [cm^{-1}]$
	8M LiOH.H2O + 5g NaOH 28d 70°C - sample 1			980.56	696.05
	8M LiOH.H2O + 5g NaOH 28d 70°C - sample 2			979.11	699.41
	8M LiOH.H2O + 5g NaOH 28d 70°C - sample 3			978.91	
	8M LiOH.H2O + 5g NaOH 28d 70°C - sample 4			979.89	
	8M LiOH.H2O + 5g NaOH 28d 70°C - sample 5			979.04	695.64
	8M LiOH.H2O + 5g NaOH 28d 70°C - sample 6			980.50	
				979.67	**697.03**

Table 125: CEM I 52.5R HES (28d).

6/04/2022	sample	$\lambda\ [cm^{-1}]$	$\lambda\ [cm^{-1}]$	$\lambda\ [cm^{-1}]$	$\lambda\ [cm^{-1}]$
	Holcim CEM I 52,5R HES 28d 70°C - sample 1			960.72	
	Holcim CEM I 52,5R HES 28d 70°C - sample 2	3642.49		950.08	
	Holcim CEM I 52,5R HES 28d 70°C - sample 3			949.75	
	Holcim CEM I 52,5R HES 28d 70°C - sample 4			948.76	
	Holcim CEM I 52,5R HES 28d 70°C - sample 5			956.58	
	Holcim CEM I 52,5R HES 28d 70°C - sample 6			951.95	
		3642.49		**952.97**	

Bijlage F FTIR RESULTS - CYLINDRICAL SAMPLES

Table 126: 6M $LiOH.H_2O + 5$ g NaOH-based geopolymers (1d).

10/03/2022	sample	$\lambda\ [cm^{-1}]$	$\lambda\ [cm^{-1}]$	$\lambda\ [cm^{-1}]$	$\lambda\ [cm^{-1}]$
	6M LiOH.H2O + 5g NaOH 1d 70°C - sample 1	3421.78		991.43	
	6M LiOH.H2O + 5g NaOH 1d 70°C - sample 2	3421.64		989.34	
	6M LiOH.H2O + 5g NaOH 1d 70°C - sample 3			985.74	
		3421.71		**988.84**	

Table 127: 8M $LiOH.H_2O + 5$ g NaOH-based geopolymers (1d).

sample	$\lambda\ [cm^{-1}]$	$\lambda\ [cm^{-1}]$	$\lambda\ [cm^{-1}]$	$\lambda\ [cm^{-1}]$
8M LiOH.H2O + 5g NaOH 1d 70°C - sample 1	3406.10		976.41	
8M LiOH.H2O + 5g NaOH 1d 70°C - sample 2	3406.04		970.91	
8M LiOH.H2O + 5g NaOH 1d 70°C - sample 3	3390.18		970.13	
	3400.77		**972.48**	

Table 128: 6M $LiOH.H_2O + 2.5$ g NaOH-based geopolymers (1d).

16/03/2022	sample	$\lambda\ [cm^{-1}]$	$\lambda\ [cm^{-1}]$	$\lambda\ [cm^{-1}]$	$\lambda\ [cm^{-1}]$
	6M LiOH.H2O + 2.5g NaOH 1d 70°C - sample 1	3357.39	1647.82	973.13	
	6M LiOH.H2O + 2.5g NaOH 1d 70°C - sample 2	3365.93		999.72	
	6M LiOH.H2O + 2.5g NaOH 1d 70°C - sample 3	3365.92		995.42	
		3363.08	**1647.82**	**989.42**	

Table 129: 8M $LiOH.H_2O + 2.5$ g NaOH-based geopolymers (1d).

sample	$\lambda\ [cm^{-1}]$	$\lambda\ [cm^{-1}]$	$\lambda\ [cm^{-1}]$	$\lambda\ [cm^{-1}]$
8M LiOH.H2O + 2.5g NaOH 1d 70°C - sample 1			972.75	
8M LiOH.H2O + 2.5g NaOH 1d 70°C - sample 2	3374.46		968.73	
8M LiOH.H2O + 2.5g NaOH 1d 70°C - sample 3	3376.99		974.93	
	3375.73		**972.14**	

Table 130: 8M NaOH-based geopolymers (1d).

17/03/2022	sample	$\lambda\ [cm^{-1}]$	$\lambda\ [cm^{-1}]$	$\lambda\ [cm^{-1}]$	$\lambda\ [cm^{-1}]$
	8M NaOH 1d 70°C - sample 1	3385.82		974.69	
	8M NaOH 1d 70°C - sample 2	3364.69	1644.87	968.11	
	8M NaOH 1d 70°C - sample 3	3387.44		972.64	
		3379.32	**1644.87**	**971.81**	

Table 131: 6M $LiOH.H_2O + 7.5$ g NaOH-based geopolymers (1d).

23/03/2022	sample	$\lambda\ [cm^{-1}]$	$\lambda\ [cm^{-1}]$	$\lambda\ [cm^{-1}]$	$\lambda\ [cm^{-1}]$
	6M LiOH.H2O + 7.5g NaOH 1d 70°C - sample 1	3367.64	1643.64	975.54	
	6M LiOH.H2O + 7.5g NaOH 1d 70°C - sample 2	3368.64		980.06	
	6M LiOH.H2O + 7.5g NaOH 1d 70°C - sample 3			980.51	
		3368.14	**1643.64**	**978.70**	

Table 132: 8M $LiOH.H_2O + 7.5$ g NaOH-based geopolymers (1d).

sample	$\lambda\ [cm^{-1}]$	$\lambda\ [cm^{-1}]$	$\lambda\ [cm^{-1}]$	$\lambda\ [cm^{-1}]$
8M LiOH.H2O + 7.5g NaOH 1d 70°C - sample 1			975.35	
8M LiOH.H2O + 7.5g NaOH 1d 70°C - sample 2	3362.90		974.96	
8M LiOH.H2O + 7.5g NaOH 1d 70°C - sample 3	3344.11		968.34	
	3353.51		**972.88**	

Table 133: 6M $LiOH.H_2O + 5$ g NaOH-based geopolymers (3d).

12/03/2022	sample	$\lambda\ [cm^{-1}]$	$\lambda\ [cm^{-1}]$	$\lambda\ [cm^{-1}]$	$\lambda\ [cm^{-1}]$
	6M LiOH.H2O + 5g NaOH 3d 70°C - sample 1			992.86	
	6M LiOH.H2O + 5g NaOH 3d 70°C - sample 2			988.29	
	6M LiOH.H2O + 5g NaOH 3d 70°C - sample 3			983.82	
				988.32	

Table 134: 8M $LiOH.H_2O + 5$ g NaOH-based geopolymers (3d).

	sample	$\lambda\ [cm^{-1}]$	$\lambda\ [cm^{-1}]$	$\lambda\ [cm^{-1}]$	$\lambda\ [cm^{-1}]$
	8M LiOH.H2O + 5g NaOH 3d 70°C - sample 1			974.93	
	8M LiOH.H2O + 5g NaOH 3d 70°C - sample 2			959.78	
	8M LiOH.H2O + 5g NaOH 3d 70°C - sample 3			959.71	
				964.81	

Table 135: 6M $LiOH.H_2O + 2.5$ g NaOH-based geopolymers (3d).

18/03/2022	sample	$\lambda\ [cm^{-1}]$	$\lambda\ [cm^{-1}]$	$\lambda\ [cm^{-1}]$	$\lambda\ [cm^{-1}]$
	6M LiOH.H2O + 2.5g NaOH 3d 70°C - sample 1			1020.34	
	6M LiOH.H2O + 2.5g NaOH 3d 70°C - sample 2			1011.05	
	6M LiOH.H2O + 2.5g NaOH 3d 70°C - sample 3			1019.47	
				1016.95	

Table 136: 8M $LiOH.H_2O + 2.5$ g NaOH-based geopolymers (3d).

	sample	$\lambda\ [cm^{-1}]$	$\lambda\ [cm^{-1}]$	$\lambda\ [cm^{-1}]$	$\lambda\ [cm^{-1}]$
	8M LiOH.H2O + 2.5g NaOH 3d 70°C - sample 1			982.65	
	8M LiOH.H2O + 2.5g NaOH 3d 70°C - sample 2			988.11	
	8M LiOH.H2O + 2.5g NaOH 3d 70°C - sample 3			976.07	
				982.28	

Table 137: 8M NaOH-based geopolymers (3d).

19/03/2022	sample	$\lambda\ [cm^{-1}]$	$\lambda\ [cm^{-1}]$	$\lambda\ [cm^{-1}]$	$\lambda\ [cm^{-1}]$
	8M NaOH 3d 70°C - sample 1			984.29	
	8M NaOH 3d 70°C - sample 2			979.13	
	8M NaOH 3d 70°C - sample 3			985.13	
				982.85	

Table 138: 6M $LiOH.H_2O + 7.5$ g NaOH-based geopolymers (3d).

25/03/2022	sample	$\lambda\ [cm^{-1}]$	$\lambda\ [cm^{-1}]$	$\lambda\ [cm^{-1}]$	$\lambda\ [cm^{-1}]$
	6M LiOH.H2O + 7.5g NaOH 3d 70°C - sample 1			972.12	
	6M LiOH.H2O + 7.5g NaOH 3d 70°C - sample 2			971.97	
	6M LiOH.H2O + 7.5g NaOH 3d 70°C - sample 3			979.25	
				974.45	

Table 139: 8M $LiOH.H_2O + 7.5$ g NaOH-based geopolymers (3d).

	sample	$\lambda\ [cm^{-1}]$	$\lambda\ [cm^{-1}]$	$\lambda\ [cm^{-1}]$	$\lambda\ [cm^{-1}]$
	8M LiOH.H2O + 7.5g NaOH 3d 70°C - sample 1			971.18	
	8M LiOH.H2O + 7.5g NaOH 3d 70°C - sample 2			968.71	
	8M LiOH.H2O + 7.5g NaOH 3d 70°C - sample 3			968.37	
				969.42	

Table 140: 6M $LiOH.H_2O + 5$ g NaOH-based geopolymers (7d).

16/03/2022	sample	$\lambda\ [cm^{-1}]$	$\lambda\ [cm^{-1}]$	$\lambda\ [cm^{-1}]$	$\lambda\ [cm^{-1}]$
	6M LiOH.H2O + 5g NaOH 7d 70°C - sample 1			994.44	
	6M LiOH.H2O + 5g NaOH 7d 70°C - sample 2			993.94	
	6M LiOH.H2O + 5g NaOH 7d 70°C - sample 3			991.83	
				993.40	

Table 141: 8M $LiOH.H_2O + 5$ g NaOH-based geopolymers (7d).

	sample	$\lambda\ [cm^{-1}]$	$\lambda\ [cm^{-1}]$	$\lambda\ [cm^{-1}]$	$\lambda\ [cm^{-1}]$
	8M LiOH.H2O + 5g NaOH 7d 70°C - sample 1			974.23	
	8M LiOH.H2O + 5g NaOH 7d 70°C - sample 2			973.18	
	8M LiOH.H2O + 5g NaOH 7d 70°C - sample 3			972.89	
				973.43	

Table 142: 6M $LiOH.H_2O + 2.5$ g NaOH-based geopolymers (7d).

22/03/2022	sample	$\lambda\ [cm^{-1}]$	$\lambda\ [cm^{-1}]$	$\lambda\ [cm^{-1}]$	$\lambda\ [cm^{-1}]$
	6M LiOH.H2O + 2.5g NaOH 7d 70°C - sample 1			1011.37	
	6M LiOH.H2O + 2.5g NaOH 7d 70°C - sample 2			1011.04	
	6M LiOH.H2O + 2.5g NaOH 7d 70°C - sample 3			1011.17	
				1011.19	

Table 143: 8M $LiOH.H_2O + 2.5$ g NaOH-based geopolymers (7d).

	sample	$\lambda\ [cm^{-1}]$	$\lambda\ [cm^{-1}]$	$\lambda\ [cm^{-1}]$	$\lambda\ [cm^{-1}]$
	8M LiOH.H2O + 2.5g NaOH 7d 70°C - sample 1			967.39	
	8M LiOH.H2O + 2.5g NaOH 7d 70°C - sample 2			980.17	
	8M LiOH.H2O + 2.5g NaOH 7d 70°C - sample 3			973.65	
				973.74	

Table 144: 8M NaOH-based geopolymers (7d).

23/03/2022	sample	$\lambda\ [cm^{-1}]$	$\lambda\ [cm^{-1}]$	$\lambda\ [cm^{-1}]$	$\lambda\ [cm^{-1}]$
	8M NaOH 7d 70°C - sample 1			987.69	
	8M NaOH 7d 70°C - sample 2			981.35	
	8M NaOH 7d 70°C - sample 3			990.43	
				986.49	

Table 145: 6M $LiOH.H_2O + 7.5$ g NaOH-based geopolymers (7d).

29/03/2022	sample	$\lambda\ [cm^{-1}]$	$\lambda\ [cm^{-1}]$	$\lambda\ [cm^{-1}]$	$\lambda\ [cm^{-1}]$
	6M LiOH.H2O + 7.5g NaOH 7d 70°C - sample 1			981.88	
	6M LiOH.H2O + 7.5g NaOH 7d 70°C - sample 2			984.08	
	6M LiOH.H2O + 7.5g NaOH 7d 70°C - sample 3			989.52	
				985.16	

Table 146: 8M $LiOH.H_2O + 7.5$ g NaOH-based geopolymers (7d).

	sample	$\lambda\ [cm^{-1}]$	$\lambda\ [cm^{-1}]$	$\lambda\ [cm^{-1}]$	$\lambda\ [cm^{-1}]$
	8M LiOH.H2O + 7.5g NaOH 7d 70°C - sample 1			991.76	
	8M LiOH.H2O + 7.5g NaOH 7d 70°C - sample 2			986.57	
	8M LiOH.H2O + 7.5g NaOH 7d 70°C - sample 3			982.99	
				987.11	

Table 147: 6M $LiOH.H_2O + 5$ g NaOH-based geopolymers (28d).

6/04/2022	sample	$\lambda\ [cm^{-1}]$	$\lambda\ [cm^{-1}]$	$\lambda\ [cm^{-1}]$	$\lambda\ [cm^{-1}]$
	6M LiOH.H2O + 5g NaOH 28d 70°C - sample 1			994.34	
	6M LiOH.H2O + 5g NaOH 28d 70°C - sample 2			1004.01	
	6M LiOH.H2O + 5g NaOH 28d 70°C - sample 3			1001.20	
	6M LiOH.H2O + 5g NaOH 28d 70°C - sample 4			996.40	
	6M LiOH.H2O + 5g NaOH 28d 70°C - sample 5			993.47	
	6M LiOH.H2O + 5g NaOH 28d 70°C - sample 6			994.93	
				997.39	

Table 148: 8M $LiOH.H_2O + 5$ g NaOH-based geopolymers (28d).

6/04/2022	sample	$\lambda\ [cm^{-1}]$	$\lambda\ [cm^{-1}]$	$\lambda\ [cm^{-1}]$	$\lambda\ [cm^{-1}]$
	8M LiOH.H2O + 5g NaOH 28d 70°C - sample 1			984.84	
	8M LiOH.H2O + 5g NaOH 28d 70°C - sample 2			989.66	
	8M LiOH.H2O + 5g NaOH 28d 70°C - sample 3			989.58	
	8M LiOH.H2O + 5g NaOH 28d 70°C - sample 4			990.28	
	8M LiOH.H2O + 5g NaOH 28d 70°C - sample 5			992.82	
	8M LiOH.H2O + 5g NaOH 28d 70°C - sample 6			987.65	
				989.14	

Table 149: 8M NaOH-based geopolymers (28d).

15/04/2022	sample	$\lambda\ [cm^{-1}]$	$\lambda\ [cm^{-1}]$	$\lambda\ [cm^{-1}]$	$\lambda\ [cm^{-1}]$
	8M NaOH 28d 70°C - sample 1			987.39	809.00
	8M NaOH 28d 70°C - sample 2			984.24	809.00
	8M NaOH 28d 70°C - sample 3			990.58	808.00
	8M NaOH 28d 70°C - sample 4			988.01	809.00
	8M NaOH 28d 70°C - sample 5			988.79	809.00
	8M NaOH 28d 70°C - sample 6			991.33	809.00
	8M NaOH 28d 70°C - sample 7			992.29	809.00
	8M NaOH 28d 70°C - sample 8			991.32	809.00
				989.24	**808.88**

FACULTEIT INDUSTRIËLE INGENIEURSWETENSCHAPPEN
CAMPUS BRUGGE
Spoorwegstraat 12
8200 BRUGGE, België
tel. + 32 50 66 48 00
iiw.brugge@kuleuven.be
www.iiw.kuleuven.be